ULTRAFAST CHARGE TRANSFER DYNAMICS IN QUANTUM DOTS AND QUANTUM DOTS/MOLECULAR ADSORBATE

By

PARTHA MAITY

CHEM01201104032

Bhabha Atomic Research Centre, Mumbai

A thesis submitted to the
Board of Studies in Chemical Sciences

In partial fulfillment of requirements
for the Degree of

DOCTOR OF PHILOSOPHY

of

HOMI BHABHA NATIONAL INSTITUTE

April, 2016

Homi Bhabha National Institute

Recommendations of the Viva Voce Committee

As members of the Viva Voce Committee, we certify that we have read the dissertation prepared by **Partha Maity** entitled **"Ultrafast Charge Transfer Dynamics in Quantum Dots and Quantum Dots/Molecular Adsorbate"** and recommend that it may be accepted as fulfilling the thesis requirement for the award of Degree of Doctor of Philosophy.

11/08/2016 Date:

Chairman - Prof. D. K. Palit

Date: 11/8/201

Guide/Convener - Prof. H. N. Ghosh

Date: 11/8/16

Examiner - Prof. A. Pandey

Date: 11/08/201

(A. K. Tyagi

Member 1 - Prof. A. K. Tyagi

Date: 11/8/2016

Member 2 - Prof. A. C. Bhasikuttan

Date: 11/8/2016

Member 3 - Prof. C. N. Patra

Final approval and acceptance of this dissertation is contingent upon the candidate's submission of the final copies of the thesis to HBNI.

I hereby certify that I have read this thesis prepared under my direction and recommend that it may be accepted as fulfilling the thesis requirement.

Date: 11/08/2016

Place: MUMBAI

Signature of Guide

STATEMENT BY AUTHOR

This dissertation has been submitted in partial fulfillment of requirements for an advanced degree at Homi Bhabha National Institute (HBNI) and is deposited in the Library to be made available to borrowers under rules of the HBNI.

Brief quotations from this dissertation are allowable without special permission, provided that accurate acknowledgement of source is made. Requests for permission for extended quotation from or reproduction of this manuscript in whole or in part may be granted by the Competent Authority of HBNI when in his or her judgment the proposed use of the material is in the interests of scholarship. In all other instances, however, permission must be obtained from the author.

Partha Maity

(Partha Maity)

DECLARATION

I, hereby declare that the investigation presented in the thesis has been carried out by me. The work is original and has not been submitted earlier as a whole or in part for a degree / diploma at this or any other Institution / University.

Partha Maity

(Partha Maity)

List of Publications arising from the thesis

Journal:

1. "Ultrafast Hole and Electron Transfer Dynamics in CdS/Di-bromofluorescein (DBF) Super-Sensitized Quantum Dot Solar Cell Materials", **Partha Maity**, Tushar Debnath and Hirendra N. Ghosh, *J. Phys. Chem. Lett.*, **2013**, *4*, 4020−4025.*

2. "Cascading Electron and Hole Transfer Dynamics in CdS/CdTe Core-Shell Sensitized Bromo-Pyrogallol Red (Br-PGR): Slow Charge Recombination in Type II Regime", **Partha Maity**, Tushar Debnath, Uday Chopra, Hirendra N. Ghosh, *Nanoscale*, **2015**, *7*, 2698-2707.*

3. "Slow Electron Cooling Dynamics Mediated by Electron-Hole Decoupling in Highly Luminescent CdS_xSe_{1-x} Alloy Quantum Dots", **Partha Maity**, Tushar Debnath and Hirendra N. Ghosh, *J. Phys. Chem. C,* **2015**, *119*, 10785−10792.*

4. "Ultrafast Charge Carrier Delocalization in CdSe/CdS Quasi-Type II and CdS/CdSe Inverted Type I Core–Shell: A Structural Analysis through Carrier-Quenching Study", **Partha Maity**, Tushar Debnath and Hirendra N. Ghosh, *J. Phys. Chem. C*, **2015**, *119*, 26202-26211.*

5. "Slow Electron Cooling Dynamics of Highly Luminescent CdS_xSe_{1-x} Alloy Quantum Dot", **Partha Maity**, Tushar Debnath and Hirendra N. Ghosh, *Ultrafast Phenomena XIX*, **2014**, Springer Proceedings in Physics 162 (pp-275-278), **DOI 10.1007/978-3-319-13242-6_67.***

6. "Charge De-localization in the Cascade Band Structure CdS/CdSe and CdS/CdTe Core-Shell Sensitized with Re (I)−polypyridyl Complex", **Partha Maity**, Tushar Debnath, Tanmay Banerjee Amitava Das, and Hirendra. N. Ghosh, *J. Phys. Chem. C*, **2016**, 120, 10051-10061.*

7. "Ultrafast Charge Transfer Dynamics in Totally Inorganic Colloidal $CsPbBr_3$ Perovskite Quantum Dots Sensitized by 4,5-di bromo fluorescence" **Partha Maity**, Jayanta Dana and Hirendra Nath Ghosh, (**Accepted in Ultrafast Phenomena 2016**).*

8. "Multiple Charge Transfer Dynamics in Colloidal $CsPbBr_3$ Perovskite Quantum Dots Sensitized Molecular Adsorbate", **Partha Maity**, Jayanta Dana and Hirendra Nath Ghosh, *J. Phys. Chem. C*, **2016,** 120 (Accepted)*

9. "Improving the Solar Cell Efficiency Utilizing CdSSe Alloy Quantum Dots" **Partha Maity**, Sourav Maiti, Tushar Debnath, Sourav K. Guin, Jayanta Dana and Hirendra Nath Ghosh, *J. Phys. Chem. C*, **2016** Submitted.*

10. "Hole Delocalization Develops Exciton Population and Extend of Charge Separation in Highly Luminescent CdSe rich $Cd_xZn_{1-x}Se$ Gradient Alloy QD" **Partha Maity**, Jayanta Dana and Hirendra Nath Ghosh, *J. Phys. Chem. C*, **2016** Submitted.*

11. "Sensitization of BODIPY Molecule through Förster Resonance Energy Transfer from Photo-excited CdS Quantum Dot" **Partha Maity**, Tushar Debnath, Thumuganti Gayathri, Surya Prakash Singh, and Hirendra N. Ghosh, *Chemistry-A European Journal* (Submitted).*

Conferences:

1. "Cascading Electron and Hole Transfer Dynamics in CdS/CdTe Core-Shell Sensitized Bromo-Pyrogallol Red (Br-PGR): Slow Charge Recombination in Type II Regime", **Partha Maity**, Tushar Debnath, Uday Chopra, Hirendra N. Ghosh, *Trombay Symposium on Radiation & Photochemistry (**TSRP-2014**)*, BARC, Mumbai, India.*

2. "Charge De-localization in the Cascade Band Structure CdS/CdSe and CdS/CdTe Core-Shell Sensitized with Re (I)–polypyridyl Complex", **Partha Maity**, Tushar Debnath, Tanmay

Banerjee Amitava Das, and Hirendra. N. Ghosh, *16th CRSI National Symposium in Chemistry (**CRSI-2014**)*, IIT Bombay, India.*

3. "Ultrafast Hole and Electron Transfer Dynamics in CdS/Di-bromofluorescein (DBF) Super-Sensitized Quantum Dot Solar Cell Materials", **Partha Maity**, Tushar Debnath and Hirendra N. Ghosh, *Sixth International Conference on Nano Science and Technology (**ICONSAT-2014**)*, INST Chandigarh, India.*

4. "Slow Electron Cooling Dynamics of Highly Luminescent CdS_xSe_{1-x} Alloy Quantum Dot", **Partha Maity**, Tushar Debnath and Hirendra N. Ghosh, *19th International Conferences on Ultrafast Phenomena (**UP-2014**)*, Okinawa, Japan.*

5. " Sensitization of BODIPY Molecule through Förster Resonance Energy Transfer from Photo-excited CdS Quantum Dot" **Partha Maity**, Tushar Debnath, Thumuganti Gayathri, Surya Prakash Singh, and Hirendra N. Ghosh, *Interdisciplinary Symposium for Materials Chemistry (**ISMC-2014**)*, BARC, Mumbai, India.*

6. "Hole Delocalization Develops Exciton Population and Extend of Charge Separation in Highly Luminescent CdSe rich $Cd_xZn_{1-x}Se$ Gradient Alloy QD" **Partha Maity**, Jayanta Dana and Hirendra Nath Ghosh, *Frontiers in Advanced Materials **(FAM-2015)***, IISC, Bangalore, India.*

7. "Ultrafast Charge Carrier Delocalization in CdSe/CdS Quasi-Type II and CdS/CdSe Inverted Type I Core–Shell: A Structural Analysis through Carrier-Quenching Study", **Partha Maity**, Tushar Debnath and Hirendra N. Ghosh, *Trombay Symposium on Radiation & Photochemistry (**TSRP-2016**)*, BARC, Mumbai, India.*

Other / Co-author Publications:

1. "Ultrafast Electron-Transfer and -Trapping Dynamics in the Inter-Band-Gap States of ZrO_2 Nanoparticles Sensitized by Baicalein", **Partha Maity**, Tushar Debnath, Arshad Akbar, Sandeep Verma, and Hirendra N. Ghosh, *J. Phys. Chem. C,* **2013**, *117*, 17531−17539.

2. "Extensive Reduction in Back Electron Transfer Reaction in Newly Synthesized Twisted Intramolecular Charge Transfer (TICT) Coumarin Dye Sensitized TiO_2 Nanoparticles/Film: A Femtosecond Transient Absorption Study" Tushar Debnath, **Partha Maity**, Hyacintha Lobo, Balvant Singh, Ganapati S. Shankarling, and Hirendra N. Ghosh, *Chem. Euro. Journal*., **2014**, *20 (12)*, 3510-3519.

3. "Electron Trap to Electron Storage Center in Specially Aligned Mn-Doped CdSe d-Dot: A Step Forward in the Design of Higher Efficient Quantum-Dot Solar Cell", Tushar Debnath, **Partha Maity**, Sourav Maiti, Hirendra N. Ghosh, *J. Phys. Chem. Lett*., **2014**, *5*, 2836-2842.

4. "Super Sensitization: Grand Charge (Hole/Electron) Separation in ATC Dye Sensitized CdSe, CdSe/ZnS Type-I, and CdSe/CdTe Type-II Core–Shell Quantum Dots", Tushar Debnath, **Partha Maity**, Hirendra N. Ghosh, *Chemistry-A European Journal*, **2014**, *20 (41)*, 13305-13313.

5. Restriction of Molecular Rotation and Intramolecular Charge Distribution in the Photo-Excited State of Coumarin Dyes on Gold (Au) Nanoparticle Surface", Jayanta Dana, Tushar Debnath, **Partha Maity**, Hirendra N. Ghosh, " *J. Phys. Chem. C,* **2015**, *119* , 2046–2052.

6. "Restriction of Molecular Twisting on a Gold Nanoparticle Surface", Tushar Debnath, Jayanta Dana, **Partha Maity**, Hyacintha Lobo, Ganapati S. Shankarling, Hirendra N. Ghosh, *Chemistry-A European Journal*, **2015**, *21 (15)*, 5704-5708.

7. "Ultrafast Electron Injection, Hole Transfer, and Charge Recombination Dynamics in CdSe QD Super-Sensitized Re (I)–Polypyridyl Complexes with Catechol and Resorcinol Moiety:

Effect of Coupling",Tushar Debnath, **Partha Maity**, Tanmoy Banerjee, Amitava Das, Hirendra N. Ghosh. *J. Phys. Chem. C,* **2015**, *119*, 3522-3529.

8. "Lattice Strain Induced Slow Electron Cooling due to Quasi Type-II Behavior in Type-I CdTe/ZnS Nanocrystals", Sourav Maiti, Tushar Debnath, **Partha Maity**, Hirendra N. Ghosh, *J. Phys. Chem. C,* **2015**, *119*, 8410-8416.

9. "Subpicosecond Exciton Dynamics and Biexcitonic Feature in Colloidal $CuInS_2$ Nanocrystals: Role of In–Cu Antisite Defects", Tushar Debnath, Sourav Maiti, **Partha Maity**, Hirendra N. Ghosh, *J. Phys. Chem. Lett.,***2015**, *6*, 3458-3465.

10. "Enhanced Charge Separation in an Epitaxial Metal–Semiconductor Nanohybrid Material Anchored with an Organic Molecule", Jayanta Dana, Tushar Debnath, **Partha Maity**, Hirendra N. Ghosh, *J. Phys. Chem. C,* **2015**, *119*, 22181–22189.

11. "Effect of Molecular Coupling on Ultrafast Electron Transfer and Charge-Recombination Dynamics in a Wide-Gap ZnS Nanoaggregate Sensitized by Triphenyl Methane Dyes" Tushar Debnath, **Partha Maity**, Jayanta Dana, Hirendra N. Ghosh, *ChemPhysChem*, **2016**, 17, 724-730.

12. "Tuning the Charge Carrier Dynamics via Interfacial Alloying in Core/Shell CdTe/ZnSe NCs" Sourav Maiti, Tushar Debnath, **Partha Maity**, Hirendra N. Ghosh, *J. Phys. Chem. C*, **2016**, *120*, 1918-1958.

13. "Demonstrating the Role of Anchoring Functionality in Interfacial Electron Transfer Dynamics in NanoparticulateTiO_2-BODIPY Composite", Sunil B. Aute, **Partha Maity**, Amitava Das, and Hirendra. N. Ghosh, *J. Phys. Chem. C,* **2016** Submitted.

Conference:

1. "Ultrafast Electron-Transfer and -Trapping Dynamics in the Inter-Band-Gap States of ZrO_2 Nanoparticles Sensitized by Baicalein", **Partha Maity**, Tushar Debnath, Arshad Akbar, Sandeep Verma, and Hirendra N. Ghosh, *Interdisciplinary Symposium for Materials Chemistry (**ISMC-2012**)*, BARC, Mumbai, India.

"*"*marked are included in the thesis.*

Partha Maity

(Partha Maity)

DEDICATIONS

To my family and well wisher

ACKNOWLEDGEMENTS

The work presented in this thesis would not have been possible without my close association with many people. I take this opportunity to extend my sincere gratitude and appreciation to all those who made their contribution in this Ph.D. thesis.

First and foremost, I would like to extend my sincere gratitude to my research guide Dr. Hirendra Nath Ghosh for introducing me to such a never ending exciting field of research and for his dedicated help, advice, inspiration, encouragement and continuous support, during my Ph.D. His enthusiasm, integral view on research and his mission for providing high-quality work, has made a deep impression on me. During our course of scientific discussion since the last four years, I have learnt extensively from him, including how to raise new possibilities, how to regard an old question from a new perspective, how to approach a new problem by systematic thinking, data-analysis etc. Every moment, when I meet with him he encourages me every point of view which help me to ameliorate my work. I owe him lots of gratitude for having me shown this way of research. Apart from the sciencetific part, I found him an honest and kind hearted person in real life. Concomitantly I learn the normal character of the human being from him. I am really delighted to be associated with a person like him in my research life as well as in my real life. Thank you very much Sir for spending such valuable time with us since four and half years.

I am equally obliged to Dr. Amitava Das (CSMCRI, Bhavnagar, India) for their excellent support. My research work benefitted immensely by the molecules you provided. The molecules were just tailor made for my work and helped improving the quality of my work.

I wish to express my words of thanks to Dr. B. N. Jagatap, Director, chemistry group, Dr. D. K. Palit, Head, Radiation and Photochemistry Division (BARC, India) and Dr. T. N. Das,

Head, Ultrafast and Discharge chemistry Section, BARC, India for providing me the facilities which are conductively favorable for carrying out my research work.

I am also thankful to Homi Bhabha National Institute (HBNI), Government of India for providing me the research fellowship and for the huge research facilities. I am really glad for having such opportunity. I must thank to the all faculties and stuff members of HBNI for their help during my one year course work in the training school. Without their cooperation this work would not have been possible.

I express my sincere thank to all of my Doctoral Committee (DC) member for their important suggestions during the annual review periods which help me to reach of the end of my dissertation.

My sincere thank to Dr. Narayan Pradhan (IACS, Kolkata), Dr. Anindya Datta (IITB, India), Dr. Divesh Srivastava (CSMCRI, Bhavnagar, India), Dr. A. K. Tyagi (BARC, Mumbai), Dr. V. Sudarshan (BARC, Mumbai), Dr. Shilpa Tawade (BARC, Mumbai), Dr. Alka Gupta (BARC, Mumbai), Dr. S. K. Guin (BARC, Mumbai) for letting me use the facilities at their laboratories.

I am grateful to Dr. S. Verma, Dr. S. Kaniyankandy, Dr. T. Banerjee and Dr. Rajib Ghosh for their precious help at the beginning of my research periods which helped me lot.

I express my warm gratitude's to all of my dear lab mates, and all the RPCD members. I am grateful to all of them for their support but Tushar, Pallavi didi, Jayanta, and Sourav da call for a special mention. The valuable discussions that we had and the co-operation they extended contributed significantly to my research work. Sunil, Ananta, Uday, Deepa, Biswajit and Kausturi, all you guys rock and it was a pleasure working with you. I learned a lot from you all. Thank you all for being such a gem of a team which made daily work enjoyable and fun.

A very special thank to Minakshmi Paramanik (Dey), Sumit Mehan, Sankar Rao Chapa, Anuj Sharma, Abhishek Koushik, Rahul, Samu Naidu, Ganga Babu, Shitaljit Sharma, Akshay Dandey for their glorious presence in my life.

My heartfelt regard goes to my family members for their big scarification. I express my eternal gratitude for their love, bless and encouragement throughout my entire life. Until their endless support my Ph.D. work would not be completed.

Finally, I am thankful to all the members of the BARC including the administrative and security stuffs for cooperation.

Partha Maity

(Partha Maity)

BARC, Mumbai

CONTENTS

SYNOPSIS

Quantum dots (QDs) are semiconductor nanocrystals in which the wave function of the charge carriers (e^- and h^+) is confined in all three special dimensions[1,2]. Due to size quantization of the charge carriers these materials have many fundamental interesting and potentially useful optical properties[3]. Because of higher extinction coefficient, optical tunability, slow carrier relaxation process, multiple exciton generation, hot electron extraction possibilities expecting to break the Shockley−Queisser limit (31%), and of course low production cost formulate the QDs as a superior sensitizer in the quantum dots solar cell (QDSC) [4-6]. Unfortunately the efficiency of the QD based solar cell has not reached double numerical figures[7], whereas DSSC has reached 13% efficiency using a porphyrin based sensitizer molecule with Co (II/III) redox shuttle electrolyte[8]. The lower conversion efficiencies observed in QDSCs are due to many reasons such as the narrow absorption range of QDs in incident light, and the slow hole transfer rate ensuing photoanode corrosion[9]. In addition to that, the lower QD loading on the TiO_2 surface (compared to the dye loading in DSSCs) results in direct electron transfer from the TiO_2 film to the oxidized redox couple in the photo-anode[9]. The strategies to ameliorate the efficiency of the QDSC are focused on the light harvesting ability, extraction of both the electron and hole from the photo-excited QDs before ultrafast exciton–exciton annihilation and better charge separation. Therefore, the understanding of the charge transfer dynamics is very crucial to know the mechanistic pathways which can assist to optimize the photocurrent conversion efficiency (PCE). Femtosecond transient absorption is the one of the great technique to investigate the charge carrier relaxation and charge transfer dynamics[10]. The nanocrystals (NCs) are exploited as sensitizer in different ways either in the form of core/shell heterostructures[11] or as an alloy structure[7]. Two main types of core/shell, type-I and type-II, have been extensively used as sensitizer to satisfy different purpose[12]. Due to smaller size of the QDs, the surface of the QDs accumulates trap states, which is the limiting factor for the application of QDs in photovoltaics[13]. The way to exclude the surface defect states which can be successfully passivated by putting a wider band gap shell in type-I core/shell structure[14]. On the other hand charge separation can be enhanced by forming a type-II core/shell structure[12]. Moreover, another type of heterostructures familiar as quasi type-II core/shell where the core QD is encapsulated by a wider band gap semiconductor, but due to smaller energy difference in either conduction band (CB) or valence band (VB) offset, the electron or hole respectively can be delocalized core and shell structure[15,16]. Therefore, quasi type-II core/shells NCs are often used in QDSC[15]. Additionally, ternary or quaternary alloy are promising candidate like the binary sensitizer in QDSC because the optical property of the alloy can be controlled by changing composition of the constituents not by the size[17]. Thus, composition plays an extra degree of freedom towards enviable property. To date, the highest efficiency in QDSC has been observed in the CdSeTe alloy[7]. Besides the II-VI semiconductor QDs, a new class of semiconductor which are isostructral with $CaTiO_3$ perovskite has been studied due to excellent performance in the low cost third generation solar cell[18]. The photophysical properties, charge relaxation and separation dynamics in these all cases are very essential to build up an optimized panchromatic solar cell.

The main endeavour in the present thesis work is the synthesis and character of the II-VI semiconductor QDs in terms of different core/shell heterostructures and ternary alloy nanocrystals. The charge carrier (e-h) relaxation, charge separation, recombination and selective charge transfer dynamics have been carried out utilizing femtosecond transient absorption measurement in presence and absence of the organic/inorganic/quencher molecules. Apart from these II-VI semiconductor QDs, a new class of totally inorganic colloidal $CsPbBr_3$ (CPB) perovskite QDs has also been synthesized. The morphology of the colloidal CPB QDs and the e-h relaxation dynamics are investigated in the present thesis work. Finally, utilizing the slow electron cooling, long excited state life time and negligible charge recombination of the highly luminescent CdS_xSe_{1-x} alloy QDs we have designed solar cell which provides unprecedented 4.5% power conversion efficiency (PCE).

CHAPTER 1: GENERAL INTRODUCTION

This chapter provides the brief introduction and definition of the nanocrystal semiconductor and a correlation energy diagram among the bulk, nanocrystals quantum dots, and atomic molecule. The basic properties and the electronic structure of the QDs have been discussed utilizing quantum mechanical model (particle-in-a sphere model). Utilizing effective mass approximation framework the structure of the QDs has been explained. The optical transition probability and the exciton fine structure of the typical II-VI QDs are also highlighted. The possible mechanism of the exciton decay through intraband hot charge carrier relaxation process in the size quantized states via phonon-assisted relaxation, Auger recombination, and energy transfer to vibration of the surface ligand is described. A brief description of longer excited state life time and slow intraband carrier cooling in different type heterostructures core/shell and alloy QDs has also been defined. Furthermore, a very short discussion of Marcus electron transfer theory in the QDs/molecular adsorbate system is mentioned.

CHAPTER 2: EXPERIMENTAL TECHNIQUES

The present thesis work involves mainly the charge transfer dynamics in the semiconductor QDs and QDs/molecular interface. Thus the details experimental setup of time resolved optical and an emission technique in terms of femtosecond transient absorption (TA) and single photon emission counting (TCSPC) is demonstrated. Including the basic principles of transient absorption spectroscopy, generation of seed pulse from the oscillator (800 nm), power amplification of the seed pulse in the amplifier, second harmonic generation through the BBO crystal as pump pulse (400 nm), white light continuum for probe pulse generation (420-1000 nm) are described. The basic principle and the optical layout of the TCSPC are also mentioned. The morphology and the spectral properties of the semiconductor QDs are characterized using X-ray diffraction pattern (XRD), high resolution transmission electron microscopy (HRTEM), and steady state optical and emission spectroscopic techniques respectively. A brief description and the working principles of the XRD, HRTEM, and steady state optical and emission spectroscopic techniques are described. Formations of dye cation radical are measured by pump-probe spectroscopy after exciting the samples with an electron beam excitation in pulse radiolysis. A brief description about pulse radiolysis technique is highlighted in this chapter. The description of solar stimulator and the working principle of the IPCE (incident photocurrent conversion efficiency) are also included in this chapter.

CHAPTER 3: CHARGE TRANSFER DYNAMICS IN CdS QUANTUM DOTS AND MOLECULAR ADSORBATE

This chapter deals the exciton quenching of CdS QDs in presence of two different dye molecules via hole transfer and through non radiative energy transfer process. In addition to the hole transfer from CdS to the 4′,5′-dibromofluorescein (DBF), direct electron transfer and electro injection to the CB of the CdS from HOMO and LUMO of the DBF has been verified through selective excitation. On the other hand non radiative energy transfer is observed from CdS to BODIPY (boron dipyrromethene, named as TG2 and TG10) derivative. The ultrafast charge-transfer (CT) processes have also been discussed in both CdS DBF and CdS/BODPY composite system. Charge separation in the CdS−DBF composite has been found to take place in three different pathways, by transferring the photoexcited hole from CdS to DBF, electron injection from photoexcited DBF to the CdS QD, and direct electron transfer from the HOMO of DBF to the CB of the CdS QD. CT dynamics has been monitored by direct detection of the DBF cation radical and electron in the QD in the femtosecond transient absorption spectra. Electron injection and the electron-transfer process are found to be pulse width- limited (<100 fs); however, the hole-transfer time has been measured to be 800 fs. The non-radiative Förster energy transfer (FRET) from photo-excited CdS QD to TG2 and TG10 has been determined which is found to be ~450 fs.

CHAPTER 4: MULTIPLE CHARGE TRANSFER DYNAMICS IN COLLOIDAL $CsPbBr_3$ QUANTUM DOTS AND ORGANIC MOLECULE

Recent research on colloidal perovskite QDs has been increased tremendously after motivated by great success in photovoltaic with the certified solar cells efficiency beyond 20%. This chapter addresses the synthesis and characterization of the highly stable totally inorganic perovskite QDs ($CsPbBr_3$, CPB). The multiple CT interaction of the CPB QD has been investigated after sensitizing with an organic dye molecule. Ultrafast charge-transfer (CT) dynamics has been verified in CPB quantum dot (QD)−4,5-dibromofluorescein (DBF) composite materials, which form a strong CT complex in the ground state and absorb more photon in the red region of the solar spectra. The energy levels of the CPB and DBF are determined on the basic of cyclic Voltammetric study. CT complex formation and carrier transfer dynamics have been confirmed from optical and PL analysis. The PL quenching of the CPB QDs luminescence with selective photo-excitation reveals photo-excited hole transfer from CPB QD to DBF molecule which is thermodynamically viable. Additionally, a red shifted CT luminescence of the CPB-DBF complex has been noticed. The hole transfer time from photo-excited CPB QD to DBF molecule are determined to be 250 fs, where as direct electron transfer from HOMO of DBF to the CB of CPB found to be pulse-width limited (< 100 fs).

CHAPTER 5: BAND EDGE ENGINEERING AND CONTROLLING CHARGE CARRIER DELOCALIZATION IN CORE/SHELL NANOCRYSTALS

Band edge engineering concept has been employed in semiconductor QDs research to enhance the stability and/or the separation of charge carriers of the NCs depending on the application. This chapter presents the band edge engineering and charge carrier delocalization in two different core/shell NCs, CdS/CdSe inverted type I and CdSe/CdS quasi type II, utilizing femtosecond transient absorption spectroscopy in absence and presence of different quencher molecule. The morphology of these two NCs core/shell has been analyzed using XRD and HRTEM techniques. Optical properties have also been examined through steady-state optical absorption and luminescence studies. Depending on their band energy level alignment, the e-h delocalization in both the core−shells have been demonstrated using electron (benzoquinone, BQ) and hole (pyridine, Py) quencher. The bleach recovery kinetics of CdS/CdSe core−shell recovers faster in the presence of both BQ and Py. However, for CdSe/CdS core−shell, the bleach recovers faster only in the presence of BQ while the bleach dynamics remain unaffected in the presence of Py. Our experimental observations suggest that in CdS/CdSe inverted type I core−shell both electrons and holes are localized in the CdSe shell; however, in CdSe/CdS quasi type II core−shell, photoexcited electrons are delocalized in core CdSe and shell CdS and holes are localized in CdSe core.

CHAPTER 6: CHARGE CARRIER DYNAMICS IN HETEROSTRUCTURE CORE/SHELL NANOCRYSTALS AND MOLECULAR ADSORBATE

This chapter describes charge carrier dynamics in different heterostructures core/shell in presence of organic and inorganic sensitizer molecule. The organic and the inorganic molecule, bromo pyrrogallol red (Br-PGR) and the Re-polypyridine complex, have been used as sensitizer because it forms CT complex and higher photo stability respectively. The ultrafast cascading charge transfer dynamics have been demonstrated in CdS and CdS/CdTe type-II core/shell after sensitizing with Br-PGR molecule. It has been observed that Br-PGR form strong CT complex with both CdS and CdS/CdTe as well as it acts as a sensitizer and hole acceptor. Charge separation in the CdS/Br-PGR and the CdS/CdTe-Br-PGR composite materials are found to take place in different pathways, by transferring the photoexcited hole of CdS (or CdS/CdTe) to Br-PGR, electron injection and direct electron transfer to the CB of the CdS (or CdS/CdTe) from the photo-excited state and the HOMO of Br-PGR molecule respectively. Charge recombination (CR) dynamics between the electron in the CB of the CdS QD and the Br-PGR cation radical are determined by monitoring the bleach recovery kinetics. The CR dynamics are found to be much slower in the CdS/CdTe/Br-PGR system than in the CdS/Br-PGR system. On the other hand the photophysical studies of CdS QD, CdS/CdSe type-I and CdS/CdTe type-II core-shell NCs sensitized with a Re-polypyridyl complex have been discussed with special emphasis on studies on charge carrier delocalization and the role of Re(I)-complex as a hole acceptor and sensitizer molecule. Experimental results suggest photo-excited hole transfer from CdS and CdS/CdSe to the Re(I)-complex, while that is not observed for CdS/CdTe system. This is rationalized by the evaluation of the relative energy levels, which revealed that such an hole migration is not energetically favorable due to low lying HOMO of the Re(I)-complex as compare to VB of CdTe shell. Moreover, electron injection from the hot states of the excited Re (I)-complex to the CB of the all three systems are confirmed by steady state and time-resolved PL studies. TA spectra have been recorded for Re (I) complex sensitized CdS and CdS/CdSe composite which revealed a broad transient absorption band in 580-750 nm region with a maximum around 595 nm and this is attributed to the cation radical formation for Re (I)-dye, either by capturing photo-excited hole from the NCs or by injecting electron to the CB of the NCs. As anticipated, no such spectrum is observed for the CdS/CdTe-Re (I)-composite system.

CHAPTER 7: CARRIER COOLING DYNAMICS IN ALLOY QDs

The charge carrier confinement of semiconductor ternary alloy QDs not only depend on the quantization of the size quantized states but it also depends on the composition of the constituent. Depending on the band alignment of the constituent QD we have been demonstrated the carrier cooling dynamics of the two different alloy QDs, CdS_xSe_{1-x} and $Cd_xZn_{1-x}Se$. Both the alloy are synthesized in a single pot process in a non coordinating solvent (1-octadecene) at ~300° C and are characterized using XRD, EDX, and HRTEM techniques. Steady state optical absorption and photoluminescence (PL) measurements of the CdS_xSe_{1-x} alloy shows the nonlinear behavior with changing chalcogenied composition. In case of $Cd_xZn_{1-x}Se$ both optical and PL spectra are red shifted with respect to the both CdSe and ZnSe. This clearly suggests that both the alloy form graded like structure where the core of the alloy is CdSe rich. The reactivity of the selenium towards cadmium oleate is more as compare to sulphur, thus the core of the CdS_xSe_{1-x} alloy structure will have CdSe rich and the graded shell are CdS rich. Similarly, the reactivity of Se is more with Cd ion than Zn ion, so like CdS_xSe_{1-x} alloy, the $Cd_xZn_{1-x}Se$ will also have CdSe core rich and ZnSe shell rich. Thus, for CdS_xSe_{1-x}, $Cd_xZn_{1-x}Se$ in both cases core is CdSe rich and shells are CdS and ZnSe rich respectively. The band alignment of these two systems suggests the quasi type-II structure. Due to smaller CB offset of the CdSe and CdS electron will be delocalized in the CdS_xSe_{1-x} graded like alloy structure. On the other hand due to smaller VB offset of the CdSe and ZnSe hole will be delocalized $Cd_xZn_{1-x}Se$ structure. Because of the delocalization of the either electron or hole in the CdS_xSe_{1-x} and $Cd_xZn_{1-x}Se$ alloy structure respectively the intraband electron cooling time is increasing due to decoupling of the e-h in these quasi type-II structures.

CHAPTER 8: IMPROVING SOLAR CELL EFFICIENCY UTILIZING ALLOY QDs

This chapter gives details demonstration and fabrication of the QD sensitized solar cell. The solar cell performance has been analyzed in terms of IPCE and IV measurements. Heterojunction colloidal QDSC using CdS_xSe_{1-x} alloy QDs has been fabricated to show unprecedented 4.5% power conversion efficiency (PCE). The deposition of the QDs sensitizer on the TiO_2 film is derived post-synthesis process via ligand assisted assembly technique. The CdS_xSe_{1-x} QDs show extremely slow electron cooling time as compare to the constituents (CdS as well as CdSe) which are beneficial for charge carrier extraction in QDSC. To prepare the solar cell assembly the pre-synthesized organic soluble oleic acid capped QDs has been made water soluble using mercaptopropionic acid (MPA) at pH 12. Details procedure of the ligand exchange process is also included in this chapter. Four layers of ZnS have been coated on the films utilizing the Successive Ion Layer absorption and reaction (SILAR) technique. The ZnS acts as a passivating layer to slowing down the charge recombination. Using polysulfide electrolyte and Cu_2S deposited ITO glass plates as photocathode the efficiency of the QD solar cell has been measured to be 1.1 (±0.05)% for CdS, 3.36 (±0.1)% for CdSe and 3.75 (±0.12)% for CdS_xSe_{1-x} QDs under 1 sun illumination. When an additional non-epitaxial CdS quasi-shell is deposited on top of CdS_xSe_{1-x} film to passivate the TiO_2 surface states followed by ZnS passivated (TiO_2/CdSSe/quasi-CdS/ZnS) QD solar cell, the PCE increased to 4.5 (±0.18)% which is the highest reported value for CdS_xSe_{1-x} alloy QDs.

CHAPTER 9: SUMMERY AND OUTLOOK

In summary, the synthesis and characterization of various forms of QDs nanocrystals and the charge carrier dynamics in presence of different adsorbate molecule depending on their different application purpose have been investigated. One of the limitations of the QDSC is the absorption of solar radiation by the QDs materials is less as compare to any dye molecule. In the present thesis we discuss different ways to increase the absorption cross section of the QDs materials by introducing various sensitizer dye molecule. The charge separation and slow carrier relaxation of QDs has been demonstrated using different heterostructures like core/shell and alloy QDs. Apart from this, multiple charge transfer process in supersensitized colloidal $CsPbBr_3$ perovskite has also been discussed. Finally, photovoltaic performance has been carried out utilizing CdS_xSe_{1-x} alloy QDs which show unprecedented PCE ~4.5 (±0.18)%.

REFERENCES:

(1) Widmann, F.; Simon, J.; Daudin, B.; Feuillet, G.; Rouvière, J. L.; Pelekanos, N. T.; Fishman, G. *Phys. Rev. B* **1998**, *58*, R15989.

(2) Kudera, S.; Zanella, M.; Giannini, C.; Rizzo, A.; Li, Y.; Gigli, G.; Cingolani, R.; Ciccarella, G.; Spahl, W.; Parak, W. J.et al. *Adv. Mater.* **2007**, *19*, 548.

(3) Alivisatos, A. P. *Science* **1996**, *271*, 933.

(4) Kamat, P. V. *Acc. Chem. Res.* **2012**, *45*, 1906.

(5) Beard, M. C.; Luther, J. M.; Semonin, O. E.; Nozik, A. J. *Acc. Chem. Res.* **2012**, *46*, 1252.

(6) Luther, J. M.; Law, M.; Beard, M. C.; Song, Q.; Reese, M. O.; Ellingson, R. J.; Nozik, A. J. *Nano Lett.* **2008**, *8*, 3488.

(7) Yang, J.; Wang, J.; Zhao, K.; Izuishi, T.; Li, Y.; Shen, Q.; Zhong, X. *J. Phys. Chem. C* **2015**, *119*, 28800.

(8) Mathew, S.; Yella, A.; Gao, P.; Humphry-Baker, R.; CurchodBasile, F. E.; Ashari-Astani, N.; Tavernelli, I.; Rothlisberger, U.; NazeeruddinMd, K.; Grätzel, M. *Nat Chem* **2014**, *6*, 242.

(9) Kamat, P. V.; Christians, J. A.; Radich, J. G. *Langmuir* **2014**, *30*, 5716.

(10) Klimov, V. I.; McBranch, D. W.; Leatherdale, C. A.; Bawendi, M. G. *Phys. Rev. B* **1999**, *60*, 13740.

(11) Shirasaki, Y.; Supran, G. J.; Bawendi, M. G.; Bulovic, V. *Nat Photon* **2013**, *7*, 13.

(12) Kim, S.; Fisher, B.; Eisler, H.-J.; Bawendi, M. *J. Am. Chem. Soc.* **2003**, *125*, 11466.

(13) Mora-Seró, I.; Giménez, S.; Fabregat-Santiago, F.; Gómez, R.; Shen, Q.; Toyoda, T.; Bisquert, J. *Acc. Chem. Res.* **2009**, *42*, 1848.

(14) Balet, L. P.; Ivanov, S. A.; Piryatinski, A.; Achermann, M.; Klimov, V. I. *Nano Lett.* **2004**, *4*, 1485.

(15) Chuang, C.-H. M.; Brown, P. R.; Bulović, V.; Bawendi, M. G. *Nat Mater* **2014**, *13*, 796.

(16) Kobayashi, Y.; Chuang, C.-H.; Burda, C.; Scholes, G. D. *J. Phys. Chem. C* **2014**, *118*, 16255.

(17) Pan, Z.; Zhao, K.; Wang, J.; Zhang, H.; Feng, Y.; Zhong, X. *ACS Nano* **2013**, *7*, 5215.

(18) Kulbak, M.; Gupta, S.; Kedem, N.; Levine, I.; Bendikov, T.; Hodes, G.; Cahen, D. *J. Phys. Chem. Lett.* **2016**, *7*, 167.

LIST OF ABBREVIATIONS

Ar	Argon
BET	Back Electron Transfer
BODIPY	Borondipyrromethene
BQ	Benzoquinone
Br-PGR	Bromopyrogallol red
CB	Conduction Band
CBD	Chemical Bath Deposition
CCD	Charge Coupled Device
CdO	Cadmium Oxide
CdS	Cadmium Sulfide
CdSe	Cadmium Selenide
CdTe	Cadmium Telluride
CPB	Ceasium lead bromide ($CsPbBr_3$)
CR	Charge Recombination
CT	Charge Transfer
CV	Cyclic Voltammetric
DBF	4',5'-Dibromofluorescence
DSSC	Dye Sensitized Solar Cell
e^-	Electron
em	Emission
ET	Electron Transfer
EVET	Electronic to Vibrational Energy Transfer
ex	Excitation

I/FTO	Indium/Fluorine doped Tin Oxide
fs	Femtosecond
h^+	Hole
HOMO	Highest Occupied Molecular Orbital
HRTEM	High Resolution Transmission Electron Microscopy
HT	Hole Transfer
ISC	Inter System Crossing
ITO	Indium doped Tin Oxide
KOH	Potassium Hydroxide
LUMO	Lowest Unoccupied Molecular Orbital
LED	Light Emitting Diode
MEG	Multiple Exciton Generation
MPA	3-Mercaptopropionic Acid
NCs	Nanocrystals
NHE	Normal Hydrogen Electrode
ns	Nanosecond
OA	Oleic Acid
OD	Optical Density
ODE	1-Octadecene
PA	Photoinduced Absorption
PL	Photoluminescence
ps	Picosecond
Py	Pyridine
QDs	Quantum Dots
QDSC	Quantum Dot Solar Cell

SAED	Selected Area Electron Diffraction
SHG	Second Harmonic Generation
SILAR	Successive Ion Layer Absorption and Reaction
TA	Transient Absorption
TCSPC	Time Correlated Single Photon Counting
TOP	Trioctyl Phosphine
UV	Ultra Violet
VB	Valence Band
WLG	White Light Generation
XRD	X-ray Diffraction
ZnSe	Zinc Selenide
ZB	Zinc Blend

LIST OF FIGURES

LIST OF SCHEMES

Process conduction band of core CdS QD. **Process 5** shows photo-excitation of CdTe shell QD. **Process 6** indicates direct transfer of electron from HOMO of Br-PGR to conduction band of CdTe shell. Electron injection and hole transfer reaction in both composite materials are shown. Dotted line in both the scheme indicates charge recombination reaction between electron in CdS QD and Br-PGR cation radical. **BET** process is slower in case of CdS/CdTe-Br-PGR composite system.

Scheme 6.2: Schematic presentation of charge transfer interaction in CdS-Re-1,2 composite system after photo-excitation. Energy levels are mentioned with respect to NHE.

Scheme 6.3: Schematic illustration of charge delocalization and charge transfer processes in (A) CdS/CdSe type-I and (B) CdS/CdTe type-II core-shell in presence of Re-1,2 complex respectively. Energy levels are mentioned with respect to NHE.

Scheme 7.1: Comparison hot carrier relaxation processes in CdSe QD and CdS_xSe_{1-x} alloy QD after exciting at 400 nm laser light in chloroform solution.

Scheme 7.2: Comparison hot carrier relaxation processes in CdSe QD and CdS_xSe_{1-x} alloy QD after exciting at 400 nm laser light in chloroform solution.

Scheme 8.1: Schematic illustration of step wise improving the PCE in QDSC; starting from CdS and CdSe QDs to CdS_xSe_{1-x} alloy and finally CdS_xSe_{1-x} alloy/quasi CdS shell has been used as sensitizer.

LIST OF TABLES

CHAPTER-1

Introduction

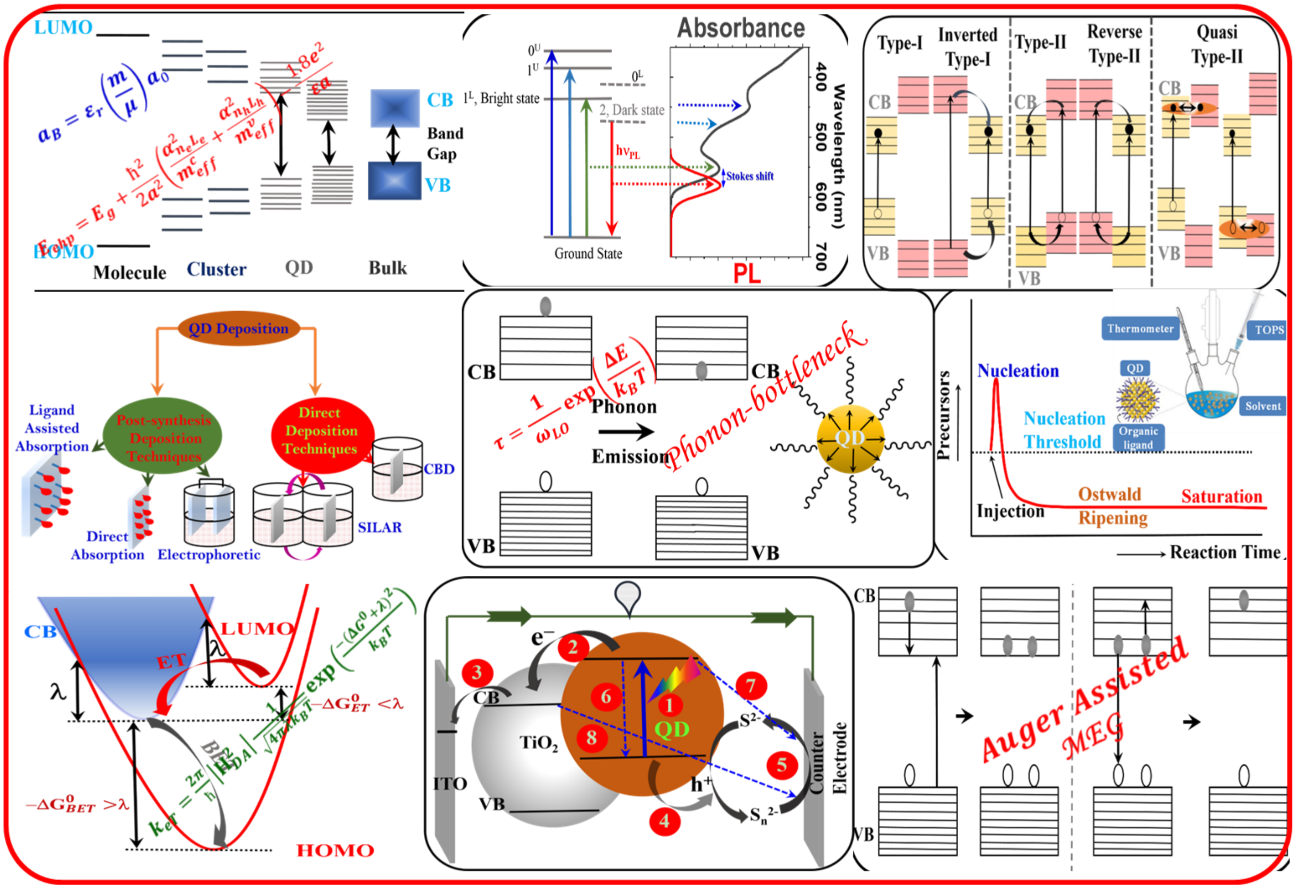

1.1. General Introduction:

Increasing demands in the field of nanotechnology have pushed several industries to improve their manufacturing techniques and produce ever better efficient systems. Utilizing the fundamental knowledge of the semiconductor nanocrystals [1-4], new approaches and ideas which are very necessary for creating ever the high performance system with less cost effect. The rapid growth of the colloidal nanocrystal has been observed in various field since past decades. The interesting observations of the nanomaterials are coming from their inherent properties. The materials which are investigated in the present thesis are named as semiconductor nanocrystal (NC) in the form of colloidal Quantum Dots (QDs), core-shell, alloy QDs etc. In this chapter we demonstrate definition of the QDs, motivation of the work, theoretical aspect of their structural properties, different photophysical behaviour, colloidal synthesis method, and its application in photovoltaics.

1.1.1. What is a Quantum Dot?

Quantum dots are man-made semiconductor nanocrystals in which the motion of the charge carrier (electron and hole) is restricted in all three special directions. Due to the confinement effect, the charge carriers obey size quantization to which the dot owes its name.[5, 6] The terms NCs and QDs are often used to indicate same system. However, in the scientific point of view they are no longer synonyms. The nanocrystal in which the size of the crystal is varied from 1 to 999 nm but the charge carrier might not follow the size quantization effects. On the other hand, QDs can be defined as a nanocrystal where few hundred or thousands of atoms are accumulate in crystal lattice and the electronic properties of the charge carrier follow quantum mechanically. Now the question is that whether the QDs can be considered as large number of molecules or a small nanocrystals. The main difference between a molecular system and a nanocrystal is that the electronic properties of the nanocrystals don't change significantly with adding a finite number of atoms to the crystal. However, this is not true in case of molecular system. The system having well defined number of atoms are known as a cluster.[7] Thus with the electronic consideration QDs are reclined in between the cluster and nanocrystal which is depicted in the Figure 1.1.

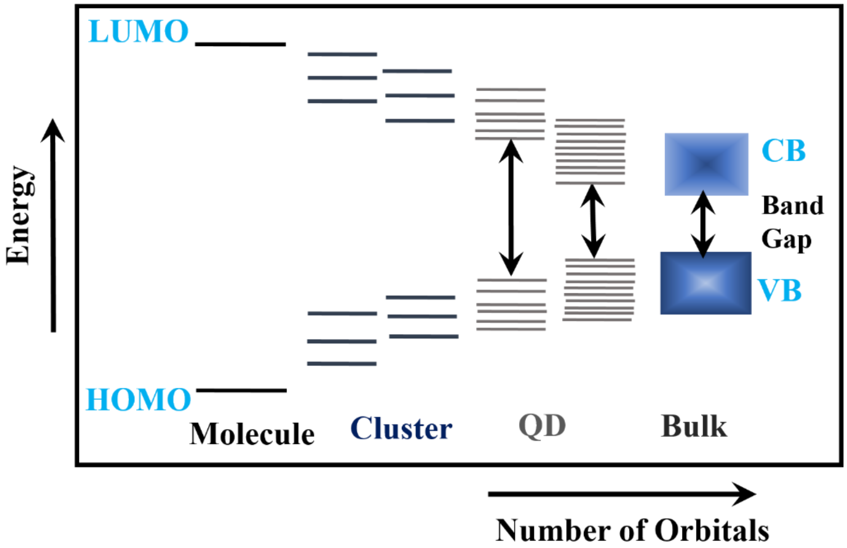

Figure 1.1: Decreasing energy gap from the molecular system to bulk bridged via cluster and quantum dots.

Although, the term QDs sounds to be relatively recent however, the confinement effect has been proposed since 1920's when the heating glass which contains CdS colloids emitted bright luminescence shifted to longer wavelength compared to the absorption onset [8, 9]. In the 1960's the researchers observed the spectral shift in absorption of the colloidal semiconductor to the corresponding macroscopic materials. However, reason behind the optical shift was unclear[9, 10]. In the late 1960's, after discovery of the Molecular Beam Epitaxy (MBE) the breakthrough originated in the nanosciences research [11, 12]. The 2D quantum well structure was first reported with the help of MBE [13]. However, in 1980's the theoretical aspect of the size quantization of the semiconductor was started by Ekimov and Efros to explore which contributed lot of knowledge [2, 4] to discover ever dimensionless semiconductor called as *Quantum Dots*.[14] Later on, in 1993 the first nearly monodispersed quantum dots base on CdX (X=S, Se and Te) was synthesised chemically by Murray et al. using organometallic reagent in hot coordinating solvent [15]. With the combination of the theoretical aspect and different synthetic protocols a new exciting field of research has been developed which has multidirectional applications.

1.1.2. Motivation of the Work: Why QD is Studied?

Quantum dots having finite size, the charge carriers are confined in the size quantized states of the band structure.[16-18] Due to confinement of the particle the electronic energy levels in the band structure become discrete unlike bulk semiconductor.[19, 20] Therefore, sometimes QDs are called as *artificial atoms*.[21, 22] So, the confinement effect of these materials is providing various fundamental interesting aspect and multiple potential applications. [23, 24] Since the materials are showing exciting properties in a certain size region and by changing the size of the NCs the optical property can easily be tuned. In addition to the size dependent optical property, these materials have very large dipole moments, high extinction coefficient and oscillator strength. [25-29] In the bulk semiconductor the electronic energy states are continuous which provide structure less optical property while in case of QD it becomes well-structured due to discrete electronic states. As a result, the excited state life time and intraband electron cooling time of the QD materials increase manifold. Additionally these materials have very high emission quantum yield which arising from radiative recombination of the excited charge carries. Thus the QDs provide a new platform for exploring new phenomenon and rapid development of novel technologies like light emitting devices (LED), [30] biological imaging, [31] coherent light emitter, composition dependent optoelectronic properties, photocatalysis,[32, 33] and photovoltaics.[34-41]

The renewable energy source like solar energy which can compensate the decrement of the non-renewable energy as a complementary energy demand.[42, 43] The materials like semiconductor, dyes, polymer, organic molecules which have absorption in the visible and NIR region can be used as a sensitizer in the low-cost third generation solar cell. It has been observed that the QDs serve light harvester due to its exciting properties like optical tunability, higher absorption coefficient, large dipole moments etc. However, the efficiency of the solar cell made out of QDs materials[44] is not crossed the DSSC[45] while it is expected to be more than Shockley−Queisser limit (32%).[46] The reasons behind the low efficiency of the QD sensitized solar cell are limited absorption of the solar radiation by the QD materials, less charge separation, photoanode corrosion due to slow hole moving rate, very fast exciton recombination which take place in sub hundreds pico-second time scale.[47, 48] Therefore, in order to increase the photocurrent conversion efficiency (PCE) of a particular sensitizer system, understanding fundamental mechanistic aspect of the QDSC is required. The present thesis work, mainly charge transfer dynamics in NCs (colloidal QDs, core-shell, alloy etc.) is motivated by the exciting properties of the QDs in light harvesting application.

1.2. Electronic Structure of the QDs: Theoretical Framework

1.2.1. Size *vs.* Confinement

As the nanocrystals serve the thrilling contribution in modern electronic and optoelectronic device so it is very important to understand the structure of the semiconductor when it becomes very small. We have already mentioned in the earlier section about confinement effect of the NCs. The QDs where the particles are confined in all three special direction therefore they are referred as zero dimensional i.e. dimensionless or dot. Again, there are two more possibilities of the confinement can arise: when particles are confined in two dimensional space they are referred as quantum wire i.e. one dimensional (1D); besides, when particles are confined in one dimensional space they are referred as quantum well *i.e.* two dimensional (2D). The present work is based on the colloidal QDs which are dimension less particle. In QDs the bound electron and hole pair is called as *exciton* which behaves like a single particle having reduced mass arising from the electron and hole. The dimension of the size quantized state in the QDs is less than the de-Broglie wavelength of the charge carrier. The quantum size effect occurs only when the size of the NCs becomes less or equal to the coherence length (i.e. the mean free path of the exciton) of the exciton is known as exciton Bohr radius which can expressed by the following equation[49]

$$\boldsymbol{a_B = \varepsilon_r \left(\frac{m}{\mu}\right) a_0} \qquad (1.1)$$

Where, "$\boldsymbol{\varepsilon_r}$" is the size dependent dielectric constant, "$\boldsymbol{\mu}$" is the reduced mass of the system, "$\boldsymbol{m}$" is the rest mass of the electron and "$\boldsymbol{a_0}$" is the Bohr radius of the H-atom (~0.052 nm).[50]

In a NC quantum dot the fundamental charge carriers are electron and hole. The bound electron and hole in a small size regime is called *exciton*. Thus, it is convenient to consider three different confine property depending on the nature of the particle [49]. If the radius (a) of the NC is smaller than the Bohr radius of electron (a_e), hole (a_h) and exciton (a_{exc}) i.e. $a < a_e, a_h, a_{exc}$, in this situation electron and hole are consider to be confined by the potential energy boundary of the nanocrystal. This condition is known as *strong confinement regime*. On the other hand when the radius, a, is smaller than both electron and hole Bohr radius but larger than the exciton Bohr radius (i.e. $a_e, a_h < a < a_{exc}$) the situation is referred as *weak confinement regime*. The intermediated situation arrives when the radius of the NC is in between a_e and a_h. In the *intermediate confinement regime* either electron or hole is strongly confined while other is not. Therefore, confinement of a particle depends on the size of the nanomaterials. For example, Bohr radius of III-V semiconductors like InAs [51] is 36 nm which is much larger than the typical size of the nanocrystal (< 10 nm). This situation is referred as strong confinement regime. Conversely due to very small Bohr radius of the CuCl (0.7 nm) these NCs are in weak confinement regime which is much smaller than the size of the NC. The II-VI semiconductor like CdS, CdSe and CdTe are in either strong or intermediated confinement regime, depend on the size of the NCs because the exciton Bohr radius of these materials are in the range of the 4–7 nm.

1.2.2. Particle-in-a-Sphere Model

From the above discussion it is clear that size quantization of the charge carriers arises due to quantum confinement effect. However, the quantitative description of the size dependent electronic properties is difficult to imagine without considering any model. As the charge carriers are confined in all three dimension of QD materials which can be considered as a particle- in-a-sphere model.[4, 52] According to the model, the particle having mass "*m*" confined in a spherical potential of radius "*a*" can be considered as follow:

$$\boldsymbol{V}(\boldsymbol{r}) = \begin{cases} \mathbf{0} & r < a \\ \infty & r > a \end{cases} \tag{1.2}$$

After solving the Schrödinger equation Flügge [53] obtained the wavefunctions:

$$\boldsymbol{\Phi}(\boldsymbol{r},\boldsymbol{\theta},\boldsymbol{\varphi}) = \boldsymbol{C}\frac{\boldsymbol{j_l}(\mathbf{k}_{\mathbf{n},\ell}\,\mathbf{r})\mathbf{Y}_{\ell}^{\mathbf{m}}(\boldsymbol{\theta},\boldsymbol{\varphi})}{\mathbf{r}} \tag{1.3}$$

where, $\boldsymbol{C}$ is a normalization constant, $\mathbf{Y}_{\ell}^{\mathbf{m}}(\boldsymbol{\theta},\boldsymbol{\varphi})$ is known as spherical harmonic, and $\boldsymbol{j_l}(\mathbf{k}_{\mathbf{n,l}}\,\mathbf{r})$ is the ℓ^{th} order spherical Bessel function, and

$$\mathbf{k}_{\mathbf{n},\boldsymbol{\ell}} = \frac{\boldsymbol{\alpha}_{\boldsymbol{n},\boldsymbol{\ell}}}{\boldsymbol{a}} \qquad (1.4)$$

Where $\boldsymbol{\alpha}_{\boldsymbol{n},\boldsymbol{\ell}}$ is the nth zero of the $\boldsymbol{j}_{\boldsymbol{l}}$. Now, the energy of the particle can be given by the following energy equation:

$$\boldsymbol{E}_{\boldsymbol{n},\boldsymbol{l}} = \frac{\hbar^2 \boldsymbol{k}_{\boldsymbol{n},\boldsymbol{l}}^2}{2\boldsymbol{m}} = \frac{\hbar^2 \boldsymbol{\alpha}_{\boldsymbol{n},\boldsymbol{l}}^2}{2\boldsymbol{m}\boldsymbol{a}^2} \qquad (1.5)$$

Due to the symmetry of the problem, the eigenfunctions of the equation are atomic like properties and can be defined by the different quantum numbers like *n* (1, 2, 3…), l (*s*, *p*, *d*…), and *m*. As the particle in the sphere model has zero potential energy, the energy term in the equation 1.5 is the kinetic energy of the free electron and it is strongly depend on the size of the particle.

The model suggests that the particle inside the sphere having freed from any kind of perturbation i.e. the sphere is empty. However, in a crystal the semiconductor contains several numbers of atoms. This limitation can be overcome after considering *effective mass approximation* theory. [54, 55]

1.2.3. Effective Mass Approximation:

In the effective mass approximation method the conduction and valence band in the bulk semiconductor are considered by simple parabolic isotopic bands. The electronic wavefunctions in a bulk semiconductor crystal can be written according to Bloch's theorem as follow:

$$\boldsymbol{\psi}_{\boldsymbol{nk}}(\boldsymbol{r}) = \boldsymbol{u}_{\boldsymbol{nk}}(\boldsymbol{r}) \exp(\boldsymbol{ik}.\boldsymbol{r}) \qquad (1.6)$$

Where "$\boldsymbol{u}_{\boldsymbol{nk}}$" is the function of periodicity in the crystal lattice and the wavefunction are labelled by the band index "$\boldsymbol{n}$" (*n* = c for conduction band and *n* = v for valence band) and wavevector "*k*". The plot of *E* versus *k* for direct semiconductor is shown in Figure 1.2 which represents typically the energy band diagram of the wavefunction. [56]

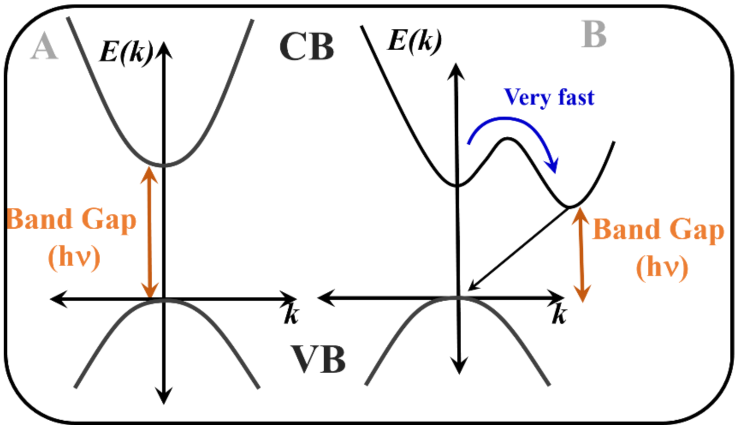

Figure 1.2: Band energy diagram of (A) direct and (B) indirect bulk semiconductor.

In case of direct semiconductor both the conduction band minima and the valence band maxima point occur at $k = 0$ (Figure 1.2 A) [56]. While in an indirect band gap semiconductor the conduction band minima and the valence band maxima remains away from $k = 0$ (Figure 1.2 B). In order to satisfy the momentum conservation it emits phonon during electronic transition. In the effective mass approximation approach, the energy of the conduction band and valence band can be given as follow:

$$E_k^c = \frac{\hbar^2 k^2}{2m_{eff}^c} + E_g \tag{1.7}$$

$$E_k^v = -\frac{\hbar^2 k^2}{2m_{eff}^v} \tag{1.8}$$

where, "E_g" stands for energy difference between the maximum point of the VB and minimum point of the CB. In this approximation, the charge carriers behave as free particles with an *effective mass*, m_{eff}^c and m_{eff}^v for electron in conduction band and hole in valence band, respectively. With these effective mass approximation techniques the periodicity of the crystal lattice is completely ignored and the charge carriers (electron and hole) are considering as free particles having different masses.

However, in the effective mass approximation method the nanocrystals are treated as bulk materials. Now, for the single particle system (i.e. for electron/hole/exciton) the Bloch's wavefunction and the effective mass approximation can be imposed with similar assumption. The combination of the Bloch's theorem and effective mass approximation in the small quantum dot provides similar energy equation and the method is known as *envelope function approximation* [57-59] which is valid only when the nanocrystal diameter is larger than the lattice constant of the materials. The single particle (*sp*) wavefunction in a small crystal lattice can be expressed in terms of linear combination of Bloch functions mentioned in the equation 1.6. Therefore the single particle wavefunction, [$\boldsymbol{\psi_{sp}(r)}$] is given by the following equation:

$$\boldsymbol{\psi_{sp}(r) = \sum_i^k C_{nk} u_{nk}(r) \exp(ik.r)} \tag{1.9}$$

where C_{nk} is the expansion coefficients, imposed to satisfy the spherical boundary condition in the small nanocrystal. The equation 1.9 becomes simplify when we consider the weak dependence of the u_{nk} on k. In this situation

$$\boldsymbol{\psi_{sp}(r) = u_{n0}(r) \sum_k C_{nk} \exp(ik.r) = u_{n0}(r) f_{sp}(r)} \tag{1.10}$$

where, the "$\boldsymbol{u_{n0}(r)}$"is referred as single particle function. Due to the periodicity in the smaller nanocrystals the periodic function "$\boldsymbol{u_{n0}(r)}$" which can be determined as the linear combination of the atomic orbital’s (LCAO). In this tight binding situation the "$\boldsymbol{u_{n0}(r)}$" can be expressed as follow:

$$\boldsymbol{u_{n0}}(\boldsymbol{r}) \approx \sum_{i}^{k} \boldsymbol{C_{nk}}\mathbf{exp}(\boldsymbol{ik.r}) \qquad (1.11)$$

the band index *n* refers for CB and VB for electron and hole respectively. Therefore, for a spherical nanocrystal with infinite potential barrier the envelope function of the electron and hole can be addressed from particle-in-a-sphere model. So, the nanocrystal problem is reduced to the single particle function, $\boldsymbol{f_{sp}}(\boldsymbol{r})$ which is nothing but particle-in-a-sphere model. In case of exciton (electron hole pair, ***ehp***) the envelope wavefunction $\boldsymbol{f_{ehp}}$ can be expressed as the combination of electron and the hole envelope function. The energy of the exciton can be written as follow

$$\boldsymbol{E_{ehp}} = \boldsymbol{E_g} + \frac{\hbar^2}{2a^2}\left(\frac{\alpha^2_{n_e L_e}}{m^c_{eff}} + \frac{\alpha^2_{n_h L_h}}{m^v_{eff}}\right) \qquad (1.12)$$

However, due to the smaller size regime the exciton suffers strong coulomb attraction which leads to the exciton into the bulk materials. As we know that the coulomb energy is inversely proportional to the size of the effective radius. In the smaller QDs the energy of the exciton depends on two opposite factors: one is confinement energy which stabilizes the smaller NCs and the other is coulomb energy which destabilizes the nanostructure. However, as the confinement energy is inversely proportional to the square of the size of the NCs and in the strong confinement regime the confinement energy dominant over the coulomb energy. [52] Therefore, the energy of the exciton in the QDs can be expressed as follow:

$$\boldsymbol{E_{ehp}} = \boldsymbol{E_g} + \frac{\hbar^2}{2a^2}\left(\frac{\alpha^2_{n_e L_e}}{m^c_{eff}} + \frac{\alpha^2_{n_h L_h}}{m^v_{eff}}\right) - \frac{1.8e^2}{\varepsilon a} \qquad (1.13)$$

So, due to the discrete nature of the energy states the electronic levels of the QDs are assigned as atomic like orbital’s such as 1S, 1P, 1D, 2S etc.

In the present thesis we used colloidal CdX (X= S, Se, Te) QDs for charge transfer investigation and finally in QDSC application. The discrete CB and VB energy levels of the CdSe QDs are demonstrated in the next section.

1.2.4. Band Structure

Although from the theoretical aspect of the approximation it is found that the bulk conduction and valence band are parabolic in nature. However, the real band structure of the II-VI semiconductor is more complicated. In case of CdSe the CB obeys the effective mass approximation however, VB does not. The CB of the CdSe arises from the cadmium's 5*s* orbital which is only 2-fold degenerate at $k = 0$. On the other hand the more complicated VB is made upon from the 4*p* orbital of the selenium which is 6-fold degenerate at $k = 0$.[18] The valence band degeneracy of the two different structural forms (diamond and wurtzite) of the CdSe is presented in the Figure 1.3. In the diamond like structure due to strong spin-orbit coupling (Δ = 0.42 eV) [60] the degenerate VB split into two, $p_{3/2}$ and $p_{1/2}$, states at $k = 0$ point. The subscript (3/2 and 1/2) arises due to spin orbit coupling and refers as *angular momentum* ($J = l+s$). For selenium atom the 4*p* orbital contains four electron, the angular contribution $l = 1$ while the spin contribution $s = 1/2$. Away from $k = 0$ point the band $p_{3/2}$ further split into two subbands, $J_z = \pm 3/2$ and $J_z = \pm 1/2$, where J_z is the projection of J. These three bands are usually referred as heavy-hole (*hh*, $J = 3/2$ and $J_z = \pm 3/2$), light-hole (*lh*, $J = 3/2$ and $J_z = \pm 1/2$) and split-off-hole (*so*, $J = 1/2$). However, in the wurtzite (hexagonal) structure the heavy-hole and the light-hole levels are no longer degenerate at $k = 0$ point due to crystal field splitting (Δ_{cf}) [18]. The effective masses are $m_{hh} = 1.14m_0$, $m_{lh} = 0.31m_0$, and $m_{so} = 0.49m_0$, respectively.[61]

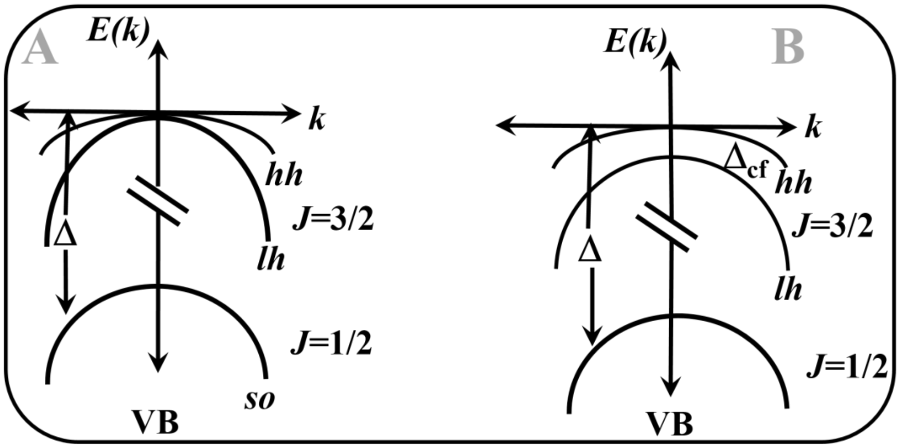

Figure 1.3: Valence band (VB) splitting of the bulk CdSe in (A) diamond and (B) wurtzite like structure at $k = 0$ point. Adopted from reference [49].

However, there are several other methods like ***k.p*** model [62, 63], the Luttinger Hamiltonian,[64, 65] Kane model [66-68] etc. to establish the structure of the semiconductor CdSe nanocrystals.

1.2.5. Electronic Structure of Quantum Dots:

From the equation 1.13 it is clear that with decreasing size of the NC the discreteness of the energy levels of VB and CB increases which also reconfirmed through size dependent optical studies.[69] In contrast to the bulk semiconductor, the VB and CB become no longer continuous in smaller NC QDs where the charge carries are confined. Therefore, the energy states of either CB or VB can be assigned by the total angular momentum of the corresponding charge carrier. The total angular momentum (F) of either electron or hole (F_e or F_h) has two contribution (a) a "unit cell" contribution (J) due to the underlying atomic basis, which forms the bulk bands and (b) an envelope function contribution (L) due to the particle-in-a-sphere orbital. It is expected that quantum number indicating each valence subband (J_h) and each envelope function (L_h) are conserved. However, in reality the valence band mixing is observed.[18, 59, 70-72] Thus, neither

L_h nor J_h are conserved. Only the parity and total hole angular momentum (F_h) are good quantum number. Therefore, for quantum dots the valence band is the mixture of all three subbands. However, on the other hand the electron levels arising from the conduction band is unaffected by such kind of perturbation. The angular momentum of electron and hole states are used as nL_e and nL_h arises due to the envelope wave function. For typical notation for L values are S, P, D etc for L = 0, 1, 2 etc. and n value varies 1, 2, 3 etc. Thus the electron states are defines as $1S_e$, $1P_e$, $1D_e$ etc. while the hole states are as $1S_h$, $1P_h$, $1D_h$ etc.

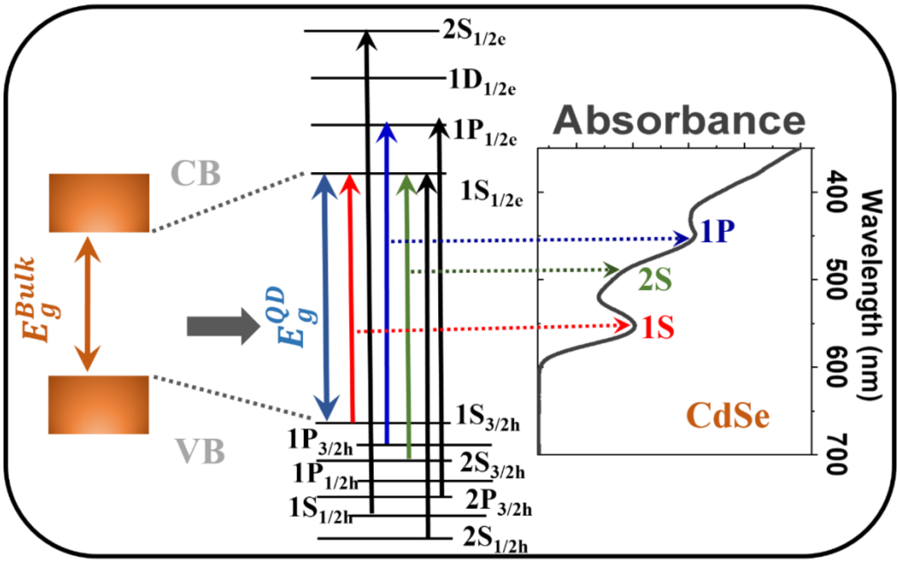

Figure 1.4: Evolution of energy levels diagram from bulk semiconductor to the QDs. The optical transitions occur between the discrete hole and the electron levels arising from the valence band and conduction band respectively.

In bulk semiconductor the valence band splits into three sub bands (Figure 1.3), and due to mixing of these subbands the VB states of the all quantum dots are complicated. In case of CdSe nanocrystals the size dependent hole energy calculation by taking into account of mixing between heavy hole, light hole and split-off hole shows the lowest energy hole states are $1S_{3/2h}$,

$1P_{3/2h}$, $2S_{3/2h}$. Therefore, the lowest energy transition [69] can be expressed as $1S_e1S_{3/2h}$ (1S), $1S_e2S_{3/2h}$ (2S) and $1P_e1P_{3/2h}$ (1P) and are shown in Figure 1.4. From the optical absorption spectra of the CdSe QDs these transition can easily be correlated and referred as first, second, third excitonic transition respectively. However, the fine structure of the exciton can be explained assuming the non-spherical shaped and exchanged interaction of the particles. The exciton fine structures of the CdSe QDs are demonstrated in the next section.

1.3.1. Exciton Fine Structure

Although the particle in a sphere model provides an idea about the band structure and energy levels of small QD, however there are several other factors which are responsible for deviation of the energy levels. In the earlier discussion we have mentioned due to non-spherical shape (wurtzite,[55] actual shape is prolate [69] like) of the CdSe QDs the valence band split in different subbands.[73] On the other hand, the CdSe form spherical cubic structure (zinc blend) in which each of the electron and hole states are highly degenerate. The interband exchange

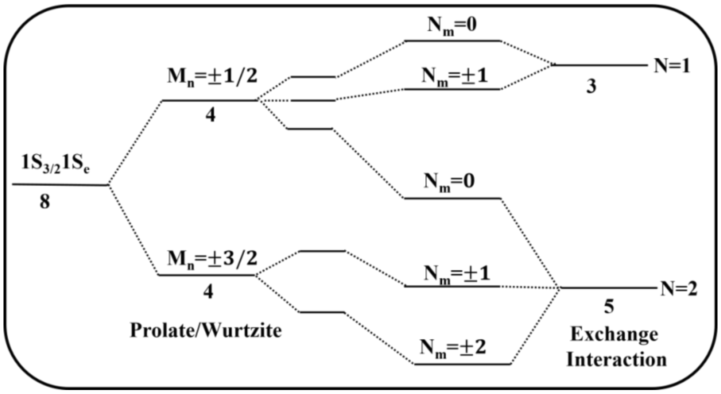

Figure 1.5: Exciton fine structure and a correlation energy level diagram between the non-spherical (wurtzite/prolate) and spherical (zinc blend) shaped CdSe QD. Number represents the degeneracy. Adopted from the references [49].

interaction increases with increasing electron hole overlap which dominant in smaller NCs QD over bulk.[74-76] As a result, the degeneracy is lifted by this second-order effects. The first excited state i.e. $1S_{3/2h}$-1Se, of the CdSe QD is eight fold degenerate. The exciton fine structure and the correlation energy level of the wurtzite and spherical shaped CdSe QD are illustrated in the Figure 1.5. To demonstrate this energy level diagram we consider two limiting conditions. The excited state $1S_{3/2h}1S_e$ is split into two states with 4-folds degenerate states due to non-spherical shaped which refers as $M_n = \pm 3/2$ and $M_n = \pm 1/2$ in the left side of the Figure 1.5. The values ± 3/2 or ± 1/2 arises due to projection of the total angular momentum of the lowest energy electron and hole in the CB and VB respectively. Again, in the small size of the QD the electron-hole interaction is enhanced strongly due to the charge carrier confinement. Considering the exchange interaction in small size regime we draw the splitting of the subband energy levels in the right side of the Figure 1.5. In the presence of strong e–h exchange, the lowest energy 1S electron and $1S_{3/2}$ hole states, which are characterized by angular momenta 1/2 and 3/2, cannot be considered independently but should be treated as a combined exchange-correlated exciton with a total angular momentum, N, of either 1 or 2. These two states are split by the exchange interaction forming a high-energy, optically active $N = 1$ *bright* exciton and a lower-energy, optically passive $N = 2$ *dark* exciton. The dark ($N = 2$) and the bright excitonic states further split into five energy levels having 5-fold and 3-fold degenerate states respectively due to deviation from the spherical shaped (e.g. wurtzite or prolate) . The correlation between this two split states is shown in the middle of the Figure 1.5 and refers as N_m, where N_m is the quantum number i.e. the projection of N along with unique crystal axis. Except the energy level $N_m = 0$, each energy state are twofold degenerate. As s results, eight fold degenerate band-edge exciton split into five subband. [77]

1.3.2. Dark exciton and Stoke shift

The excited state charge carrier recombination of the bulk II-IV semiconductor is reported ~1 ns [78] while for smaller NCs it extend up to several μs. Many researchers reported the long life time of the NCs is due to the surface state life time which is increased as the electron hole decoupled from each other. However, for very high quality NCs the longer excited state life time can't be explained. The long life time of the exciton in the smaller QD can be described in terms of dark exciton. The exciton fine structure can be explained in terms of e-h exchanged interaction and anisotropy associated for the non-spherical shaped of the NCs. From the above discussion we found that the fine structure of the $1S_{3/2}$-$1S_e$ excitonic state split into five different sub levels. Since these levels having same N_m value these can be labelled as "U" for upper and "L" for lower states (Figure 1.6). Fortunately the combination of level splitting does not change the nature of the states i.e. the lowest state ($|N_m| = 2$) remains optically passive. The anomalous emission behaviour of the smaller NCs QD was first proposed by Calcott et al.[76], on the basis of exciton fine structure and dark exciton transition. The photoluminescence of the QDs (red solid line in the Figure 1.6) are due to electron-hole radiative recombination from the lowest excitonic state ($|N_m| = 2$, dark excitonic) to the ground sate which is also known as *dark exciton*. The transition from the $|N_m| = 2$ state to the ground state is the forbidden transition in terms of electric dipole approximation. For the angular momentum conservation two photons are to return to the ground state from the $|N_\mathrm{m}| = 2$ sublevel thus this transition is one-photon forbidden. Conversely, the optical transition from the ground state to the 1^Lstate is the lowest optically allowed transition which is active state. The broad optical absorption spectrum of the QDs (Figure 1.6 right side) is due to transition from ground state to the 1^U and 0^U state. On photoexcitation the excited charge carriers are thermalized to the dark state from the higher excitonic state. The energy separation between the dark state and the first allowed state (1^L) is larger than the $k_B T$ (where k_B is Boltzmann constant). Therefore, the thermalized electron does not return to the upper allowed state and finally recombine with the ground state. As a result, the emission of the NCs from the dark state (2) to the ground state is red shifted as compare to the lowest allowed transition. So, the energy difference between the lowest bright state (allowed optical transition) and the dark state is referred as the resonant Stokes shift (Δ_S^r) energy. [17, 49] The value of Δ_S^r is depend on the size of the NCs. [77]

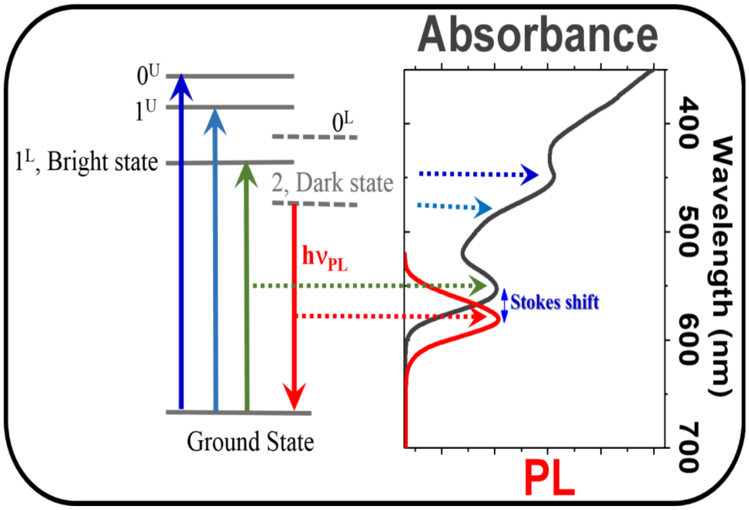

Figure 1.6: Optical transition in CdSe NCs considering electron-hole exchange interaction and anisotropy associated with crystal field in the wurtzite lattice structure. Optical absorption and photoluminescence (PL) are due to bright state and dark state transition. The energy difference between the lowest absorption and emission energy levels is referred as Stokes shift.

1.4. Density of States (DOS) in Different Size NCs

The number of states present with in an energy level refers as density of states.[79] The important properties like steady state optical property and the charge carrier relaxation process depend on the density of the states involve in a semiconductor. The number of DOS can be derived from the confinement of the charge carrier. Assuming the particle confined in a potential barrier following the boundary condition

$$k_x = \frac{2\pi}{L} n_x, \quad k_y = \frac{2\pi}{L} n_y, \quad k_z = \frac{2\pi}{L} n_z \tag{1.14}$$

Where "k" and "n" refers as wavevector and a real value respectively.

Therefore, the electron density of the state can be defined as

$$N = 2 \times \frac{4\pi}{3} \times k_f^3 \times \frac{V}{8\pi^3} \tag{1.15}$$

Where, "V" is the volume per state ($k = \frac{8\pi^3}{V}$) and the factor "2" arise due to two spin states.

The density of state (DOS) can be given as

$$\boldsymbol{g(E) = \frac{1}{V}\frac{\partial N}{\partial E}} \tag{1.16}$$

Considering the isotropic parabolic energy distribution of a bulk (3D) semiconductor with respect to wave vector (k) the DOS can be expressed by,

$$\boldsymbol{g(E)^{3D} = \frac{\sqrt{2Em^3}}{\pi^2\hbar^3}} \tag{1.17}$$

which is highly dependent of energy. In case of quantum well (i.e. two dimensional system) the DOS is independent of energy, and can be expressed as

$$\boldsymbol{g(E)^{2D} = \frac{m}{\pi\hbar^2}} \tag{1.18}$$

Thus the particles are independent of energy. For one dimensional particle (quantum rod) the DOS can be as follow

$$g(E)^{1D} = \frac{m}{\pi\hbar}\sqrt{\frac{2m}{E}} \tag{1.19}$$

So, DOS of 1D particle decreases as the energy increases. For zero dimension system (quantum dot) the charge carriers are confined in all three special directions as a result energy states are discrete and the DOS can be simply expressed as a delta function. Figure 1.7 illustrates the variation of DOS with decreasing carrier confinement in nanocrystal semiconductor.

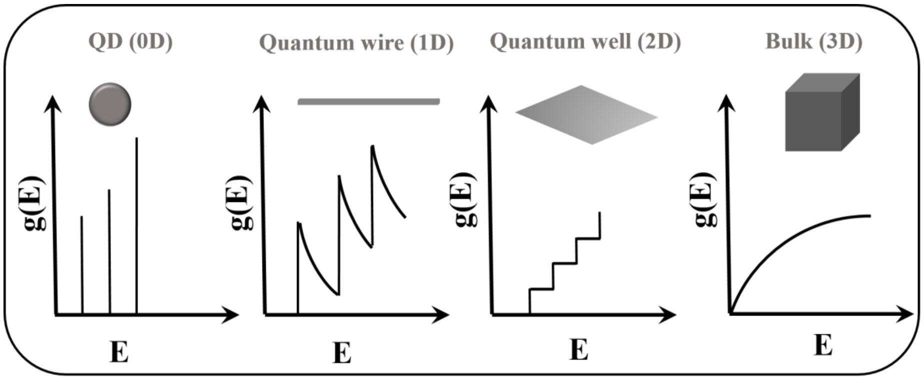

Figure 1.7: Change in density of states with decreasing carrier confinement.

1.5. Carrier Relaxation

In the present thesis we have synthesized the smaller QDs through wet chemical method where the surface of the NCs is surrounded by the surface passivated organic ligand. The intraband charge carrier relaxation in this quantum confinement NCs system occurs through three major mechanisms such as phonon-assisted relaxation (i.e. phonon modes of the crystal lattice), Auger recombination, and electronic to vibrational energy transfer (EVET) from QD to ligand.[80]

1.5.1. Phonon-Assisted Intraband Electron Relaxation

In bulk II-VI semiconductor the carrier relaxation time leads by very fast carrier cooling dynamics (typically subpicosecond) which is dominated by Fröhlich interaction with longitudinal optical (LO) phonons mechanism.[81] The typical energy difference between the intraband levels of the CB is varied hundreds of milli eV [69, 82] while the phonon has energy in the order of sub ten milli eV [83]. Now, the phonon mediated energy relaxation time (τ) of the hot electron can be expressed as follow [81]

$$\tau = \frac{1}{\omega_{LO}} \exp\left(\frac{\Delta E}{k_B T}\right) \tag{1.20}$$

Where, ΔE is the energy spacing between the subband states of the CB and ω_{LO} is the frequency of the longitudinal optical phonon. Thus carrier relaxation mediated by interaction by the electron-LO phonon which increases the cooling time of the NCs with decreasing size of the NCs due to restriction imposed by momentum and energy conservation.[81, 84] This effect is referred as "*phonon bottleneck effect*".[85] For the NC having strong confinement regime the energy relaxation occurs via weak multiphonon processes.

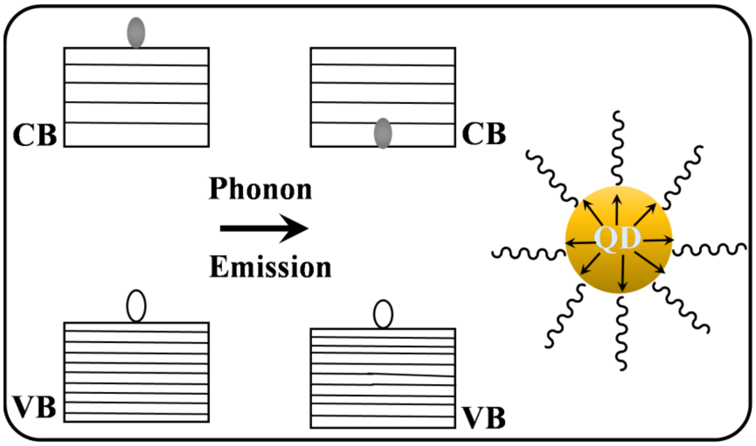

Figure 1.8: Schematic illustration of intraband electron cooling through phonon emission.

Since the energy spacing between the intraband electron state is more compare to the hole state, thus "phonon bottleneck effect" affect electron cooling time over hole cooling. In case of smaller NC QDs the relaxation time varies few hundreds of femtosecond (fs) and its decreases with decrease the size of the QD. Thus the energy relaxation in the strong confinement system is no longer taken place through phonon assisted mode. However, the phonon bottleneck effect is observed in limited number of epitaxially grown QDs. [61,84,86]

1.5.2. Relaxation through Auger Process:

As the hot electron relaxation time of the QDs decreases with decreasing the size of the NCs. This mechanism can be explained in terms of Auger type electron hole energy transfer. In case of II-VI QDs, the energy levels of the CB and VB become discrete and due to more degeneracy of the VB the intraband energy spacing between the hole levels is smaller than the electron energy. In the smaller size regime due to large coulomb attraction the electron-hole become couple each other strongly. Thus the energy transfer from the hot electron to the more dense hole state (as the energy release by the electron overlapped with hole states) occurs through non-radiative manner

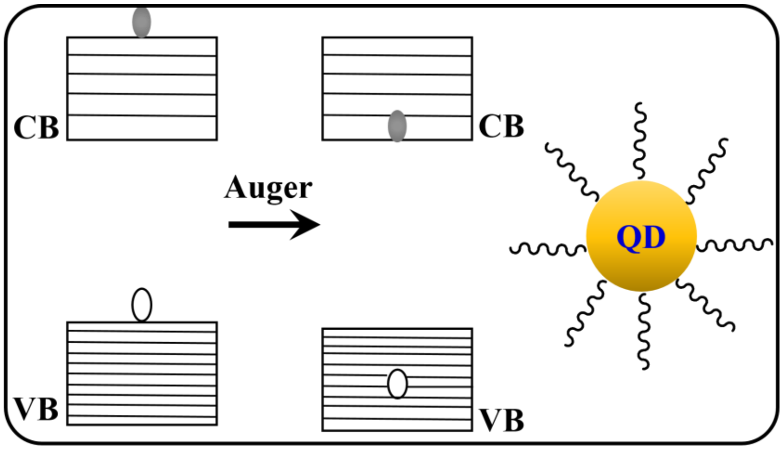

Figure 1.9: Schematic illustration of intraband electron cooling through Auger process.

which leads to extend of electron hole wavefunction overlap. This energy loss mechanism involves transfer of the excess energy of an electron to the hole and subsequently fast hole relaxation through dense spectrum state. This is an intrinsic electron cooling mechanism which involves Auger type electron-hole interaction and leads to significantly faster cooling over multiphonon emission.[87-94] When the excitation energy is much higher than the band edge energy (i.e. $h\nu >> E_g$) of the NCs, the hot electron release excess energy which can generate another exciton in the same NCs– resulting formation of bi-exciton. Depending the band gap of the NCs (usually the lower band gap NCs such as PbS, PbSe etc.) and the photon energy some time more than two exciton generate which is known as “multiple exciton generation” (MEG).[95-100] As the released excess energy of the hot electron help to harvest another exciton, this process sometimes can be referred as impact ionization.

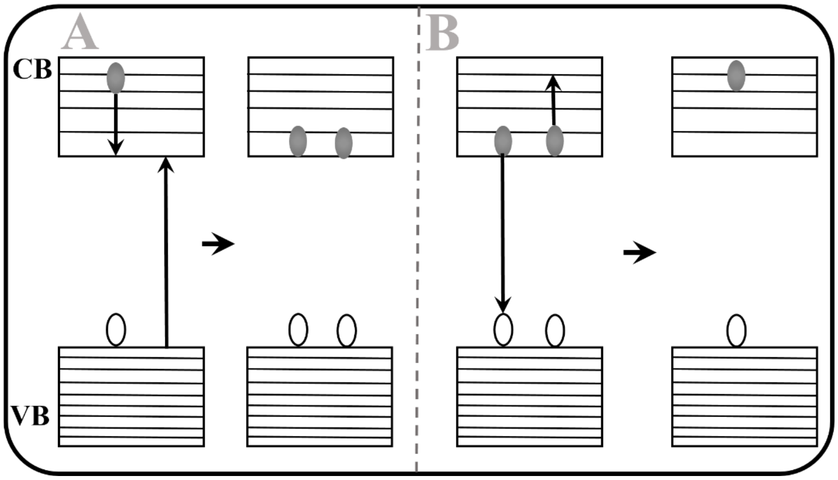

Figure 1.10: Auger assisted multiple exciton generation (A) and Auger recombination (B) process.

1.5.3. Relaxation via EVET process:

Apart from these carrier relaxation, another mechanism of the cooling process is the energy transfer from electronic state of the QDs to vibrational state of the surface molecule.[82, 101] As we already discussed that the synthesized QDs are well passivated by the organic surface ligands like oleic acid, trioctylphosphine, trioctyl phosphine oxide (TOPO) etc. When the energy of the intraband spacing matches with vibrational state of the ligand molecule, the hot carrier releases its excess energy through non-radiative manner. Thus transfer of energy of the either of the charge carrier increases the relaxation of the other carrier through Auger process via decoupling of the charge carrier. [93, 102-104] As we have discussed that the energy transfer from hot electron to the hole dominants in smaller QDs during intraband electron cooling process in the CB. However, due to smaller inter-level spacing of the VB the phonon emission by the hot hole can provide an efficient mechanism for relaxation.

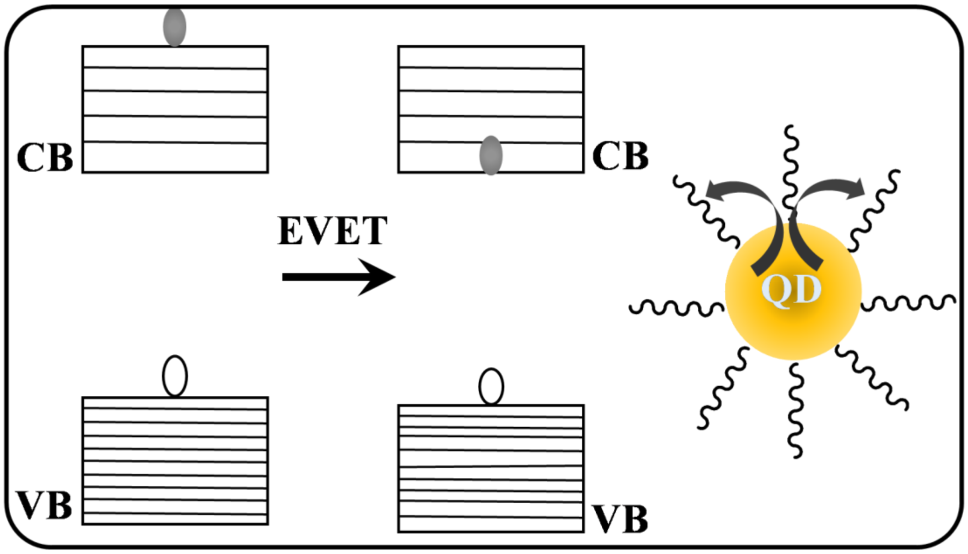

Figure 1.11: Schematic illustration of intraband electron cooling through electronic to vibrational energy transfer (EVET) process.

1.5.4. Trapping and Recombination:

The energy relaxation process is nonradiative and the excess energy can be released as heat energy. In smaller QDs due to very high surface to volume ratio the NCs accumulates surface defect states.[105, 106] These surface defect states could arise due to different reasons like smaller size than the bulk, dangling bonds, capping agent, crystal mismatched etc. The hot charge carrier gets trapped in the surface state with very fast non radiative process. As a results, the cooling of the charge carrier become slowing down. The charge carrier tapping dynamics depends on the nature of the trapped state. Finally the charge recombination of the charge carrier slowed down due to decoupling of electron hole.[107, 108]

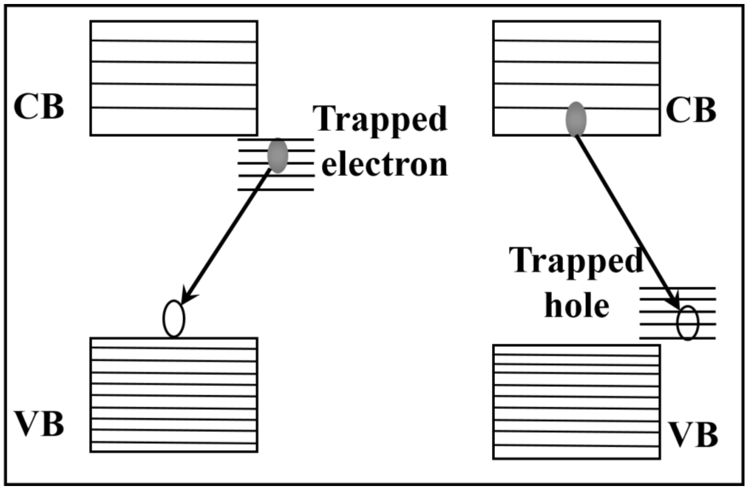

Figure 1.12: Electron and hole trapping and their recombination dynamics in NCs quantum dots.

1.6. Heterostructure

1.6.1. Core-Shell Nanocrystal:

Nanocrystal QD comprises very high surface to volume ratio which leads to the different trapped states. To increase the quality and the electronic structure of the semiconductor QDs often core/shell nano-architecture are used for different application. These core/shell NCs possess more than one semiconductor in a single nanostructure which is referred as heterostructure (HS). Depending on the band energy alignment of the semiconductor NCs, type-I and type-II core/shell heterostructure are recognized.[109-113] In a type-I heterostructure, the smaller band gap materials are confined in the core which is surrounded by a wider band gap materials.[114] The reverse band alignment of these heterostructure is referred as inverted type-I core-shell.[115] Conversely, in a type-II core/shell structure, the lowest energy states of the VB and CB are separated in different materials. Thus on photo excitation both electron and hole are localized in the core material while in case of type-II either of the charge carrier are localized either in core or shell.[116-118] Apart from these type-I and type-II heterostructure, another important class of heterostructure are well established depending on the charge carrier delocalization. This type of heterostructure is known as quasi type-II or type-I$^{1/2}$core/shell.[119-122] In quasi type-II core/shell the band alignment of the heterostructure are like type-I however, due to low CB or the VB offset energy difference either of the charge carrier are delocalized in two nanocrystal. This type of heterostructure is more useful in terms of quality as well as application. The wider band materials passivate the core of the NC while the charge delocalization increase charge separation. The energy level band structure and extend of charge carrier localization of these kinds of core-shells heterostructure are shown in the Figure 1.13.

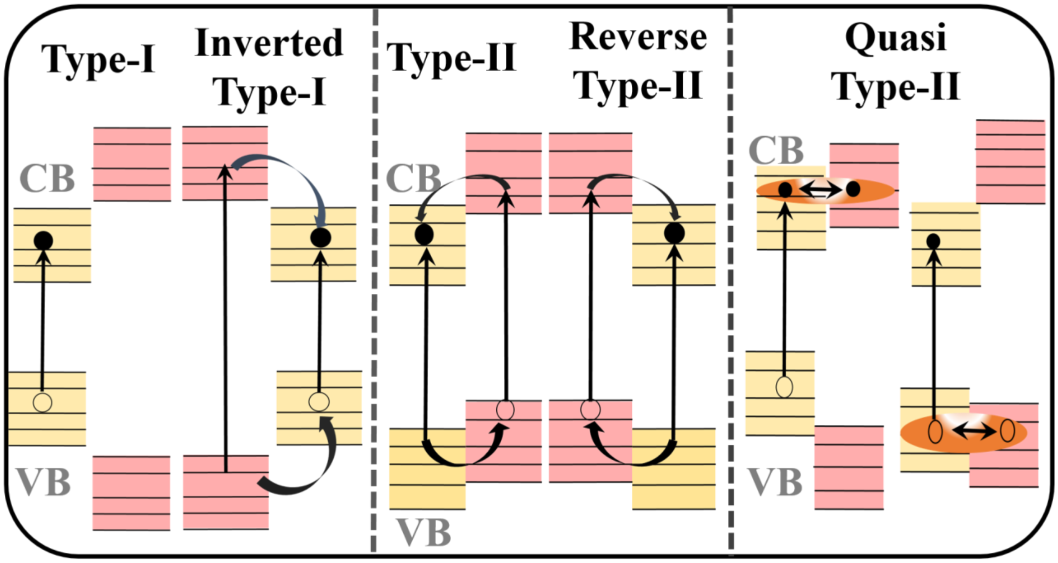

Figure 1.13: Illustration of charge carrier distribution in different types of core-shell heterostructure.

In the present thesis CdS/CdSe, CdSe/CdS and CdS/CdTe are used to investigate the charge carrier dynamics as inverted type-I, quasi type-II and type-II core-shell respectively. The carrier cooling dynamics of the CdS_xSe_{1-x} and $Cd_xZn_{1-x}Se$ alloys are investigated utilizing graded quasi type-II core-shell structure where electron and hole are delocalized in CB and VB of the alloy structure respectively due to low corresponding band edge energy difference.

1.6.2. Alloyed QDs

Band edge engineering in semiconductor nanocrystals is very essential for different application purpose. It is more challenging for II-VI semiconductor quantum dot to manipulate the band gap without changing the size of the nanocrystals that can be easily achieved by alloying. Alloy QDs are the new class of versatile semiconductor nanocrystals.[123, 124] The quantum confinement effect of the alloy also achieve by the dual behavior, size of the NC and composition. Therefore, the physical and opt-electronic properties of the alloy QDs depend on both size of the NC as well as the composition of the constituents. Thus, composition of alloy nanocrystals plays an extra degree of freedom towards selecting desirable properties which can help to design better nanostructure for several applications. Alloy QDs consists two or more heterojunction semiconductor surfaces that exhibit new rearrangement of the charge carrier in the energies levels of the adjoining segments. Due to high surface to volume ratio the smaller NCs accumulate lots of surface defect states where charge carriers are trapped as a result non-radiative processes are increased. The surface trapped states can be reduced down by forming the alloy where the wider band gap semiconductor material acts as a passivated layer. Utilizing these exciting properties of the alloy QDs these materials are used in various applications like photovoltaics, light-emitting diodes, photocatalysis, in vivo imaging etc.[125-130] Depending on the structural property these NCs are classified as homogeneous and graded alloy. In homogeneous alloy, the distribution of the constituent through the nanocrystals is same, while in graded structure due to difference in reactivity of the constituent they form quasi core-shell type structure.[129, 131] Thus, the charge carrier dynamics in homogeneous alloy and the in graded alloy varies with their structure.

In the present work, we have synthesized CdS_xSe_{1-x} and $Cd_xZn_{1-x}Se$ alloy QDs and their carrier cooling and charge separation dynamics has been investigated using femtosecond transient absorption spectroscopy. Utilizing the slow intraband electron cooling dynamics of the CdS_xSe_{1-x} alloy QD we successfully incorporate these materials as light harvesting in QDSC.

1.7. Colloidal Semiconductor Quantum Dots

In 1959, Richard Feynman proposed that devices and materials could one day be invented to atomic specifications without violating the laws of physics. His thinking nowadays are successfully used in nanotechnology after developing two major methodologies of nanocrystal synthesis technique like *top down* and *bottom up* approaches. Top-down approaches use larger assembly of nanostructures.[132, 133] During self-assembly the physical forces operating at nanoscale are used to combine basic units into larger stable structures. Typical examples are quantum dot formation during epitaxial growth and formation of nanoparticles from colloidal dispersion (macroscopic) initial structures, which can be externally-controlled in the processing of nanostructures. Typical examples are etching through the mask, ball milling, and application of severe plastic deformation. On the other hand bottom-up approaches include the miniaturization of materials components (up to atomic level) with further self-assembly process leading to the formation of nanoparticles from the colloidal dispersion. In general, methods for preparing nanomaterials also can be divided into two categories: physical and chemical. Physical preparation methods include: vapor condensation, physical fragmentation, amorphous crystallization etc. Chemical preparation methods Chemical methods include: sol-gel synthesis, chemical precipitation, hydrothermal, metal-organic chemical vapor deposition (MOCVD), molecular beam epitaxy (MBE)etc.[134] In this chemical approach one can have significant reproducibility for given reaction conditions.

In the present thesis apart from the charge carrier dynamics of the NC QDs, the synthesis of these NCs has been performed using different synthesis protocols. To study charge carrier dynamics it is very important to have very high quality monodispersed size distributed NCs. Therefore, in the present study we use colloidal protocols for synthesis of the quantum dots NC. Again during the colloidal synthesis nucleation, growth and precipitation can take place simultaneously. Thus it is difficult to control the sharp size distribution. Separate nucleation and growth process can lead the narrow size distribution.[19] This can be achieve by controlling precursor concentration (self focusing) [135] and a capping ligand during synthesis. The capping ligand binds to the surface of the NC which controls the growth process via inhibiting the agglomeration. At the same time it helps to passivate the surface trapped states. One of the most familiar methods to colloidal synthesis of quantum dots is arrested precipitation technique. In this technique one of the precursors in solution is maintained at high temperature and the other precursor is injected rapidly into the solution leading to formation of nuclei and subsequent growth takes place over these nuclei forming monodispersed nanoparticles at a lower temperature to reduce further nucleation. The present work involves mainly synthesis of the II-VI (CdX, X=S, Se, Te) semiconductor where cadmium precursor (CdO, $CdAc_2$) is dissolved in oleic acid and the selenium precursor is injected into the reaction mixture at ~300˚C. Details experimental procedure of the NC QDs is described in the chapter 2. The selenium precursor is added to the cadmium precursor at high temperature which leads to super-saturation. As a results formation of nuclei instantaneously this is also referred as burst nucleation. Formation of nuclei is a high barrier process however due to high super-saturation and temperature, nucleation commences. On addition of the selenium precursor into the reaction mixture the temperature of the reaction reduced by ~20˚C and additionally precursor concentration also decreases due to formation of nuclei leading to lower probability of formation of further nuclei. After nucleation the growth process begins. Thus the monodispersity of the nanoparticles can be achieved utilizing these separate nucleation and growth process. The overall nucleation and growth process can be described in terms on precursor concentration and reaction time using La Mer's model.[19, 136] Figure 1.14 illustrates the La Mer model of precursor concentration versus reaction time which clearly shows the distinct temporal separation between nucleation and growth process. As soon as the precursor is injected the burst nucleation commences which take place till the concentration of the precursor is above the nucleation threshold. Below the nucleation threshold concentration the no new nuclei is formed and the remaining precursors lead to growth process.

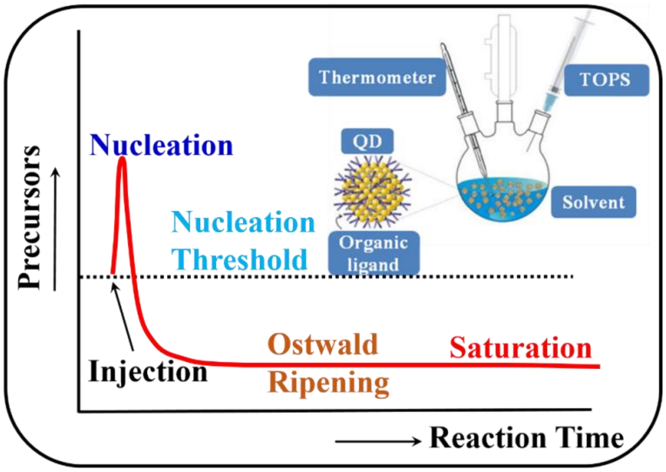

Figure 1.14: Schematic presentation of the La Mer's model for the growth of monodispersed colloidal QDs starting from nucleation. Adopted from reference [136].

Therefore this method can be achieved where the nucleation threshold is tuned to optimize monodispersity of nanoparticles. The model shows that monodispersity is achieved when consumption of precursor does not exceed precursor addition rate. Again, the growth process is much slower during the nucleation process leads to sharp size distribution. Initial stage monodispersity is maintained by the nucleation while the ultimate monodispersity is controlled by the growth process. The growth process can be divided by two processes; fast growth stage and slow growth stage. The fast growth stage occurs from the remaining precursor in the solution in which the smaller particle grows faster than larger particles due to minimize the excess surface energy.[19] When the monomer concentrations are sufficiently depleted, the growth of the nanoparticles proceeds through slow growth rate refers as *Ostwald ripening*. The sacrificial dissolution of the smaller nanoparticles results in growth of larger particles as a results size defocusing takes place. The Ostwald ripening can be controlled by rapid changing the reaction mixture.

The supersaturation and nucleation of the reaction can also be achieved by slow changing the reaction temperature. In this situation the precursor are mixed at low temperature and the supersaturation and decomposition occur with increasing temperature. Similarly, the supersaturation is again revealed by a nucleation burst after which temperature is controlled to avoid additional nucleation events, allowing monomer addition to existing nuclei to occur more rapidly than new monomer formation. Therefore, nucleation does not need to be instantaneous, but in most cases it should be a single, temporally discreet event to provide for the desired nucleation-controlled narrow size dispersions.

The very good size distribution (standard deviation, $\sigma < 10\%$) can be achieved by controlling precursor concentration, reaction time and temperature of the reaction mixture. [137] The unreacted precursor can be separated out using solvent mixture. In case of oleic acid capped QDs polar solvent like ethanol, methanol or acetone etc. are used to clean the QDs. [138, 139]

1.8. Electron Transfer:

1.8.1 Theory of Electron Transfer

The electron transfer theory of the donor (D) acceptor (A) pair are based on the Marcus electron transfer model.[140, 141] To describe the model, harmonic oscillator approximation is used where the reactant (D-A) transform to the products (D^+-A^-) via transition states (D---A). The potential energy fluctuation of the reactant and product are shown in Figure 1.15. During the electron transfer process the internuclear distance remain unchanged (Franck-Condon principle)[142] Therefore, during the electron transfer process only the solvent coordinate change with respect to activation energy ($\Delta G^{\#}$).

According to classical theory of electron transfer, the crossing rate of T.S. is Arrhenius function of activation energy ($\Delta G^{\#}$) along with pre-exponential factors which are frequency ($\boldsymbol{\nu_n}$) of nuclear motion passing through transition state and crossover transmission probability ($\boldsymbol{\kappa_t}$). The activation energy is formulated in terms of driving force ($\boldsymbol{\Delta G^0}$) and solvent reorganization energy (λ) by applying Gibbs free energy as quadratic function of solvent reaction coordinates. Rate of electron transfer is given by

$$\boldsymbol{k_{eT} = \kappa_t \nu_n \exp\left(\frac{-\Delta G^{\#}}{k_B T}\right)} \tag{1.21}$$

$$\text{and, } \boldsymbol{\Delta G^{\#} = \left(\frac{-(\Delta G^0 + \lambda)^2}{4\lambda}\right)} \tag{1.22}$$

The reorganization energy, λ, can be expressed as sum of energy involved in solvation and vibration as, ($\lambda = \lambda_s + \lambda_v$). The equation 1.21 suggests that the electron transfer rate depend on the parameters, reorganization energy as well as the change in free energy ($\boldsymbol{\Delta G^0}$). Depending the value of the λ and $\boldsymbol{\Delta G^0}$ the electron transfer process can be recognized in three different regions which are illustrated in the Figure 1.16. Figure 1.16 suggests that when the value of the λ is greater than the value of $\boldsymbol{-\Delta G^0}$, the rate of electron transfer increases with increasing the value of $\boldsymbol{-\Delta G^0}$. This region is referred as Marcus *normal region* of electron transfer. When the value of λ is equals to the value of $\boldsymbol{-\Delta G^0}$ the situation is known as barrier-less region. For barrier-less transition the change in free energy of activation is zero. The situation when the value of the $\boldsymbol{-\Delta G^0}$ is greater than the value of λ, rate of electron transfer decreases with increasing $\boldsymbol{-\Delta G^0}$ value. This is referred as Marcus inverted region. [143, 144]

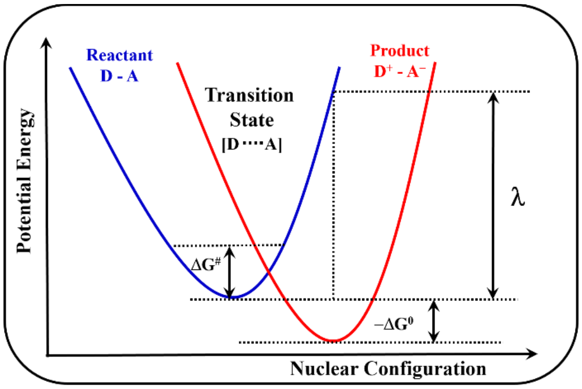

Figure 1.15: Potential surface energy versus nuclear configuration plot of a donor acceptor system in electron transfer reaction. ΔG^0 and the $\Delta G^\#$ are the free energy change and free energy of activation respectively.

In order for electron transfer to occur, an overlap between the populated orbital of the donor and the empty orbital of the acceptor is necessary in the activated complex. This electronic interaction involves a split of electronic energy levels. If the electronic states are of the same symmetry, rupture of the Frank-Condon principle at the saddle point causes in turn a split of

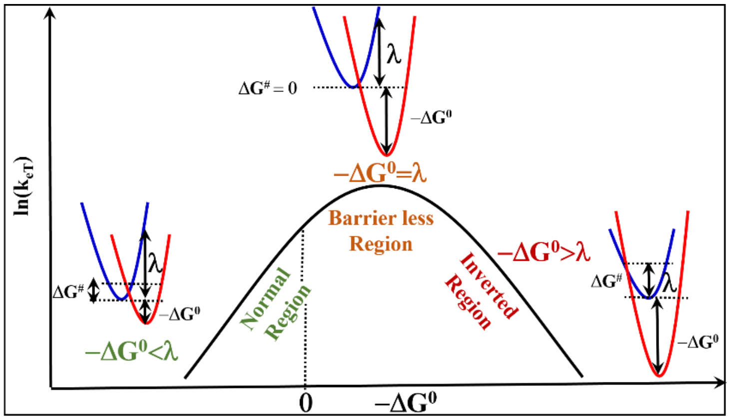

Figure 1.16: ln (k_{eT}) *vs.* change in free energy (ΔG^0) plot shows three different region of electron transfer reaction.

potential energy levels and *avoided crossing* of the two curves.[142, 145] As a result two potential surfaces are created that are separated at the configuration of the activated complex by

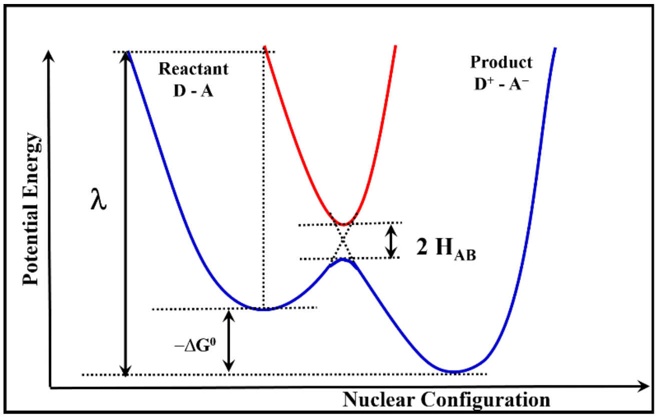

Figure 1.17: Schematic representation of electronic coupling matrix element (H_{AB}) for an electron transfer reaction.

an energy gap 2|H_{DA}| (Figure 1.17). |H_{DA}| is a matrix element for *electronic coupling* between the donor and the acceptor. Depending on the value of the H_{DA} the electron transfer process can be referred as *adiabatic* (When (|H_{DA}| >> k_BT) and *diabatic* (or *non-adiabatic*) (|H_{DA}| < k_BT). For most of the cases, the electron transfer rate depends on the electronic coupling parameter, $|H_{DA}|$. In such cases, the electron transfer rate can be expressed by the Marcus-Hush theory:[146]

$$\boldsymbol{k_{eT}} = \frac{2\pi}{\hbar}\left|\mathrm{H}_{DA}^{2}\right|\frac{1}{\sqrt{4\pi\lambda k_B T}}\,\mathbf{exp}\left(\frac{-(\Delta G^0+\lambda)^2}{4\lambda k_B T}\right) \qquad (1.23)$$

1.8.2. Interfacial Electron Transfer

The Marcus-Hush theory is the model for measuring the electron transfer rate in heterogeneous system. In the present thesis the interfacial electron transfer which involves between the semiconductor nanocrystals and the dye molecules is investigated. Most of cases, the electron transfer occurs due to coupling between the conduction band (CB) of the semiconductor nanocrystal and the lowest unoccupied molecular orbital (LUMO) of the adsorbate molecules. Thus the forward electron transfer (ET) from LUMO of the dye molecule to the conduction band of the semiconductor observe while the back electron transfer (BET) takes place from the CB of the semiconductor to the highest occupied molecular orbital (HOMO) of the dye molecule. The ET and BET processes in semiconductor/dye interface are illustrated in the Figure 1.18. In ET process the reactant state is mostly localized on dye LUMO while product state is consisting of continuous states of conduction band. Therefore an average density of state of product state is considered for ET process. Figure 1.18 shows that the value of λ is greater than the $-\Delta G_{ET}^{0}$ for forward ET (from the LUMO of the dye molecule to the CB of the NCs) process. Intuitively, the ET rate between these interface increases with increasing the value of $-\Delta G_{ET}^{0}$ where $(-\Delta G_{ET}^{0} = E_{CB} - E_{LUMO})$. So this forward ET process is located in the Marcus normal region. On the other hand the BET (from CB of the NCs to the HOMO of the dye molecule) takes place in Marcus inverted region because $\boldsymbol{-\Delta G^{0}_{BET}}$ (where $\boldsymbol{-\Delta G^{0}_{BET} = E_{CB} - E_{HOMO}}$) is greater than the value of reorganization energy (Figure 1.18). Thus, the rate of BET decreases with increasing the value of change in free energy. Due to presence of the trapped states in the NCs sometimes the electrons may trapped in the surface states which located in the lower energetic than CB edge of semiconductor as a result the rate BET varies for system to system.

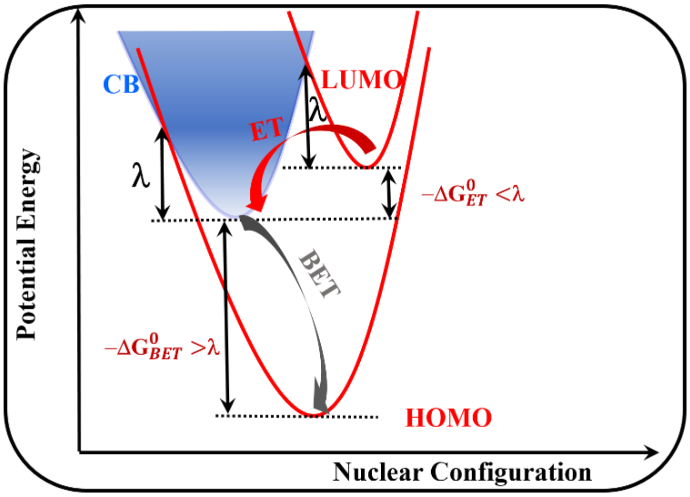

Figure 1.18: Electron transfer (ET) and back electron transfer (BET) in semiconductor (electron acceptor)/molecular adsorbate (electron donor) system.

1.9. Photovoltaic QDSC

Quantum dot sensitized solar cell (QDSC) is one of the low cost third generation devices which serves as solar to electrical energy conversion.[147-151] The schematic diagram of the QDSC is shown in the Figure 1.19. The scheme suggests that upon absorption of the solar light by the sensitizer QD materials results in generation of photoelectron which is responsible for producing photocurrent. In a typical QDSC, the sensitizer QDs is deposited on another wide band mesoporous semiconductor NC like TiO_2, ZnO etc. The centre of the QDSC contains nanocrystalline TiO_2 film for electron conduction, a sensitizer i.e. QD as light harvester,

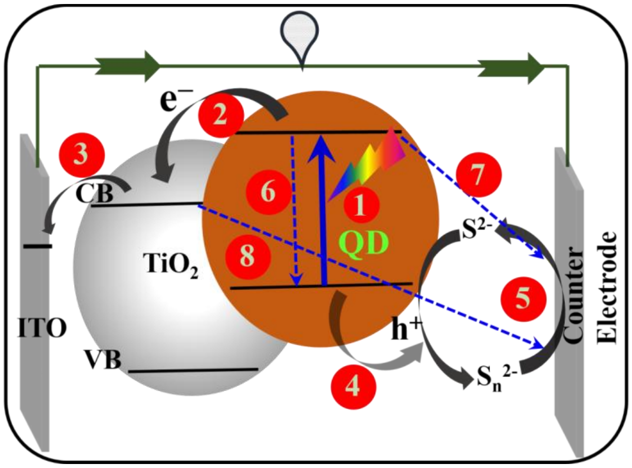

Figure 1.19: Schematic illustration of QDSC.

and a redox potential for hole neutralization. Being large surface area and the mesoporous nature of the TiO_2 film help to absorb the QD on its surface. The photoexcited electron from the CB of the QD injects to the CB of the TiO_2 nanoparticles. The photoexcited holes are neutralized by the redox couple to generate the neutral QDs. The photogenerated electrons are separated through fluorine doped tin oxide coated glass surface and with the help of counter electrode (Cu_2S) return the system into its initial state with a gain of photocurrent.

The working principle of the QDSC is quite similar as DSSC. In contrast to the p-n junction photovoltaic, the generated electrical field is absent in QDSC as the nanocrystalline TiO_2 material does not support any band bending (conduction band) near interface, a phenomena,[152] that produces potential gradient after redistributing free charge carrier between two components of different electrochemical potential (Fermi level) *viz*. macrocrystalline TiO_2 and electrolyte solution.[153] In dark condition, the Fermi level of TiO_2 electrode stays in equilibrium with midpoint potential of redox electrolyte which lies deep within band gap of TiO_2 semiconductor material. So, net photocurrent and photovoltage is zero in dark. When the CB energy of the QD lies energetically above the CB of the TiO_2 electron injection from QD to TiO_2 take place. The increase in local concentration of electron on TiO_2 interface lifts the Fermi level close to conduction band edge and flow the electron flux towards FTO contacts. The hole transfer to fairly concentrate redox electrolyte have no effects on its chemical potential and remain same as that in dark condition. Thus, the photoexcitation energy is stored in the form of free energy of injected electrons which produces photo-voltage and the net electron and hole transfer to respective electrodes results in photocurrent.

The major process take place in the QDSC is shown in the figure by giving sequential number. Photoelectron extraction from QD to the FTO takes place by the process 1 to 3. On the other hand the photogenerated hole is neutralized through process 4 and 5. The efficiency of the QD sensitized solar cell depends on the how fast the process 1 to 5. However, due to strong attraction between the charge carrier in the smaller size regime the some charge become recombine before separation via process 6 (Figure 1.9). Again, the processes like 7 and 8 (Figure 1.9) which are also reducing down the charge separation through recombination in different ways.

Moreover, research on QDSC by several research groups trying to optimizing these charge loss processes through different ways. As the QDs accumulate surface trapped states due to large surface to volume ratio which enhance the process 7 (Figure 1.9). This assignment we try to solve by using alloy QDs which is demonstrated details in chapter 8. The charge losses through process like 8 (Figure 1.19) can occur either less deposition of the QDs or for the surface states of the TiO_2 films.

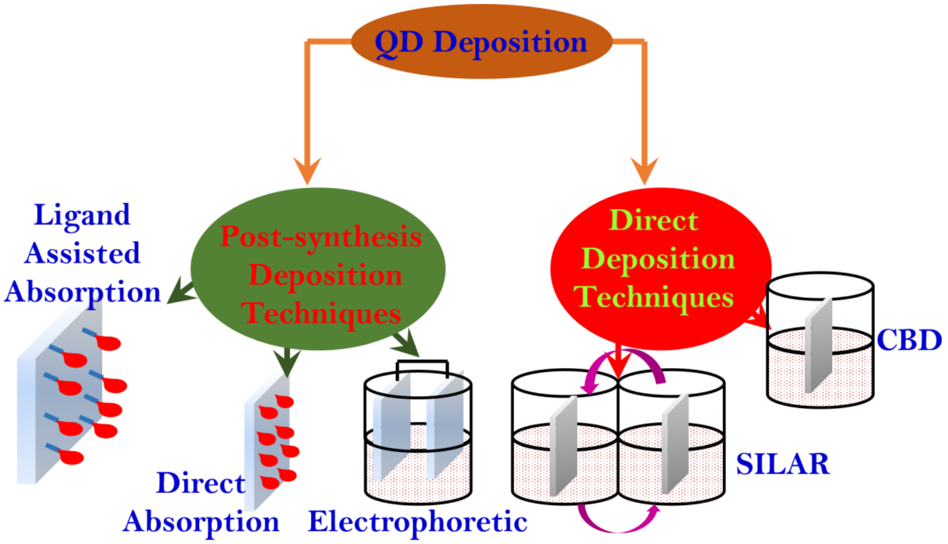

Figure 1.20: Different deposition techniques of QD on TiO_2 film to perform QDSC.

Deposition of QDs on the TiO_2 surface can be performed by direct growth technique which includes chemical bath deposition (CBD) [147, 154-156] and successive ion layer absorption and reaction (SILAR) [157, 158]. Another way is the post synthesis deposition technique which includes direct deposition, electrophoretic technique [159] and by ligand assisted assembly [160]. Different deposition techniques of the QD material on TiO_2 film is summarized in Figure 1.20.

Although in the direct growth technique a homogeneous high coverage film can be formed however, the size and the size quantized quantum confinement of the QD can't be controlled. As a result, lots of surface defect states will generate which kills the charge carrier through non radiative trapping process [38, 160]. In the post synthesis deposition process; the size, size quantized states, high crystallinity, optical properties, band gap tenability and surface passivation of the sensitizer QD can easily be controlled. The direct deposition and electrophoretic techniques is not used so far due long chain ligand which prevent the loading of the QD on the

TiO_2 surface. In the ligand assisted deposition processes both high quality and very good deposition is maintained.

1.10. Overview and scope of the thesis

In the present thesis the ultrafast charge transfer dynamics of different NCs in terms of colloidal QD, core/shell heterostructure, alloyed structure, with various molecular species (dye or different quencher molecule) are investigated. Different synthesis protocols are utilized to synthesize high quality, nearly monodispersed crystalline NCs like colloidal QDs mainly II-VI (CdX, X=S, Se, Te), perovskite QDs, type-I, type-II, quasi type-II core-shells and alloy QDs. The morphology of the synthesized materials is characterized utilizing XRD and HRTEM techniques. The steady state and time resolved optical absorption and PL spectroscopic techniques are used to extract the charge transfer information of the NCs in absence or in presence of the different dye or quencher molecules. With the knowledge of the charge transfer dynamics of this nanostructure we have successfully incorporated these materials in the application of light harvesting purpose through QDSC. Different charge transfer interactions of cadmium sulphide (CdS) QD with dibromofluorescence (DBF) are presented which suggest that CdS_DBF composite form strong charge transfer (CT) complex. More light absorption through CT complex and extend of charge separation of the composite system help to show highest efficiency in solar cell as compare to free CdS QD as well as DBF molecule. Multiple charge transfer dynamics in colloidal $CsPbBr_3$ QDs with DBF are presented in this study. Band edge engineering and controlling charge carrier delocalization in CdS/CdSe inverted type-I and CdSe/CdS quasi type-II core-shells are investigated with simple quenching experiments. Excited state life time and charge separation in core-shells are found to be more in contrast to the free QDs. The assignment of the cascading charge carrier dynamics in CdS/CdTe type-II core-shell with bromopyrogallol red is demonstrated. More charge separation and less charge recombination is observed in type-II regime as compare to only core CdS QD_Br-PGR composite system. Moreover, the charge delocalization in CdS/CdSe type-I and CdS/CdTe type-II in presence of Re-polypyridine complex are also addressed. The multiple ways of charge separation are observed in both the cases however, extend of charge separation is observed in CdS/CdSe-Re composite system. In addition to this charge transfer dynamics in QDs and core-shell NCs, the assignment on the carrier cooling dynamics of the two alloy QDs, CdS_xSe_{1-x} and $Cd_xZn_{1-x}Se$, is solved. Due to different reactivity of the constituents these two alloys form graded like structure where both the cases the core of the NCs is CdSe rich. The band alignment of the constituent semiconductor suggest that both the graded alloy form quasi type-II electronic structure because of either low conduction or valence band offset energy. Due to low CB offset energy of the CdSe and CdS, the electron in CdS_xSe_{1-x} is delocalized throughout the CB of the alloyed structure. As results, due to decoupling of electron from hole the intraband electron cooling is found to be slow in CdS_xSe_{1-x} as compare to both CdS and CdSe. Similarly, in $Cd_xZn_{1-x}Se$ due to low VB offset energy hole is delocalized as a result slow electron cooling is observed. Both the cases the charge recombination is found to be less. Finally, utilizing the slow electron cooling time and less charge recombination of the CdS_xSe_{1-x} alloy we fabricate a QDSC which provide unprecedented ~4.5 % photo current conversion efficiency.

The ultrafast charge transfer dynamics of the NCs QD is the main endeavour of the present thesis. Carrier cooling, charge separation, charge carrier recombination is the key factors which can control the efficiency of a solar cell sensitized by the nanostructured QDs materials. The knowledge of charge transfer dynamics in QDs_Dye which can help to perform more work towards light harvesting in QDSC. The energy transfer in CdS_BODIPY which can be used in bioimaging as the luminescence quantum yield of the bodipy increasing in presence of the CdS QD. Our study, the multiple charge transfer processes in $CsPbBr_3$ perovskite QDs and DBF which reveal that more light absorption and better charge separation by the complex which can be a suitable candidate in third generation solar cell. Band edge engineering is one of the demanding areas of research in nanosciences. Depending on different application we can use different core-shell heterostructure materials. By simple charge carrier quenching investigation in CdS/CdSe and CdSe/CdS core-shell, the structural analysis can be easily done in these NCs. Depending on application one can design core-shell by preferably extract either of the charge carrier. Our investigation of Br-PGR dye on different NCs surface reveals that maximum charge separation and less charge recombination is observed in CdS/CdTe type-II regime which can be utilized in QDSC performance. Cascading nature of charge separation in CdS/CdSe with Re complex which can be used in QDSC as well as photocatalysis application. Slow intraband electron cooling dynamics in highly luminescent CdS_xSe_{1-x} alloy QD gives fundamental study on carrier relaxation process. Higher emission quantum yield, less charge recombination and higher excited state life time of the CdS_xSe_{1-x} alloy are the constructive criteria in photovoltaic, photocatalysis, bioimaging etc. We have successfully incorporated the CdS_xSe_{1-x} alloy as sensitizer in QDSC where we observe unprecedented 4.5 % solar to electrical energy conversion efficiency. In addition to photovoltaic, the alloy can be used in photocatalysis, bioimaging etc. In case of $Cd_xZn_{1-x}Se$ alloy, the hole is delocalized through the entire VB of the nanostructure. This alloy can be used in bioimaging and blinking application. Therefore, the total investigation of charge transfer dynamics in NCs and its application in QDSC must provide sufficient contribution in nanosciences research both in fundamental as well as in application.

CHAPTER-2

Experimental Techniques

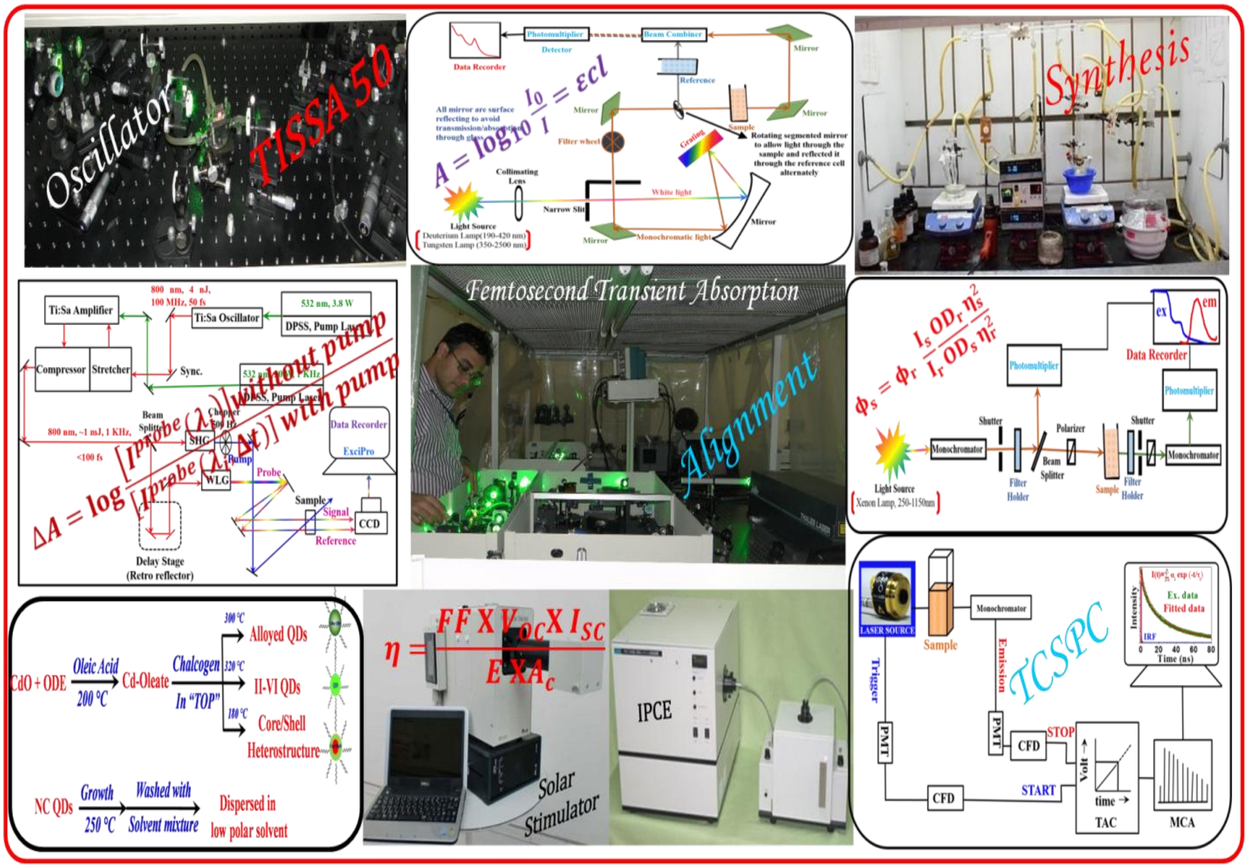

2.1. Introduction

The main endeavour of the present thesis works is the investigation of charge carrier dynamics in the semiconductor NC (colloidal QDs/core-shell, alloyed) in absence and in presence of some molecular adsorbate (dye molecule and the quencher molecule). To perform the charge carrier dynamics of the composite system we have deliberately synthesized all the novel NCs in our laboratory. Therefore it is very important to characterize the NCs before performing the charge carrier dynamics. Various methods, structural and optical techniques, have been employed to characterize these materials. The structural morphology of the synthesized NCs have been analyzed using X-ray diffraction (XRD), high resolution transmission electron microscopy (HRTEM) and energy dispersive X-ray analysis (EDXA) methods. Optical characterization performed includes UV-Vis absorption and photoluminescence (PL) spectroscopy. Charge separation, carrier relaxation, charge recombination are detected by time correlated single photon counting (TCSPC) and femtosecond two color (pump-probe) transient absorption spectroscopy. Transient absorption spectroscopy using electron beam as excitation pump (pulse radiolysis) is used to characterize the cation spectra of the dye molecule. Finally, the photovoltaic performance has been carried by measuring the incident photon to current conversion efficiency (IPCE) and current density *vs.* voltage (IV) spectra using solar stimulator. The principle of detection, optical layout, working methods of the instruments is described in this chapter.

2.2. X-Ray Diffraction

2.2. 1. Introduction

X-ray crystallography is a tool used for identifying the atomic and molecular structure of a crystal, in which the atomic planes of a crystal cause an incident beam of x-rays to interfere with one another as they leave the crystal.[161, 162] The phenomenon is called x-ray diffraction. A beam of x-rays directed at a crystal interacts with the electrons of the atoms in the crystal. The electrons oscillate under the impact and become a new source of electromagnetic radiation. The waves emitted by the electrons have the same frequency as the incident x-ray frequency. This emission is in all directions. As there are millions of atoms in a crystal, the emission in a particular direction is the combined effect of the oscillation of the electrons of all the atoms. The emission will be in phase and reinforce one another only in certain specific direction, which depend on the direction of the incident x-ray beam, their energy and the spacing between the atoms in the crystal. This is known as constructive interference. Diffraction occurs only when Bragg's Law is satisfied for constructive interference from planes with spacing d_{hkl}. Where hkl are the Miller indices.

In Figure 2.1 shows the parallel plans in crystal. A beam of x-rays of wavelength λ is directed towards the crystal at an angle θ to the atomic planes. Considering the atomic planes is semi-

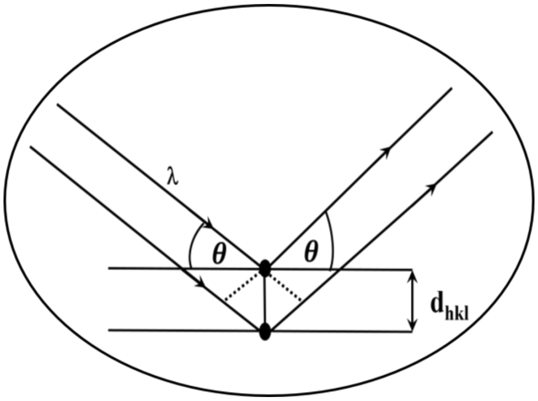

Figure 2.1: Illustration of Bragg law in crystal of d_{hkl} interplanar spacing.

transparent so, the incident x-rays beam pass through and reflected at the incident angle. The two reflected rays are reinforced each other, only when this path difference is equal to an integral multiple of the wavelength. So, in a crystal if d_{hkl} is the interplanar space, the Bragg condition for reflection can therefore be written as

$$n\lambda = 2d_{hkl}\sin\theta \qquad (2.1)$$

Where *n* is an integer; for first order diffraction n = 1, second order diffraction n = 2 and so on. For cubic crystal the interplanar space varies with Miller indices as follows,

$$\frac{1}{d_{hkl}^2} = \frac{h^2+k^2+l^2}{a^2} \qquad (2.2)$$

where *a* is the unit cubic cell length.

Intensity of the scattered x-rays beam is depending on the atomic scattering factors and miller indices of the planes. The atomic scattering factors depend on the density of the electrons in the scattering centre. Therefore higher the number of electrons, greater is the scattering from that particular atom. In addition to that, the intensity of the scattered x-rays depends on the size of the crystals. As the size of the crystal decreases the peak for the corresponding planes become broad. In case of nanocrystal QDs the XRD peaks are broader as compare to bulk one. This peak broadening can be expressed due to combination of instrumentation broadening and the size broadening. The instrumentation broadening can be omitted by performing the standard sample. However, the size broadening arises due to the less number of atoms. In NCs in a certain volume number of atom is million times less than bulk. Thus the probability of constructive interference of the scattered x-rays is decreases. As results, we observe broad peak for NC QDs instead of sharp peak. The phase characterization of the NCs can be done just by comparing the diffraction pattern obtained for samples with that of previously reported patterns as given by database from by Joint Committee on Powder Diffraction Standards (JCPDS, 1969), replaced by International Centre for Diffraction Data (ICDD, 1978). [163]

2.2. 2. Instrumentation

The typical schematic of XRD instrument is shown in Figure 2.2. X-rays are produced by bombarding a metal target (Cu, Mo usually) with a beam of electrons emitted from a hot filament (often tungsten). The incident beam will ionize electrons from the K-shell (1s) of the target atom and X-rays are emitted as the resultant vacancies are filled by electrons dropping down from the L (2p) or M (3p) levels. This gives rise to K_α and K_β lines. As results, instead of broad distribution of X-rays created due to deceleration on electrons also called Bremsstrahlen, sharp lines are also created which are superimposed on the broad distribution. The sharp intense monochromatic X-rays are necessary for performing the diffraction experiment which can be done by using filter. The filtering of broad distribution is accomplished by using a filter which has a 1 unit atomic number less than the target material (i.e. Z-1). Again the resultant beam is

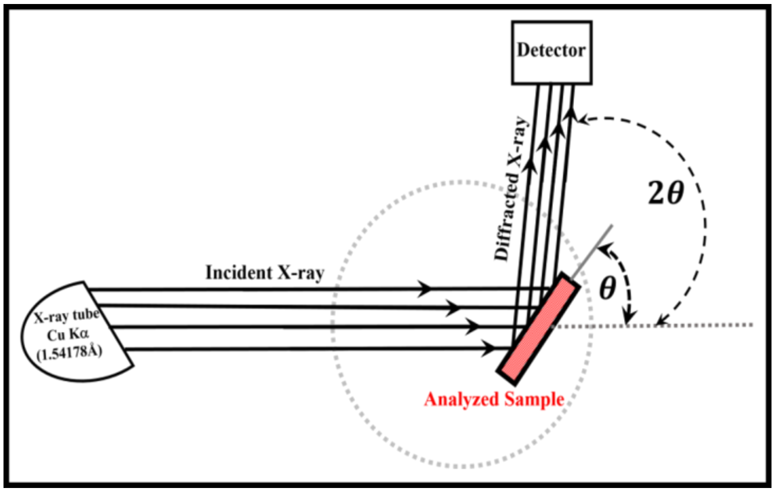

Figure 2.2: Schematic presentation of a XRD instrument.

further monochromatised by using a single crystal (Such as Si) monochromator. For powder x-ray diffraction, the samples are taken in powder form on an amorphous substrate (glass window) in presence of some binder. The scattered x-rays are detected by a detector which is scanned over different angles and intensities are plotted with respect to angle of diffraction of incident x-ray beam. The peak position observed are angle where Bragg condition is satisfied.

In the present thesis, we have used a Philips X-ray machine, model-PW 1710 with Ni filtered Cu K_α radiation (λ=1.54178 Å), using silicon as an external standard. As the scattering intensity drops as $1/2(1+\cos^2 2\theta)$. This means that we don't get much intensity post 70° (2θ). Thus the experiments are performed in an angle range 10°-70° in a continuous scan mode, with a step width of 0.02°, and scan of 1° per minute. The measurement of θ corresponding to each peak position and peak intensity is important for identification of materials. The datas are analyzed through finger print techniques that is previously reported by Joint Committee on Powder Diffraction Standards (JCPDS, 1969), replaced by International Centre for Diffraction Data (ICDD, 1978).

2.3. Transmission Electron Microscopy (TEM)

2.3. 1. Introduction

Morphology analysis is one of the important studies in nanosciences research. The particles size distribution, presence of different planes, nature of crystallinity can be analyzed through transmission electron microscopy (TEM) study.[164, 165] First TEM was built by Max Kroll and Ernst Ruska in 1931, with this group developing the first TEM with resolution power greater than that of light in 1933 and the first commercial TEM in 1939. Transmission electron microscopy (TEM) is a microscopy technique whereby a beam of electrons is transmitted through an ultra thin specimen, interacting with the specimen as it passes through. When electrons are accelerated up to high energy levels (few hundreds of keV) and focused on a material, they can scatter or backscatter elastically or inelastically, or produce many interactions, source of different signals such as X-rays, Auger electrons or light. Some of them are used in transmission electron microscopy (TEM).[166] An image is formed from the interaction of the electrons transmitted through the specimen; the image is magnified and focused onto an imaging device, such as a fluorescent screen, on a layer of photographic film, or to be detected by a sensor such as a CCD camera.

The probable interaction between an electron and a specimen is shown in Figure 2.3.

Figure 2.3: Different interaction of electron with matter.

The interaction of electron with the material was obtained due to the inherent nature of electron which is a quantum mechanical object. Since the electrons have both wave and particle nature and the de Broglie wavelength of electrons are significantly smaller than that of light and so they have higher resolution capability. The de Broglie wavelength ($\boldsymbol{\lambda}$) of an electron with 30 keV accelerating potential is ~0.07 Å having resolution ~4.1 Å [calculate using $\boldsymbol{\lambda}$ (Å) $= \frac{\mathbf{12.27}}{\sqrt{\boldsymbol{V}\ (\boldsymbol{Volts})}}$ and $\boldsymbol{\rho} = \frac{\mathbf{0.6}\times\boldsymbol{\lambda}}{\boldsymbol{\eta}\sin\boldsymbol{\alpha}}$, where, $\boldsymbol{\lambda}$ is wavelength of the electron and $\boldsymbol{V}$ is the applied voltage; As the resolution of the imaging system ($\boldsymbol{\rho}$) is depend on wavelength ($\boldsymbol{\lambda}$), index of refraction of lens ($\boldsymbol{\eta}$)

and illumination angle ($\boldsymbol{\alpha}$)] considering $\boldsymbol{\eta}$ = 1 in vacuum and $\boldsymbol{\alpha} \leq 1°$.] Therefore TEM can be used in principle for imaging lattice planes. However due to aberrations involved, the resolution of a TEM instrument is limited. However, state-of-the-art TEM machines have overcome these problems in aberration corrected TEM. Additionally one can perform electron diffraction and obtain crystallinity and crystal structure. Additional information can also be obtained from inelastic scattering of electrons. These inelastic scattering events can arise from a number of processes like phonon scattering, plasmon scattering, ionization etc. These energies can be used for chemical characterization of the sample. Contrast of the TEM image is depending on the interaction of the sample with the electron. Thicker regions of the sample, or regions with a higher atomic number will appear dark (dark filed), while regions with no sample in the beam path will appear bright– hence the term "bright field" is used. Bright field image is collected by monitoring un-scattered electrons after passing through the sample and objective aperture. Therefore regions where sample is not present will appear bright and region with samples will appear black due to scattering of electrons leading to reduced intensity. Image produced with scattered electrons (after interaction with the sample) gives rise to a dark field image. The contrast produced in a dark field is much higher; however, the intensities are lower. Therefore dark field imaging requires larger exposure times. The dark field imaging is carried out by moving objective aperture to monitor un-scattered beam. However, this is of poor quality as we intercept electrons in region where aberrations are dominant. In crystalline samples the diffraction spots or rings are monitored therefore specific planes are monitored. [167]

2.3.2. Layout

The typical layout of TEM instrument is shown in Figure 2.4. This instrument consists several parts is described below in brief.

2.3.2. a. An electron gun

An electron gun is used as source of electron based on thermionic emission metal. The thermionic emission current density (J) of metal is depend on the work function of the metal and cathode temperature (T_C) through Richardson's law

$$J = AT_C^2 \exp\left(-\frac{\varphi}{k_B T_C}\right) \tag{2.3}$$

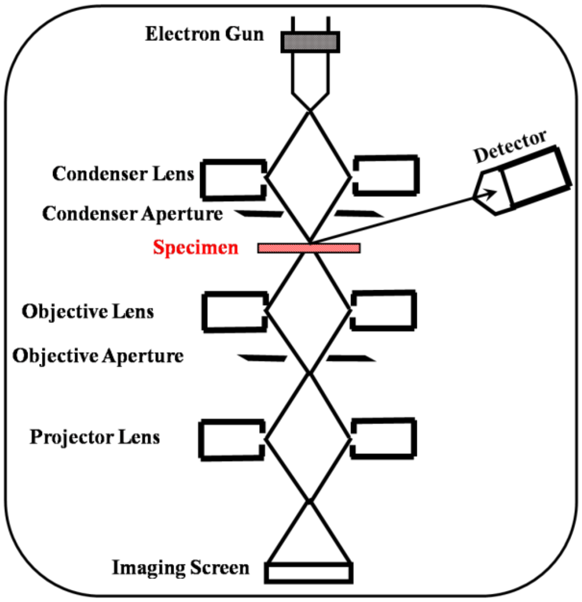

Figure 2.4: Schematic illustration of a typical TEM instrument.

where, "A" is the Richardson constant and "φ" is the work function of the metal, respectively. k_B and T_C are the Boltzmann constant and cathode temperature of the metal, respectively. Due to the higher melting temperature (T_M) of the tungsten filament (W, T_M~3650 K and T_C~2500-3000 K) and lower work function of the single crystal of lanthanum hexaboride filament (LaB_6,T_C~1400-2000 K) are used as cathode that is wreathed with Wehnelt electrode (Wehnelt Cap, negative potential, Figure 2.5) for the source of electron. Due to negative potential of the electrode, the electrons are emitted from a small area of the filament (point source). A point source is important because it emits monochromatic electrons (with similar energy). In this, a positive electrical potential is applied to the anode, and the filament (cathode) is heated until a stream of electrons is produced. The electrons are accelerated by the positive potential down the column, and because of the negative potential of cap, all electrons are repelled toward the optic axis.

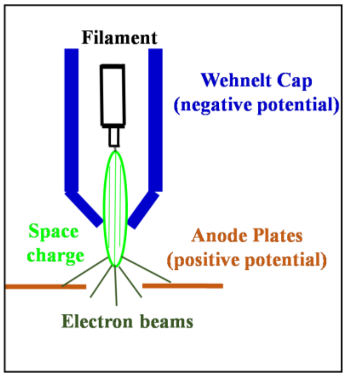

Figure 2.5: Schematic of electron gun in a TEM instrument.

A collection of electrons occurs in the space between the Filament tip and Cap, which is called a space charge. Those electrons at the bottom of the space charge (nearest to the anode) can exit the gun area through the small (<1mm) hole in the Wehnelt Cap and then move down the column to be later used in imaging. [168]

2.3.2. b. Condenser lens and aperture

The condenser lens is necessary to focus the stream of the electron beam to a single spot size as the emitted electron beams from the metal surface is diverging in nature. A condenser aperture is a thin disk or strip of metal with a small circular through-hole. It is used to restrict the electron beams and filter out unwanted scattered electrons before image formation.

2.3.2. c. Sample

The sample should be thin enough to interact with the electron. The beam from the condenser aperture strikes the sample and the electron-sample interaction takes place in three different ways. One is unscattered electrons (transmitted beam), elastically scattered electrons (diffracted beam) and inelastically scattered electrons. In the present thesis work we used copper coated grid as sample holder.

2.3.2. d. Objective lens and aperture

The main imaging system in a TEM instrument is the objective lens system. This lens is highly converging with a very small focal length. The objective lens produces an enlarged image on a screen placed several cm below the lens. Due to small focal length of the lens the image produced at a large distance is highly magnified. Apart from producing magnified image the objective lens reduces aberrations by rejecting electrons scattered at large angles.[165, 168-170] The most common aberrations involved in lenses are chromatic and spherical aberration. These two are limitation of the electron microscopy. The spherical and chromatic aberrations are arising due to lens and kinetic energy of the electrons, respectively.

2.3.2. e. Selected aperture

It enables the user to examine the periodic diffraction of electron by ordered arrangements of atoms in the sample.

2.3.2.f. Projector lens

The projector lenses are used to expand the beam onto the imaging screen.

2.3.2.g. Imaging

Imaging systems in a TEM consists of a phosphor screen, film, CCD camera, image plate etc. The image strikes the phosphor screen and light is generated, allowing the users to see the image. The darker areas of the image represent those areas of the sample that fewer electrons are transmitted. The lighter areas of the image represent those areas of the sample that more electrons are transmitted.

2.3.3. Selected Area Electron Diffraction (SAED)

Besides imaging operation, TEM instrument can also be used in different purpose like SAED and EELS. Figure 2.3 shows different possibilities of interaction of electron with matter. Elastic scattering is one of the possible interactions. In a crystalline sample presence of long range order gives rise to rings or spots arising from constructive interference of scattering from different planes. The angular position of spots or rings is related to crystalline structure or symmetry. In a particular crystalline sample there will be several ring or spots placed radially from the central point or un-diffracted beam. The rings that are seen consist of large number of merged spots. The spots arise from diffraction from a particular plane of a crystalline. The radial distance from the centre is related to the lattice spacing and TEM parameters. Since the magnification parameters of TEM are known, lattice spacing can be obtained. Now in a polycrystalline sample azimuthal orientation of crystals with respect to the optic axis is random. Therefore each of these crystals will diffract at different azimuthal angle creating a series of spots radially arranged around an axis as a result it appears like a ring. The position of the rings from the central maxima helps in phase characterization of a material.

2.3.4. Electron Energy Loss Spectroscopy (EELS)

In general Electron Energy Loss Spectroscopy bases on the energy losses of the electrons when inelastically scattered on matter. An incident beam of electrons with a known energy (E_i) is scattered on a sample. The scattering of these electrons can excite the electronic structure of the sample. If this is the case the scattered electron loses the specific energy (ΔE) needed to cause the excitation. Those scattering processes are called inelastic. It may be easiest to imagine that the energy loss is for example due to an excitation of an electron from an atomic K-shell to the M-shell. This energy for this excitation is taken away from the electrons kinetic energy. Then the energies of the scattered electrons (E_s) are measured and the energy loss can be calculated. From the measured data intensity versus energy loss diagram is established. In the case of scattering on phonons the so called energy loss can also be a gain of energy. Very often EELS are used to obtain elemental mapping in a particular sample.

2.4. UV-Visible Absorption Spectroscopy

Atoms and molecules have discrete electronic levels and transition from ground to different excited states can be affected by light. Since electronic levels in a particular chemical species are unique, these can be used as fingerprint for identification of molecules. The absorption of light in ultraviolet-visible (UV-Vis) region can be used to characterize chemical species. Since a particular peak height is proportional to concentration of the species, one can use the technique for both quantitative and qualitative evaluation of a chemical species.[171-173] UV-Vis absorption spectra were collected using JASCO-640 model UV-visible spectrophotometer with a range of 200-900 nm and resolution of 1 nm.

Because only small numbers of absorbing molecules are required, it is convenient to have the sample in solution (ideally the solvent should not absorb in the ultraviolet/ visible range however, this is rarely the case). In conventional spectrometers electromagnetic radiation is passed through the sample which is held in a small square-section cell (usually 1 cm wide internally). Radiation across the whole of the ultraviolet/visible range is scanned through the sample and radiation of the same frequency and intensity is simultaneously passed through a reference cell containing only the solvent. Photocells then detect the radiation transmitted and the spectrometer records the absorption by comparing the difference between the intensity of the radiation passing through the sample and the reference cells (Figure 2.6). No single lamp provides light source across the whole of the range required, so two are used. A deuterium lamp covers the ultraviolet range (190-420 nm), and a tungsten filament (350-2500 nm) covers the visible range. The radiation is separated according to its wavelength by a diffraction grating followed by a narrow slit. The slit ensures that the radiation is of a very narrow waveband- i.e. it is monochromatic. The cells in the spectrometer are made of pure silica for ultraviolet spectra because soda glass absorbs below 365 nm, and pyrex glass below 320 nm. Detection of the radiation passing through the sample or reference cell can be achieved by a photomultiplier that converts photons of radiation into tiny electrical currents. The spectrum is produced by comparing the currents generated by the sample and the reference beams. Wavelength checks are made by passing the sample beam through glass samples (containing holmium oxide) that have precise absorption peaks, and the absorption is calibrated by passing the sample beam through

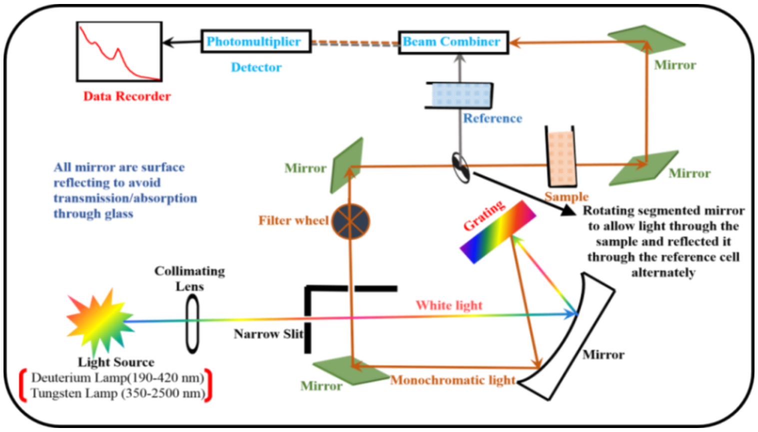

Figure 2.6: Optical layout of double beam UV-Vis spectrophotometer.

either a series of filters, each with a specific and known absorption, or a series of standard solutions. Beer's law tells us that absorption is proportional to the number of absorbing molecules – i.e. to the concentration of absorbing molecules (this is only true for dilute solutions) – and Lambert's law tells us that the fraction of radiation absorbed is independent of the intensity of the radiation and depends on absorption path length. Combining these two laws, we can derive the Beer-Lambert Law:

$$\boldsymbol{A = \log_{10}\frac{I_0}{I} = \varepsilon c l} \qquad (2.4)$$

Where "I_0" = the intensity of the incident radiation,

I = the intensity of the transmitted radiation,

ε = a constant for each absorbing material, known as the molar extinction coefficient and having the units "$\mathrm{mol^{-1}\ dm^{3}\ cm^{-1}}$",

l = the path length of the absorbing solution in "cm"

c = the concentration of the absorbing species in "$\mathrm{mol\ dm^{-3}}$"

The value of "$log_{10}\ (I_0/I)$" is known as the absorbance of the solution (it is also referred to as the optical density), and can be read directly from the spectrum, often as 'absorbance units'. A useful constant is the molar absorption coefficient, ε, because it is independent of concentration and path length, whereas absorption depends upon both. The other useful piece of information is the wavelength at which maximum absorption occurs. This is given the symbol "λ_{max}". These two pieces of information alone are frequently sufficient to identify a substance, although identification is not the most common use of this technique. Conversely, if the values of "ε" and "λ_{max}" are known, the concentration of its solution can be calculated – this is the more common application. The values of both "ε" and "λ_{max}" are strongly influenced by the nature of the substance. We assume that decrease in intensity arises from absorption of light by sample and not scattering. Scattering is especially large in cases where solubility of sample is poor. Additionally concentration of samples are expected to be kept low as at higher concentration factors like intermolecular interactions and changes in refractive index affect measurement. The scan over entire UV-Vis region gives rise to absorption spectra which forms the basis of this technique.

2.5. Photoluminescence (PL) Spectroscopy

Photoluminescence spectroscopy is commonly known as Fluorescence spectroscopy used to detect the radiative decay channel of fluorophore/light emitting materials.[174, 175] A species will show emission when it will be excited by a light source. After absorbing the photon from a light source the molecular species undergoes electronic transition in which the higher vibrational states of the excited electronic states are directly populated ("*Franck Condon principle*"). The photoexcited species undergoes vibration relaxation via non-radiative manner and finally returns to ground electronic state either by emitting light photon or through non-radiative decay. The emission generally occurs from a vibrationally relaxed configuration of excited electronic state, therefore is generally red shifted with respect to absorption spectra of that particular transition. The shift between absorption and emission maxima is referred to as Stoke shift. Stoke shift can be due to vibrational relaxation, intramolecular charge transfer etc. The PL is a random process and the average time spent in a molecular system for singlet and triplet excited states are typically ~1ns-100ns and 1μs-100 seconds, respectively. In case of the semiconductor QDs the band edge emission life time varies sub 100 ns while the surface (shallow and deep trapped) state life times are >100 ns to sub μs. Apart from the PL, the excitation spectra of the samples can also be measured which is overlapped with the absorption spectra. In excitation spectra, emission wavelength is held constant and excitation wavelength (till position of emission wavelength) is varied. This gives rise to a plot of emission intensity versus excitation wavelength.

In the present thesis work the PL of the semiconductor QDs, core/shell, alloys and the dye molecules are measure using Hitachi model 4010 Spectrofluorometer which employed 75W high pressure xenon lamp as excitation source, different monochromators for excitation and emission wavelengths and photomultiplier tube (PMT) as detector. Figure 2.7 shows an optical layout of a spectrofluorometer. The instrument has an excitation light source (xenon lamp, 250-1150 nm). The instrument shown is equipped with monochromators to select both the excitation and emission wavelengths. In addition, these monochromators use concave gratings, produced by holographic means to further decrease stray light. Both monochromators are motorized to allow automatic scanning of wavelength. The fluorescence is detected with photomultiplier tubes

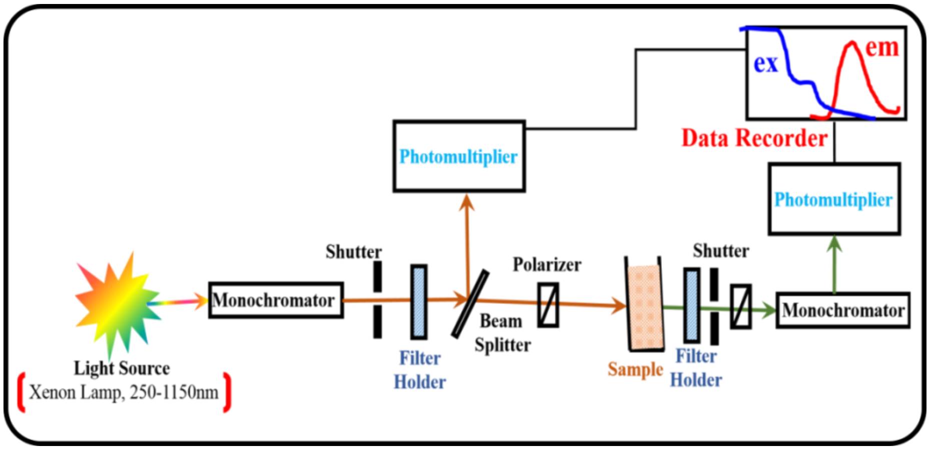

Figure 2.7: Optical layout of photoluminescence spectrofluorometer.

and quantified with the appropriate electronic devices. The output is usually presented in graphical form and stored digitally.

The PL spectrum and quantum yield [174, 176] is frequently used to characterize the properties of any fluorophore or semiconductor quantum dots. Besides, the most important applications of PL spectroscopy are bio-imaging, light emitting diode etc. therefore a high emission quantum yield is the desirable feature for such purpose. The emission quantum yield (ϕ) is relative measure of radiative (*r*) and non-radiative (*nr*) events, given by:

$$\boldsymbol{\phi} = \frac{\mathbf{k_r}}{\mathbf{k_r+k_{nr}}} = \frac{\tau}{\tau_{0(natural)}} \qquad (2.5)$$

where, "τ_0" is intrinsic lifetime which is related with oscillator strength and "τ" is average life time a molecule spent in excited state before emitting a photon. However, emission quantum yield of an unknown sample can be measured by using the following equation

$$\boldsymbol{\phi_s} = \boldsymbol{\phi_r} \frac{\mathbf{I_s}}{\mathbf{I_r}} \frac{\mathbf{OD_r}}{\mathbf{OD_s}} \frac{\boldsymbol{\eta_s^2}}{\boldsymbol{\eta_r^2}} \qquad (2.6)$$

Where *"ϕ"* is the quantum yield, *"I"* is the integrated area of the emission intensity, *"OD"* is the optical density at excited wavelength, and *"η"* is the refractive index of the solvent. The subscript *"s"* and *"r"* refer to the measured and reference sample, respectively. The equation becomes simplify when the experimental and the reference samples are taken in same solvent

$$\boldsymbol{\phi_s} = \boldsymbol{\phi_r} \frac{\mathbf{I_s}}{\mathbf{I_r}} \frac{\mathbf{OD_r}}{\mathbf{OD_s}} \qquad (2.7)$$

To avoid the inner filter effect the optical density of the measured and reference samples are kept below 0.1.

Apart from the characterization of the NCs and steady interaction of the NCs with the molecular species, the charge carrier dynamics in the ultrafast time domain have been performed using time resolved PL and absorption spectroscopy. The time correlated single photon emission counting and the femtosecond transient absorption is used to investigate the charge carries dynamics in the present thesis work. The next section we have demonstrated the experimental setup of these mentioned techniques in brief.

2.6. Time Correlated Single Photon Counting (TCSPC)

2.6.1. Introduction:

Operation of the time resolved spectroscopic techniques have found in a wide range of applications like fluorescence spectroscopy, bio-imaging, in different applications in nanosciences because these are non-destructive and deliver relevant information about the investigated system. [174] Time correlated single photon counting (TCSPC) is one of the sophisticated technique which provided the excited state life time of a fluorophores or the luminescent species. [177, 178] The TCSPC technique makes use of the fact that for low-level, high-repetition-rate signals, the light intensity is so low that the probability of detecting one photon in one signal period is far less than one. Therefore, it is not necessary to provide for the possibility of detecting several photons in one signal period. The detector signal is a train of randomly distributed pulses corresponding to the detection of the individual photons. There are many signal periods without photons; other signal periods contain one photon pulse. Periods with more than one photon are very rare. When a photon is detected, the time of the corresponding detector pulse in the signal period is measured. The events are collected in a memory location with an address proportional to the detection time. After many photons, the distribution of the detection times, i.e. the waveform of the optical pulse, builds up in the memory. It is sufficient to record millions of photons, measure their time in the signal period, and build up a histogram of the photon times.

2.6.2. TCSPC Instrument:

The conventional TCSPC consists the building blocks is shown in Figure 2.8. The detector, usually a photomultiplier tube (PMT), delivers pulses for individual photons of the repetitive light signal. Due to the random amplification mechanism in the detector, these pulses have a considerable amplitude jitter, which imposes stringent requirements on the input discriminator. Constant Fraction Discriminator (CFD) is used to trigger based on the PMT pulses. These trigger pulse is routed through the CFD to start input of the time to-amplitude converter, (TAC) which initiates charging of a capacitor. In the meantime the optical pulse excites the sample, which subsequently fluoresces. An aperture is adjusted so that at most one photon is "detected" for each exciting event. The signal resulting from this photon stops the charging ramp in the TAC,

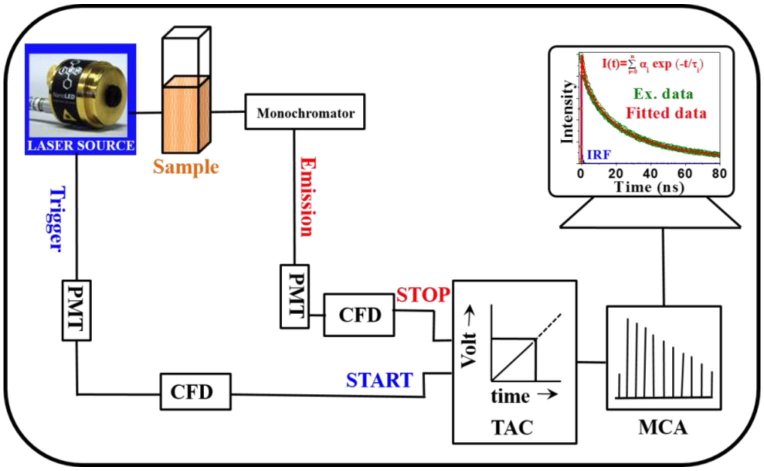

Figure 2.8: Block diagram of a traditional (forward mode) TCSPC system. PMT= Photo Multiplier Tube, CFD= Constant Fraction Discriminator, TAC= Time to Amplitude Converter, ADC = Analogue to Digital Converter. The START and STOP is reverse in case of the reverse mode operated TCSPC.

which puts out a pulse, the amplitude of which is proportional to the charge in the capacitor, and hence to the time difference between START and STOP pulses. The TAC output voltage is sent through a Biased Amplifier. The amplifier has a variable gain and a variable offset. The amplified TAC signal is passed by analogue to digital converter (ADC) and feed to multichannel analyzer (MCA). The MCA register the count in different channels which are ordered in 1 to 2042 numbers for producing the histogram. The output of the ADC is the digital equivalent of the photon detection time. The effective time resolution of TCSPC experiment is characterized by its instrument response function (IRF) and can be measured by the deconvolution of the decay profile of the scattered sample. With ultrashort laser pulses, the IRF width at half-maximum for TCSPC is typically 150 to 250 ps for conventional short-time PMTs. The sensitivity of the TCSPC depends on the dark count rate of the detector. Defining the sensitivity as the intensity at which the signal is equal to the noise of the dark signal the following equation applies:

$$S = \frac{1}{Q}\sqrt{R_d \times \frac{N}{T}} \qquad (2.8)$$

Where, (R_d = dark count rate, N = number of time channels, Q = quantum efficiency of the detector, T = overall measurement time). Typical values (uncooled PMT with multialkali cathode) are R_d = 300s^{-1}, N = 256, Q = 0.1 and T = 100s. This yields a sensitivity of S = 280 photons/second. This value is by a factor of 10^{15} times smaller than the intensity of a typical laser (10^{18} photons/second). Thus, when a sample is excited by the laser and the emitted light is measured, the emission is still detectable for a conversion efficiency of 10^{-15}.

In present thesis work, IBH make TCSPC instrumental set-up is used and it works at reverse mode (we have discussed the reversed mode in the next section). Different laser sources like 292 nm, 374nm, 406nm, 445nm, 592 nm are used to investigate the charge transfer and carrier dynamics of the present thesis work. The emission polarizer is set at an angle (54.7° w.r.t the excitation polarization) known as magic angle to avoid effect of anisotropy coming from rotational motion of the species. The time resolved PL decay traces are fitted with non-linear least square analysis supported by instrument fitting program of IBH make. All the decay traces are fitted using the software and by using the equation $I(t) = \sum_i^n \alpha_i \ e^{-t/\tau_i}$ where, $I\ (t)$ is the total intensity remaining at time t. α_i and τ_i are the amplitude and decay time of i^{th} component respectively.[174]

2.6.3. Forward and Reverse Mode

There are two different operating modes in TCSPC applications: In Forward Mode the pulse rate from the light source is connected to the START input. This rate (with generally equally spaced pulses in time) is substantially higher than the (more or less random) pulses from the detector connected to the STOP input. At high rates of the light source, however, the forward mode has a clear disadvantage. Because the vast majority of TAC circles will be started by the START pulse, but never stopped by a STOP signal, it needs to be reset at overflow. To avoid this TCSPC electronics can be operated in reverse mode. This is where the signal cable carrying the high count rate from the light source is connected to the STOP input and the low rate is connected to START. In this reverse mode the reference pulses from the light source need to be shifted by a long delay, so that they arrive at the input of the TAC later than the START pulses from the detector.

2.7. Femtosecond Upconversion Spectroscopy:

Femtosecond upconversion is one of the sophisticated techniques for the investigation of the fluorescence decay traces in the sub 100 of fs temporal resolution. [179, 180] In the present thesis we use Femtosecond Optical Grating (FOG 100) set up from CDP, Russia to determine the electron transfer rate from dye molecule to the QDs. Figure 2.9 shows the simple optical layout of the upconversion set up. Sum frequency generation (up-conversion) method is used in the femtosecond optically gated (FOG) fluorescence kinetic measurement system FOG100 to achieve a temporal resolution better than 100 femtoseconds. This FOG100 system is the first complete measurement system for femtosecond kinetic spectroscopy, designed to be matched with any type of femtosecond oscillator or amplifier operating at 1 KHz pulse repetition rate. The system includes optical and mechanical components (including optical delay line) installed on a breadboard, monochromator, selected photon counting PMT, electronic control unit and Lumex 5.1 software. The control unit is connected to a computer via serial port.

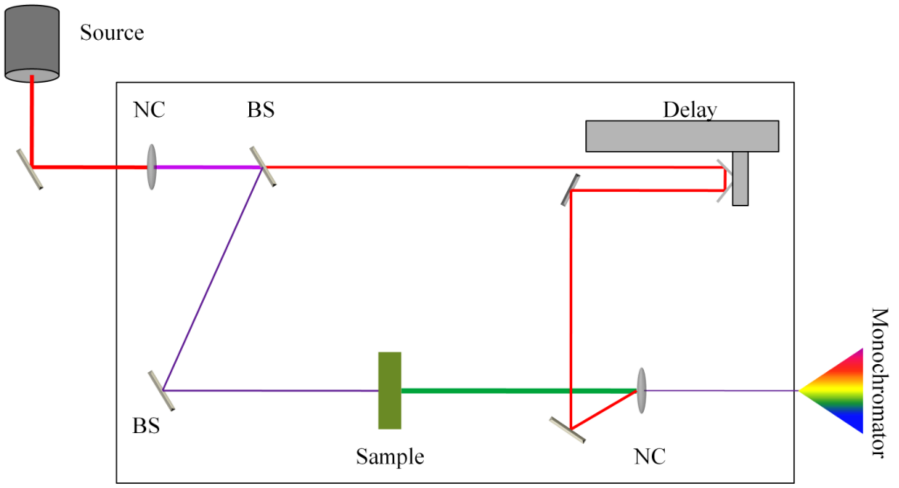

Figure 2.9: Optical layout of fluorescence upconversion.

The femtosecond optically gated (FOG) system uses the sum frequency generation nonlinear technique (up-conversion) to obtain the best time resolution. Laser induced fluorescence (LIF) is produced by a femtosecond laser pulse and directed onto a nonlinear element. Sum frequency radiation (SFR) is generated in the nonlinear element only during the time that a delayed femtosecond gate pulse and fluorescence are temporally overlapped in the nonlinear crystal. SFR photons are counted by the photon counting system resulting in high sensitivity. The SFR signal is proportional to fluorescence signal. Fluorescence kinetics is recorded when a delay between gate and excitation pulses is scanned. As a result of optical delay scanning, the fluorescence rise or decay kinetics is measured at a wavelength determined by the monochromator and the nonlinear element adjustment. Temporal response function of the system is determined by the convolution of the excitation and gate laser pulses only, and does not depend on any electronic circuits. The temporal resolution depends on the laser pulse-width used and it is better than 150 fs at <100 fs laser pulse width. The system sensitivity depends on the average power of the fluorescence excitation light, pulse repetition rate, radiative lifetime of the sample, the conversion efficiency of the FOG system and the measurement time. For the weak fluorescence, one can improve the S/N ratio and reach the best sensitivity of the photon counting method by using longer measurement times. The most important factor in this case is the laser stability during the kinetic measurements. For Ti: sapphire oscillator, operating at about 100 MHz pulse repetition rate, the maximum photon counting signal is 2×10^6 counts/sec, limited by the FOG100 electronic unit. Taking into accounts that the PMT used has < 5 dark counts/sec, a dynamic range of about 10^5 can be reached for specific fluorescence kinetics.

2.8. Femtosecond Transient Absorption (TA) Spectroscopy

2.8.1. Introduction:

As we know the charge transfers in semiconductor NCs in absence and presence of different molecular species take place in sub ps time domain. Thus ns time resolution (TCSPC) is not enough to investigate the exact time scale of the corresponding process. Again, the major drawback in TCSPC is that until the experimental samples have photoluminescence it can't be analyzed. Thus, charge carrier relaxation, intraband carrier cooling, extend of charge separation, charge recombination etc. which are known as non-radiative process can't be identified through time resolved PL studies.[181] Two colours, pump-probe absorption spectroscopy is one of the demanding techniques for investigation of such non-radiative photo-events. [182] In the current thesis works all the excited states non-radiative events have been studied utilizing femtosecond transient absorption spectroscopy. In TA spectroscopy, the experimental sample is promoted to an electronically excited state by means of an excitation (by pump) pulses and the excited state properties are monitored by a probe pulse at time *t*. The kinetic properties of the samples are measured by giving an optical delay between pump and probe pulses either by increasing the optical path length of probe pulses or by decreasing the path length of pump pulses (1μm displacement is equivalent to 3.3 fs). The optical layout of typical pump-probe technique is shown in Figure 2.10.

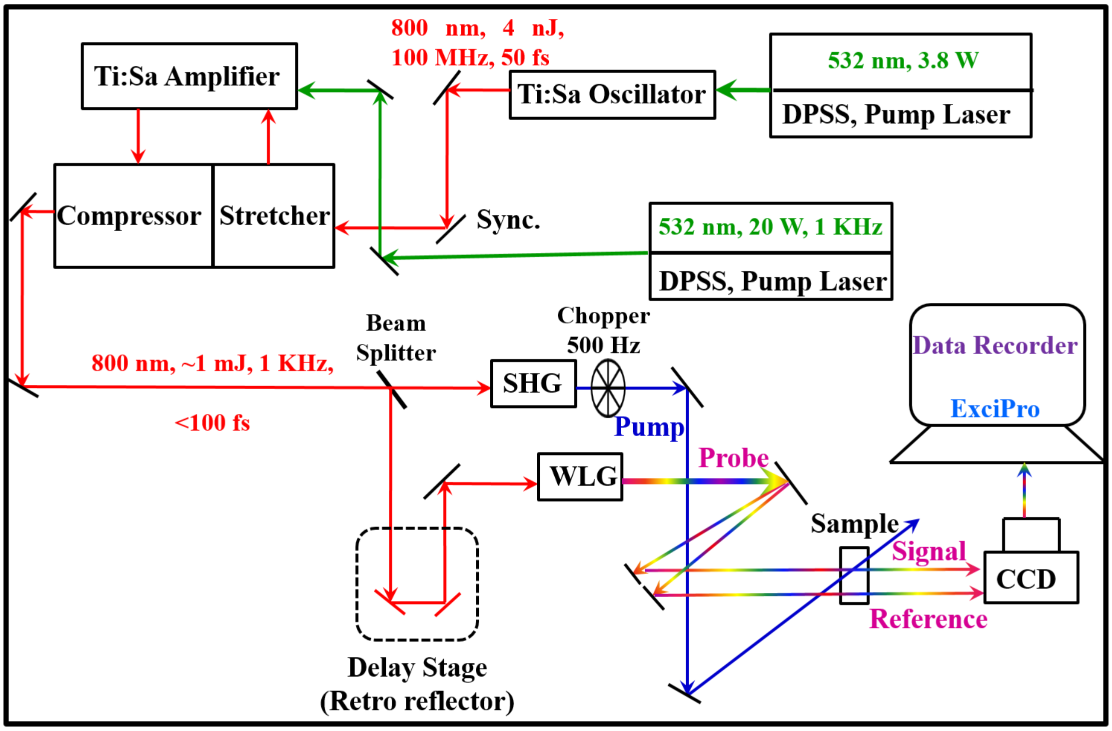

Figure 2.10: Schematic layout of femtosecond transient absorption spectroscopy.

In order to eliminate noise introduced by the fluctuations of the laser pulse intensity, the monitoring pulse is divided into a probe and a reference pulse. The probe pulse is spatially overlapped with the pump pulse in the sample, while the reference pulse passes through a region of the sample which is unaffected by the pump. Details of the setup are demonstrated in the next section of this thesis. The experimental signal, i.e. the change in optical density [ΔA, Δt], which can be obtained from Beer-Lambert law. The probe pulse intensity before [$\boldsymbol{I_0(\lambda_i)}$] and after [$\boldsymbol{I(\lambda_i, \Delta t)}$] pump pulse excitation can be given by,

$$I(\lambda_i\,, \Delta\boldsymbol{t}) = I_0(\lambda_i) \times \mathbf{10}^{-\boldsymbol{\varepsilon_{\lambda_i} N_{(\Delta t)} l}} \qquad (2.9)$$

So, change in absorption, ΔA (Δt), can be expressed as

$$\Delta\boldsymbol{A}\ (\Delta\boldsymbol{t}) = \Delta\boldsymbol{OD}(\boldsymbol{\Delta t}) = \mathbf{log}\frac{\boldsymbol{I_0(\lambda_i)}}{\boldsymbol{I(\lambda_i, \Delta t)}} = \boldsymbol{\varepsilon_{\lambda_i} N_{(\Delta t)} l} \qquad (2.10)$$

Assuming an exponentially decay of transient species considering, $\left[\boldsymbol{N_{\Delta t}} = \boldsymbol{N_0 e^{-\Delta t/\tau}}\right]$ we have,

$$\boldsymbol{ln}\big(\Delta\boldsymbol{A}\ (\Delta\boldsymbol{t})\big) = \boldsymbol{ln}\big(\boldsymbol{\varepsilon_{\lambda_i} N_0 l}\big) - \frac{\boldsymbol{\Delta t}}{\boldsymbol{\tau}} \qquad (2.11)$$

Thus, in a pump-probe transient absorption spectroscopy, population dynamics, $\boldsymbol{N_{(\Delta t)}}$, are monitored by change in optical density as a function of delay time, $(\Delta\boldsymbol{t})$, at given wavelength of the probe beam (λ_i) where $\Delta\boldsymbol{t}$ $(= \frac{\mathbf{2\Delta}\boldsymbol{L}}{\boldsymbol{C}})$, L is the optical path length and $\boldsymbol{C}$ is the speed of the light. The measured signal can be expressed as

$$\Delta\boldsymbol{A} = \boldsymbol{A_{with\,pump}} - \boldsymbol{A_{without\,pump}} \qquad (2.12)$$

Where, $\boldsymbol{A_{with\,pump}} = \mathbf{log}\frac{\boldsymbol{I_0^{probe}(\lambda_i)}}{\boldsymbol{I^{probe}(\lambda_i, \Delta t)}}$ and $\boldsymbol{A_{without\,pump}} = \mathbf{log}\frac{\boldsymbol{I_0^{probe}(\lambda_i)}}{\boldsymbol{I^{probe}(\lambda_i)}}$

So, $$\Delta\boldsymbol{A} = \mathbf{log}\frac{\boldsymbol{I_0^{probe}(\lambda_i)}}{\boldsymbol{I^{probe}(\lambda_i, \Delta t)}} - \mathbf{log}\frac{\boldsymbol{I_0^{probe}(\lambda_i)}}{\boldsymbol{I^{probe}(\lambda_i)}} = \mathbf{log}\frac{\boldsymbol{[I^{probe}(\lambda_i)]without\,pump}}{\boldsymbol{[I^{probe}(\lambda_i, \Delta t)]\,with\,pump}} \qquad (2.13)$$

The value of change in absorption, $\boldsymbol{\Delta A}$ can have negative and positive value and the term known as bleach and photo induced absorption (PA), respectively. The probable processes in the pump-probe experiment are summarized in the Figure 2.11. From the equation (2.13), it is clear that $\boldsymbol{\Delta A}$ will negative when $\left[\boldsymbol{I^{probe}(\lambda_i, \Delta t)}\right] \boldsymbol{with\, pump} > \left[\boldsymbol{I^{probe}(\lambda_i)}\right] \boldsymbol{without\, pump}$ which is referred as bleach. This is possible only when sample has ground state absorption and stimulated emission [processes (i) and (iii), respectively are illustrated in the Figure 2.11]. When sample has ground state absorption, after excitation by the pump pulse ground state population will be depleted as a results more light will be transmitted in the signal probe with respect to reference probe. A similar observation, i.e. increase of transmitted light in the signal with respect to reference also possible when the probe wavelength coincides with emission spectrum (termed as *stimulated emission*). The reverse phenomena i.e. PA is observed when $\boldsymbol{\Delta A}$ is positive. This is possible only when $\left[\boldsymbol{I^{probe}(\lambda_i, \Delta t)}\right] \boldsymbol{with\, pump} < \left[\boldsymbol{I^{probe}(\lambda_i)}\right] \boldsymbol{without\, pump}$.This positive

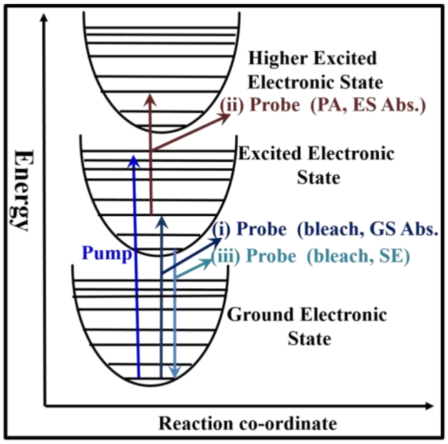

Figure 2.11: Scheme of the states involved in a pump-probe experiment in an experimental sample. (i) Depletion of ground state (bleach) (ii) excited state photoinduced absorption (positive absorption) and (iii) stimulated emission (bleach) by the probe pulses.

absorption, ***PA*** arises due to higher excited state transition caused for the probe pulse which is referred as process (ii) in the Figure 2.11.

2.8.2. Instrumentation:

The femtosecond transient absorption spectrometer consists of the following major segments such as

(i) ultrashort pulse generation: Ti-sapphire oscillator,

(ii) chirped pulse amplification: pulse stretcher, pulse picker, confocal multipass amplification, pulse compressor,

(iii) second harmonic generation: pump pulse,

(iv) white light continuum and

(v) pump-probe system.

Details of the each part are described below.

2.8.2. a. Ultrashort Pulse Generation: TiS Oscillator

In our pump-probe setup the ultrashort pulse is generated from an oscillator which contains titanium doped sapphire (Al_2O_3) crystal represent as Ti:Sapphire (TiS). In this oscillator, a diode pump solid state (DPSS) laser (CW mode, 532 nm, 3.8 W) is used as excitation source as a results the Ti^{3+} emit a broad PL band in the NIR region (650-1050 nm) [183]. At very high intensity of the pump laser, the non-linear phenomena which implies that the index of refraction (η) is a function of light intensity (I) and varying according the equation[184]

$$\boldsymbol{\eta\,(\nu) = \eta_0(\nu) + \eta_2(\nu) I} \qquad (2.14)$$

Where the $\eta_0(\nu)$ is the refractive index is a function of frequency in normal condition and $\eta_2(\nu)$ is the non-linear component which is positive in case of TiS. Again, the refractive index is the function of distance (r) as the laser cavity works in the TEM$_{00}$ mode in which the intensity of the light beam follow Gaussian distribution $[I(r) = \exp(-\rho r^2)]$.[184-186] Therefore, the refraction index is not homogeneously distributed in the medium, and corresponds to a situation as by inserting an additional material in a shape of a Gaussian lens into an optical resonator. This is known as "Kerr effect" and the medium is known as "Kerr medium" (i.e. TiS) [187]. Due to this stronger Kerr less focusing in the TiS medium the higher intense modes are transmitted through the medium while the lower intense modes can't.

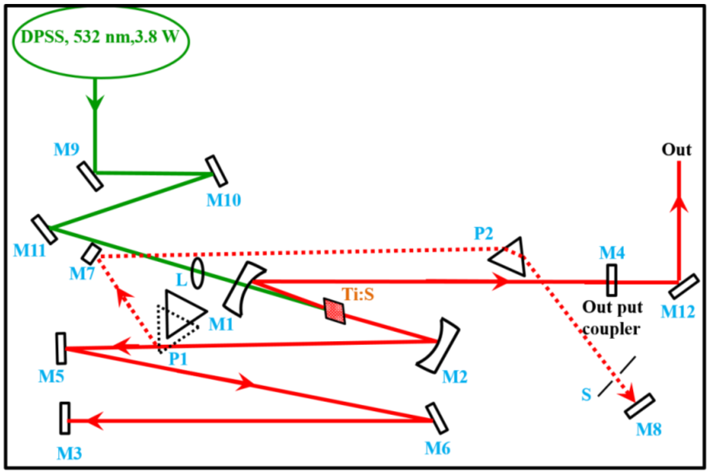

Figure 2.12: Optical scheme of TISSA 50 femtosecond Ti:Sapphire oscillator (CDP, Russia).

During every round trip process the lost-amplification is repeated. This power dependent loss makes the cavity unstable in CW mode and a slight disturbance of the laser cavity produce a laser pulse. This phenomenon is known as Kerr-lens mode-locking (KLM). This is also referred as *"self mode-locking"* as the Kerr-lens medium is the crystal itself.[188-190] Due to higher bandwidth of the gain medium (TiS, >350 nm) the passive mode locking (Kerr lens is passive object) can give pulse width as short as ~6fs ($6X10^{-15}$ s). During round trip, the fs pulse is subject to GVD (group dispersion velocity) dispersion which can be compensated by introducing chirped mirror or two prisms inside the laser cavity.[191, 192] Since, the bandwidth of gain medium (Ti:sapphire) is very large (> 350nm), to avoid the non-linear Birefringent effect due to self focusing, the TiS crystals is placed at Brewster angle. In the present thesis the oscillator CDP from Avesta, Russia is used. The two prism and high reflector (HR, ~100% of reflection) mirror assembly (for negative GVD) generates the ~50 fs pulse, 80-90 MHz pulse repetition rate and 4 nJ/pulse energy from Ti:Sapphire which is named as TISSA50 (Ti:Sapphire 50 fs). The optical layout of this oscillator is given in the Figure 2.12. The seed pulse is directed in an amplification system for amplification which is demonstrated in the next section.

2.8.2. b. Chirped Pulse Amplification (CPA)

The seed pulse obtained from TiS oscillator has energy nJ/pulse which is insufficient to excite the sample for performing pump-probe measurement. Therefore, the pulses are amplified several orders of magnitude as compare to the energy of the seed pulses. [193] Before amplification of the ultrashort pulse, it needs to be stretched to avoid the optics damage due to very high peak power (in the order of GW). Again, owing to Kerr effect of the TiS (amplifier medium) self focusing of the crystal may damage the crystal during amplification process. By introducing a pulse stretcher, one can easily overcome the condition of the damage threshold value of the optics and the active medium of the amplifier. After stretching the seed pulses temporarily in the order of hundreds of pico-second are subject to amplify in Ti: Sapphire active medium. This process is known as chirped pulse amplification (CPA).[187, 194, 195] The fs pulse of mJ/pulse energy is generated after compression. The CPA consists of the following segments:

i. Pulse Stretcher:

As we know that the velocity of different frequency light is different (red component travels faster than blue part) in a medium which is known as group dispersion velocity (GVD). Utilizing the negative GVD the incoming seed pulse can be stretched from <100 fs to few ps.[187, 195] The principal pulse stretching is shown in the Figure 2.13. This is purely optical device containing diffraction grating, spherical mirror and plane mirrors. Femtosecond pulse going into pulse stretcher has a broad bandwidth. For a 100 fs Gaussian pulse the corresponding bandwidth is about 9 nm. A diffraction grating sends different frequencies in different directions at different angles of diffraction. After double pass, bluer and redder components exit from the stretcher as shown in the Figure 2.13.From the figure it is clear that bluer frequency components have to travel further through the stretcher than the red frequency components. As a result the red frequency components exit the stretcher first, the pulse has been stretched.

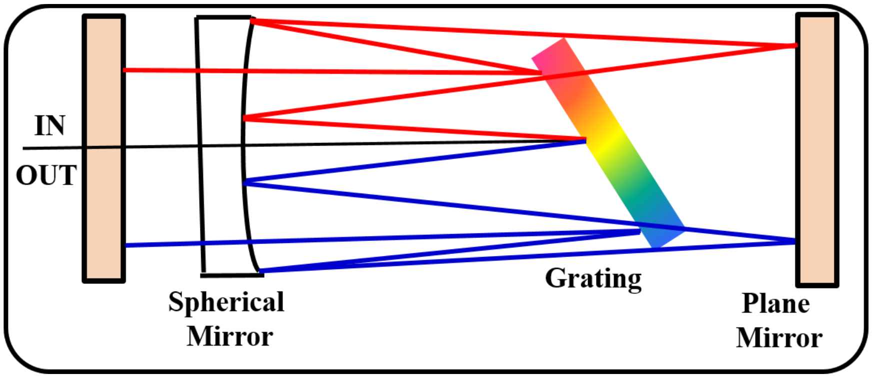

Figure 2.13: Illustration of the principle of femtosecond pulse stretcher.

In the MPA50, the pulse stretcher (Figure 2.13) the input pulse is dispersed in the horizontal plane. The stretched pulse is directed back to the stretcher with help of vertical retroreflector, and four passes through the stretcher are achieved. Four-pass configuration is necessary to ensure that the stretched beam is spatially reconstructed. Femtosecond pulses with pulse duration 100 fs are stretched to more than ten ps pulses before amplification. High reflective gold coated holographic grating gives stretcher efficiency higher than 50% for specific wavelength regimes.

ii. Pulse Picker:

After stretching, the stretched seed pulse is passing through a pulse picker which is installed for one pulse selection from a train of stretched pulse. As a result, seed pulses are qualified for the amplification. The pulse picker utilizes well known electro-optical Pockels effect. Pulse train having horizontal polarization goes through the Pockels cell. Without applied voltage pulses do not change polarization and exit pulse picker with help of polarizers as shown in the Figure 2.16. When half wave voltage is applied to the Pockels cell, an input pulse changes its polarization from horizontal to vertical, goes through polarizer and is used as a seed pulse for the amplifier. Applied voltage is synchronized with femtosecond pulse train and Nd:YAG pump pulses, and seed pulses have pulse repetition rate equal to the repetition rate of Nd:YAG (JADE Laser, France) pump pulses. Input polarizer is used to increase polarization ratio for input pulses.

iii. Confocal Multipass Ti:sapphire Amplifier (MPA):[196]

The low repetition rate (1 KHz) stretched pulse is allowed to pass into amplifier which consists an optically active heavily doped Ti: Sapphire crystal. The gain medium is pumped with another DPSS laser (532 nm) having same repetition rate (1 KHz) and power ~20W. The schematic of the confocal multipass amplifier has been shown in Figure 2.14. This telescopic configuration provides six, eight, ten passes of the light beam through the common focus where Ti: sapphire crystal is placed. Due to different focal lengths of the mirrors, beam cross section are decreased after each pass and the beam waist diameter is increased accordingly (bottom of Figure 2.14).

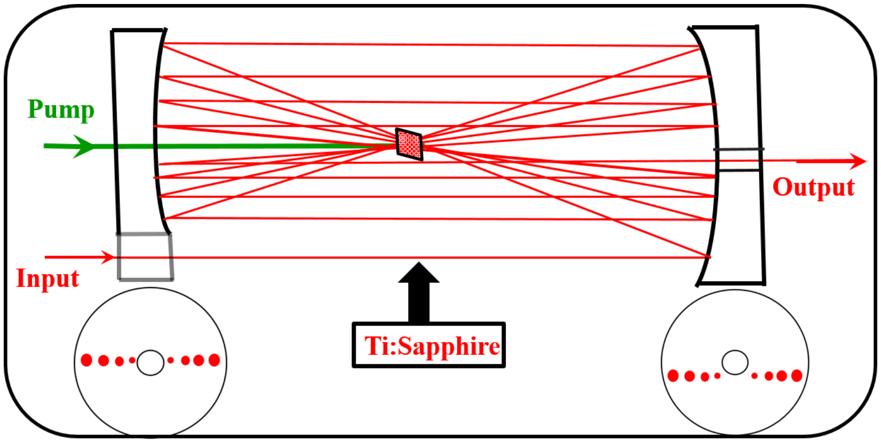

Figure 2.14: Optical schematic of two-mirror confocal multipass Ti: Sapphire amplifier. The respective radiation pattern on the confocal mirror has shown below of the corresponding mirror.

The pump radiation is focused by the lens through an aperture in the input mirror. The number of multiple passes depends on geometrical configuration of the mirrors. To avoid the crystal damage threshold (10 J/cm^2) typically 8-10 passes is optimized as a results we observe gain in the order of ~10^6.

iv. Pulse Compressor:

The principle of two grating pulse compressor is shown in the Figure 2.15. In contrast to the pulse stretcher, red frequency components have to travel further through the compressor than

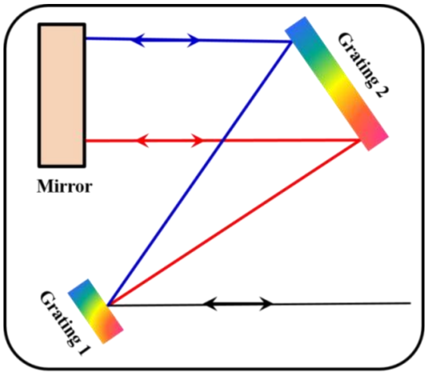

Figure 2.15: Illustration of the principle of two grating pulse compressor.

the blue frequency components (negative GVD).[187, 195, 197] The result is that the pulse has been compressed. Varying distance between the gratings, the compression can compensate the stretching precisely giving almost the same pulse duration as obtained from the seed laser pulse. In the present thesis the stretched picosecond pulses is amplified by MPA50 multipass Ti:sapphire amplifier and compress to pulses as short as 50-100 fs. The seed pulse generates from the TiS oscillator has pulse width ~50 fs is send for amplification due to very less energy. The MPA-50 amplifier which contains stretcher (having one grating), pulse picker unit (Pockel cell electronics), TiS gain medium and finally compressor (two grating). The overall amplification system (MPA-50, CDP, Russia) is shown in Figure 2.16.

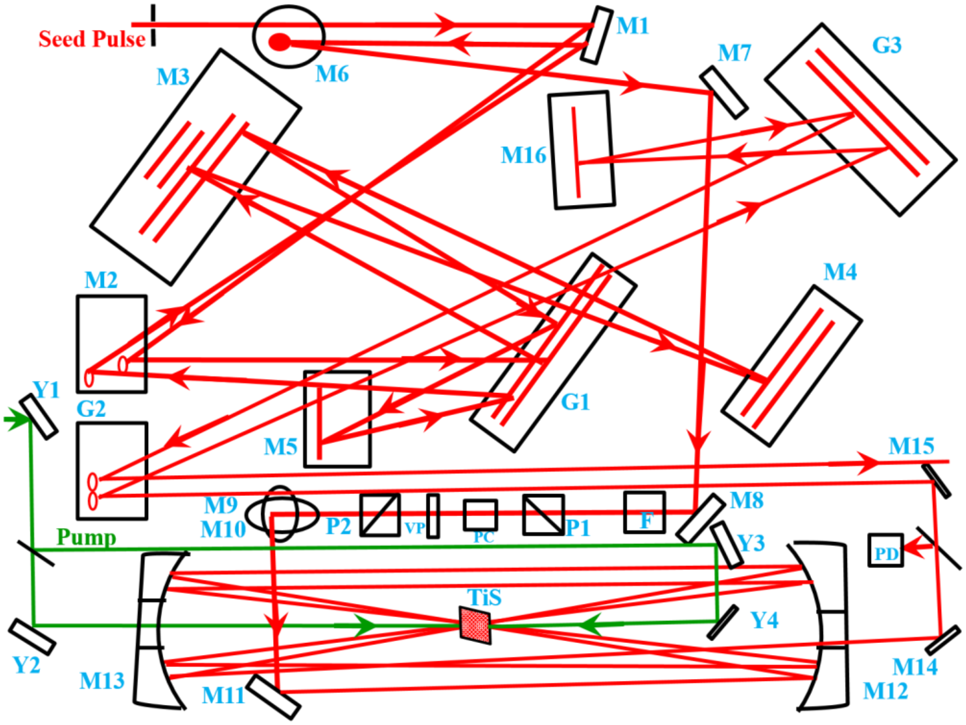

Figure 2.16: Complete optical scheme of MPA50 (CDP, Russia).

2.8.3. Second Harmonic Generation (SHG)

In the present thesis the experimental samples are excited by 400 nm pump laser radiation. To obtain the 400 nm laser excitation source, the 800 nm fundamental output of the TiS amplifier is passed through the β-barium borate (BBO) crystal for frequency doubling. This is called *second harmonic generation (SHG)*.[187, 195] SHG is a non-linear optical phenomena which is based on non-linear polarization of crystal due to very high pulse energy (peak power~ GW/cm^2). When the electric field, $\boldsymbol{E}$, of the incident light increases, the polarization of the medium ($\boldsymbol{P}$) which is depends on individual particle position (r) and time (t), is no longer linearly dependent on $\boldsymbol{E}$ and can be expanded in a Taylor series expansion

$$\boldsymbol{P}(\boldsymbol{r},\boldsymbol{t}) = \boldsymbol{\chi}^{(1)}\boldsymbol{E} + \boldsymbol{\chi}^{(2)}\boldsymbol{EE} + \boldsymbol{\chi}^{(3)}\boldsymbol{EEE} \ldots \ldots \tag{2.15}$$

At very high power, the second order susceptibility ($\boldsymbol{\chi}^{(2)}$) (10^{-10} V/cm) has significance contribution in polarization of a medium. In this situation the non-linear phenomena can be expressed in the form of second order term, i.e. [Since, $\boldsymbol{E} = \boldsymbol{E_0}\cos(\boldsymbol{\omega}\mathbf{t} - \mathbf{k}.\mathbf{r})$, where, $\boldsymbol{\omega}$ and $\boldsymbol{k}$ are the incident wave frequency and wave vector respectively.]

$$\boldsymbol{P}^{(2)} = \chi^{(2)}\boldsymbol{EE} = \chi^{(2)}[\boldsymbol{E_0}(\boldsymbol{\varphi})\cos(\boldsymbol{\omega t} - \boldsymbol{k_\omega}.\boldsymbol{r})]^2 \tag{2.16}$$

On phase matching condition i.e.$k_{2\omega} = k_\omega + k_\omega$ the polarization can be written as

$$\boldsymbol{P}^{(2)} = \frac{1}{2}\chi^{(2)}\boldsymbol{E_0^2}(\boldsymbol{\varphi}) + \frac{1}{2}\chi^{(2)}\boldsymbol{E_0^2}(\boldsymbol{\varphi})\cos(2\boldsymbol{\omega t} - \boldsymbol{k_{2\omega}}.\boldsymbol{r}) \tag{2.17}$$

Therefore, the polarization induced by the interaction of two waves, each of frequency $\boldsymbol{\omega}$, consists of two terms; a constant time-independent polarization i.e. $\frac{1}{2}\chi^{(2)}\boldsymbol{E_0^2}(\boldsymbol{\varphi})$, and other is the polarization modulated at the frequency $2\boldsymbol{\omega}$. Thus, the second order nonlinearity generates light photon having frequency $2\boldsymbol{\omega}$ that is the energy twice of the incident light photon $\boldsymbol{\omega}$. This kind of phenomena observes in the bi-refringent crystal like BBO. In our present setup the amplified pulse (800 nm) is divided into two parts and one of the part having <100 mJ/pulse energy is passed through the BBO crystal to generate the excitation pump laser i.e. 400 nm.

2.8.4. White Light Generation (WLG)

In order to perform pump-probe experiment, the probe pulse i.e. the white light continuum (WLC) is needed for detection of transient species. WLC generation is governed by the effect of the *self-phase modulation* (SPM). [195, 198] SPM arises from the third-order susceptibility, and is a nonlinear third-order effect. When an amplified pulse has energy ~10μJ with pulse duration <100 fs travels through medium it will create the SPM. We have already discussed in the section 2.8.2.a. that the index of refraction (η) of a medium depends on the intensity (I) of the incident light (equation 2.14). Due to Gaussian distribution of the pulse, the intensity dependent index of refraction changes the electric field of the light photon. The phase difference of the light (passing through an optical path length, L) will change with the index of refraction accordingly: $\phi(\omega, t) = \frac{\omega\eta\,(\omega,t)}{c} L$. Thus the time dependent phase change leads to frequency change that can be expressed as follow,

$$\boldsymbol{\partial\omega = \frac{\partial\varphi(t)}{\partial t}} \tag{2.18}$$

Therefore, the change in frequency difference which changes the pulse passes on the leading edge to the trailing edge due to the Gaussian shaped pulse structure. As a result, the broad frequencies of different wavelength pulses are obtained known as white light. Due to the third order non-liner effect all frequencies are well ordered with same phase difference. In our present setup we use a 1.5 nm sapphire crystal to generate WLC from ~1μJ pulse energy of the fundamental pulse (800 nm).

2.8.5. Pump-probe Transient Absorption Spectrometer:

After generation the WLC, the probe (350-1000 nm) pulse is divided into two parts by a beam splitter. The pump pulse (400 nm) is overlapped on the one of the probe pulse on the sample. This probe is treated as signal. Other probe beam which is not overlap with pump pulse but passing through the sample is providing the reference signal. The experimental sample solutions are circulating to avoid the photo-bleaching. The pump pulse is passes through a polarizer having an angle 54.7° to avoid the effect of anisotropy. A mechanical chopper operating at 500 Hz is placed after the pump pulse but before the sample, which block every alternate pump pulses so that ratio of transmitted intensities of consecutive probe pulses corresponds to transient absorbance. The change in absorption (ΔA) is calculated using the equation 2.13. In the present setup we use the Exipro transient absorption spectrometer where we use a retroreflector for delay stage and CCD (charge coupled device) to detect the signal. The excited state kinetics of the samples can be measured in 0.66 fs-4 ns time resolution providing the time delay in the probe pulse using retroreflector. Typical temporal resolution of this pump-probe set up is measured by bleach signal of meso-tetrakis-(4-sulphanatophenyl) porphyrin dianion (TPPS) at 710 nm (λ_{pump} 400 nm, aqueous solution at pH 1) and found to be ~100fs. Finally the data are analyzed with the help of Lab-view programme.

2.9. Pulse radiolysis:

Pulse radiolysis is one of the secondary technique has been used to investigate the formation of dye cation radical.[199, 200] This is again a pump-probe experiment. The main difference from the transient absorption is that, the samples is excited here by the electron and probe the transient species by light in UV-visible region (300 nm-900 nm). In brief, the electron pulses of 50 ns duration from a 7 MeV linear accelerator are used for irradiation source. The transients produced are detected by kinetic spectrophotometer using 450 W pulsed xenon lamp along with monochromator, photomultiplier and digital oscilloscope. The absorbed radiation dose is measured by thiocyanate dosimetry. The typical dose is ~10 gray (G). A one electron oxidation reaction is carried out in typical pulse radiolysis experiments in N_2O saturated solution of aqueous dye (10^{-4}mol dm^{-3}) and NaN_3 ($5x10^{-3}$ mol dm^{-3}). During the electron beam irradiation, water molecules are dissociated in several transient species like $H^{\cdot}$ (hydrogen radical), $OH^{\cdot}$ (hydroxyl radical), e^{-}_{aq} (hydrated electron) etc. The hydrated electron reacts with the nitrous oxide form oxide radical ($O^{\cdot-}$). The reacted species which is responsible for the formation dye cation, azide radical ($N_3^{\cdot}$), is generated after successive reaction of oxide radical with water molecule and the azide anion respectively. Finally, the dyes are oxidized to cation radical by reacting with azide radical through a one electron oxidation. The overall reaction of the entire process can be summarized in below:

$$H_2O \rightsquigarrow H\cdot, OH\cdot, e^{-}_{aq} \text{ etc.}$$

$$e^{-}_{aq} + N_2O \longrightarrow N_2 + O^{-}\cdot$$

$$O^{-}\cdot + H_2O \longrightarrow OH\cdot + OH^{-}$$

$$N_3^{-} + OH\cdot\,(O^{-}) \longrightarrow N_3\cdot\,(\text{radical}) + OH^{-}\,(O^{2-})$$

$$N_3\cdot\,(\text{radical}) + \text{Dye} \longrightarrow N_3^{-} + \text{Dye}\cdot^{+}$$

2.10. Photovoltaic Measurement (IPCE and IV):

In the present thesis to measure the photovoltaic performance (J-V curves) of QD solar cells a 100 W/m^2 AM 1.0 G short-arc Xe lamp solar simulator (Peccell, model: PEC-L01) has been used as the illuminating source with 100 mW/cm^2 intensity calibrated using a standard Si-photodiode provided by Peccell. Keithley 2400 source meter is used to record the J-V characteristic of the QD solar cell. To record the Incident IPCE data Action Spectrum

Measurement System (Peccell, model: PEC-S20) with a xenon lamp (150 W) as the light source and 400-800 nm measurement wavelength range is used.

The efficiency (η) of the solar cell is defined as the ratio of the electrical output of a working cell to the incident energy in the form of sunlight. In other word, the efficiency of the solar cell is the percentage of the solar energy to which the cell is exposed that is converted into electrical energy. This is calculated by dividing a cell's power output (in watts) at its maximum power point (P_m) by the input light (E, W/m^2).

$$\boldsymbol{\eta = \frac{P_m}{E\, X A_c}} \qquad (2.19)$$

where "A_c" (in m^2) is the area of the working solar cell.

Again, the efficiency of the solar cell can be written in terms of fill factor (*FF*), open circuit voltage (V_{OC}) and short circuit current (I_{SC}). Fill factor (*FF*) is a parameter which characterizes the non-linear electrical behaviour of the solar cell. Fill factor is defined as the ratio of the maximum power from the solar cell to the product of V_{OC} (when a cell is operated at open circuit i.e. I = 0 and the voltage across the terminals is defined as open circuit voltage.) and I_{SC} (when a cell is operated in short circuit i.e. V = 0 and the current through the terminals is defined as short-circuit current). So,

$$\boldsymbol{FF = \frac{P_m}{V_{OC} \times I_{SC}}} \qquad (2.20)$$

From equation (2.19) and (2.20) one can write the efficiency of the solar cell as follow,

$$\boldsymbol{\eta = \frac{FF\, X\, V_{OC} X\, I_{SC}}{E\, X A_c}} \qquad (2.21)$$

The terms of the right hand side of the equation (2.21) are the experimentally measured quantity and using this value we have measured the solar cell efficiency.

2.11. Experimental Samples Preparation:

2.12.1. Material Used

Cadmium oxide (CdO, 99.5%), zinc acetate ($ZnAc_2.2H_2O$, 99.9%), selenium shot (Se,99.99%), sulphur powder (S, 99.99%) and tellurium powder (Te, 99.99%), cesium carbonate, lead bromide ($PbBr_2$), olylamine (OAm), technical grade oleic acid (90%), tri-octly phosphine (TOP, 90%), 1-octadecene (ODE) (90%) was purchased from Aldrich and used as received without further purification. 4',5'-dibromo fluorescene (DBF), bromo-pyrogallol red (Br-PGR) were purchased from Aldrich and were used without further purification. AR grade chloroform and AR methanol were used for precipitation for all the nanocrystals. Nano pure water used as solvent to prepare all the aqueous solution. Benzoquinone (TCI) and pyridine (HPLC) were used as electron and hole quencher, respectively. All the solvents and chemicals used for synthesis were procured from S D fine chemicals (India) and were used without further purification.

2.12.2. Synthesis of CdSe& CdS QDs:

High-quality non-aqueous CdX (X = Se and S) QDs were synthesized by following the previously reported method by Yu and Peng [201, 202] with some modifications. In a typical synthesis, 1 mmol (0.128 g) of CdO, 4.5 mmol (~1 mL) of OA, and 10 mL of ODE were loaded in a 50 mL three-neck round-bottom flask. The mixture was degassed in an Ar gas atmosphere for 30 min at 120 °C. The reaction mixture was then heated and the mixture became colourless above 260 °C. Previously prepared 0.5 mmol chalcogen (0.039 and 0.016 g of Se and S, respectively) in 1 mL of TOP solution was immediately injected into the reaction mixture at 300 °C. The temperature of the reaction mixture was reduced to 280 °C and the growth of the nanocrystal (NC) was monitored at 260 °C. Purification of the synthesized NC was carried out in methanol solution and finally dispersed in a low polarity solvent such as chloroform.

2.12.3. Preparation of ZnSe QD:

Oleic-capped ZnSe NCs were synthesized by following the similar approach adopted from previous literature [202] for synthesis of CdSe QD by high-temperature hot injection method with minor modification. Briefly, a stock zinc oleate solution was prepared by heating zinc acetate (4.0 mmol) in oleic acid (10.6 mmol) and 10-12 ml octadecene in a three-neck round-bottom flask to 180 °C until a clear solution was obtained. During this reaction an inert gas (Ar) was passed through one of the neck of the flask. After a colourless solution was obtained the reaction temperature was allowed to increase up to 240-250 °C. To prepare the stock selenium injection solution, selenium powder (2 mmol) was reacted with TOP (2.5mmol) in 4-5 ml octadecene. This TOP-Se solution was swiftly injected through a syringe to the reaction mixture at 240-250 °C. Typically rapid color changes from colourless to light yellow were observed within 1min of injection. The solution temperature was allowed to settle at room temperature and then it was dissolved with chloroform and finally re-precipitated with methanol for 2-3 times.

2.12.4. Preparation of $CsPbBr_3$ QDs

Caesium lead tribromide perovskite ($CsPbBr_3$, CPB) quantum dots were synthesized after following the previously reported literature with little modification.[203] This synthesis involves two steps. In a three neck flask 1.25 mmol (~0.41 g) Cs_2CO_3, 20 mL ODE and 4 mmol OA (~1 mL) were loaded and heated the mixture at 100 ºC for 1h to dry. Then the mixture was heated at 150 ºC for complete dissolution of Cs_2CO_3 in an inert gas (Ar) atmosphere. Complete dissolution of the Cs_2CO_3 indicates the formation of the caesium oleate. To prepare the $CsPbBr_3$ QDs, 0.188 mmol $PbBr_2$ (~0.069 g) and 5 mL ODE were taken in a three neck flask. The resulting mixture was heated at 120 ºC for 1h in an Ar gas atmosphere. 0.5 mL dried OA and 0.5 mL dried OAm were added at 100 ºC in the reaction mixture. The reaction mixture was heated at 140 ºC for complete dissolution of $PbBr_2$. The previously prepared (~0.4 mL) Cs-oleate was swiftly injected in the reaction mixture at 150 ºC. A rapid fluorescent color change was observed immediately after addition and the reaction was quenched within 5-10 seconds by ice cold water. Finally the product was precipitated by ODE and ^{t}BuOH (ODE:^{t}BuOH= 1:1) solvent mixture.

2.12.5. Synthesis of CdSe/CdS Quasi-Type II Core−Shell:

The CdSe/CdS core−shell was synthesized by following the previously reported literature method [204, 205] with minor modification. To synthesize CdSe/CdS core−shell, previously prepared CdSe QD solution was used directly as core. The CdS shell on the CdSe core was prepared by using Cd-oleate as the cadmium precursor and sulphur powder as the S precursor. Cadmium and sulphur precursor concentrations were kept for 1 μmole of CdSe core. The cadmium oleate was prepared by adding 0.31 mmol (0.04 g) of CdO and 0.85 mL of OA (2.6 mmol) in 5 mL of ODE under reflux conditions (at 180 °C) into a three-neck round-bottom flask in inert Ar gas atmosphere. This cadmium oleate was allowed to cool down at room temperature and added to the degassed CdSe core solution. Then the mixture was heated at 120 °C for 20 min for complete removal of chloroform, and the sulphur solution was added dropwise into the mixture at 200 °C. The sulphur solution was prepared by adding 0.31 mmol (0.01 g) of S powder in 0.25 mL of TOP (0.6 mmol) and 10 mL of ODE. After adding the sulphur precursor, the resulting mixture was heated for 1 h at 200 °C and finally dispersed in chloroform after precipitation in methanol.

2.12.6. Synthesis of CdS/CdSe Inverted Type I Core−Shell:

To synthesize CdS/CdSe core−shell NC, previously prepared CdS QD solution was used directly as core. The CdSe shell on CdS core was prepared by using cadmium oleate as cadmium precursor and selenium powder as Se precursor. Cadmium and selenium precursor concentrations were kept for 1μmol of CdS core. The cadmium oleate was prepared by adding 0.66 mmol (0.085) g of CdO and 0.85 mL of OA (2.6 mmol) in 5 mL of ODE under reflux conditions (at 180 °C) into a three-neck round-bottom flask in an inert Ar gas atmosphere. This cadmium oleate was allowed to cool down at room temperature and added to degas CdS core solution. Then the mixture was heated at 120 °C for 20 min for complete removal of chloroform, and the selenium solution was added dropwise into the reaction mixture at 180 °C during the time duration of 1 h. The selenium solution was prepared by adding 0.66 mmol (0.052 g) of Se powder in 0.25 mL of TOP (0.6 mmol) and 10 mL of ODE. After adding the selenium precursor, the resulting mixture was heated for another 4 h at 180 °C and finally cooled down to the room temperature and dispersed in chloroform after precipitation in methanol.

2.12.7. Preparation of CdS/CdTe core-shell:

To synthesize CdS/CdTe type II core-shell, prepared CdS QD solution in chloroform was directly used as core. CdTe shell on CdS QD was prepared by using Cd-oleate as cadmium precursor and tellurium precursor as tellurium precursor. Cd-oleate was prepared by adding 0.112 g of CdO (0.876 mmol) and 0.74 ml oleic acid (2.3 mmol) in 2.5 ml octadecene under reflux condition (at 180°C) into a three-neck round bottom flask in inert atmosphere. This Cd-oleate was added to a 1 μmole CdS solution in a three-neck round bottom flask. The mixture of 0.112 g Te (0.876 mmol), 0.5 ml TOP (1.09 mmol) and 10 ml octadecene was dropwise added to the solution through a syringe at 180°C. Precipitation done in methanol solution.

2.12.8. Synthesis of CdS_xSe_{1-x} alloy QDs:

Monodispersed highly luminescent alloy QDs were synthesized after following previous reported procedure with some modifications.[128] In brief, a stock cadmium oleate solution was prepared by heating a mixture of 1.6 ml oleic acid (5 mmol), 0.128 g cadmium oxide (1.0 mmol) and 14.0 ml ODE in a three-neck round-bottom flask at 200 °C in an inert Ar gas atmosphere. The resulting solution was degassed at this temperature for 30 minutes. The solution became colourless; indicating formation of Cd-oleate and the required mixture of chalcogenide solution were swiftly injected through a syringe to the reaction mixture at 320 °C. Temperature of the mixture was reduced to 20 °C and growth of QD monitored at 250 °C. To prepare the chalcogen solution, 0.25 mmol of the corresponding chalcogen was mixed with 0.28 ml TOP (1 mmol) in Ar atmosphere. The resulting colourless solution was obtained in 2.72 ml octadecene to give a final stock solution volume of 3 ml. A rapid color changes from colourless to fluorescent color were observed in all the cases. Precipitation was done in methanol solution.

2.12.9. Synthesis of $Cd_xZn_{1-x}Se_{1-x}$ alloy QDs:

Synthesis procedure and the experimental condition of $Cd_xZn_{1-x}Se$ alloy quantum dot is quite similar to that of CdS_xSe_{1-x} alloy. In brief, a mixture of cadmium and zinc oleate solution was prepared by heating a mixture of 1.6 ml oleic acid (5 mmol), 1.0 mmol of Cd and zinc (with stoichiometric ratio) and 14.0 ml ODE in a three-neck round-bottom flask at 200 °C in an inert Ar gas atmosphere. The resulting solution was degassed at this temperature for 30 minutes. The solution became colourless; indicating formation of metal oleate and the required mixture of chalcogenide solution were swiftly injected through a syringe to the reaction mixture at 320 °C. Temperature of the mixture was reduced to 20 °C and growth of alloy QD monitored at 250 °C. To prepare the Se solution, 0.25 mmol of the Se was mixed with 0.28 ml TOP (1 mmol) in Ar atmosphere. The resulting colourless solution was obtained in 2.72 ml octadecene to give a final stock solution volume of 3 ml. A rapid color changes from colourless to fluorescent color were observed in all the cases. Precipitation was done in methanol solution.

2.12. Solar Cell Assembly:

2.12.1. Phase Transfer of the Organic Capped QD through Ligand Exchange:

The OA capped QDs were water solubilised through phase transfer technique using MPA as a surfactant following literature techniques [160]. The pH of the MPA solution in methanol-water mixture (3:1) was adjusted to 12 using a 40% aq. KOH solution. This solution was dropwise added to the QD solution in chloroform until precipitation and stirred for 15 min. 5 ml of water was added followed by 15 min of further stirring. The pH of the aqueous phase was maintained at 12. The QDs phase transferred to the aqueous phase which was collected and precipitated with acetone. After centrifugation, the water soluble MPA capped QDs was dispersed in required amount of water for further use.

2.12.2. Preparation of TiO_2 Photoanodes:

In:SnO_2 (ITO) coated glass plates (8Ω/square) were cleaned sequentially using soap water, DI water and ethanol in a ultrasonic bath for 20 minutes each, followed by drying at 150°C for 2 hours. On cleaned ITO plates a transparent layer (or the active layer) of TiO_2 (dyesol, DSL 18NR-T, average particle size 20 nm) was deposited using doctor blade technique and dried in air for 2 hours. Then the films were sintered at 450°C for 30 min and at 500°C for 15 min in a muffle furnace. Then a scattering layer of TiO_2 (dysol,WER2-O, average particle size 150-200 nm) was deposited on top of the transparent layer followed by sintering again at 450°C for 30 min and at 500°C for 15 min. The water soluble QD solution (OD ~ 2 at excitonic peak, 1-2 drops) was dropcasted on the TiO_2 mesoporous film electrode and kept for 3 hours before rinsing it with DI water. After immobilizing the MPA capped QDs on TiO_2, a quasi-shell of CdS was deposited utilizing successive ionic layer adsorption and reaction (SILAR) technique by alternately dipping the film into 0.1 M methanolic solution of $Cd(NO_3).4H_2O$ and 0.1 M methanol: water (1:1) solution of Na_2S for 1 min. The films were rinsed with DI water in-between each step. Four SILAR cycles were performed for each film. on QD/quasi-CdS TiO_2 films a thin passivating layer of ZnS (4 cycles) was deposited using the same SILAR technique by alternatively immersing the films in 0.1 M methanolic $Zn(NO_3)_2$. $6H_2O$ solution and 0.1 M methanol: water (1:1) solution of Na_2S for 1 min. Finally, the films were cleaned with DI water and dried in air.

2.12.3. Counter Electrode:

For solar cell assembly Cu_2S counter electrodes were used. At first Cu was deposited on ITO glass by multiple potentiostatic pulse strategy from a nitrogen purged solution of 10 mM Cu(II) in 0.005 M H_2SO_4 in a standard three electrode electrochemical cell consisting of ITO as working electrode, platinum wire as counter electrode and Ag/AgCl as reference electrode [206]. The pulse potentials were chosen from the cathodic scan and anodic scan segments of the cyclic voltammograms of 10 mM Cu(II) in 0.005 M H_2SO_4 on FTO at a scan rate of 0.1 V s^{-1}. Under optimized condition, a potential train of 0.3 V for 0.4 s and -1.9 V for 0.25 s was applied for 3000 cycles. Then the Cu-coated ITO glass is thoroughly rinsed with water and dried in air followed by immersed in a polysulfide solution prepared by dissolving 1 M Na_2S, 1 M S and 0.1 M KCl in 3:7 methanol water mixture for 1 min. The electrodes were then rinsed with DI water and dried in air. The XRD pattern of the product materials on the ITO was matched with the JCPDF file #26-1116 confirming the formation of Cu_2S on ITO. Polysulfide solution containing 0.6 M Na_2S, 0.2 M S and 0.2 M KCl in 7:3 methanol water mixtures was used as electrolyte. The TiO_2/QD/quasi-CdS/ZnS photoanodes were then sandwiched using binder clips with the Cu_2S counter electrode separated by scotch tape spacer with ~ 100μL electrolyte droplet in between.

CHAPTER-3

Charge Transfer Dynamics in CdS Quantum Dots and Molecular Adsorbate

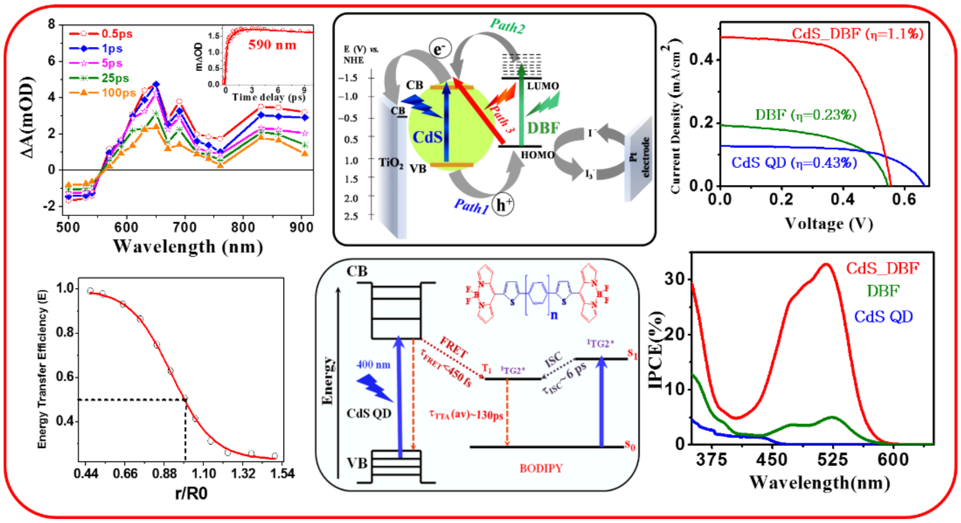

- ***J. Phys. Chem. Lett.*,2013, *4*, 4020–4025.**
- ***J. Phys. Chem. C (Submitted).***
- ***Manuscript Under Preparation.***

3.1. Introduction:

The demand of harvesting of solar energy has generated immense scientific research interest on various kinds of nano-architect quantum dots (QDs) materials.[37, 207, 208] Since the semiconductor QDs have dimension in the range of the Bohr radius, the electronic transition energies become size dependent which leads to tunable optical absorption and emission properties.[16, 209] High extinction coefficients, low production cost, possibility of easy charge carrier separation, multiple exciton generation (MEG) [48, 97, 100, 210] and facile energy transfer process involving the QD materials [211] make them suitable candidates for light harvesting materials in quantum dot sensitized solar cell (QDSC).[147, 150, 212-214] Although the QDs have all the promising properties, the photocurrent conversion efficiency is not as high as dye sensitized solar cell (DSSC) due to limited absorption in solar spectrum and energy loss due to ultrafast exciton annihilation.

Charge transfer in QD-molecular adsorbate composite is extremely important for their application in many electronic devices like quantum dot based solar cells. [215-217] In addition to that interest of charge transfer in molecule-QD system has been increased manifold due to report on MEG in quantum dot. It has been realized and partially verified that efficiency of solar module can be enhanced significantly by dissociating or separating the multi-exciton before ultrafast exciton-exciton annihilation.[97, 218] Using suitable adsorbate molecule (electron or hole acceptors) on photoexcited QD materials ultrafast exciton dissociation can be a reality. Exciton dissociation in fast and ultrafast time scale through electron transfer in QD/molecular adsorbate and QD/semiconductor nanoparticle (TiO_2) systems have been widely investigated. [219-222]

So far the highest conversion efficiency in QDSC has been reported by Zhong and co-workers to be >11 %.[44] However the efficiency of the QDSC is much lower than conventional dye-sensitized solar cell (DSSC).[45] The main factors for overall lower efficiency are mainly due to limited absorption of solar radiation of the QD materials and slow hole transfer rate. Size of the QD are higher (more than 2-3 nm sometimes larger) as compared to dye molecule (size is less than 1 nm) as a result QD loading on TiO_2 electrode in QDSC is much less as compared to dye loading in DSSC. As a result injected electrons in QDSC are in direct contact with the electrolyte which is undesirable. Finding a suitable hole transporting material in QDSC is always a challenging task. All the problems can be tackled by introducing concept of super sensitization in solar cell. [212, 223, 224] In super sensitization, quantum dot and molecular adsorbate can exchange charge carriers where molecular adsorbate in addition to photosensitizing the quantum dot material, it also can act as hole transporting materials, where holes are generated out of photo-excitation of QD. As a result total charge separation can take place in the QD-molecular composite material and it can be used as a super sensitizer. Lian [225] and Ghosh [226] and co-workers have observed in dye-nanoparticles (TiO_2) system charge separation facilitated drastically if the composite materials form charge transfer (CT) complex in the ground state. Similarly one can envisage charge separation between quantum dot – molecular adsorbate can be drastically improved if they form charge transfer complex in the ground state, where on photo-excitation electron from dye molecules can be transferred directly to the QD materials.

In addition to the electron and hole transfer, exciton quenching can take place via non radiative energy transfer process. Energy transfer is a non-radiative phenomenon [227] where the excited donor transfers its energy to an acceptor via long range dipole-dipole interaction.[228] The spectral overlap between the donor emission and the acceptor absorption is the key factor to determine the rate and efficiency of the energy transfer process. The non radiative energy transfer of the donor to acceptor is based on Förster resonance energy transfer (FRET) mechanism. FRET principles have been extensively used in several research realms such as fluorescence chemistry especially dye-dye interaction,[229, 230] biological system including medical diagnostic, optical imaging, DNA analysis, single molecule FRET etc.[174] Recently Banin *et al.* [231] have demonstrated the FRET between semiconductor nanocrystal and the dye molecule which are used as a sensing application even in the single molecular level concentration. However, the FRET process is also well known in various systems such as metal nanoparticle-dye surface,[232, 233] and metal-semiconductor hetero-structure composite.[234] Most importantly FRET process has been well demonstrated in photovoltaic performance in molecular adsorbate-QD composite systems [235-245] and QD-QD [246, 247] systems. The size dependent spectral properties of the QD, can make them suitable candidate as a donor for an efficient FRET pair in molecular adsorbate-QD composite system. In particular, the spectral overlap can be tuned by altering the size of the QDs materials. Kamat *et al.*[248] have demonstrated size dependent Förster versus Dexter energy transfer processes in CdSe Quantum Dot−Squaraine light harvesting assemblies. Zaban and co-workers demonstrated higher efficiency built-in quantum dot antennas in dye-sensitized solar cells where the QD materials serve as transmitter and channelling the absorbed solar radiation to the dye molecules through nonradiative energy transfer process.[245]

In this chapter we have demonstrated the exciton quenching of CdS QDs in presence of two different dye molecules via hole transfer and through non radiative energy transfer process. In addition to the hole transfer from CdS to the 4′,5′-dibromofluorescein (DBF), direct electron transfer takes place from HOMO of the DBF molecule to the CB of the CdS QDs. Electron injection from the LUMO of the DBF molecule to the CB of the CdS also possible as the LUMO energy level of the DBF is energetically higher than the CB energy level of CdS. On the other hand non radiative energy transfer is observed from CdS to BODIPY (boron dipyrromethene, named as TG2 and TG10) derivative. The charge transfer interaction of the composite systems has been carried out using femtosecond transient absorption spectroscopy.

3.2. Results and Discussion:

3.2.1. UV-vis Optical absorption, Steady State and Time Resolved PL Study

i. *CdS QD and DBF composite:*

Formation of charge transfer complex in the ground state between molecular adsorbate and oxide semiconductor (TiO_2 and ZrO_2) is quite well known in the literature. [249] In our earlier investigation we have also reported formation of CT complex between molecular adsorbate and TiO_2 [226, 250] and ZrO_2 [250] nanoparticles, where appearance of new charge transfer optical absorption band was detected in the ground state. To the best of our knowledge till date no report is available where QD (CdSe, CdS, CdTe etc) and molecular adsorbate form CT complex in the ground state. Figure 3.1 shows the optical absorption spectra of DBF after addition of different concentration of CdS QD. Pure DBF molecule shows weak optical absorption up to 550 nm with a peak at 465 in addition to an absorption band below 280 nm as depicted in trace a in Figure 3.1. The CdS QDs (spherical in size) were synthesised adopting high temperature injection method. Trace b in Figure 3.1 depicts the optical absorption spectrum of 0.49 µM CdS QD in chloroform which shows an exciton at 433 nm and corresponding band gap can be calculated to be ~2.69 eV. Now on addition of increasing concentration (0.049 µM to 0.49 µM) of CdS QD in DBF solution the optical absorption band become broader and shifted to the red region of the spectrum. The color of the solution becomes deep red (while the color of free DBF and CdS is light orange and yellow respectively) indicating formation of strong charge transfer (CT) complex between CdS QD and DBF. The intensity of charge transfer band increases drastically. BH plot for the above CdS-DBF system is shown in the inset of Figure 3.1, where extinction coefficient of the complex is calculated to be 2.14 X 10^6 M^{-1} cm^{-1}. High extinction co-efficient of the CdS-DBF complex suggest that the composite materials form strong CT complex where partial charge transfer takes place in the ground state. This observation clearly suggests that CdS-DBF composite material is a potential material for super-sensitizer, which can absorb more solar radiation as compared to that of the individual CdS QD and DBF molecule. Trace a in Figure 3.2 shows steady state PL spectra of CdS QD in chloroform after exciting the sample at 375 nm, which consist an emission peak at 450 nm with high quantum yield ($\varphi_f = 0.24$). Figure 3.2 b shows the emission spectra of CdS QD

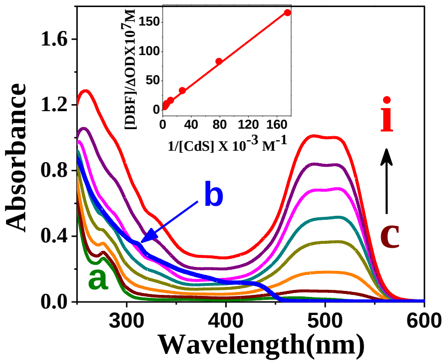

Figure 3.1: Optical absorption spectra of (a) DBF dye (0.3 mM) (b) CdS QD (0.49 µM), (c-i) DBF-CdS complex at constant DBF concentration (0.3 mM) with increasing CdS QD concentration in chloroform (in the mixture [CdS] are (c) 0.049, (d) 0.098, (e) 0.147, (f) 0.196, (g) 0.294, (h) 0.392, (i) 0.49 µM). Inset: Benesi−Hilderband (B-H) plot of DBF-CdS CT complex. Details for B-H plot *J. Am. Chem. Soc.* **1949**, *71*, 2703.

in presence of 0.3 mM DBF. It is clearly seen that CdS emission is completely quenched in presence of DBF. As we have already mention that the valence band (1.35 V vs NHE) of CdS lies below the HOMO (0.8 V vs NHE) of DBF (Scheme 3.1), so photo-excited hole can be captured by DBF which is thermodynamically viable. Hole transfer reaction can be expressed by the equations below:

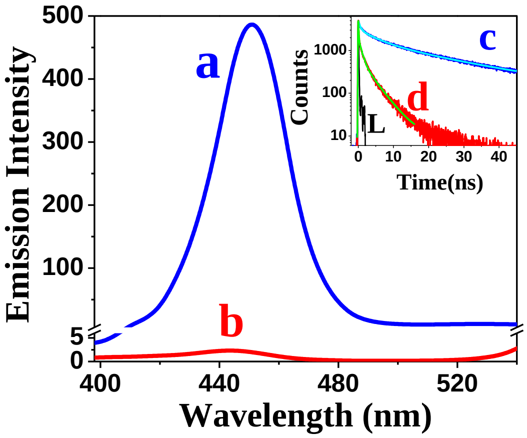

Figure 3.2: Photoluminescence (PL) spectra of CdS QD (a) in absence and (b) in presence of DBF in chloroform solution after exciting at 375 nm. **Inset:** Emission decay traces of (c) CdS QD and (d) CdS-DBF composite after exciting at 406 nm and monitoring at 450 nm. **L** is excitation profile. [CdS] = 0.49 μM and [DBF] = 0.3 mM.

$$\mathrm{CdS} + h\nu \rightarrow \mathrm{CdS}\ (e^- + h^+) \qquad (3.1)$$

$$\mathrm{CdS}\ (e^- + h^+) + \mathrm{DBF} \rightarrow \mathrm{CdS}\ (e^-) + \mathrm{DBF}^+ \qquad (3.2)$$

To find the hole transfer dynamics we have carried out time-resolved emission studies of free CdS QDs and also in presence of DBF and shown in Figure 3.2 inset. The emission decay traces of CdS QD and CdS/DBF composite have been monitored at 450 nm after exciting the samples at 406nm. The emission decay traces can be fitted multiexponentially with time constants of τ_1 =

0.58 ns (39%), τ_2 = 23.8 ns (32%), τ_3 = 5.2 ns (29%) with τ_{avg} =9.4 ns for CdS QD and of τ_1 = 0.12 ns (61%), τ_2 = 0.94 ns (22%), τ_3 = 3.4 ns (17%) with τ_{avg} =0.9 ns for CdS/DBF system. The average lifetime of CdS/DBF system is ten times shorter as compared to that of CdS QD, which confirms hole transfer process in the composite materials as suggested in equation 3.2. Presumably the observed decrease in lifetime arises due to hole transfer (HT) from CdS QD to DBF molecule, then the HT rate constant can be determined through the following expression

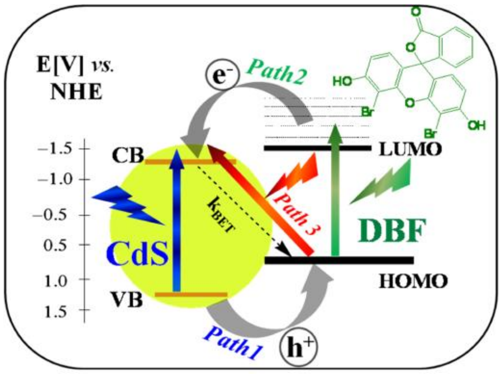

Scheme 3.1: Charge transfer processes (hole transfer, electron injection and charge recombination reactions) involving CdS QD and DBF dye in chloroform. Molecular structure of DBF is shown in the scheme.

$$k_{HT} = 1/\tau_{CdS+DBF} - 1/\tau_{CdS} \qquad (3.3)$$

Using the average lifetime values of 9.4 ns (CdS) and 0.9 ns (CdS-DBF) the hole transfer rate constant can be determined to be 1.1×10^9 sec^{-1}. From Scheme 3.1 it is clear that photo-excited DBF molecule can inject electron into the conduction band of CdS QD. To monitor this electron transfer process from photo-excited DBF to CdS QD we have carried out emission spectroscopy in the present investigation after exciting DBF molecule. Electron injection dynamics from photo-excited xanthenes dyes (DBF is a xanthene dye) to the conduction band of TiO_2 have been demonstrated by us[33]. Since xanthenes dye molecules are highly luminescent, it is easy to demonstrate electron transfer process by monitoring the luminescence quenching measurements. Figure 3.3 depicts the emission spectra of DBF and DBF-CdS composite after exciting the samples at 500 nm. Trace a in Figure 3.3 shows the emission spectra of DBF which has emission peak at 557 nm with a hump at 584 nm. However in presence of CdS the emission intensity drastically reduces as shown in trace b in Figure 3.3. Again as we have already mention that LUMO (-1.5 V) of DBF lies above the conduction band (-1.3 V vs NHE) of CdS QD (Scheme 3.1), so photo-excited DBF can inject electron into the conduction band of CdS. The emission quenching can be attributed to electron injection from photoexcited DBF to CdS, and can be expressed by the equations below:

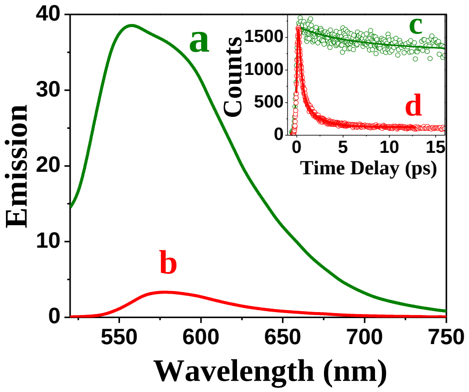

Figure 3.3: Photoluminescence (PL) spectra of DBF (a) in absence and (b) in presence of CdS QD after exciting at 500 nm. Inset: Fluorescence upconversion traces of (c) DBF and (d) CdS-DBF composite after exciting at 435 nm and monitoring at 560 nm. [CdS] = 0.49 μM and [DBF] = 0.3 mM.

$$\mathrm{DBF} + h\nu \rightarrow \mathrm{DBF}^* \tag{3.4}$$

$$\mathrm{DBF}^* + \mathrm{CdS\ QD} \rightarrow \mathrm{DBF}^+ + \mathrm{CdS\ QD}\ (e^-) \tag{3.5}$$

To monitor electron injection dynamics we have carried out fluorescence upconversion measurements for free DBF and also in presence of CdS QD after exciting the samples at 435 nm laser pulse and monitoring at 560 nm and shown in Figure 3.3 inset. We would like to make a point that exciting pure CdS at 435 and monitoring at 560 nm, no emission signal was observed. It is clear from emission decay trace of pure DBF (Figure 3.3c) that emission lifetime of DBF is too long to measured in fluorescence up-conversion technique. So to measure the emission lifetime of DBF we performed nanosecond life time measurements (TCSPC) and determined to be 1.6 ns. Trace d in Figure 3.3 depicts the emission kinetics of DBF in presence of CdS QD which can be fitted bi-exponentially with time constants of $\tau_1 = 618$ fs (85%) and $\tau_2 = 1.8$ ps (15%) with average life time τ_{avg}=800 fs. If we presume that the observed decrease in lifetime arises due to electron injection from photoexcited DBF to CdS QD, then we can determine the electron injection time constant by the following expression.

$$k_{inj} = 1/\tau_{DBF+CdS} - 1/\tau_{DBF} \tag{3.6}$$

By following the above expression electron injection rate can be determined to be $1.2 * 10^{12}$ sec^{-1}. With the help of time-resolved emission technique we have demonstrated both electron injection from photo-excited DBF to CdS QD and also hole transfer from photo-excited CdS QD to DBF molecule.

ii. *CdS QD and BODIPY composite:*

To monitor ground state interaction between CdS QD and the bodipy molecule steady state optical absorption and emission measurements have been carried out. Figure 3.4 shows the UV-vis spectra of pure CdS QD (trace a) and the TG2 in absence (trace b) and in presence of CdS QD (trace c) in chloroform solution. The optical spectrum of the CdS QD shows an excitonic absorption at 460 nm due to 1S ($1S_{3/2}$-$1S_e$) transition. On the other hand TG2 molecule shows a broad absorption (trace b) below 575 nm with a maximum absorption at 516 nm which is due to the electronic transition between HOMO to the LUMO. In presence of CdS QD the optical behaviour of the TG2 molecule(trace c) does not change significantly which clearly indicates very weak ground state interaction exists between TG2 and the CdS QD. Steady state PL spectra of CdS QD (trace a'), TG2 (trace b') and the CdS-TG2 composite (trace c') are shown in Figure 3.4 after exciting the samples at 400 nm. The PL spectrum of CdS QD shows an emission peak at 479 nm due to excitonic band edge luminescence with ~24% emission quantum yield. In contrast to CdS QD, a broad luminescence spectrum of TG2 appears at 550 nm to 750 nm peaking at 640 nm with very low quantum yield ~0.5-1%. It is interesting to see that luminescence a spectrum of TG2 quite broad and highly stokes shifted. The highly red-shifted luminescence cannot be attributed to the emission from singlet state as majority of the singlet state emission of bodipy molecules is the mirror image of absorption spectra with 20-30 nm Stokes shift. [251] The red shifted emission spectra of TG2 can be either due to emission from twisted intra-molecular charge transfer state (TICT) or from the triplet state. The

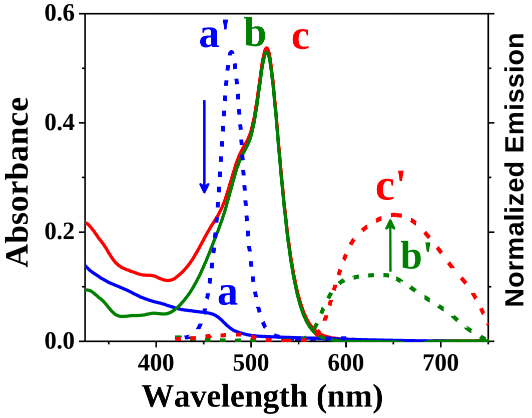

Figure 3.4: Steady state **(A)** optical absorption spectra of (a) CdS QD, (b) TG2 and (c) TG2-CdS QD composite system and (**B**) emission spectra of (a') CdS QD, (b') TG2 and (c') TG2-CdS QD composite system in chloroform. [CdS] = 0.05 μM and [TG2] = 0.1 mM.

emission spectra do not change much with changing the polarity of the solvent. It is widely reported in the literature in low polar solvent (cyclohexane) emission appears only from locally excited (LE) state.[252] Tang and co-workers [253] reported TICT emission from bodipy derivative in chloroform solvent, where blue shifted emission from LE state was observed in low polar hexane solvent. So the TG2 luminescence cannot be attributed to emission from TICT state. Earlier Castellano and co-workers [251] reported luminescence from the triplet state of iodine derivative of BODIPY molecule, which appears in the red region of the spectrum as compared to that singlet state emission band. So the broad emission band of TG2 can be attributed to luminescence from the triplet state of TG2. Now it is interesting to see that the luminescence of the CdS QD is completely quenched in presence of TG2 (Figure 3.4c') and simultaneously TG2 luminescence increases after 400 nm excitation. It is clearly seen in Figure 3.4 that there is significant spectral overlap between emission spectra of CdS QD (Figure 3.4a') and the optical absorption of TG2 (Figure 3.4b). So efficient fluorescence resonance energy transfer (FRET) is expected from excited CdS QD to TG2 molecule. So the quenching of CdS luminescence in presence of TG2 can be assigned mainly due to energy transfer from photo-excited CdS QD to TG2 molecule. The redox energy level of the composite system (Scheme 3.2) shows that both photo-excited electron and hole from CdS QD can be transferred to TG2 as both the processes are thermodynamically viable. Either of the two processes can also be cause for decrement of luminescence intensity of CdS QD. To reveal the real mechanism of luminescence quenching in the CdS-TG2 composite system steady state emission studies have been carried out after changing the size of CdS QD particles. Size dependent PL (Figure 3.5 B) quenching suggests that maximum quenching of CdS luminescence can be observed where there is maximum overlap between the optical absorption spectra of and the emission spectra of CdS

QD (Figure 3.5A). This experimental result clearly suggests that the major process responsible for decreasing luminescence quantum yield of the CdS QD in presence of TG2 is due to non radiative

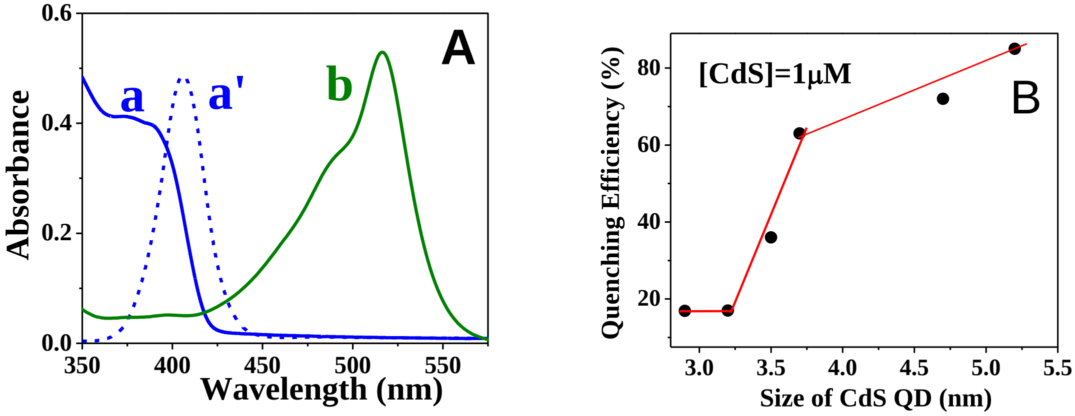

Figure 3.5 : (A) Steady state optical absorption spectra of (a) CdS QD, (b) TG2 and emission spectra of (a') CdS QD. **(B)** Size dependent photo-luminescence quenching of CdS QD in presence of TG2 molecule in chloroform solution. In all the cases concentration of CdS QD and TG2 were kept 1 μM and 0.1 mM respectively.

energy transfer from photo-excited CdS QD to TG2 molecule, not due to electron or hole transfer from the photo-excited CdS QD. The excited CdS QD exchange its energy through non radiative process according to the following equation

$$\text{CdS} + h\nu \longrightarrow \text{CdS}^* \qquad (3.7)$$

$$\text{CdS}^* + \text{TG2} \longrightarrow \text{CdS} + \text{TG2}^* \qquad (3.8)$$

To determine energy transfer rate between CdS QD-TG2 donor-acceptor pair we have carried time-resolved emission studies. Figure 3.6 illustrates the time resolved emission decay traces of CdS QD in absence and in presence of TG2 molecule after exciting at 445 nm and monitoring at 479 nm. The time resolved PL decay trace of CdS QD can be fitted multi-exponentially with decay time constants τ_1 = 0.43 ns (33%), τ_2 = 2.93 ns (21%), τ_3 = 19.06 ns (46%), with τ_{avg} =9.6 ns (Figure 3.6a). The emission decay trace of CdS-TG2 composite also can be fitted multi-exponentially with time constants τ_1 = 0.22 ns (77%), τ_2 = 2.8 ns (15%), τ_3 = 19 ns (8%), with τ_{avg} =2.1 ns (Figure 3.6b). The emission lifetime of CdS QD decreases in presence of TG2 which clearly suggest that non-radiative relaxation channel (energy transfer) is actively involved in the of CdS-TG2 composite system. Now we can determine the energy transfer rate by following the equation below:

$$k_{FRET} = 1/\tau_{CdS\text{-}TG2} - 1/\tau_{CdS} \qquad (3.9)$$

and using our experimental results we found the non-radiative energy transfer rate in the CdS-TG2 donor-acceptor pair is ~ 3.7 X 10^8 s^{-1}.

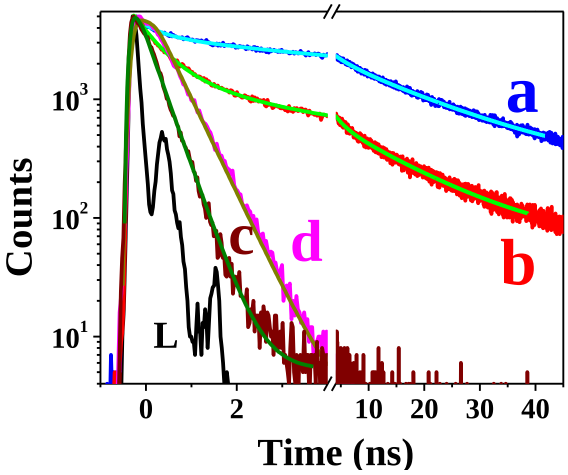

Figure 3.6: Time resolved PL decay traces of CdS QD **(a)** in absence and (b) in presence of TG2 in chloroform after monitoring at 479 nm. Time resolved PL decay traces of TG2 (c) in absence and (d) in presence of CdS QD in chloroform after monitoring the emission at 640 nm. Excitation wavelength was kept at 445 nm in all the above systems.

We have also monitored the change of excited state lifetime of TG2 both in absence and in presence of CdS QD as shown in Figure 3.6. Here we would like to mention that, the excited state life time of the TG2 (Figure 3.6c) is very short (τ_{avg}=0.38 ns) as compared to that of CdS QD. However it is clearly seen in Figure 3.6d that emission life time of TG2 increases (τ_{avg}=0.55 ns) in presence of CdS QD with a growth component. This observation reconfirms that indeed energy transfer takes place from photo-excited CdS to TG2.

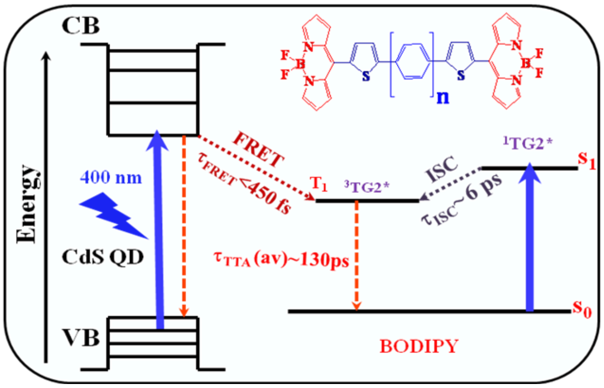

Scheme 3.2: Schematic presentation of non-radiative energy transfer (FRET) from photo-excited CdS QD to triplet state of the BODIPY molecule. ISC and TTA stand for intersystem crossing and triplet-triplet annihilation respectively.

3.2.2. Femtosecond Transient Absorption Study

To corroborate charge (both electron and hole) transfer dynamics/processes in early time scale with more accuracy we have carried out femtosecond transient absorption spectroscopic measurements by exciting pure and composite system at 400 nm laser light.

i. *CdS QD and DBF composite:*

Figure 3.7 shows the transient absorption spectra of photoexcited CdS/DBF QD composite materials in different time delay, which comprises a bleach below 550 nm and two broad absorption bands at 550-750 nm and 750-900 nm respectively. The broad spectral absorption in the 750-900 nm regions can be attributed to the electrons in the conduction band in CdS QD. The transient absorption band at 550-750 nm can be attributed to DBF cation radical. The band having maximum at 650 nm is assigned to DBF cation radical (DBF$^{\cdot+}$). Assignment of this band has been made on the basis of the results obtained in separate pulse radiolysis experiments, where DBF$^{\cdot+}$ was generated selectively by the reaction of N$_3^{\cdot}$ radical with DBF molecule in N$_2$O saturated aqueous solution. We have already demonstrated that at 400 nm photo-excitation both electron injection and hole transfer process can occur in DBF/CdS composite materials. Now to understand the charge transfer dynamics we have monitored the kinetics at 500 nm (bleach wavelength), 650 nm (DBF cation radical) and at 900 nm (electron in QD) and shown in Figure 3.8. The bleach recovery kinetics at 500 nm (trace a in Figure 3.8) can be fitted with time constants of τ_1 = 800 fs (25%), τ_2 = 90 ps (37%) and τ_3 > 400 ps (38%). The transient signal due to cation radical of DBF at 650 nm can be fitted multi-exponentially with a

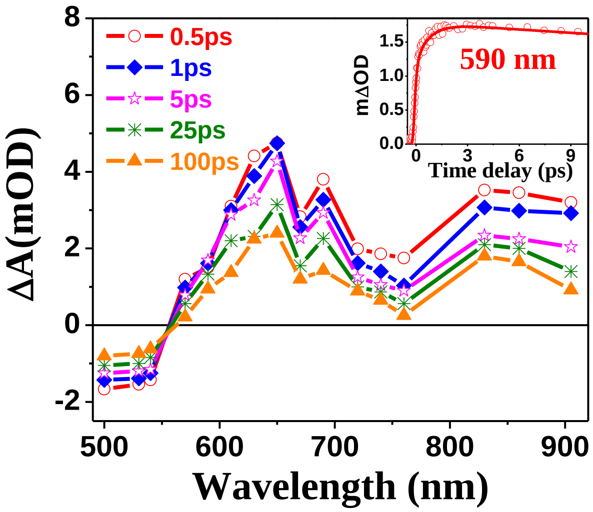

Figure 3.7: Transient absorption spectra of CdS-DBF composite materials in chloroform at different time delay after excitation at 400 nm laser light. Inset: Kinetic decay trace at 590 nm.

growth of ~350 fs and decay components of τ_1 = 15 ps (47%), τ_2 = 90 ps (13%) and τ_3 > 400 ps (40%). Interestingly the transient signal decay due to electron in CdS QD can be fitted multi-exponentially with time constants of τ_1 = 1.2 ps (40%), τ_2 = 15 ps (27%), τ_3 = 90 ps (12%) and τ_4 > 400 ps (21%). Although the transient peak at 650 nm indicates the peak of DBF cation radical, however contribution due to electron at 650 nm cannot be ignored. So to observe the kinetic for cation radical we have also monitored the growth signal at 590 nm which can be fitted bi-exponentially with τ_1 = ~100 fs (61%) and τ_2 = 800 fs (39%) and is shown in the inset of Figure 3.7

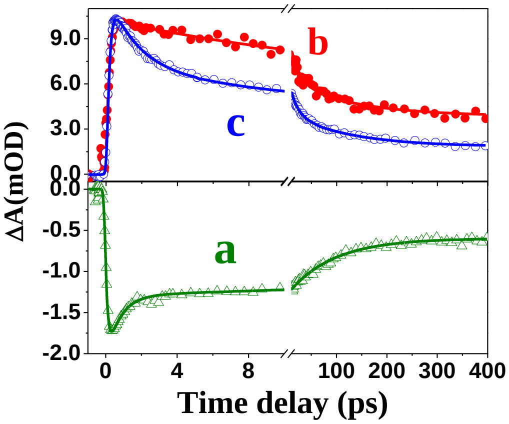

Figure 3.8: Kinetic decay traces at (a) 500 nm (b) 650 nm and (c) 900 nm for CdS-DBF system in chloroform after the samples at 400 nm laser light.

In our previous study [250] we have observed in dye-sensitized TiO_2 nanoparticle systems the growth kinetics for both injected electron and oxidised dye cation radical are similar, which indicate that charge separation take place through one process only i.e. through electron injection from photo-excited state to conduction band of TiO_2. However in the present investigation we have observed that growth and decay kinetics for DBF cation radical at 590 nm is different from that of electron at 900 nm.

Recent investigation on quantum dot solar cell suggests removal of charges (holes and electrons) from photo-excited quantum dots can be key factor to improve the conversion efficiency. In CdS-DBF composite materials it is clear from Scheme 3.1 that DBF can extract the photo-excited hole from CdS QD (path 1, Scheme 3.1). In addition to that photo-excited DBF can inject electron to the conduction band of CdS (path 2, Scheme 3.1) suggesting CdS-DBF is a typical type II system of QD-molecular system. Over and above the formation of type II system, from steady state optical absorption measurements (Figure 3.1) it is clear that CdS QD and DBF form strong CT complex with very high molecular extinction co-efficient, which has absorption band in the red region of the solar radiation as compared to both CdS QD and DBF molecule, as a result the absorption cross-section of CdS-DBF composite system towards solar radiation increase dramatically. Excitation of CT CdS-DBF complex electron from HOMO of DBF can move directly to the conduction band of CdS (path 3, Scheme 3.1) which ensure much higher charge separation as compared to both hole transfer from CdS to DBF and also electron injection from photoexcited DBF to the CB of CdS. We have demonstrated that blue part, green part and red part of the solar radiation will be absorbed by CdS QD, DBF and CdS-DBF CT complex respectively as shown in Scheme 3.1. Now it’s very important unravel the charge transfer dynamics in the CdS-DBF composite system as excited by 400 nm femtosecond laser pulse. We have already mentioned that absorption cross-section of pure DBF is very poor however both CdS QD and CdS-DBF complex can absorb 400 nm light quite effectively. We have observed growth kinetics for DBF cation radical at 590 nm can be fitted bi-exponentially with time constants ~100 fs (61%) and 800 fs (39%). The fast growth component (<100 fs) can be attributed to direct electron transfer on excitation of CT complex (path 3, Scheme 3.1), on the other hand 800 fs component can be attributed to photoexcited hole transfer from VB of CdS to

DBF (path 1, Scheme 3.1). To the best of our knowledge this is one of the first report on hole transfer dynamics in ultrafast time scale in super-sensitized quantum dot solar cell. It is interesting to see that unlike the slower and bi-exponential appearance time for DBF cation we have observed single exponential and pulse-width limited (<100 fs) appearance time for electron in CdS. Excitation of CdS and direct excitation of CdS-DBF complex populates electron in the CB of CdS. As a result we have observed pulse-width limited growth time for the appearance of electron signal. Now let us discuss on charge recombination dynamics in CdS-DBF composite materials. To monitor charge recombination dynamics one can either monitor the bleach recovery kinetics at 500 nm or transient decay kinetics at 650nm for DBF cation radical or at 900 nm for electron in CdS QD. However it is interesting to see that dynamics are quite different, where it expected that the dynamics should be similar as it demonstrates same charge recombination reaction. Comparing the dynamics of 650 nm and 900 nm it is seen that an extra fast component

Table 3.1: Life Times of the Transients for CdS/DBF composite system at Different Wavelengths (λ, nm)

λ (nm)	τ_{growth}	τ_1 (%)	τ_2 (%)	τ_3 (%)	τ_4 (%)
500	<100fs	800fs (25%)	90 ps (37%)	>400ps (38%)	
650	<350fs	15ps (47%)	90ps (13%)	>400ps (40%)	
905	<150fs	1.2 ps (40%)	15ps (27%)	90ps (12%)	>400ps (21%)

(1.2 ps) exist at 900 nm (Table 3.1). This extra fast component can be attributed to trapping dynamics of electron CdS QD, where some surface state exist in QD material. On the other hand at bleach recovery kinetics at 500 nm we have observed a 800 fs fast bleach recovery components which might be due to hole transfer process as at this wavelength there is a good overlap for both ground state bleach and DBF cation radical. So the kinetics at 650 nm can be attributed to charge recombination dynamics. This is a direct correlation of transient absorption and luminescence data and photoaction spectra which describes higher charge separation through super-sensitization. CdS-DBF composite not only effectively removes the hole from quantum dot it can also absorbs more solar radiation due to formation of charge transfer complex which has very high molar extinction coefficient. Considering the fact that QDSC photoaction is exclusive outcome of kinetic competitions of electron injection, hole transfer, back electron transfer and dye-regeneration processes, this super-sensitization scheme can bring significant improvement in QDSC without much changing the devise fabrication.

***ii.** CdS QD and BODIPY composite:*

The TA spectra at 0.5 ps to 100 ps time delay of TG2 and CdS-TG2 composite systems are depicted in Figure 3.9. Transient spectra at early time scale shows transient bleach below 650

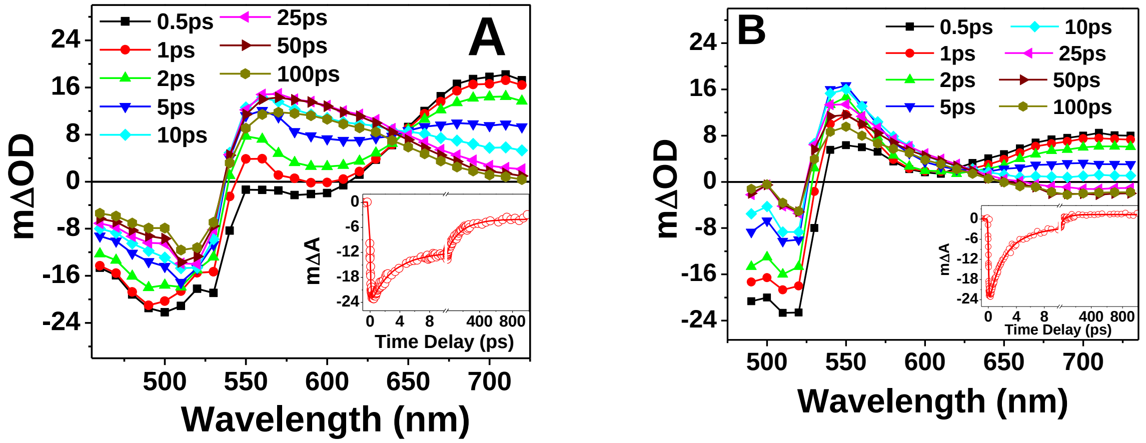

Figure 3.9: Ultrafast transient absorption spectra of **(A)** TG2 and **(B)** CdS QD-TG2 at different time delay after exciting at 400 nm laser pulse and probing at visible region. **Inset:** Transient bleach recovery kinetics of **(A)** TG2 and **(B)** TG2/CdS probed at 500 nm.

nm and positive absorption band above 650 nm peaking at 700 nm. The negative absorption band in the TA spectrum can be attributed to the bleach due to ground state depletion of TG2. Interestingly the bleach spectrum exactly matches with the steady state UV-Vis spectra of TG2 (Figure 3.4). Bleach recovery kinetics at 500 nm is shown in the inset of Figure 3.9A. The kinetics can be fitted multi-exponentially with time constants of τ_1= 3ps (47%), τ_2 = 20ps (15.6%) τ_3 =150ps (19.6%) and τ_4 = >1 ns (17.8%) (Table 3.2). Interestingly with the evolution of time a new transient band appears at ~ 550 nm with the decrement of 700 nm band with an isobestic point at 645 nm. The transient band at 700 nm can be attributed to the excited singlet

state of TG2. The absorption band at 537-645 nm peaking at 550 nm can be attributed to triplet state which is formed via intersystem crossing (ISC) from singlet excited state.[254] The decay kinetics at 700 nm can be fitted bi-exponentially with time constants τ_1 = 6 ps (90%), and τ_2 = 30ps (10%). On the other hand the kinetics at 550 nm can be fitted multi-exponentially with

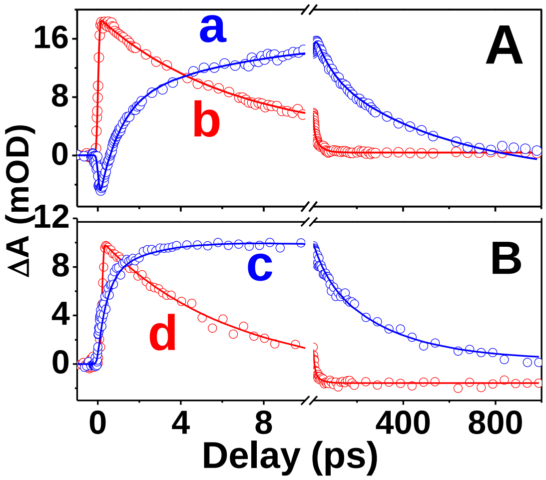

Figure 3.10: (A) Normalized transient absorption kinetics at (a) 550 nm and (b) 700 nm for TG2 in chloroform. **(B)** Normalized transient absorption kinetics at (c) 550 nm and (d) 700 nm) for TG2/CDS QD composite system in chloroform.

growth time constants of τ_1 = 0.5ps (43%), τ_2 = 8.5ps (80%) and decay time constants of τ_3 = 60ps (-56%) and τ_4 = 300ps (-44%) (Table 3.2). Due to overlap of different transients like triplet state and bleach at 550 nm, inter-system crossing (ISC) rate from the growth of triplet state cannot be determined correctly. So to find out ISC rate excited singlet state decay at 700 nm (Figure 3.10b) has been monitored. The 6 ps decay component at 700 nm can be attributed to ISC rate from excited singlet to triplet state of TG2. Finally the triplet state at 550 nm decay bi-exponentially with time constants of 60 ps and 300 ps, which can be attributed to triplet-triplet annihilation time.

Now to understand the excited state interaction between CdS QD and TG2 in ultrafast time scale transient absorption spectroscopy has been carried out in CdS/TG2 system in chloroform exciting at 400 nm and shown in Figure 3.9B. It is interesting to see that the transient spectra of the CdS/TG2 is different as compared to pure TG2 (Figure 3.9A). Figure 3.9B shows two transient absorption bands peaking at 550 nm and 700 nm in addition to the bleach due to ground state absorption below 525 nm. The transient band at 550 nm and 700 nm can be attributed to excited triplet and singlet states respectively. Unlike TG2 transient absorption at 550 nm appears at the end of the laser pulse in CdS/TG2 system. Intensity of triplet state at 550 nm is higher as compared to excited singlet state at 700 nm in CdS/TG2 system. This observation clearly suggests that generation of triplet states of TG2 is not only through intersystem crossing from excited singlet states of TG2 but also through direct sensitization by photoexcited CdS QD. Now to unravel the mechanism of excited state interaction in ultrafast time scale in CdS/TG2 system kinetics at different wavelengths have been monitored. The bleach recovery kinetics at 500 nm can be fitted multi-exponentially with time constant τ_1= 1.8ps (85%), τ_2 = 10ps

(15%), τ_3= 70ps (5.4%) and τ_4> 1 ns (5.4%) (Table 3.2). The bleach recovery is much faster in CdS/TG2 system as compared to that of TG2.

In addition to that in longer time scale unlike TG2 system the bleach recovers completely by 40 ps with appearance of positive signal. The faster bleach recovery and positive signal is due to ultrafast generation of triplet state of TG2 in CdS/TG2 system which has contribution at 500 nm. The kinetics at 700 nm can be fitted with pulse-width limited growth (< 100 fs) and bi-exponential decay with time constants with τ_1= 5ps (95%) and τ_2 = 25ps (5%). It has been observed that the kinetic decay trace at 500 nm for TG2 has little negative absorption (due to ground state bleach) at early time scale and with progression of time it becomes positive due to formation of triplet state through intersystem crossing from singlet to triplet state. However the kinetics at 550 nm for CdS/TG2 system look quite different (Figure 3.10c) which can be fitted with bi-exponential growth with time constants of 450 fs (98%) and 2.5 ps (2%) with bi-exponential decay with time constants of τ_1= 60 ps (-63%) and τ_2 = 300 ps (-37%). Most

Table 3.2: Exponential fitting parameters of TG2 and CdS-TG2 at different wavelengths after exciting the samples at 400 nm laser pulses. The percentage at the parenthesis represents amplitude of the corresponding exponential functions.

Systems	λ (nm)	τ_{rising}	τ_1	τ_2	τ_3	τ_4
TG2	500	<100fs (-100%)	3ps (47%)	20ps (15.6%)	150ps(19.6%)	>1 ns (17.8%)
TG2	550	<100fs (-23%)	0.5ps(43%)	8.5ps (80%)	60ps (-56%)	300ps (-44%)
TG2	700	<100fs	6ps (90%)	30 (10%)		
TG2-CdS	500	<100fs (-110.8%)	1.8ps(85%)	10ps (15%)	70ps (5.4%)	>1ns (5.4%)
TG2-CdS	550	450 fs (98%)	2.5ps(2%)	60ps (-63%)	300ps (-37%)	
TG2-CdS	700	<100fs	5ps (95%)	25 (5%)		

fascinating part of this investigation is that in case of CdS/TG2 system majority of the triplet state grow with time constant of 450 fs. We have already observed in pure TG2 system that the triplet formation time constant from excited singlet is ~ 6 ps. So in CdS/TG2 system 450 fs time constant can be attributed to formation triplet state induced by non-radiative energy transfer from excited CdS QD. Surprisingly the bi-exponential decay constants (60 ps, 300 ps) at 550 nm exactly match with that of pure TG2 system. The efficiency of the energy transfer interaction and the nature of exciton quenching of the CdS QD in presence of the BODIPY molecule are demonstrated in the next section.

3.2.3. Energy Transfer Mechanism and Efficiency in CdS QD-BODIPY Systems:

From the above experimental measurements it is obvious that de-excitation of photo-excited CdS QD take place mainly due to transfer of excited energy of the CdS QD to the nearby BODIPY molecule via long range dipole-dipole interaction. The energy transfer rate between a donor-acceptor pair separated by a distance "r" can be expressed as [174]

$$k_T(r) = \frac{Q_D \kappa^2}{\tau_D r^6}\left(\frac{9000(\ln 10)}{128\pi^5 N_A \eta^4}\right) J(\lambda)d\lambda \tag{3.10}$$

Where, Q_D and τ_D are the quantum yield and radiative life time of the donor in the absence of acceptor molecule, N_A is Avogadro's number, η is the reflective index of the solvent and $J(\lambda)$ is the overlap integral between donor luminescence and acceptor absorbance. The energy transfer efficiency is usually measured using the relative fluorescence intensity of the donor, in absence and presence of the acceptor, and thus energy transfer efficiency, E, can be easily calculated by using the following expression [174]

$$E = 1 - \frac{F_{DA}}{F_D} \tag{3.11}$$

From the overlap integral (*J(λ)*) of the CdS QD emission and TG2 absorption (Figure 3.4) we have calculated the Förster distance (R_0) which was found to be 27 Å. Using the equation 3.11 we have measured the energy transfer efficiency. Figure 3.11A shows decreasing sigmoidal pattern of energy transfer efficiency with increasing interaction distance. The energy transfer efficiency was determined to be 0.5 at Förster distance. The sigmoid behaviour of the energy transfer efficiency (Figure 3.11 A) and non linear Stern-Volmer plots (Figure 3.11 B) suggest that quenching of CdS luminescence is distance dependent and CdS QD emission quenching in presence of TG2 is dynamic in nature. Femtosecond transient absorption studies it is clear that photo-excited CdS QD transfer its energy directly to the triplet state TG2 and the energy transfer mechanism is demonstrated in Scheme 3.2. It is clearly seen in Scheme 3.2 that in case CdS/TG2 system on photo-excitation by 400 nm both CdS QD and TG2 get excited where direct excitation of TG2 generated excited singlet state with pulse-width limited time, which eventually converted to triplet state in ~ 6 ps time. On the other hand photo-excited CdS QD transfer its energy to TG2

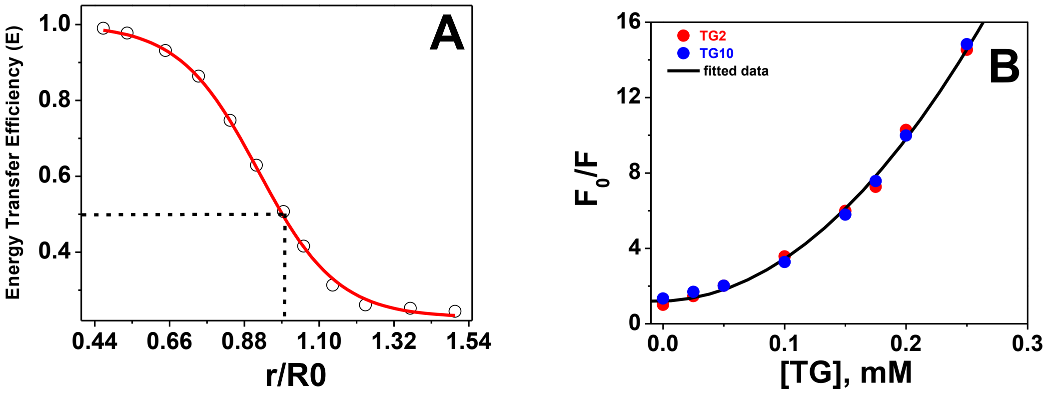

Figure 3.11: (A) Distance dependent energy transfer efficiency (E) plot of CdS QD-TG2 pair, where "r" and "R_0" are the distance between CdS QD and TG2 and Förster distance respectively. **(B)** Stern-Volmer plots for the quenching of CdS PL in presence of different BODIPY (TG2 and TG10) concentration in chloroform solution.

with time scale in < 450 fs. However triplet-triplet annihilation of TG2 takes place with average time scale of ~ 130 ps in both absence and presence of CdS QD (Scheme 3.2).

3.2.4. Photovoltaic Performance of CdS/DBF Supersensitized System

Steady state and time-resolved spectroscopic analysis suggest that CdS-DBF composite can be used as a great sensitizer in QDSC. The photo-electrochemical performance of mesoscopic TiO_2 films modified with CdS, DBF, and CdS/DBF was monitored under similar illumination condition of AM 1.5 irradiation ($100mWcm^{-2}$) using I^-/I_3^- redox couple, where Pt-coated FTO is used as counter electrode. The electrolyte composition: 0.6 M 1,2 dimethyl 3-propyl imidazolium, iodide, 0.1 M LiI, 0.05 M I_2, and 0.5 M, 4-tert-butylpyridine in acetonitrile is used. It is noteworthy that Figure 3.12 purely shows a comparison of solar cells based on CdS QD, DBF dye and CdS/DBF composite and actual photocurrent action spectra can be improved

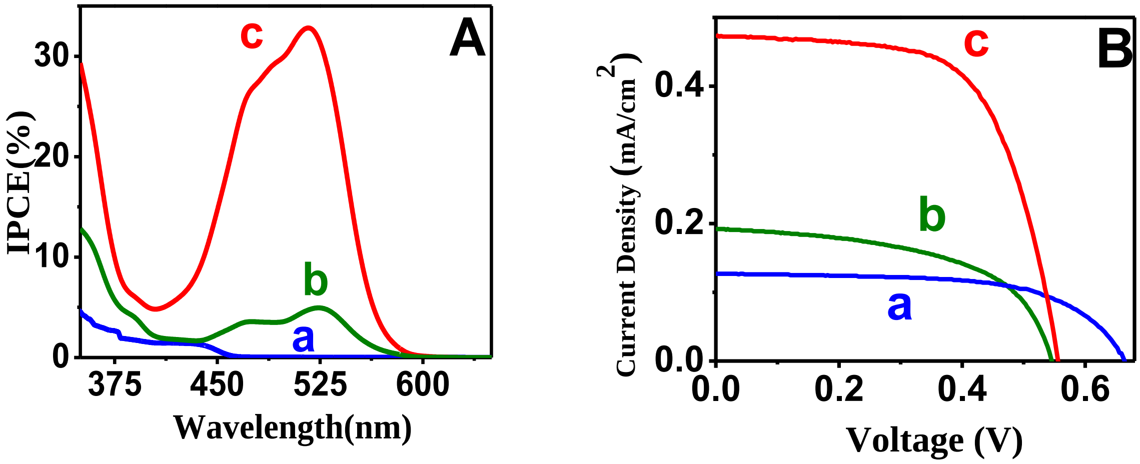

Figure 3.12: Photovoltaic performance of DBF-CdS super-sensitizer in terms of **(A)** IPCE *vs.* wavelength and **(B)** Current density (J) as a function of Voltage (V) for (a) CdS QD, (b) DBF molecule, and (c) CdS-DBF composite.

further by optimized fabrication of QDSC. The Incident photon-to current conversion efficiencies (IPCE) *vs.* wavelength and Current density (J) as a function of Voltage (V) spectra of CdS, DBF and CdS_DBF composite system are plotted in the Figure 3.12 A and B, respectively. The efficiency of the measured photo cell is summarized in the Table 3.3. It is interestingly to see that impressive to see dramatic improvement of photovoltaic response for the CdS-DBF composite on TiO_2 photo anode, which represents the high efficiency of super-sensitization in stabilizing interfacial charge separation of QDSC. This is a direct correlation of transient absorption and maximum IPCE observed for TiO_2/CdS/DBF electrode which is much higher as compared to both TiO_2/CdS electrode and TiO_2/ DBF electrode, confirming efficient hole transfer from CdS QD to DBF molecule and also super sensitization through CdS-DBF charge transfer complex (Scheme 3.3). Multiple directional charge separation in the CdS_DBF are depicted in the Scheme

Table 3.3: QDSC performance in terms of IPCE and IV of CdS QD, DBF and CdS_DBF.

Systems	Voc(V)	I_{sc}(mA)	FF(%)	Efficiency(η,%)
DBF	0.54	0.19	54	**0.23**
CdS	0.66	0.12	62	**0.43**
CdS_DBF	0.56	0.47	64	**1.1**

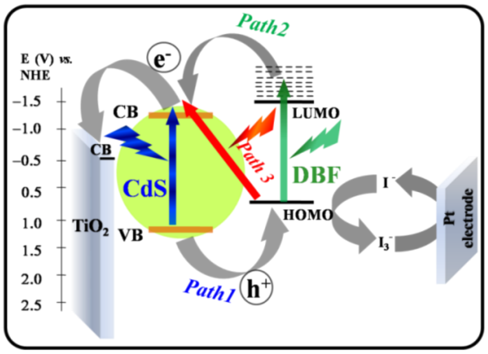

Scheme 3.3: Schematic presentation of CdS_DBF supersensitized QDSC.

3.3 are responsible for higher photovoltaic performance. This synergy between the CdS and the dye in facilitating higher photocurrent generation indicates an additional role of the dye in shuttling holes across the CdS/dye electrolyte interface. With this proposition, it becomes quite luminescence data and photoaction spectra which describe higher charge separation through super-sensitization. CdS_DBF composite not only effectively removes the hole from quantum dot it can also absorbs more solar radiation due to formation of CT complex which has very high molar extinction coefficient. Considering the fact that QDSC photoaction is exclusive outcome of kinetic competitions of electron injection, hole transfer, back electron transfer and dye-regeneration processes, this super-sensitization scheme can bring significant improvement in QDSC without much changing the devise fabrication.

3.3. Conclusion:

In conclusion ultrafast hole and electron transfer dynamics in CdS_DBF composite are explored and verified as a super-sensitizer in QDSC. Optical absorption studies indicate CdS QD and DBF form strong charge transfer complex in the ground state. Steady state and time-resolved absorption and emission studies confirmed that on photo-excitation charge separation in CdS-DBF composite take place in three different pathways: through hole transfer from photo-excited CdS QD to DBF (path1), electron injection from photo-excited DBF to CdS QD (path 2) and finally direct electron transfer from ground state (HOMO) DBF to CB of QD (path 3) (photo-excitation of CT complex). As a result, charge separation takes place in CdS-DBF composite, which confirms the usefulness as a super-sensitizer in QDSC. On the other hand the non radiative energy transfer processes between CdS_BODIPY composite systems have been demonstrated. Femtosecond TA studies reveal that on photo excitation of BODIPY molecules excited singlet are formed with pulse-width limited time, which eventually convert to the excited triplet state through intersystem crossing with ~ 6 ps time. Both PL spectroscopy and ultrafast TA studies suggest photo-excited CdS QD directly transfer its energy to the triplet state of BODIPY molecules with time scale of <450 fs. Efficient energy transfer from CdS QD to BODIPY molecules will facilitate overall efficient charge separation for the broader spectral region of solar radiation.

CHAPTER-4

Multiple Charge Transfer Dynamics in Colloidal $CsPbBr_3$ Quantum Dots and Organic Molecule

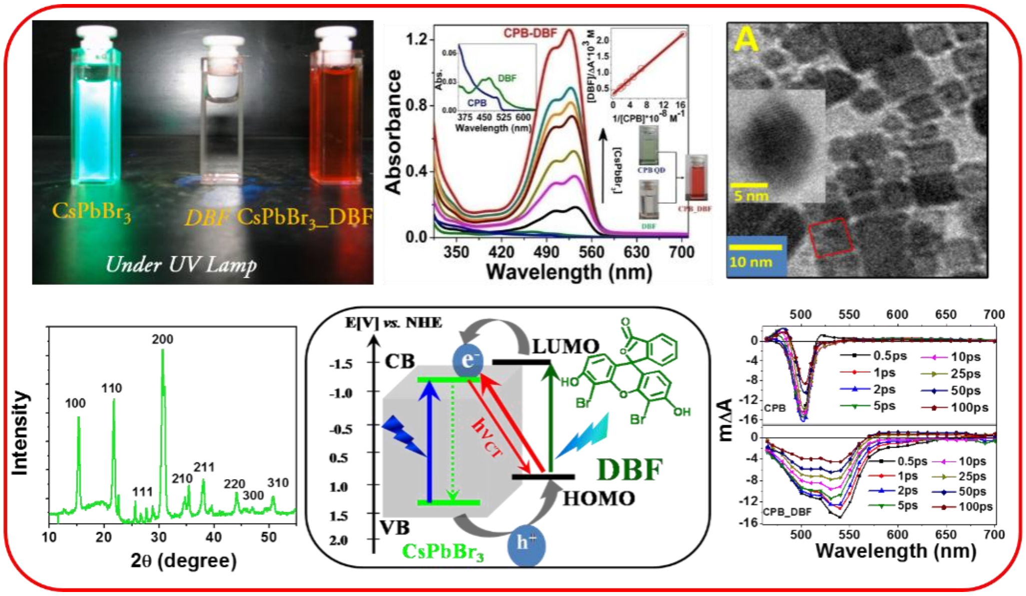

➢ ***J. Phys. Chem. C*, 2016, *120* (Accepted)**

4.1. Introduction:

Semiconductor NCs QDs are rigorously studied for the next generation optoelectronic materials in various applications.[255-257] Mostly, the synthesis, tunable size, optical and photophysical properties of the II-IV semiconductor especially the metal chalcogenied in terms of binary and multinary nanocrystal, heterostructures are well established. [15, 110] Apart from this II-VI metal chalcogenied semiconductor nanocrystals (NCs), organic inorganic lead halide based semiconductor materials ($MPbX_3$: M= CH_3NH_3, HC $(NH_3)_2$ Cs; X= Cl, Br, I) which are isostructral with $CaTiO_3$ Perovskite has been extensively studied due to their excellent performance in the low cost third generation solar cell. [208, 258-261] Although the organic inorganic lead based perovskite provides >20% photocurrent conversion efficiency yet the thermal stability of these solar cell is a matter of major concern. To improve the thermal stability, a new class of completely inorganic based caesium lead trihalide perovskite material has been incorporated in perovskite solar cell by Kulbak *et al.* [262] which shows stable ~6.6% solar efficiency. Interestingly over a long period of time $CsPbBr_3$ (CPB) solar cell show much higher stability as compared to organic-inorganic $CH_3NH_3PbBr_3$ solar cell. The bright and novel optoelectric properties with wide color gamut of these caesium lead trihalide ($CsPbX_3$: X= Cl, Br, I) based colloidal perovskite QDs was first reported by Kovalenko *et al.*[203]. In addition to the thermal stability the synthesized lead based metal halide perovskite ($CsPbX_3$) colloidal QDs are found to have higher order absorption cross-section, narrow photoluminescence (PL) band width, tunable PL behaviour and high emission quantum yield (~90%).[203, 263-267] With these exciting properties, the lead based caesium trihalide semiconductor NCs ($CsPbX_3$) have also been concomitantly started in research for several applications such as light-emitting diodes, photovoltaic, bio-imaging, lasers etc.[263, 268-273]

Moreover, various synthesis protocol, different shape dependent quantum confinement effect, the composition dependent optical properties, doping, charge carrier dynamics of the different $MPbX_3$ NC has also been discussed.[266, 274-281] The $MPbX_3$ perovskite materials are mainly characterized in thin films, [282] different forms such as nanosheets, [278, 283] nanowires, [276] single crystals [284] as well as colloidal QDs [269, 277, 285] have also been reported. In addition to the photovoltaic, [275, 286, 287] the perovskites materials ($CH_3NH_3PbX_3$) have been concomitantly studied in the various research arena such as photoditector, [284] LED,[259] lasing [288] etc. due to their huge absorption coefficient,[208] optical tunabilities [277, 289], very fast charge carrier mobility[290], long charge carrier diffusion length.[290-293] In the semiconductor QDs based photovoltaic cell the details mechanism of the charge carrier (e-h) movement is also well established [147]. In the conventional solar cell the photo-excited electron is injected to the CB of the mesoscopic TiO_2 while the photo generated hole is captured by the electrolyte from the photo anode [147]. But in the perovskite solar cell the efficiency of the working cell mainly depends on the extraction rate of the photo generated hole not the photo generated electron. Earlier Lee *et al.*[258] have demonstrated the efficiency and carrier mobility of the meso-superstructured organometal halide perovskites using n-type TiO_2 semiconductor and insulator Al_2O_3. They have shown better V_{OC} and tenfold faster charge collection efficiency in Al_2O_3 based device as compared to n-type TiO_2 based devise. It is very clear that to revolutionize the photovoltaic performance, the photo-generated hole has to be removed very fast before it corrode the photo anode. The most commonly used hole transporting agent in perovskite solar cell is 2,2',7,7'-tetrakis N,N-di-p-methoxyphenylamine)- 9,9'-spirobifluorene (spiro-MeOTAD).[294] Apart from this, conducting polymers, [286, 289] pyrene arylamine derivatives, [295] copper iodide (CuI) [296], copper thiocyanate (CuSCN) [297] are also used as hole transporting materials in perovskite solar cell. Thus, finding a suitable hole transporting agent is a challenging task. The hole transfer process can be enhanced by introducing an organic accepting molecule along with the perovskite semiconductor. In addition to that one of main factor for lower efficiency (~6.6%) of $CsPbBr_3$ (CPB) solar cell is mainly due to limited absorption of solar radiation (absorbs below 520 nm) of the CPB materials.[203] Both the problems can be tacked efficiently by introducing concept of super-sensitization [224, 298] where the QD and molecular adsorbate can exchange charge carriers. Here the molecular adsorbate shows dual role like photosensitizing the QD material as well as a hole-transporting material. As a result QD-molecular adsorbate composite materials absorb more solar light and also give better charge separation.

In this chapter we have demonstrated the charge transfer dynamics between newly synthesized highly luminescent colloidal CPB perovskite QDs and a molecular adsorbate (di-bromo fluorescene, DBF) using steady state and time-resolved absorption and emission techniques in both fast and ultrafast time scale. The characterization of the CPB QDs was carried out through steady state optical absorption and emission spectroscopy as well as X-ray diffraction (XRD) and high resolution TEM (HRTEM) studies. Redox energy levels of the CPB QD and DBF molecule imply that the VB of CPB lies below the HOMO level of DBF, which allows transfer of photo-excited hole from CPB QD to DBF. To our surprise we have observed that the CBP QDs form strong charge transfer (CT) complex with DBF molecules which absorb in the red region of the solar spectrum. It also suggests upon photo-excitation of CT complex direct electron transfer from the DBF to CPB QD is feasible. Hole transfer from the CPB QDs to the DBF molecule was confirmed after following the decrement of CPB luminescence in presence of DBF after selective photo-excitation. In addition to that a new red shifted luminescence band was observed in the steady state PL studies after exciting the CT complex which has been assigned as CT luminescence ($h\nu_{CT}$) of the CPB QDs-DBF complex. Multiple charge transfer and charge recombination dynamics in ultrafast time scale in the CPB QDs-DBF composite system was demonstrated through femtosecond pump-probe spectroscopy after exciting the samples at 400 nm laser light and detecting the transients in the visible region.

4.2. Results and Discussion:

4.2.1 Morphology Analysis:

The morphology of the synthesized perovskite QD has been analyzed through HRTEM and XRD results. The HRTEM images of the CB QDs are depicting at Figure 4.1A. The average size of the cubic shaped CPB QDs are measured to be 7.35 ± 1.3 and 6.8 ± 1.2 nm (for long and short edges respectively) which is comparable and slightly smaller than the measured exciton Bohr diameter (~7.0 nm) [203]. Figure 4.1 B depicts the XRD spectrum of the purified perovskite CPB QDs. The XRD pattern matches with crystalline cubic phases of the CPB QDs which has three major peaks (2θ) at ~15, 21.69 and 30.5° for [100], [110] and [200] planes respectively. The CPB particles were also characterised by steady state optical absorption and emission spectroscopy. First excitonic absorption and PL peaks of CPB QDs were found to be 502 nm and 508 nm respectively (Figure 4.2 and Figure 4.3). It is interesting to see that these CPB QDs show very narrow (~ 83meV) FWHM (full width at half maxima) in their photoluminescence spectra and very high emission quantum yield. Redox energy levels of both CB and VB were found to be -1.24 and 1.26 eV with respect to NHE respectively as determined through cyclic voltametric measurements. Although the particle sizes of the CPB QDs in the present investigation are slightly larger (7.4 nm) as compared to exciton Bohr diameter (7 nm) [203] still exceedingly high emission quantum yield of photoluminescence and narrow emission band width with respect to the II-IV semiconductor QDs was observed, which can be attributed due to less difference in the effective masses of the charge carriers ($m_h/m_e\sim$ 0.93).[203, 265] Recently Nag and co-workers [263] have also reported higher emission quantum yield for 11 nm $CsPbBr_3$ QDs which show very good size distribution with temperature and wavelength independent emission lifetime. These properties ensure perfect candidate for solar cell application and light emitting devices.

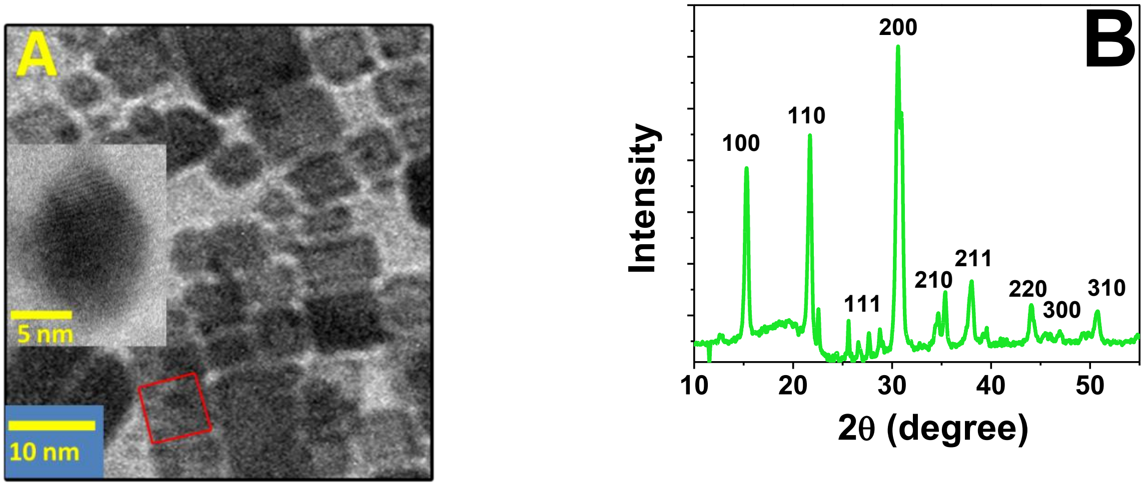

Figure 4.1: **(A)** HRTEM image and **(B)** powder X-ray diffraction (XRD) pattern of purified CPB perovskite QDs. The XRD spectrum shows the cubic crystal structure, in accordance with the HRTEM images.

4.2.2. Charge Transfer Complex: Steady state optical absorption

Main aim of the present investigation is to use these CPB QDs more effectively in solar cell to increase the solar efficiency with help of suitable molecular adsorbate. Recently Hodes and Cahen [262] reported extremely high stability of $CsPbBr_3$ solar cell as compared to that organic-inorganic analogue ($CH_3NH_3PbBr_3$) with much lower efficiency (~6%) as compared to the historical value of above 20 % for $CH_3NH_3PbBr_3$. By increasing molecular absorvity on CPB with the help of molecular adsorbate where CPB and molecular adsorbate form CT complex can be one of the modus operandi to increase the efficiency of the solar cell. Enhancement of light absorption through formation CT complexes in semiconductor quantum dots and molecular adsorbate are not widely reported except few reports from our group.[298, 299] In the present investigation DBF has been used as molecular adsorbate. In this regard we have carried out the optical absorption study after sensitizing the CPB QDs with the DBF molecule. Figure4.2 shows the steady state optical absorption spectra of the dye molecule after sensitizing with different concentrations of the colloidal CPB QDs in toluene solution. Trace a in Figure 4.2 illustrates the optical absorption spectrum of the purified CPB QD, which shows the lowest excitonic

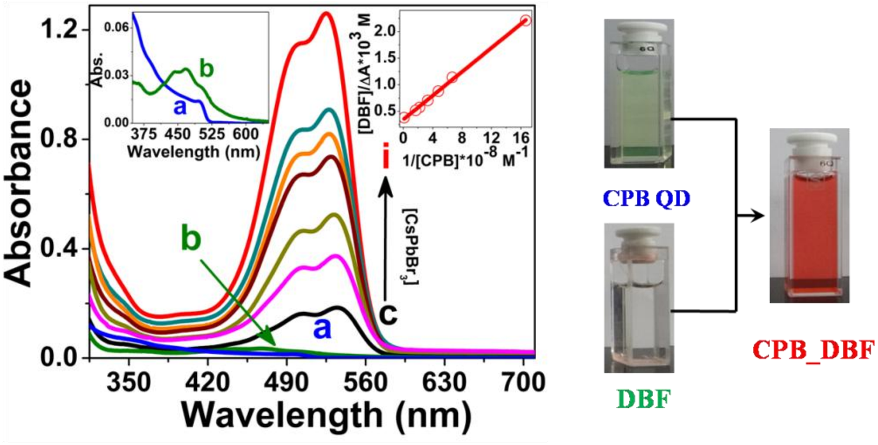

Figure 4.2: **(Left Panel)** UV-Vis. optical absorption spectra of (a) CPB QDs, (b) DBF, and (c-i) CPB QDs-DBF with increasing concentration of CPB QDs (0.01 μM, 0.025 μM, 0.04μM, 0.05μM, 0.06μM, 0.075μM and 0.1μM) in toluene solution. **Left Inset**: Zoomed out optical absorption of maximum concentration of CPB QDs (0.1μM) and DBF (0.45 mM). **Right Inset**: BH plot of the CPB-DBF CT complex. **(Right Panel)** photograph of pure CPB QDs, DBF and their complex at daylight. [DBF]=0.45 mM

absorption at 502 nm, and the corresponding band gap can be calculated from the extrapolation of the absorption spectra and is found to be ~2.5 eV. The pure DBF molecule shows weak optical absorption band up to 580 nm with an absorption peak at 469 in toluene solution, as depicted in trace b in Figure 4.2. To understand the CT interaction between CPB and DBF, steady state optical absorption studies of DBF have been carried out with increasing concentration of CPB QDs. The optical absorption spectra of the CPB/DBF mixtures become broad and shifted to the red region of the spectra with increased intensity. It is clearly seen that absorption spectra of the mixture is completely different with respect to both pure CPB QDs as well as pure DBF. It is worth to mention that the color of the pure DBF and CPB QDs are light orange and bright fluorescent green respectively but the CPB QD-DBF mixture form strong red color which clearly indicates the formation of CT complex. Formation of this complex can be attributed to partial transfer of charge from the HOMO of the DBF molecule to the CB of the CPB QDs even in the ground state. Indeed it is very much clear from the above observation that the CPB QD and DBF form very strong CT complex in the ground state which help to absorb more solar radiation as well as prompt to separate the charge carriers. Details of the charge transfer processes are demonstrated in the later portions of the manuscript. Now, to calculate the equilibrium constant and the molar extinction coefficient of the CT complex we have drawn the Benesi−Hilderband (BH) plot for the composite system and are plotted in the inset (right side) of Figure 4.2. The calculated extinction coefficient and the association constant of the complex are found to be 2.8×10^3 M^{-1} cm^{-1} and 3×10^8 M^{-1} respectively.

4.2.3. Photoluminescence Study:

To monitor the charge separation processes we have performed the steady state and time resolved PL measurements after selective excitation of both CPB QDs and the DBF. The PL spectra of the CPB QD show the emission peak at 508 nm after excitation at 450 nm in toluene and shown in Figure 4.3a. The emission quantum yield of CPB determined to be extremely high (φ_{CPB} = ~0.9). Interestingly, the emission intensity of the CPB QDs is completely diminished in presence of DBF molecule which depicts in the Figure 4.3 trace b. The redox energy levels of the CPB QDs and DBF suggest that the VB of the CPB QDs lies energetically higher than the HOMO of the DBF molecule (Scheme 4.1). Thus on photoexcitation the photo-excited hole can be captured by the DBF molecule from the CPB QDs,

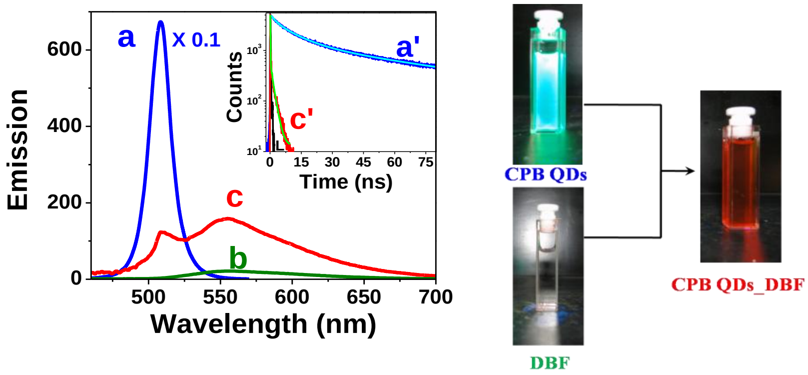

Figure 4.3: (**Left Panel**) Steady state PL spectra of (a) pure CPB QDs, (b) pure DBF and (c) CPB QDs-DBF in toluene after 440 nm excitation. **Inset:** Time resolved PL decay traces spectra of (a') CPB QDs and (c') CPB-DBF complex monitor at 508 nm after 445 nm laser excitation. "L" stands for excitation laser profile. (**Right Panel**) Photograph of CPB QDs, DBF and their CT complex under UV lamp.

as the hole transfer process is thermodynamically feasible. The above mentioned hole transfer process can be expressed by the following equations (1) and (2);

$$\textbf{CPB QDs} + h\nu \rightarrow \textbf{CPB QDs}\ (e^- + h^+) \qquad (4.1)$$

$$\textbf{CPB QDs}\ (e^- + h^+) + \textbf{DBF} \rightarrow \textbf{CPB QDs}\ (e^-) + \textbf{DBF}\ (h^+) \qquad (4.2)$$

Moreover, the hole transfer process has been reconfirmed by monitoring the time resolved PL decay traces after exciting the samples at 445 nm laser radiation and monitoring at 508 nm. Figure 4.3 inset trace a' shows the time resolved PL decay of the CPB QD at 508 nm which can be fitted with multi-exponentially with time constants τ_1 = 2.26 ns (27%), τ_2 = 10.8 ns (51%), and τ_3 = 37 ns (22%) with τ_{avg} = 14.2 ns. Interestingly, the faster decay trace (Figure 4.3 inset trace b') of the CPB-DBF clearly indicates the non-radiative channel owing to hole transfer from the photo-excited CPB QDs to the DBF molecule which has less than pulse width limited (<0.15 ns) average life time.

In addition to the luminescence quenching of CPB QDs in presence DBF, a red shifted PL band was observed after exciting the samples at 440 nm. To find out the origin of this luminescence we have carried out steady state PL measurements after exciting CPB QDs, DBF and CPB-DBF systems at 520 nm and compared their luminescence in Figure 4.4. It’s interesting

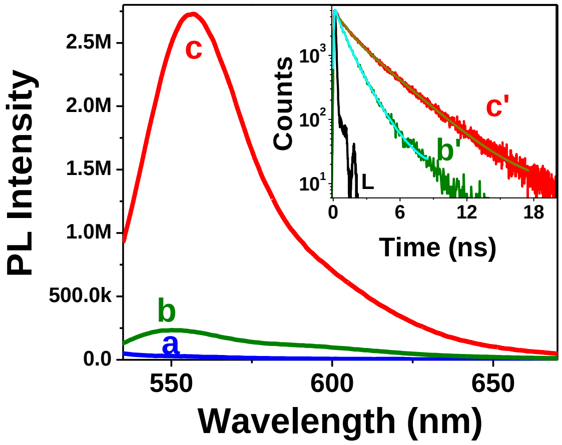

Figure 4.4: Steady state PL spectra of (a) pure CPB QDs, (b) pure DBF and (c-i) CPB QDs-DBF systems in toluene after 520 nm excitation. Concentrations of CPB and DBF were kept 0.1 μM and 0.45 mM respectively. **Inset:** Time resolved PL decay traces of (b') pure DBF and (c') CPB-DBF monitor at 555 nm after 445 nm laser excitation. "L" stands for excitation laser profile.

to see that at 520 nm excitation CPB QDs have not shown much luminescence (Figure 4.4a). However, DBF shows (trace b) low intensity PL band with the emission maximum at 548 nm. Intriguingly, red shifted emission band for CPB QDs-DBF complex shows emission peak at 555 nm with much higher intensity as compared to even DBF. This red-shifted broad emission band looks quite different from pure DBF emission. This emission can be attributed at CT luminescence ($h\nu_{CT}$) which generate due to radiative recombination of electron in the conduction band of CPB QDs and hole in the DBF molecule (Scheme 4.1) in the composite system. Steady state optical absorption studies suggest at 520 nm excitation mainly the CT complex gets excited. So the charge separation reaction followed by charge recombination reaction which gives charge transfer luminescence can be explained as follows:

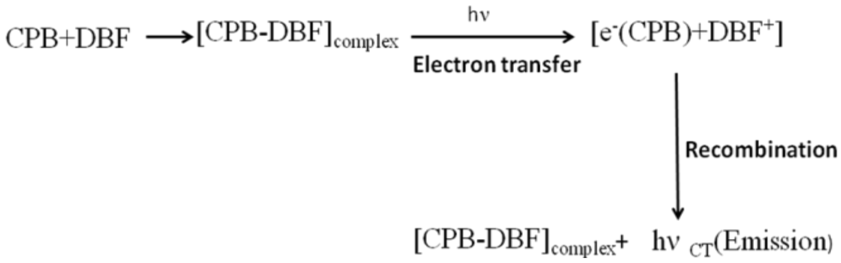

(4.3)

In our earlier investigation [250] we have observed CT luminescence in dye sensitized TiO_2 and ZrO_2 nanoparticles which was generated due to recombination between electron in the conduction band of TiO_2/ZrO_2 nanoparticles and cation radical of the sensitized dye molecules. To monitor the excited state life time of the CT luminescence we have carried out time-resolved emission studies of the composite system and compared with pure DBF and shown in Figure 4.4 inset. Figure 4.4b' shows the time resolved PL decay trace of the pure DBF at 555 nm after 406 nm laser excitation which can be fitted bi-exponentially with time constant τ_1 = 0.55 ns (25%), and τ_2 = 1.9 ns (75%) with τ_{avg} = 1.56 ns. Interestingly, the luminescence decay trace of the complex at 555 nm is slower as compare to pure DBF and can be fitted with time constant τ_1=

0.8 ns (20%), and τ_2 = 3.5 ns (80%) with τ_{avg} = 2.96 ns. As the emission at 555 nm in CPB QDs-DBF complex system is mainly dominated by CT luminescence so the emission lifetime can be attributed to the charge recombination reaction between electron in the conduction band of CPB and DBF cation radical. In addition to the direct electron transfer from HOMO of DBF to the CB of the CPB QDs, the photo-excited DBF molecule can also inject electron to the CB of the CPB QDs as the LUMO of the DBF lies energetically higher than the CB of the CPB QDs (Scheme 4.1). However, we have not observed any luminescence quenching of DBF in presence of the CPB QDs. This is because of the presence of the CT luminescence of the complex at the same spectral region.

4.2.4. Femtosecond Transient Absorption:

As the charge transfer interaction in semiconductor material take place in ultrafast time scale so nanosecond time resolution is not enough to conclude multiple charge transfer processes and their corresponding time scales. Ultrafast transient absorption (TA) is one of the unique technique which helps to investigate the charge carrier and charge separation dynamics at shorter time scale. Before going to the details of charge transfer dynamics of the CPB-DBF composite system we have carried out the TA experiment of the pure CPB QDs and DBF. Figure 4.5 A shows the TA spectra of the pure CPB QDs at different time delay in toluene after 400 nm laser excitation. The TA spectra consists of a negative absorption band (bleach) in 483-523 nm spectral range peaking at ~502 nm and a very little positive absorption at 515-545 nm in early time delay which are attributed due to ground state exciton depletion and red shifted hot exciton induced absorption respectively. [265] The photoinduced absorption in the blue region (480 nm) at longer time delay can be attributed to the excited state absorption of the excited charge carriers. We have already observed earlier with the help of steady state and time-resolved emission studies through selective excitation that charge separation in CPB-DBF composite system takes place through multiple processes like photo-excited hole transfer from CPB QD to DBF and direct electron transfer HOMO of DBF to the conduction band of CPB QD. In addition to that, electron injection from photo-excited DBF to the conduction band of CPB (Scheme 4.1) is also possible. Now to monitor charge transfer processes in ultrafast time scale we have carried out transient absorption studies exciting the samples at 400 nm where charge transfer takes place in multiple ways.

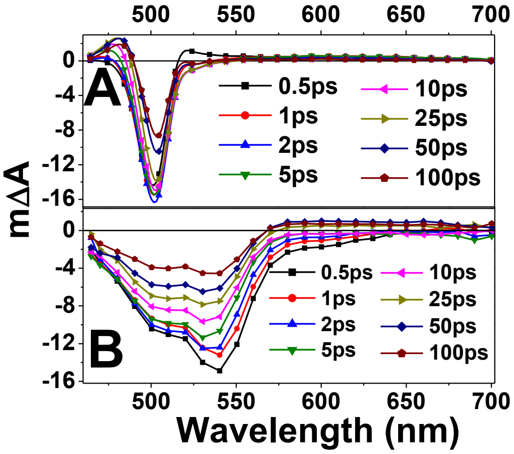

Figure 4.5: Transient absorption spectra of (A) pure 0.5μM $CsPbBr_3$ and (B) $CsPbBr_3$-DBF at different time delay after pumped at 400 nm laser excitation. Concentrations of CPB and DBF in the composite are 0.1μM and 0.45 mM respectively.

Figure 4.5B depicts the TA spectrum of the CPB QDs-DBF at different time delay after 400 nm laser excitation in toluene solution. In contrast to both, CPB QDs and DBF, the TA spectra of the composite materials comprised of a broad bleach below 650 nm peaking at 540 nm due to ground state depletion of the CT complex between CPB-DBF and excited absorption band 560-700 nm region at longer time scale. Intriguingly, DBF form strong CT complex with CPB

QDs which absorbs more light in the red regions also proved by the TA spectrum. Large red shifted broad bleach signal of the composite materials as compare to the pure material indicates strong complexation between CPB and DBF which facilitate higher charge separation on photo-excitation. On photo-excitation CPB-DBF composite materials at 400 nm, both hole transfer from photo-excited CPB QD to DBF or direct electron transfer from DBF HOMO to CB of CPB QD, and in both cases formation DBF$^{\bullet+}$ cation radical is expected. However in the transient spectra (Figure 4.5B) signature of DBF$^{\bullet+}$ cation radical which appears at 650 nm [298] is absent at early time scale. The absence of transient absorption signal due DBF cation radical can be attributed due to the overlap of CT complex bleach in the same spectral region. However, at longer time scale positive absorption band appears at 560-700 nm region which can be attributed to the transient absorption due to DBF$^{\bullet+}$ cation radical. Now to understand charge separation and recombination dynamics in the above composite system we have monitor the kinetics at

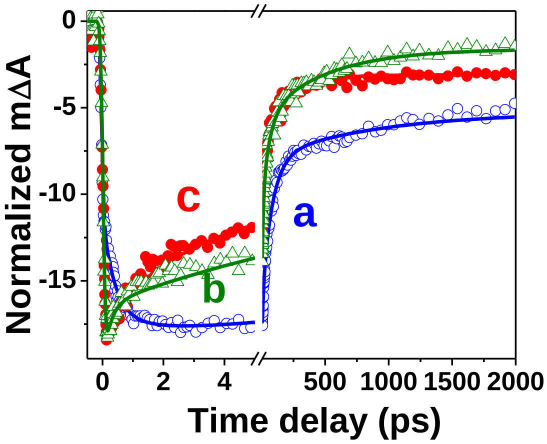

Figure 4.6: Normalized bleach recovery kinetic traces of (a) at 502 nm for pure CPB QDs and (b) at 502 nm and (c) at 540 nm for CPB-DBF complex respectively after 400 nm laser excitation in toluene.

excitonic wavelength (502 nm) for pure CPB QD and both at excitonic wavelength (502 nm) and at bleach maxima (540 nm) for CPB-DBF complex system and shown in Figure 4.6.

Now before monitoring the charge transfer dynamics in CPB-DBF complex it's important to monitor charge carrier dynamics of CPB QD after 400 nm photo-excitation. Figure 4.6a demonstrates the bleach recovery kinetics which can be fitted with bi-exponential growth with time constants $\tau_1^g = < 100$ fs (58%) and $\tau_2^g = 600$ fs (42%) and multi-exponential recovery with time constants of $\tau_1 = 10$ ps (31%), $\tau_2 = 60$ ps (30%), $\tau_3 = 300$ ps (8%), and $\tau_4 = > 2$ns (31%) (Table 4.1). The second growth component can be attributed to electron cooling time from upper excitonic state to conduction band edge of CPB QD. The bleach recovery kinetics can be attributed to the recombination reaction between photo excited electron and hole in CPB QDs. Now, to find out correctly the hole transfer time we have compared the bleach recovery kinetics of the CPB-DBF system with pure CPB QD at the excitonic bleach position (502 nm) and shown

Table 4.1. Transient Fitting Data (τ) of CPB QDs and the CPB QDs-DBF composite at key wavelength (λ, nm). The percentage in parenthesis represents the amplitude of the corresponding time constants.

System(λ)	τ_{g1}	τ_{g2}	τ_1	τ_2	τ_3	τ_4	τ_5
CPB (502)	<100fs (58%)	0.6 ps (42%)	10ps (-31%)	60ps (-30%)	300ps (-8%)	>2 ns (-31%)	
CPB - DBF(502)	<100fs (100%)		0.25ps (-13%)	10 ps (-43%)	60ps (-23%)	500ps (-12%)	>2 ns (-9%)
CPB - DBF(540)	<100fs (100%)		0.25ps (-16%)	3ps (-31%)	40ps (-28%)	200ps (-8%)	>2 ns (-17%)

in the Figure 4.6. Bleach recovery kinetics can be fitted with pulse-width limited (< 100 fs) single exponential growth time and multi-exponential recovery time constants of τ_1 = 250 fs (13%), τ_2= 10 ps (43%), τ_3= 60 ps (23%), τ_4 = 500 ps (12%) and τ_5= > 2ns (9%) (Table 4.1). Interestingly, the bleach kinetics of CPB-DBF at 502 nm recovers faster at early time scale and the faster component (250 fs) can be attributed as hole transfer time from the photoexcited CPB QDs to the DBF molecule. Slower components of the bleach recovery kinetics can be attributed to the recombination dynamics between electron in the CPB QD and DBF cation radical.

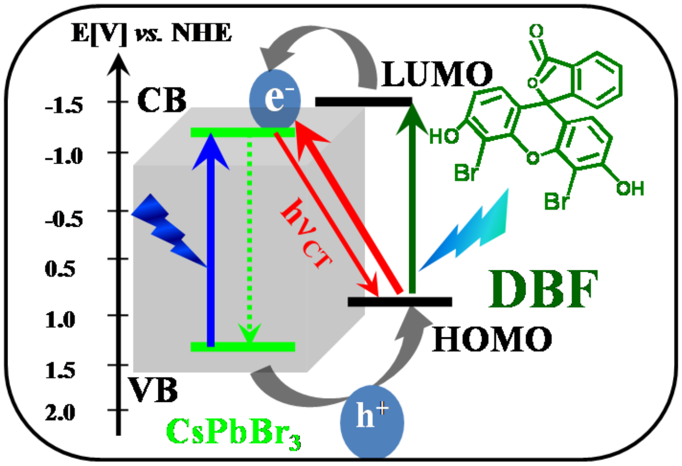

Scheme 4.1: Schematic presentation of the interfacial charge transfer interaction between cubic cesium lead trihalide perovskite QDs (CPB QDs) and an organic acceptor molecule (DBF). **Inset**: The molecular structure of the DBF.

4.2.5. Charge Transfer Interaction:

The multiple charge transfer processes in the CPB QDs-DBF interface are shown in the Scheme 4.1. The major processes are photo-excited hole transfer from CPB QD to DBF, direct electron transfer from HOMO of DBF to the CB of the CPB QDs (Scheme 4.1). In addition to that, electron injection from photo-excited DBF to the conduction band of CPB is also thermodynamically feasible (Scheme 4.1). Photocurrent conversion efficiency of hybrid organic−inorganic methylammonium lead bromide ($MAPbBr_3$) is reported to be above 18%. However due to lower stability in ambient condition using these materials in the devices for longer time is the greatest challenge.[259, 260] On the other hand all- inorganic caesium lead bromide ($CsPbBr_3$) have shown prospective perovskite material with much higher stability but shown conversion efficiency of ~ 6% by using poly aryl amine-based derivative as hole transport material.[262, 270] Thus by introducing a molecular adsorbate into the highly stable total inorganic perovskite one can improve the absorption cross section up to red region which absorb more solar radiation as compared to pure CBP QD. In addition to that, the molecular adsorbate also helps to neutralize the photoexcited hole from the photo-anode. In the present investigation steady state and time-resolved transient absorption and luminescence data confirm that CPB form strong charge transfer complex with DBF, where DBF not only extract the photo-excited hole from CPB, the composite can also absorbs more solar radiation due to formation of a CT complex that has a very high molar extinction coefficient. Considering the fact that perovskite photoaction is the exclusive outcome of kinetic competitions of electron injection, hole transfer, higher degree of charge separation, charge recombination processes, the CPB-molecular composite material can bring significant improvement in perovskite solar cell without much changing the device fabrication.

4.3. Conclusion:

In summary, the multiple charge transfer interaction of $CsPbBr_3$ with DBF molecule has been demonstrated after synthesized and characterized highly luminescent colloidal CPB QDs. Optical absorption studies reveal that DBF form strong charge transfer complex with CPB which absorbs in the red region of solar spectrum with extremely high molecular extinction co-efficient. Steady state and time resolved photoluminescence studies indicate that the emission intensity of the CPB QDs is completely diminished in the presence of DBF molecule which suggests the efficient hole transfer from photo-excited CPB QD to the DBF molecule. Furthermore, a new red shifted luminescence band as compared to both CPB and DBF has been observed from CPB-DBF composite materials in steady state PL studies after exciting the CT complex which has been assigned as CT luminescence. Charge carrier dynamics was monitored from transient kinetics and the hole transfer and electron transfer time were found to be 250 fs and < 100 fs respectively. As, hole transfer is the key factor in perovskite solar cell, so by introducing an hole acceptor molecule which also can for strong charge transfer complex with $CsPbBr_3$ perovskite material resulting higher molecular absorbity in the red region of the solar spectra can improve solar performance drastically through its dual behaviour.

CHAPTER-5

Band Edge Engineering and Controlling Charge Carrier Delocalization in Core/Shell Nanocrystals

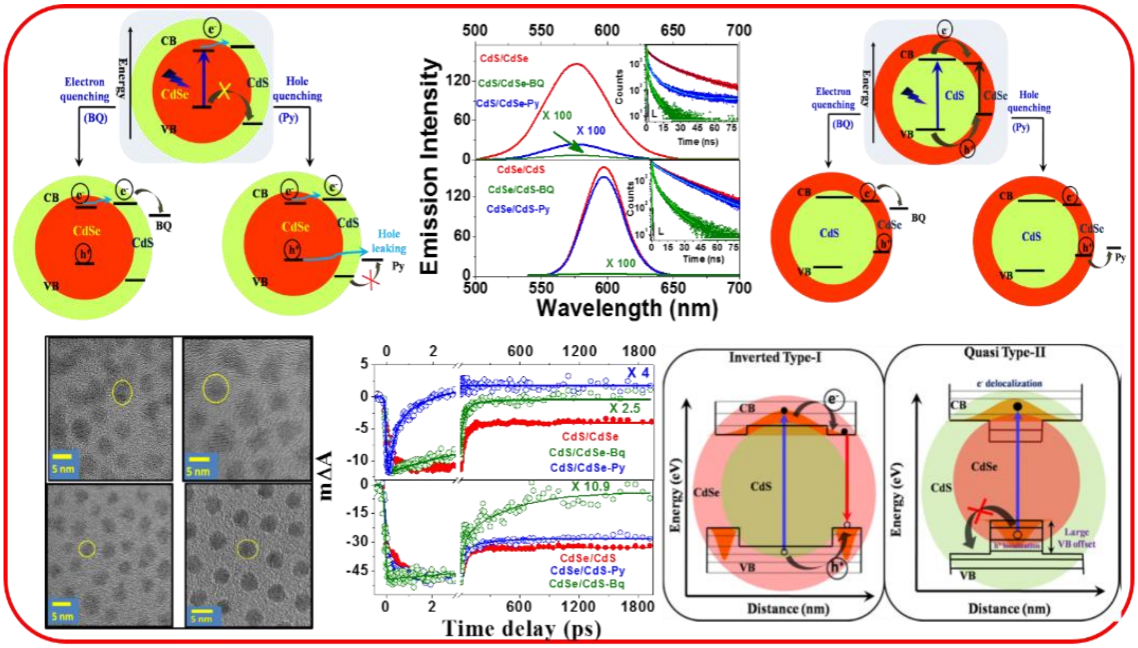

- ***J. Phys. Chem. C, 2015, 119, 26202–26211.***

5.1. Introduction

Nanocrystals, especially II−IV semiconductors quantum dots (QDs), are generating enormous interest in research in the last three and a half decades owing to their exciting properties, such as quantum confinement of the charge carriers, size-dependent optical tunabilites, high extinction coefficient, exotic electronic properties, and band gap engineering.[16, 30, 31, 300-302] The combination of two different NCs in one nanostructure is called heterostructure, and such heterostructures are usually categorized as core−shell, [109, 110, 112, 303, 304] tetrapods, [113] dot in rods (DR), [119, 305-307] etc., depending on their shape and size. The heterostructure core−shell NCs are typically recognized to be of three different forms type I, type II, and quasi-type II depending on their valence band (VB), conduction band (CB) alignment, and the charge carrier delocalization. In type I core−shell, the core NC is confined by a wider band gap NC where the VB and CB of the core NC lies in between the VB and CB of the shell NC materials. Thus, on excitation, both the charge carriers (electron and hole, e−h) are localized in the core structure. As a result, the charge carriers are strongly confined in the core materials, and increased photoluminescence quantum efficiency is achieved. [114] However, if the wider band gap material occupies the core and is covered by small band gap material (shell), then inverted type I core−shell structure can be realized. In inverted type I structure, both e−h are localized in the lower band gap shell material upon photoexcitation. [115, 308-310] On the other hand, in type II core−shell structure, the energy levels of both CB and VB of the core material lie above the CB and VB of the shell material or vice versa. So on photoexcitation of type II core−shell, photoexcited electron and hole are localized in two different semiconductors, either core or shell, depending upon the band alignment. [118, 120, 131, 299, 311-313] In addition to the above core− shell structures, there is an intermediate core−shell structure, known as quasi-type II core−shell, [119-122] in which the band gap alignment is like the type I structure however due to smaller band offset between the CB of both the semiconductors the electron can be delocalized in the CBs of both of the NCs. Similarly, if the VB offset energy is smaller between the holes, they can be delocalized in the VBs of both of the NCs. In contrast to type I and II structures, the quasi-type II NCs are now routinely used in different applications due to heir higher emission quantum yield as well as better charge separation.[314] CdSe/CdS semiconductor composite is the one of the widely studied NC,[205, 314-318] in which the band gap alignment of bulk materials suggests a type I core−shell structure; however, due to low energy offset between the conduction bands of CdSe and CdS, the semiconductor pair can easily make a quasi-type II core−shell structure, depending on the size of the core NC and thickness of the shell NC. [119, 121] It is reported in the literature [204]that CdS shell on CdSe core helps to remove the surface states, and with increasing shell thickness, the emission quantum yield increases tremendously (close to unity). [314] Due to the higher quantum yield of the CdSe/CdS core−shell, it has been extensively studied in various fields with potential applications such as light emitting diodes (LED), bioimaging, lasing materials, PL blinking, and optical gain performance.[319] In addition to the higher emission quantum yield, due to staggered band alignment, CdSe/CdS core−shell materials are successfully utilized in various practical application such as photovoltaic and photocatalysis due to higher effective charge separation. As the lattice mismatch between CdSe and CdS is very small (<3%), the semiconductor pair can easily form inverted type I CdS/CdSe core−shell [115] as well as alloy structure.[128] Earlier Pan et al. have demonstrated the efficient CdS/CdSe inverted type I core−shell in QD-sensitized solar cell. [115] This inverted band alignment helps to extract the photogenerated electron into the shell and hence increased the electron injection efficiency.[156, 308, 320]

Upon photoexcitation of the core–shell NCs, the photoexcited charge carriers are distributed in the heterostructure according to their electronic band alignment. These photogenerated charge carriers are responsible for the application purpose, such as photocatalysis and photovoltaic. Thus, the charge carrier dynamics and charge separation dynamics are very important factors for optimization of the device efficiency. In this regard, several time-resolved spectroscopic techniques are used, such as time-resolved emission, femtosecond transient absorption, fluorescence upconversion to monitor the charge carrier cooling, electron–phonon interaction, carrier trapping, Auger cooling, and charge recombination processes. [93, 94, 101, 218, 321] Recently, Boldt et al. have reported the electronic structure and band gap engineering of ZnSe/CdS [322] and ZnSe/ZnS/ CdS [312] with the help of transient absorption studies. Moreover, these time-resolved techniques are often used to locate the charge carriers of the core–shell NCs using quencher molecules.[323] Earlier, we have demonstrated the charge carrier dynamics in thiol-capped CdTe QDs using electron [benzoquinone (BQ)] and hole (n-butylamine) quencher. However, detailed structural analysis of core–shell NC with the help of quencher molecules has not been discussed so far in the literature, except in our previous report.[323]

To demonstrate band gap engineering and charge carrier delocalization in CdSe/CdS core–shell materials, we have deliberately synthesized CdSe/CdS quasi-type II and CdS/CdSe inverted type I core–shell. Both of the core–shell materials were characterized by steady-state absorption, luminescence, X-ray diffraction, and high-resolution TEM techniques. The location of electron and hole in the core–shell structure was monitored by steady-state and time-resolved emission techniques in the absence and presence of an electron quencher (BQ) and hole quencher [pyridine (Py)]. Moreover, to investigate the charge carrier dynamics and charge carrier delocalization in a precise way, we have carried out femtosecond transient absorption experiments for both the core−shell NCs in the absence and presence of quencher molecules. Charge carrier (e−h) transfer time and their location in the core-shell structure are discussed in the present investigation.

5.2. Results and Discussion

5.2.1. Morphology and Structural Analysis.

The X-ray diffraction (XRD) patterns of core CdS QDs and CdS/CdSe inverted type I core−shell and CdSe QDs and CdSe/CdS quasi-type II are plotted in parts A and B of Figure 5.1,

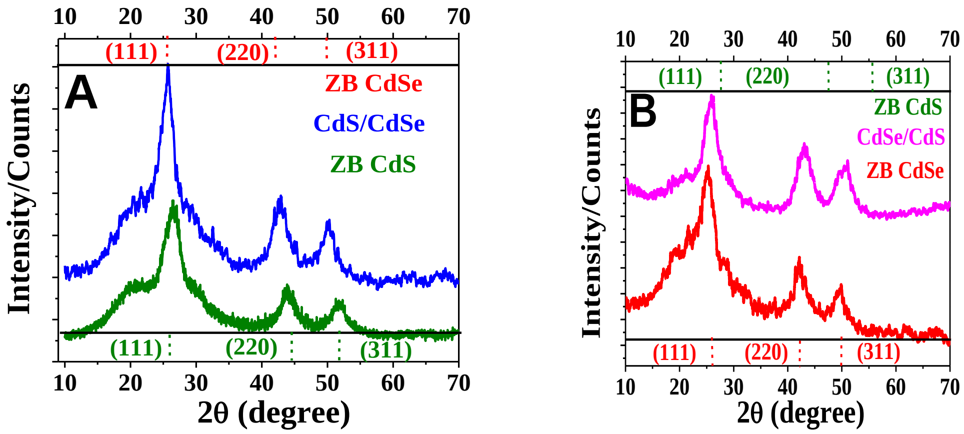

Figure 5.1: Powder X-ray diffraction pattern of (A) CdS QD and CdS/CdSe inverted type I core-shell and (B) CdSe QD and CdSe/CdS quasi type-II core-shell respectively. Vertical dotted lines olive, and red represent (111), (220) and (311) diffraction plane position of ZB CdS, and ZB CdSe phases respectively.

respectively. The XRD patterns of the CdS and CdSe QDs match with the crystal structure of bulk cubic zinc blende (ZB).[324] Figure 5.1A shows three major peaks at 26.01°, 44.52°, and 51.84° for the diffraction of the planes of (111), (220), and (311), respectively. However, CdS/CdSe depicts three peaks at 25.82°, 42.96°, and 50.4°, where the peaks are shifted to the lower angle as compared to that of CdS QDs, suggesting the formation of CdSe shell on CdS core. Similarly, in case of CdSe/CdS core−shell, three diffraction peaks due to (111), (220), and (311) planes are shifted toward higher angle (25.92°, 43.36°, and 51.11°) as compare to core CdSe (25.58°, 42.14°, and 49.89°), which clearly suggests the formation CdS shell on the cubic ZB phase of CdSe core. Figure 5.2 shows the HRTEM images of the CdS QDs (Figure 5.2a) and CdS/CdSe core−shell (Figure 5.2b), and the size (diameter) of the particle is measured to be 5.2 ± 0.25 and 6 ± 0.3 nm, respectively. The nearly monodispersed and highly crystalline nature of the NCs is reflected by the HRTEM images of the particles. HRTEM images of the CdSe QDs (Figure 5.2c) and CdSe/CdS core− shell (Figure 5.2d) also show monodispersed spherical nanocrystals with very good crystalline structure. The particle size was determined to be 3.7 ± 0.18 nm for CdSe QDs and 4.5 ± 0.22 nm for CdSe/CdS respectively.

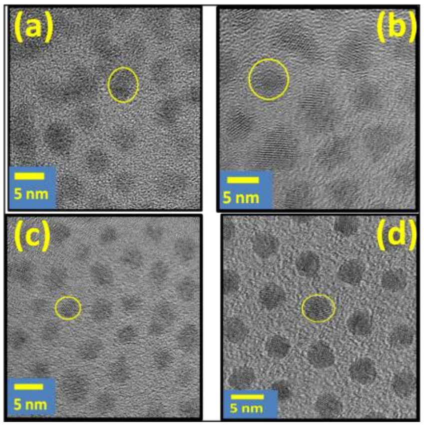

Figure 5.2: The HRTEM images of (a) CdS QD, (b) CdS/CdSe inverted type-I core-shell, (c) CdSe QD, and (d) CdSe/CdS quasi type-II core-shell NCs.

5.2.2. Steady-State Optical Absorption and Photoluminescence (PL) Spectroscopy.

Steady-state optical absorption and PL measurement techniques are some of the tools that assist to characterize the core−shell NCs from the core QDs. Figure 5.3 depicts the UV−vis optical absorption and PL spectra of the two QDs and their corresponding core−shell NCs. Figure 5.3a shows the first excitonic (1S) absorption of CdSe QDs at 555 nm, and the corresponding band edge PL appears at 583 nm (Figure 5.3a′). However, the CdSe/CdS core−shell shows the 1S excitonic absorption band (Figure 5.3b) and the band edge PL peak (Figure 5.3b′) at 578 and 596 nm, respectively. Upon growth of the CdS shell on the CdSe core, both the optical absorption and the PL peak shifted to the red region of the spectra, and at the same time, the emission quantum yield of the CdSe/CdS ($\phi_{CdSe/CdS}$ = 0.7) core−shell increases enormously as compared to that of the CdSe core QDs (ϕ_{CdSe} = 0.24). On the other hand, the 1S excitonic absorption of the CdS QDs appears at 462 nm (Figure 5.3c) and the band edge PL appears at 482 nm (Figure

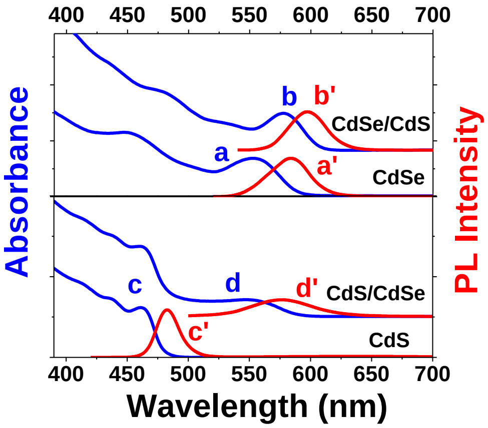

Figure 5.3: UV-Vis and PL spectra of CdSe QD (a, a', λ_{ex}=480 nm); CdSe/CdS quasi type II core-shell (b, b', λ_{ex}=480 nm); CdS QD (c, c', λ_{ex}=400 nm) and CdS/CdSe inverted type I core shell (d, d', λ_{ex}=400 nm) in degassed chloroform solution.

5.3c′). Traces d and d′ of Figure 5.3 show the steady-state optical absorption and photoluminescence spectra of CdS/CdSe inverted type I core− shell, respectively. The optical absorption spectra of the inverted core−shell shows two bands at 465 and 555 nm for CdS core and CdSe shell, respectively. Interestingly, upon photoexcitation of the CdS/CdSe core−shell at 400 nm, only one PL peak appears at 575 nm. The emission quantum yield was determined to be 0.22 for CdS/CdSe core−shell, which is comparable to that of CdS QDs (ϕ_{CdS} = 0.18).

5.2.3. Core−Shell Band Structure through Electron−Hole Quenching Experiments.

To find out the location of the charge carrier (electron and hole) in both the CdSe/CdS quasi type II core−shell and CdS/CdSe inverted type-I core−shell upon photoexcitation, we have carried out hole and electron quenching experiments in the presence of Py and BQ, respectively. It is widely reported in the literature that Py [323, 325, 326] and BQ [89, 327] are molecules that quench holes and electrons, respectively. Recently Weiss et al. have been showed temperature-dependent

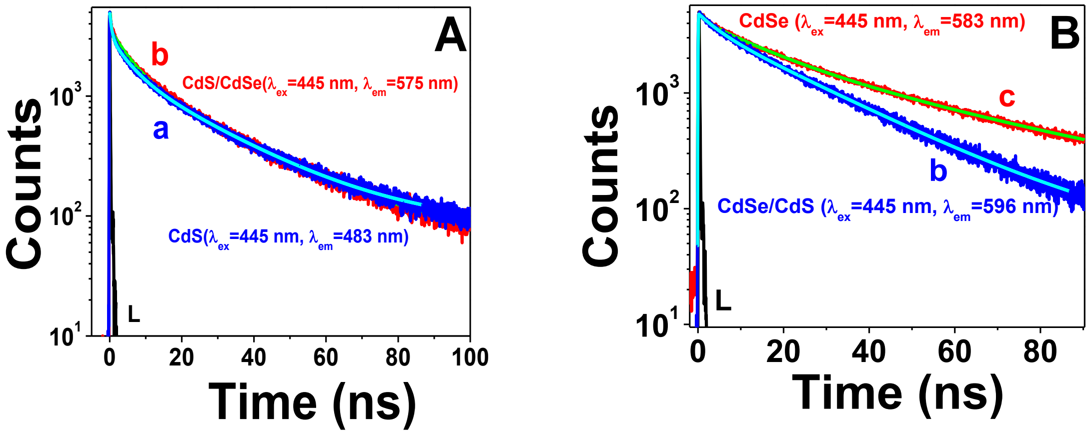

Figure 5.4: (A) Time resolved PL decay traces of (a) CdS (λ_{ex}=445nm, λ_{em}=482 nm), (b) CdS/CdSe (λ_{ex}=445nm, λ_{em}=575 nm) (B) (c) CdSe (λ_{ex}=445nm, λ_{em}=583 nm), and (d) CdSe/CdS 1 ML (λ_{ex}=445nm, λ_{em}=596 nm). "L" stands for excitation lamp profile.

electron transfer from PbS QDs to BQ molecules.[328] Before going to details of the quenching experiment we have carrier out the excited state radiative life time of the CdS/CdSe and CdSe/CdS and compare with corresponding core NCs. The time resolved PL decay traces of CdS (trace a), CdS/CdSe(trace b), CdSe(trace c) and CdSe/CdS(trace d) are plotted in the Figure 5.4 (A) and (B) respectively and their fitting data are summarized in the Table 5.1.

i. CdS/CdSe Inverted Type I Core−Shell.

CdS/CdSe forms an inverted type I core−shell structure, so it is expected that upon photoexcitation both of the charge carriers will be localized in the CdSe shell, as the CB and VB of the CdSe shell lies energetically lower than the core CdS CB and VB, respectively (Scheme 5.1). To reconfirm the location of both of the charge carriers, steady-state emission experiments for CdS/ CdSe inverted core−shell have been carried out in the absence (Figure 5.5a) and presence of both Py and BQ and are shown in Figure 5.5A. It is clearly seen that the emission intensity of the core−shell completely quenches in the presence of both hole quencher (Figure 5.5b) and electron quencher (Figure 5.5c). To the reconfirm electron- and hole-quenching effect, time resolved emission studies have also been carried out in the above systems. Figure 5.5A inset shows the time-resolved emission decay traces of CdS/CdSe core−shell in the absence (Figure 5.5a′) and presence of hole (Figure 5.5b′) and electron quencher (Figure 5.5c′) using Py and BQ, respectively. Figure 5.5a′ indicates the emission decay trace of the CdS/ CdSe at 575 nm and can be fitted multiexponentially with time constant τ_1 = 1.54 ns (58%), τ_2 = 5.12 ns (23%), and τ_3 =24.29 ns (19%) with τ_{avg} = 18.3 ns (Table 5.1). However, the time-resolved PL traces of the CdS/CdSe decay faster in the presence of both Py and BQ. The emission decay traces of CdS/CdSe-Py and CdS/CdSe-BQ can be fitted multiexponentially with time constant τ_1 = 0.19 ns

(75%), τ_2 = 2.2 ns (21%), and τ_3 = 13.2 ns (4%) with τ_{avg} = 7 ns and τ_1 = 0.04 ns (85%), τ_2 = 0.65 ns (12%), and τ_3 = 4 ns (3%) with τ_{avg} = 2.3 ns respectively (Table 5.1). Electron and hole localization and quenching processes can be visualized in Scheme 5.1 where upon photoexcitation of the CdS/CdSe core−shell, both electron and hole from CdS core QDs can be transferred to the CdSe shell QDs, as they are thermodynamically viable processes. Finally, both the hole and electron in CdSe QDs shell can be quenched by Py and BQ, respectively, as both the

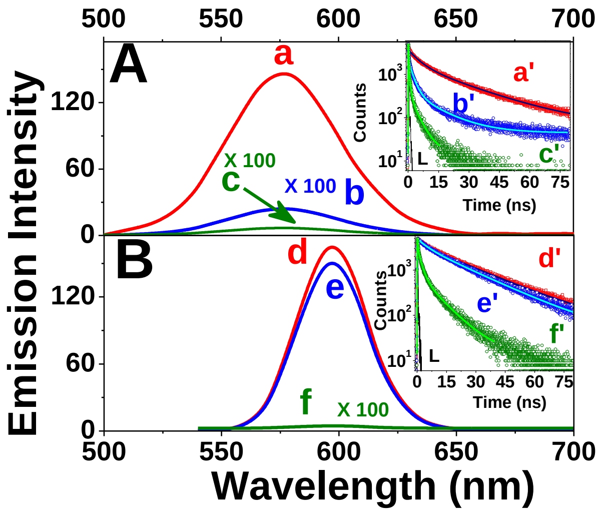

Figure 5.5: (A) Steady state PL spectra of CdS/CdSe inverted type-I core-shell (a) in absence of any quencher, (b) in presence of hole quencher and (c) in presence of electron quencher (λ_{ex}=400 nm). **Inset:** Time resolved PL decay trace of CdS/CdSe at 575 nm (a') in absence of any quencher molecule, (b') in presence of py and (c') in presence of BQ after exciting at 445 nm laser source. **(B)** Steady state PL spectra of CdSe/CdS quasi type-II core-shell (d) in absence of any quencher, (e) in presence of py and (f) in presence of BQ (λ_{ex}=500 nm). **Inset:** Time resolved PL decay trace of CdSe/CdS at 596 nm (d') in absence of any quencher molecule, (e') in presence of py and (f') in presence of BQ after exciting at 445 nm laser source in degassed chloroform. "L" stands for excitation laser profile.

processes are thermodynamically viable (Scheme 5.1). Thus, the above observation clearly suggests that upon photoexcitation of CdS/CdSe inverted core−shell all the photoexcited holes and electrons are finally localized in CdSe shell QDs.

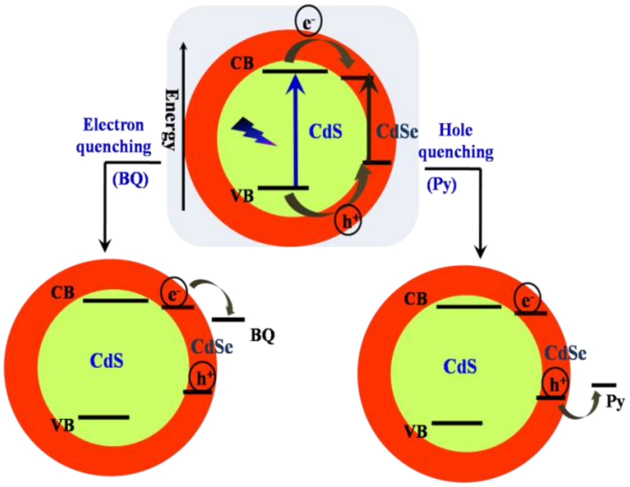

Scheme 5.1: Schematic representation of quenching experiment in CdS/CdSe inverted core-shell in presence of hole and electron quencher using pyridine (Py) and benzoquinone (BQ) respectively. benzoquinone (BQ) respectively.

ii. CdSe/CdS Quasi Type II Core−Shell.

Again, similar to the above studies, we have also carried out hole- and electron quenching experiments in CdSe/CdS quasi-type II core−shell with Py and BQ, and they are shown in Figure 5.5B. The PL intensity of the CdSe/CdS-BQ is completely diminished in the presence of the BQ molecule. Interestingly, the emission intensity remains unchanged in the presence of the hole quencher, Py molecule. In the CdSe/CdS core−shell, the electron in the core is no longer localized in the CdSe due to the small CB offset (< 0.2 eV) and lower effective mass of the electron. As a result, the electron is delocalized throughout the CdS shell materials. In contrast to the electron delocalization, the hole is strongly confined in the VB of CdSe in the CdSe/ CdS core−shell structure due to large band offset (> 0.5 eV) and high effective mass of the hole. So, to reconfirm the electron−hole delocalization in CdSe/CdS quasi-type II core− shell, we have carried out time-resolved PL measurements, and they are plotted in the inset of Figure 5.5B. The PL decay trace of CdSe/CdS at 596 nm (Figure 5.5d′) can be fitted biexponentially with time constants τ_1 = 2.3 ns (47%) and τ_2 = 23.5 ns (53%) with τ_{avg} = 21.8 ns (Table 5.1). It is worth mentioning that the excited state radiative decay of the CdSe/CdS core−shell is faster (Table 5.1) compared to that of the core CdSe, and the decay trace is fitted biexponentially rather triexponential for CdSe.

Table 5.1: Time resolved Photo-luminescence decay parameter of CdS/CdSe and CdSe/CdS in absence and in presence of quencher molecule.

System	λ_{ex}	λ_{em}	τ_1	τ_2	τ_3	τ_{avg}
CdS	445 nm	483 nm	1.5 ns (55%)	5 ns (27%)	25.2 ns (18%)	18.2 ns
CdS/CdSe	445 nm	575 nm	1.54 ns (58%)	5.12 ns (23%)	24.29 ns (19%)	18.3 ns
CdS/CdSe-Py	445 nm	575 nm	0.19 ns (75%)	2.2 ns (21%)	13.2 ns (4%)	7 ns
CdS/CdSe-BQ			0.04 ns (85%)	0.65 ns (12%)	4 ns (3%)	2.3 ns
CdSe	445 nm	583 nm	2.05 ns (55%)	6.12 ns (26%)	35.29 ns (19%)	26.4 ns
CdSe/CdS	445 nm	596 nm	2.3 ns (47%)	23.5 ns (53%)		21.8 ns
CdSe/CdS-Py	445 nm	596 nm	2.2 ns (45%)	22.6 ns (55%)		21.1ns
CdSe/CdS-BQ	445 nm	596 nm	0.23 ns (59%)	1.86 ns (32%)	9.3 ns (9%)	5.67 ns

Recently, Nan et al. have reported the single exponential PL decay of ZB CdSe/CdS NC with a 3−4-monolayer CdS shell. [204] In presence of the Py (hole quencher) molecule, the PL decay trace of CdSe/CdS core−shell (Figure 5.5e′) can be fitted multiexponentially with time constants of τ_1 = 2.2 ns (45%) and τ_2 = 22.6 ns (55%) with τ_{avg} = 21.1 ns (Table 5.1). It is interesting to see that in the presence of Py the average emission lifetime decreases marginally. This clearly suggests that photoexcited holes are pretty much confined in the CdSe core of CdSe/CdS core−shell (Scheme 5.2). The negligible difference (5%) in emission lifetime for the core−shell can be attributed to leaking of photoexcited hole in the core−shell and it finally reacting with Py (Scheme 5.2). However, the emission trace of CdSe/CdS core−shell can be fitted with time constant τ_1 = 0.23 ns (59%), τ_2 = 1.86 ns (32%), and τ_3 = 9.3 ns (9%) with τ_{avg} = 5.67 ns (Table 5.1). So, from the experimental results it can be concluded that photoexcited electron in the CdSe core of CdSe/CdS core−shell can be transferred to the CdS shell due to delocalization and eventually can be quenched by BQ (Scheme 5.2). However, to monitor the electron and hole transfer times in the core−shell composites in the absence and presence of the quenchers more

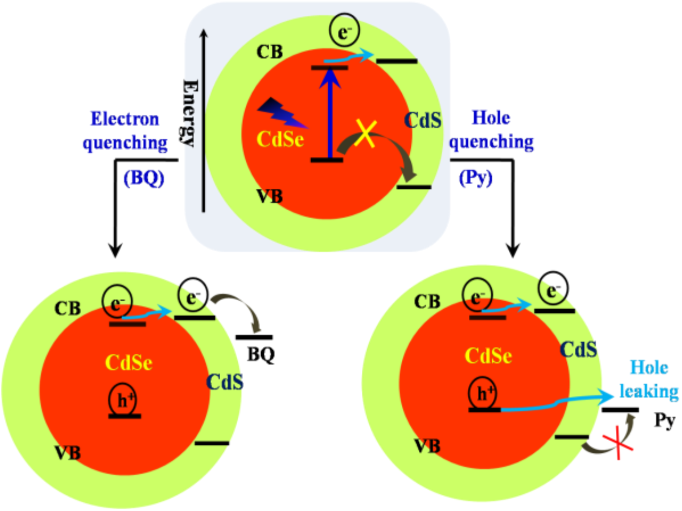

Scheme 5.2: Schematic presentation of quenching experiment in CdSe/CdS quasi type II core-shell in presence of hole and electron quencher using pyridine (Py) and benzoquinone (BQ) respectively.

accurately, we have carried out ultrafast transient absorption spectroscopic measurements on the above systems and these are discussed in the next section.

5.2.4. Femtosecond Transient Absorption Measurement.

Ultrafast transient absorption measurement is a sophisticated technique in which one can measure charge carrier dynamics, carrier cooling time, electron and hole transfer, and charge carrier recombination dynamics, etc. in QD materials. [87, 93, 94, 218, 319] In the above discussion, we have noticed complete quenching of CdS/CdSe PL in the presence of both BQ and Py; however, the PL of the CdSe/CdS is fully quenched in the presence of only BQ and not in the presence of Py. Thus, it is quite obvious that the excited properties of the composite will provide the important results toward determining charge carrier delocalization. To know about the electron and hole transfer processes on the ultrafast time scale, in the present investigation we have carried out transient absorption measurements after exciting the sample with 400 nm laser light and probing the visible region. Before monitoring the effect of electron and hole quencher on the charge transfer dynamics in both the core−shells, we have carried out details TA

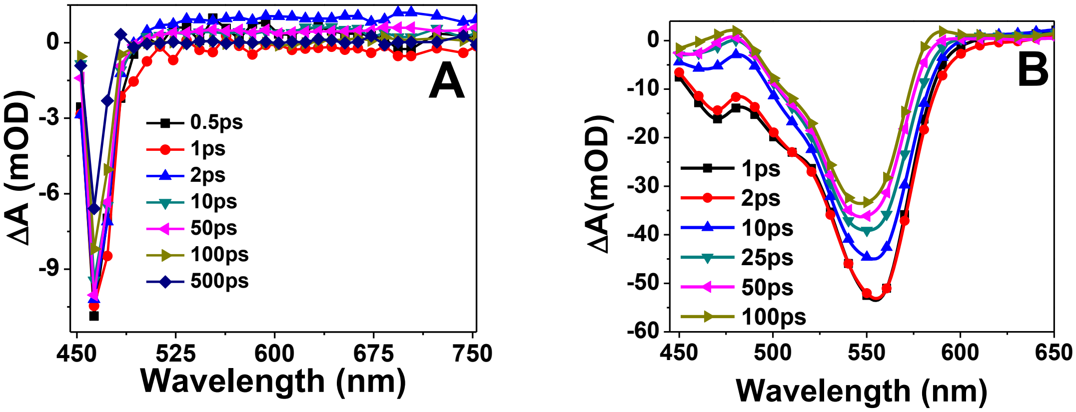

Figure 5.6: TA spectrum of the core CdS (A) and CdSe (B) at different time delay following 400 nm laser excitation in chloroform.

spectroscopy of the pure materials. We have drawn the TA spectrum of the core CdS and CdSe in the Figure 5.6 (A) and (B) respectively. The TA spectrum of the CdS shows a bleach maxima at 462 nm which can be assigned as 1S ($1S_{3/2}$-$1S_e$) electronic transition. Similarly CdSe shows bleach due to 1S electronic transition at 555 nm. The bleach at 510 and 470 nm is due to 2S ($2S_{3/2}$-$1S_e$) and 1P ($1P_{3/2}$-$1P_e$) electronic transition respectively. Figure 5.7A depicts the TA spectra of CdS/CdSe core−shell at different time delays after exciting with 400 nm laser light in chloroform solution. TA spectra of photoexcited CdS/CdSe shows two negative absorption bands below 600 nm. The negative absorption change band (500−600 nm) peaking at 552 nm can be assigned as ground-state depletion due to excitonic absorption band of the CdSe shell. It is interesting to see that the excitonic bleach is quite broad as compared to the bleach-pure CdSe QDs (Figure 5.6 B). The broadness of the transient bleach signal might be due to the overlap transitions of the 1S and 2S states of CdSe QDs as well as the interface alloying [312] of the core

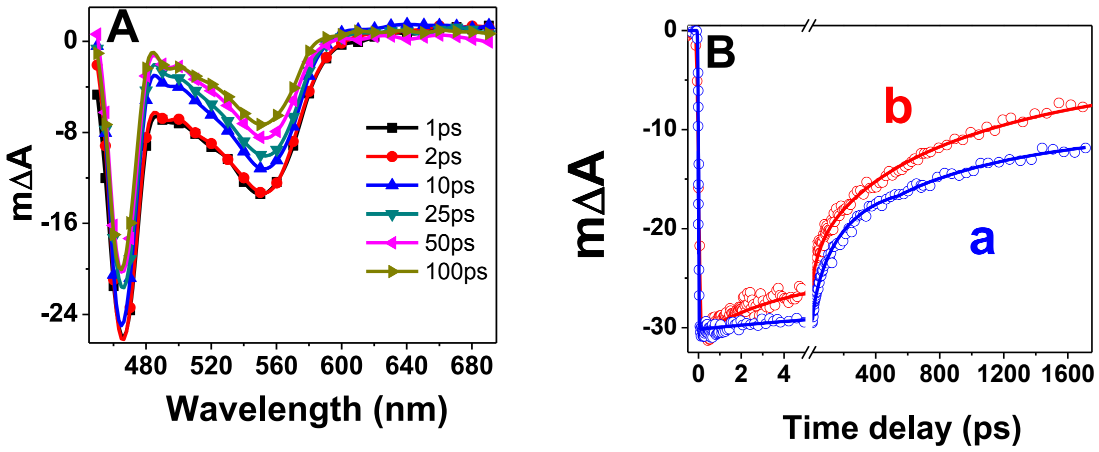

Figure 5.7 (A) TA spectrum of CdS/CdSe inverted type I core/shell at different time delay and (B) bleach recovery dynamics of CdS (a), CdS/CdSe (b) at 465 nm after 400 nm laser excitation in chloroform.

CdS and CdSe shell QDs. In addition to that, another negative absorption band has been observed in the 450−480 nm region with a bleach maximum at 465 nm, which can be attributed to the 1S excitonic transition of the CdS core itself. We have also carried out TA studies of pure CdS QDs (Figure 5.6 A), and compare the bleach dynamics at 465 nm of the CdS/CdSe with 1S bleach of the CdS (Figure 5.7 B). Bleach recovery kinetics at the 1S excitonic wavelength was found to be faster in the case of CdS/CdSe inverted core−shell as compared to that of pure CdS QDs. This can be attributed to the transfer of both electron and hole from CdS core QDs to CdSe shell QDs. In the CdS/CdSe structure, we prepared a 1 ML (monolayer) CdSe shell on CdS core, and owing to low CB offset energy, the tunneling effect cannot be neglected. So the bleaching due to the CdS core in the CdS/CdSe structure is not completely diminished. Parts A and B of Figure 5.8 show the transient absorption spectra of CdS/CdSe inverted type I core−shell in the presence of BQ and Py, respectively. Interestingly, the TA signal in both cases decreases

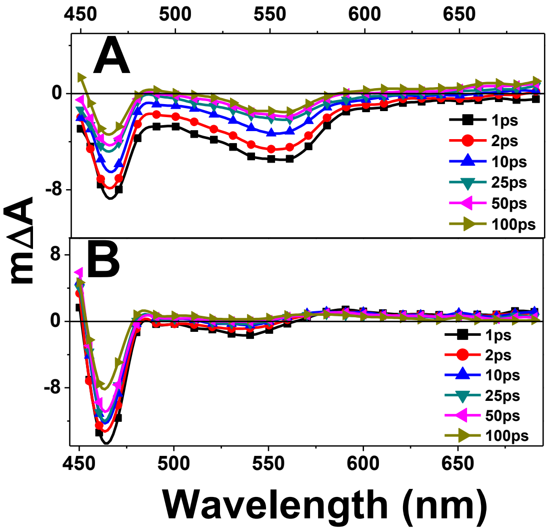

Figure 5.8: TA spectra of CdS/CdSe inverted type I core-shell (A) in presence of electron quencher (BQ) and (B) in presence of hole quencher (Py) in chloroform after exciting at 400 nm laser excitation.

drastically. It is worth mentioning that in all the cases the OD of the CdS/CdSe core−shell samples was kept similar. The transient bleach signal of the CdS/CdSe in the presence of BQ is reduced drastically due to efficient electron transfer from the CB of the core−shell to the BQ. In case of CdS/CdSe−Py the photoexcited hole from the CdS core is captured by the Py molecule through the CdSe shell, so bleach recovery should be slower but the bleach recovers faster due to recombination between CdS/CdSe (e^-) and Py (h^+). Here Py^+ facilitates fast charge recombination reaction. However, due to the very thin CdSe shell, the electron became delocalized in both the core (CdS) and shell (CdSe) structure. As a result, some percentage of bleach still exists in presence of Py. To monitor charge transfer dynamics, the kinetics at the bleach wavelengths in the absence and presence of both the quenchers was monitored as discussed in the next section. Similarly, we have also carried out TA measurement of the CdSe/CdS quasi-type II core−shell in the absence and presence of BQ and Py. The TA spectra of CdSe/CdS (Figure 5.9 A) shows three distinct bleach appearing at 578, 530, and 481 nm, which can be attributed to 1S, 2S, and 1P electronic transitions of CdSe core QDs, respectively. The TA spectrum of the pure CdSe shows 1S and 1P distinct bleach. However in addition to the 1S and 1P the TA spectrum of the CdSe/CdS shows separate bleach at 530 nm due to 2S electronic transition. This might be due to the strong confinement of the CdSe core QDs by the CdS shell QDs, by which the electronic levels of the core CdSe become more distinct (Figure5.6 B and Figure 5.9 A). It is interesting to see that in the presence of BQ the transient signal for the CdSe/CdS core−shell (Figure 5.9 B) is drastically reduced. As we have already discussed in an earlier section, due to the low effective mass of the electron and smaller conduction band offset energy of the CdSe and CdS, the electron in the CdSe/CdS structure becomes delocalized into the entire CB of both CdSe core QDs as well as the CdS shell QDs. Thus, upon photoexcitation the excited electron can be easily captured by the quencher (BQ) molecule. Notably, no change was observed in the transient spectra in the presence of Py (hole quencher) (Figure 5.9 C). Due to the higher effective mass of the hole and large VB offset energy of the core CdSe QDs with respect to the CdS shell QDs, the hole becomes strongly confined in the core structure. As a result, hole quenching by Py was not observed. However, a minor change in signal intensity was observed that can be attributed to the leaking of photoexcited hole through CdS shell. The charge transfer dynamics of both the

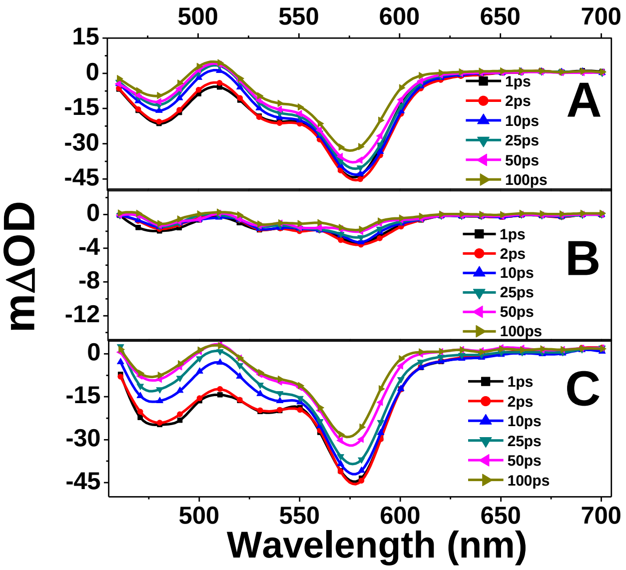

Figure 5.9: Transient absorption spectra of CdSe/CdS quasi type II core-shell (A) in absence of any quencher, (B) in presence of electron quencher (BQ) and (C) in presence of hole quencher (Py) in chloroform after exciting at 400 nm laser excitation.

core–shell NCs in the presence of both the quencher molecules will give a more clear idea about the charge carrier delocalization in the core–shell structures. In the next section, we have demonstrated the charge carrier delocalization through the kinetics decay trace in the absence and presence of the quencher molecules.

5.2.5. Charge Transfer and Charge Carrier Dynamics:

From the above experimental observations it is clear that both photoexcited electron and hole are localized in the shell of the CdS/CdSe inverted type I structure. However, in case of CdSe/ CdS core−shell, the hole is strongly confined in the core and the electron is delocalized throughout the shell; as a result, quasi-type II alignment is achieved. Now to reconfirm the e−h delocalization we have compared the bleach kinetics of the core−shell in both the presence and absence of the quencher molecules. Figure 5.10 A illustrates the normalized bleach recovery kinetics of the

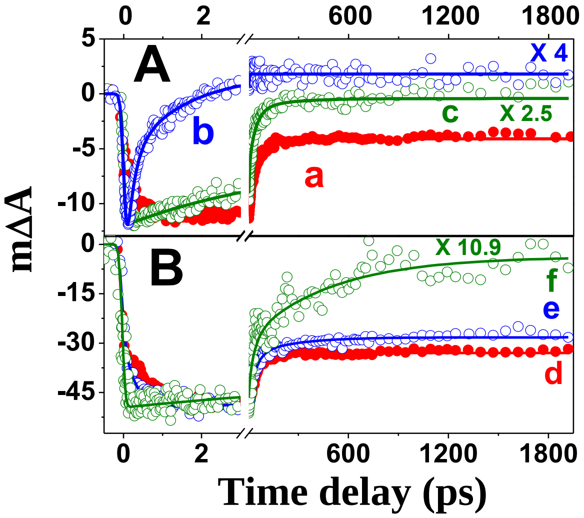

Figure 5.10: (**Panel A)** Normalized bleach recovery dynamics of CdS/CdSe inverted type I core shell (a) in absence of any quencher, (b) in presence of electron quencher (BQ) and (c) in presence of hole quencher (Py) at 578 nm in chloroform solution. (**Panel B)** Normalized bleach recovery dynamics of CdSe/CdS quasi type II core shell (d) in absence of any quencher, (e) in presence of electron quencher (BQ) and (f) in presence of hole quencher (Py) at 560 nm in chloroform solution.

CdS/CdSe core−shell probed at 560 nm in the absence and presence of the electron and hole quencher molecule. The bleach kinetics of the CdS/CdSe at 560 nm has biexponential growth (Table 5.2) with time constant $\tau_1(g) < 100$ fs (65%) and $\tau_2(g) = 0.3$ ps (35%), and it recovers multiexponentially with time constants $\tau_1 = 8$ ps (38%), $\tau_2 = 40$ ps (22%), $\tau_3 = 200$ ps (5%), and $\tau_4 > 2$ ns (35%) (Table 5.2). The second bleach growth time can be attributed to electron cooling time in the core−shell material, and the recovery kinetics can be attributed to recombination dynamics between electron and hole. However, it is interesting to see that the bleach kinetics of CdS/CdSe core−shell in the presence of BQ is completely different and can be fitted with pulse-width limited growth (<100 fs) and multiexponential recovery with time constants of $\tau_1 = 4$ ps (58%), $\tau_2 = 30$ ps (33%), $\tau_3 = 200$ ps (6.1%), and $\tau_4 > 2$ ns (2.9%) (Table 5.2).

Table 5.2: Multi-exponential fitting parameters for both CdS/CdSe type I inverted core-shell and CdSe/CdS quasi type II core-shell in absence and in presence of BQ and Py at their 1S bleach wavelengths (λ). The percentages at the parenthesis represent amplitude of the corresponding exponential functions.

System/λ(nm)	**τ_1(g)**	**τ_2(g)**	**τ_1**	**τ_2**	**τ_3**	**τ_4**
CdS/CdSe/560	<100fs (65%)	0.3ps (35%)	8ps (38%)	40ps (22%)	200ps (5%)	>2ns (35%)
CdS/CdSe-BQ/560	<100fs (100%)		4ps (58%)	30ps (33%)	200ps (6.1%)	>2ns (2.9%)
CdS/CdSe-Py/560	<100fs (100%)		0.2ps (81%)	1.5ps (19%)		
CdSe/CdS/578	<100fs (63%)	0.8ps (37%)	50ps (32%)	>2ns (68%)		
CdSe/CdS-BQ-578	<100fs (100%)		8ps (36%)	40ps (22%)	350ps (33%)	>2ns (9%)
CdSe/CdS-Py-578	<100fs (63%)	0.5ps (37%)	40ps (36%)	250ps (5%)	>2ns (59%)	

It is interesting to see that in the presence of BQ the second growth component of the bleach kinetics is missing, which clearly indicates that the electrons are captured by BQ before it cools down to the conduction band edge. Faster bleach recovery time can be attributed to the recombination dynamics between hole in the core−shell and BQ−. Here, BQ− reacts with the hole and it gets annihilated from the system. Actually, in the entire process, the electron and hole recombination process gets facilitated by BQ, which actually works as an electron shuttler.[323, 325] Similarly, the transient kinetics in the presence of Py can be fitted with pulsewidth- limited growth (<100 fs) and biexponential recovery with time constants of τ_1 = 0.2 ps (81%) and τ_2 = 1.5 ps (19%) (Table 5.2). The faster bleach recovery dynamics in the presence of the Py molecule suggests that the photoexcited holes are captured by Py with the formation of Py^+. Here the 200 fs time constant can be attributed to the hole transfer time from the core−shell to Py. Finally, the bleach signal is annihilated due to recombination between the Py^+ and the CdS/CdSe (e^-). Figure 5.10 B shows the normalized bleach recovery dynamics of the CdSe/CdS quasi-type II core−shell in the presence and absence of BQ and Py molecules at 578 nm in chloroform solution. The bleach kinetics of the CdSe/CdS can be fitted with biexponential growth with time constants of $\tau_1(g)$ = 100 fs (63%) and $\tau_2(g)$ = 0.8 ps (37%) and biexponential recovery with time constants of τ_1 = 50 ps (32%) and τ_2 = 2 ns (68%) (Table 5.2). Again the slow growth component (800 fs) can be attributed to electron cooling time.[82, 127] We have also compared the bleach kinetics at the 1S excitonic position for CdSe/CdS quasi-type II core−shell with that of pure CdSe QDs, as shown in the Figure 5.11. The bleach dynamics of the CdSe at 555 nm (Figure 5.11 a) which can be fitted with bi-exponential growth and multi-exponential recovery. However, the bleach of the CdSe/CdS (Figure 5.11 b) fitted with bi-exponential growth and bi-exponential recovery. In the case of CdSe QDs, the cooling time of the electron was determined to be 500 fs. The slower cooling time (800 fs) in CdSe/CdS quasi-type II core−shell as compared to CdSe QDs (500 fs) can be attributed to decoupling of the electron due to delocalization from the hole in the quasi-type II band structure (Scheme 5.2). In the presence of BQ (electron quencher), the kinetics can be fitted with pulse-width-limited growth (<100 fs) and multiexponential recovery with time constants of τ_1 = 8 ps (36%), τ_2 = 40 ps (22%), τ_3 = 200 ps (33%), and τ_4 > 2 ns (9%) (Figure 5.9f and Table 5.2). Here, also in the presence of BQ, the second growth component of the bleach kinetics is missing, which clearly indicates that the electrons are captured by BQ before it cools down to the conduction band edge. The faster bleach recovery time can be attributed to recombination dynamics between the hole in the core−shell and BQ−. However, most interestingly, no significant changed has been observed in the bleach recovery kinetics in the presence of Py (hole quencher). The bleach kinetics at 578 nm can be fitted with biexponential growth with time constants of τ_1(g) < 100 fs (36%) and τ_2 = 0.5

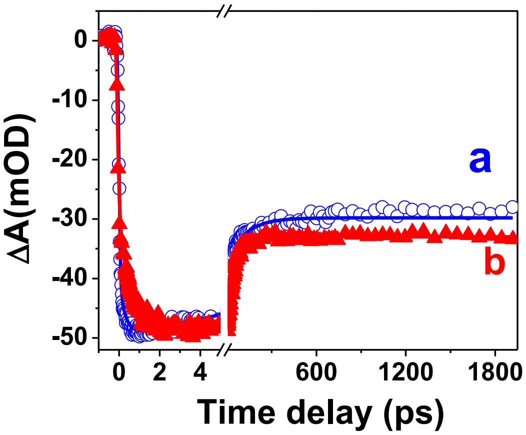

Figure 5.11: Comparison 1S bleach recovery kinetics of CdSe (555 nm) (a) and CdSe/CdS quasi type II core-shell (578 nm) (b).

ps (37%) and it recovers multiexponentially with time constants of τ_1 = 40 ps (36%), τ_2 = 250 ps (5%), and τ_3 > 2 ns (59%). The similar bleach recovery in the presence of Py (hole quencher) suggests that the photoexcited hole is not transferred to the Py through the CdS shell very efficiently. Very little change in the kinetic trace can be attributed as hole leaking from the core CdSe to Py through CdS shell.

5.3. Conclusion

In summary, we have synthesized two core−shell NCs, CdSe/ CdS quasi-type II and CdS/CdSe inverted type I, and characterized them by steady-state absorption, luminescence, XRD, and high-resolution TEM techniques. The location of charge carriers in the heterostructures has been demonstrated with the help of quenching studies with BQ (electron quencher) and Py (hole quencher) using steady-state and time-resolved luminescence and absorption spectroscopic techniques. Steady-state and time-resolved PL studies reveal quenching of both electron and hole in CdS/CdSe inverted type I core−shell in presence BQ and Py, respectively; however, only electron-quenching was observed in CdSe/CdS quasi-type II core−shell in the presence of BQ. Our experimental observation suggests that in CdS/CdSe inverted type I core− shell both electrons and holes are localized in CdSe shell QDs; however, in CdSe/CdS quasi-type II, holes are localized in CdSe core QDs and electrons are delocalized in the conduction band of both CdSe core and CdS shell QDs due to the low conduction band offset. Electron transfer times from the core QDs to the BQ quencher through shell QDs in both the above systems are found to be pulse-width-limited (<100 fs); however, the hole transfer time from CdS core QDs to Py molecule through CdSe shell was found to be ~200 fs. Prior to charge (either electron or hole) separation in core−shell/quencher composite systems, fast charge recombination occurs between either electron or hole in core−shell and Py^+ or BQ^-, respectively. This observation clearly suggests that quencher molecules initially captured either electron or hole, depending upon thermodynamic feasibility, and later on facilitate fast charge recombination. From our studies we can suggest that it is possible to design and synthesize core−shell heterostructures through band gap engineering where one can selectively localize electron or hole, depending upon application.

CHAPTER-6

Charge Transfer Dynamics in Heterostructure Core/Shell Nanocrystals and Molecular Adsorbate

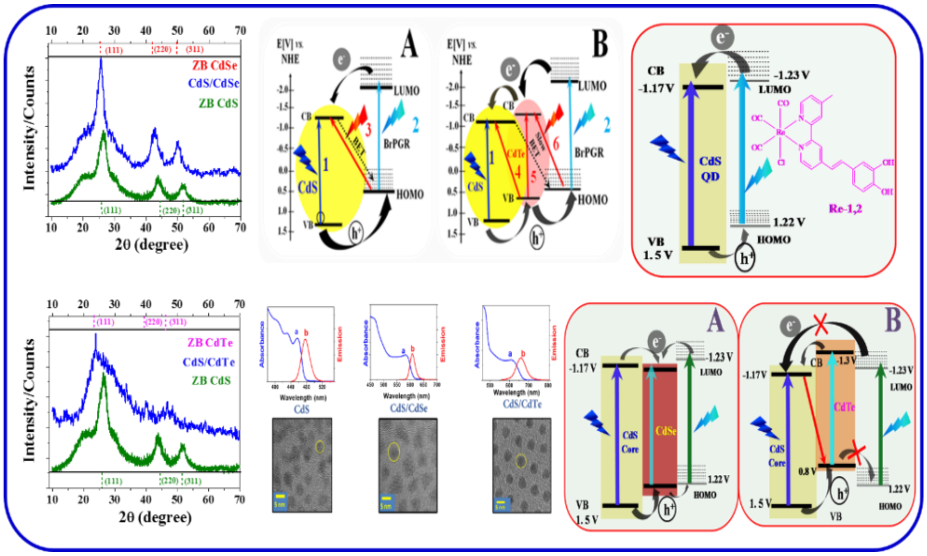

- ➢ ***Nanoscale***, **2015,** ***7***, **2698–2707.**
- ➢ ***J. Phys. Chem. C***, **2016,** ***120***, **10051–10061.**

6.1. Introductions:

Recent worldwide research, the fundamental studies and the inherent properties such as band gap tunability, high extinction coefficient, MEG and the high photostability of the semiconductor QD help to robust in widespread application in several exciting field including photovoltaic performance in the low cost third generation QDSC.[16, 31, 44, 48, 97, 98, 245, 256, 300, 329-332] Despite its interesting photo-physical properties, the photo-current conversion efficiency in the QDSC has failed to achieve theoretical expected value [46] because of their sub picoseconds charge carrier annihilation [87, 93, 333] owing to strong coulomb attraction in the short distance size quantized state. To preclude exciton annihilation and alleviate charge separation often core-shell NCs are used as a photo-anode in QDSC.[218, 334] For type-I core-shell, [319, 335] both the charge carriers (electron and hole) are localized in the low band gap material, while for type-II core-shell,[116] one of these two charge carriers are either localized in core or in shell and eventually two well recognized heterojunction NCs exploit these charge carriers for better performance.

In addition, the QD and the core-shell NCs absorb limited solar radiation and lower loading on TiO_2 film adversely influence the solar cell performance. Moreover, due to slower hole transfer rate as compare to electron injection, the photo anode corrosion is induced by the excess photo-generated hole.[47] To address these issues and improve the efficiency in QDSC, molecular adsorbates are also used as a co-sensitizer, which actually perform dual functions; injecting electron and accepting the hole from the NCs materials. Earlier Kamat et al.[224] and several other research groups [212, 298, 310, 336, 337] have demonstrated better efficiency in such supersensitized system. To ameliorate QDSC performance, it is essential to develop a better insight in charge separation and charge recombination dynamics of the composite system.

As the charge separation of the type-II core/shell is more due to their inherent heterojunction band alignment, type-II NCs are widely used as light harvester in QDSC. Introducing an organic molecular adsorbate with type-II core-shell it is possible to improve further charge separation where both photo-excited QD and molecular adsorbate actively take part in charge separation process. In addition to that the dye molecule form strong CT complex which absorb more and broad light in the solar spectrum.

Organic dye molecules are being widely used as sensitizer for DSSC application. Photo stability is an important issue for such dye molecules and in general metal polypyridyl complexes are superior to these organic dyes in terms of photostability and thus, more suitable for sustained usages. It is even more challenging if the photo-anode of a QDSC is made on metal polypyridyl complex instead of organic sensitizer molecule. There are many literature reports on charge transfer process associated with QD coupled Ru(II)-polypyridyl complex. However, information and literature reports on such hybrid involving Re(I)-bipyridyl complex are scarce in the contemporary literature. [338, 339] Earlier Lian et al.[340] demonstrated photoinduced ultrafast electron transfer from CdSe QD to Re-bipyridyl complex in such a hybrid system and there was a distinct evidence for energy transfer pathway along with the electron transfer process. However, there are only limited recent examples on the hole and electron transfer dynamics in a composite system having metal polypyridyl coupled QD.[341] To improve any kind of device efficiency using different core-shell and molecular adsorbate it is very important to understand charge transfer dynamics in ultrafast time scale where both electron and hole transfer processes are involved.

In this chapter we have demonstrated the charge transfer dynamics of CdS QDs and CdS/CdTe type-II core shell sensitized by Br-PGR in fast and ultrafast time scale using time-resolved emission and femtosecond time-resolved absorption techniques. Redox energy levels of the CdS QD and Br-PGR molecule imply that the HOMO and LUMO levels of the Br-PGR molecule lies energetically above the VB and CB of CdS QD and CdS/CdTe core-shell. In the composite materials photo-excited Br-PGR can inject electron into the CB of both CdS QD and CdS/CdTe core-shell and Br-PGR also can extract hole from VB of photo-excited CdS QD and CdS/CdTe core-shell. Cascading electron and hole transfer in the type II regime help to separate more charge carrier as a results we have observed slow charge recombination as compare to only CdS. Concomitantly, the charge carrier separation and restriction of charge carrier delocalization has also been investigated using CdS, CdS/CdSe and CdS/CdTe sensitized by Re (I)- polypyridyl complex. Charge separation in the CdS and CdS/CdSe is observed due to favourable energy levels which also supported from the time resolved absorption and emission studies. However, in the CdS/CdTe core-shell due to larger energy barrier we could not able to see the separation of the charges.

6.2. Results and Discussion:

6.2.1. Morphology Analysis and Optical Properties:

To analyze the structural morphology of the synthesized NCs we have carrier out XRD measurements and plotted in the Figure 6.1. The XRD pattern of the CdS/CdSe inverted type-I and CdS/CdTe type-II with respect to CdS are depicted in the Figure 6.1 A and B respectively. For CdS core all the peaks corresponding to 111, 220 and 311 planes matches with ZB crystalline phase of CdS. For CdS/CdSe core-shell the peaks are shifted towards low angle and the peaks are matches with ZB planes of CdSe nanocrystals. The XRD pattern clearly shows the formation of CdSe shell on CdS core. Similarly in case of CdS/CdTe core-shell XRD peaks due to the CdTe ZB crystalline phase appear in the low angle in the XRD spectrum.

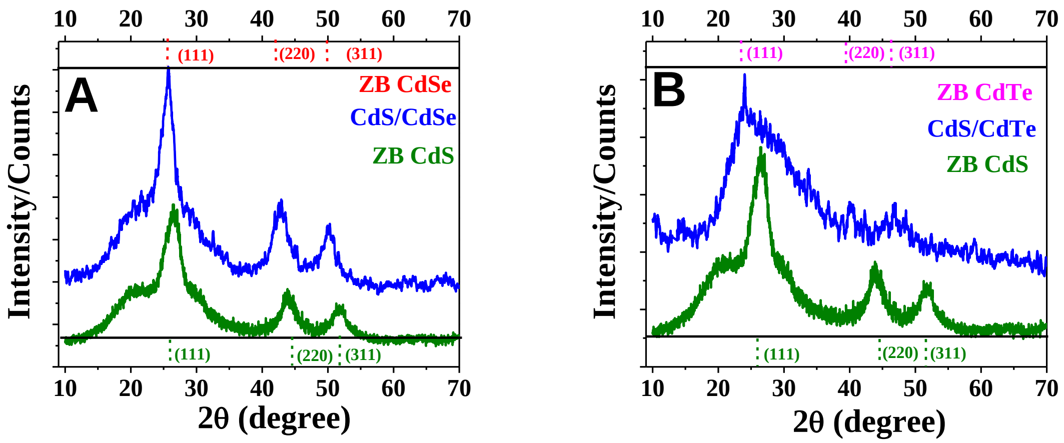

Figure 6.1: Powder XRD pattern of (A) CdS QD and CdS/CdSe type-I core-shell and (B) CdS and CdS/CdTe type II core-shell respectively. Vertical dotted lines olive, red and magenta represent (111), (220) and (311) diffraction plane position of ZB CdS, CdSe and CdTe phases respectively.

After synthesizing both CdS QD and CdS/CdTe core-shell, we have carried out steady state optical absorption and emission properties and also measured the size of the particle by high resolution TEM. Figure 6.2 **(I)** (top panel) shows the optical absorption and emission spectra of CdS QD and Figure 6.2 **(II)** depicts the HRTEM image of that CdS QD. From steady state spectra it is clear that the first exciton of the QD appeared at 434 nm and the corresponding size was measured to be 2.5 nm from TEM image. Photoluminescence peak of CdS QD was observed to be 452 nm with emission quantum yield of 36% after exciting the QD at 375 nm and shown in Figure 6.2 (top panel, Figure 6.2 **I** trace “b”). Figure 6.2 **(III)** (bottom panel) shows the optical absorption and emission spectra of CdS/CdTe core/shell QD and Figure **6**.2 (**IV**) depicts the HRTEM image of synthesized CdS/CdTe core/shell. In optical absorption spectra one sharp peak appears at 436 nm and a broad absorption band appears in 500-600 nm regions. The absorption peak at 436 nm can be attributed to excitonic absorption due to CdS core and broad absorption

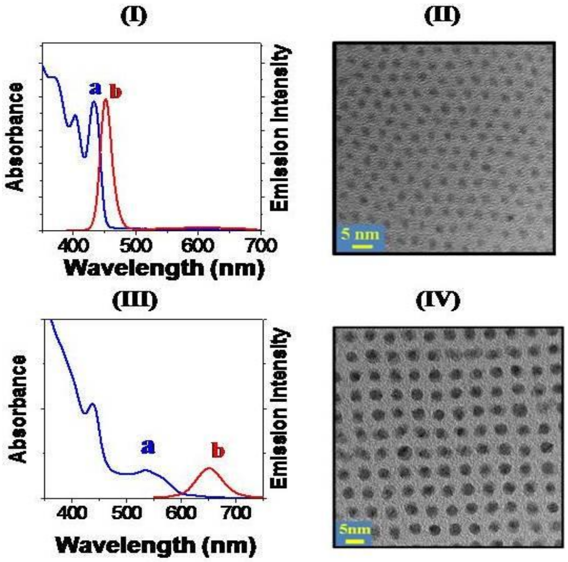

Figure 6.2: (I), **(III)** Optical absorption (a) and emission spectra (b) **(II), (IV)** HRTEM image of CdS QD and CdS/CdTe respectively.

band can be attributed to indirect band-gap transition in CdSe/CdTe type II core-shell. Size of the particle was determined to be 3.2 nm as measured from HRTEM studies. Photoluminescence peak of CdS/CdTe core-shell was detected at 652 nm after exciting at 530 nm with relatively low emission quantum yield of 2.9% which is might be due to indirect band transition and also due to leaking of hole through surface induced non-radiative channels. Even after exciting CdS/CdTe core-shell at 374 nm, emission only due to indirect band transition at 652 nm was observed.

Similarly to perform the charge carrier movement in two different heterostructure regime we have deliberately synthesized CdS core and CdS/CdSe inverted type I and CdS/CdTe type II core shell. The optical properties and HRTEM images of CdS, CdS/CdSe and CdS/CdTe are depicted in the Figure 6.3. Corresponding band edge emission and monodispersed size distribution of the NCs suggest the formation very good crystalline materials. The sensitization of the NCs with the molecular adsorbate have been demonstrated in the next section.

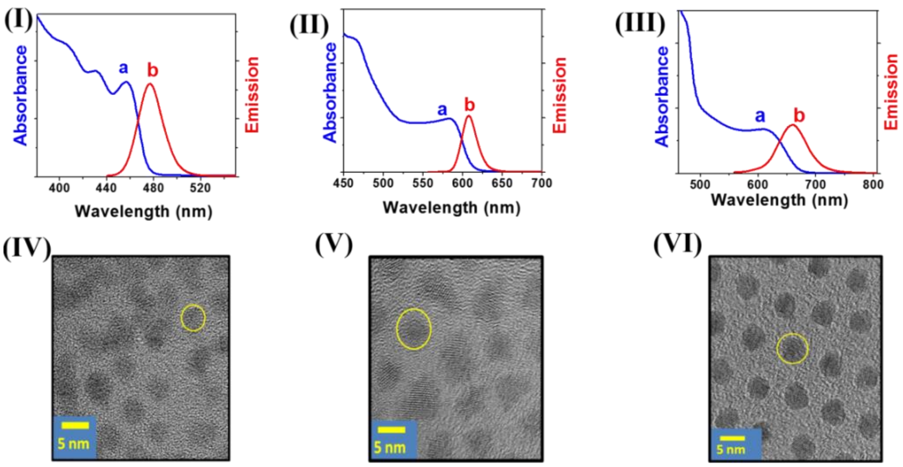

Figure 6.3: (I), **(II), (III)** Optical absorption (a) and emission spectra (b) **(IV), (V)** and **(VI)** HRTEM image of CdS QD CdS/CdSe and CdS/CdTe respectively.

6.2.2. Ground State Interaction: Steady state optical absorption measurement:

i. CdS, CdS/CdTe with Br-PGR.

Main aim of the present chapter is to understand charge transfer behaviour in the excited state of CdS and CdS/CdTe with Br-PGR and CdS, CdS/CdSe and CdS/CdTe with Re (I) complex composite materials and its applicability as a super sensitizer [224, 298, 342] in QDSC. In this circumstance it is very important to monitor the ground state interaction between the NCs and the molecular species. Charge transfer interaction between QD and molecular adsorbate are not widely reported in the literature except our few report,[298, 299, 310] where the composite materials form strong charge transfer complex. In our earlier investigation [226] we have demonstrated that Br-PGR is one of the molecules in tri-phenyl methane series of dyes which can be potential sensitizer molecule in DSSC where LUMO of Br-PGR lies above the conduction band of TiO_2. Figure 6.4A shows steady state optical absorption spectra of CdS QD (Figure 6.4 a), Br-PGR (Figure 6.4 b) and Br-PGR/CdS QD composite (Figure 6.4 c) in chloroform. Free Br-PGR shows optical absorption up to 650 nm with a peak at 480 nm which is attributed to lowest optical transition between HOMO and first excited state (S_1) of the Br-PGR molecule (Figure 6.4 b). Interestingly on addition of Br-PGR in CdS solution, the color of the solution becomes deep blue (while the color of free Br-PGR and CdS are brown red and yellow respectively). The composite mixture shows broad absorption spectra (Figure 6.4c) in the entire visible region (beyond 750 nm) with a red shifted peak at 552 nm which indicates formation of strong charge transfer complex. We have also carried out steady state optical absorption studies of CdS/CdTe core-shell after sensitizing with Br-PGR. Figure 6.4 B shows the optical absorption spectra of CdS/CdTe (Figure 6.4d), Br-PGR (Figure 6.4e) and CdS/CdTe sensitized Br-PGR (Figure 3f). Optical absorption spectra of CdS/CdTe/Br-PGR composite mixture become much broader and red-shifted with absorption maxima at 570 nm. A higher extinction coefficient of the QDs-Br-PGR composites suggest that Br-PGR form strong charge transfer complexes with both the QDs (CdS QD, CdS/CdTe type II core-shell) where partial charge

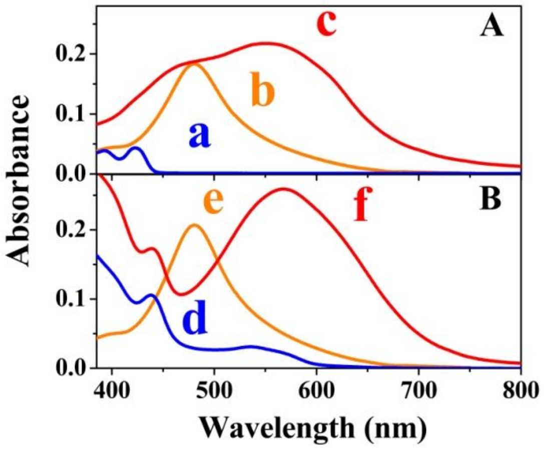

Figure 6.4: (A) Optical absorption spectra of (a) CdS QD (0.1µM), (b) Br-PGR (36µM) and (c) CdS QD sensitized PGR in chloroform. **(B)** Optical absorption spectra of (d) CdS/CdTe core/shell (0.1µM), (e) Br-PGR (b, 40µM) and (c) CdS/CdTe core-shell sensitized Br-PGR in chloroform.

transfer take place in the ground state. It is interesting to see that Br-PGR form better complex with CdS/CdTe type II core-shell as compared pure CdS QD. This observation clearly suggests that both the composite systems potential material for supersensitizer, which can absorb more solar radiation as compared to that of the individual QDs and Br-PGR molecule.

ii. CdS, CdS/CdSe and CdS/CdTe with Re(I)-bipyridyl complex.

On the other hand the steady state interaction of CdS QD with the Re (I) complex has also been investigated. The steady state optical absorption spectrum of CdS (Figure 6.5 a) shows the first excitonic absorption (1S) at 451 nm due to $1S_{3/2h}$-$1S_e$ electronic transition. Re-1,2 in chloroform (Figure 6.5b) shows a broad absorption up to 750 nm with a maximum absorption at ~ 406 nm region. Unlike to above observation, the optical absorption spectrum of the CdS/Re (I) (Figure 6.5c) does not change significantly and the spectral signature of the composite system is more like to the additive optical spectra of the nanocrystal and Re-1,2. Absence of any red shifted optical band for the QD/dye composite system in the absorption measurement indicates that

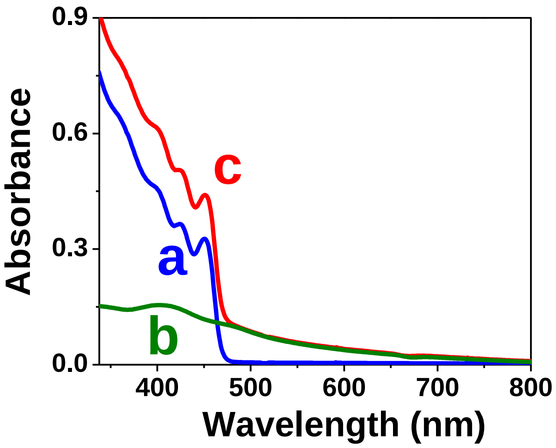

Figure 6.5: UV-Vis spectra of (a) CdS QD (0.5 µM), (b) Re1,2 dye (0.2 mM), (c) CdS-Re1,2 composite mixture in chloroform.

there is very weak interaction between the QDs and Re-1,2. In our earlier investigation also we have not observe formation of CT complex between Re-1,2 and CdSe QD. [341] However, we have observed that Re 1,2 molecule form strong CT complex with TiO_2 nanoparticle.[343] This might be due to higher density of state in the CB of TiO_2 NP as compared to that of CdS QD. The other interest of the present chapter is to understand the charge transfer interaction between Re-1,2 complex and the core -shells. To do so we have synthesized two different core-shell structures, CdS/CdSe type I and CdS/CdTe type II and investigated the charge transfer interaction. We have carried out optical absorption studies of both the core-shell in absence and in presence of Re-1,2 dye and shown in Figure 6.6 A and Figure 6.6 B respectively. In both the

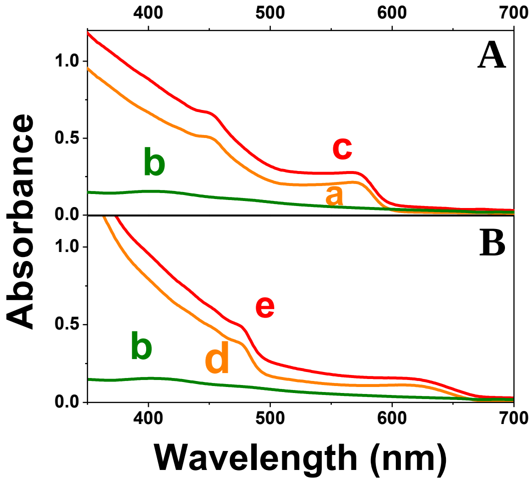

Figure 6.6: **(A)** UV-Vis spectra of (a) CdS/CdSe, (b) Re-1,2, and (c) CdS/CdSe-Re1,2 mixture and **(B)** UV-Vis spectra of (d) CdS/CdTe, (e) CdS/CdTe-Re1,2 mixture in chloroform.

core-shell structures, the core QD is common i.e. CdS. The CdS/CdSe core-shell shows type I band alignment where the VB and CB energy levels of the CdSe shell lie energetically lower than the core CdS energy level. Optical absorption spectra of CdS/CdSe core-shell shows two absorption bands at 571 nm and 451 nm which can be attributed to excitonic absorption bands due to CdSe shell and CdS core QDs respectively (Figure 6.6 a). On the other hand Figure 6.6 d shows optical absorption spectra of CdS/CdTe type II core-shell which has two distinct absorption peaks at 475 and 622 nm due to CdS core and the indirect band transition from VB of the CdTe to the CB of the CdS respectively. Figure 6.6A and Figure 6.6B suggest that Re-1,2 dye does not make any CT complex with both CdS/CdSe and CdS/CdSe core-shells. The charge carrier localization is demonstrated in the next section following selective excitation.

6.2.3. Hole Transfer Reaction:

i. CdS, CdS/CdTe with Br-PGR.

From steady state optical absorption measurements we have observed that Br-PGR form strong CT complex with both CdS QD and CdS/CdTe type II core-shell. Now to understand charge transfer dynamics in the excited state in CdS/Br-PGR composite material steady state emission spectroscopy have been carried out by exciting Br-PGR, CdS QD and CdS/Br-PGR composite material at 375 nm and shown in Figure 6.7. No luminescence was observed from the Br-PGR molecule after exciting at 375 nm, which might be due presence of multiple hydroxyl group adjacent to the phenyl ring that facilitate faster non-radiative decay process. At the same time presence of heavy atom (Br) which increases the nonradiative ISC process. Figure 6.7a shows photoluminescence spectra of the CdS QD in chloroform after exciting at 375 nm, which consists an emission peak at 452 nm with high emission quantum yield (ϕ_{CdS} = 36%). Figure 6.7b shows the emission spectra of CdS QD in the presence of 36 μM Br-PGR in chloroform solution. It is very interesting to see that the emission intensity of the CdS QD is drastically reduced in presence of Br-PGR molecule. Due to close proximity between QD and molecular adsorbate in the CdS/Br-PGR composite system one can envisage emission quenching might be due to energy transfer. To realize energy transfer it's very important to have overlap between QD luminescence and Br-PGR absorbance. It has been observed that there is some overlap between CdS luminescence and Br-PGR absorbance.

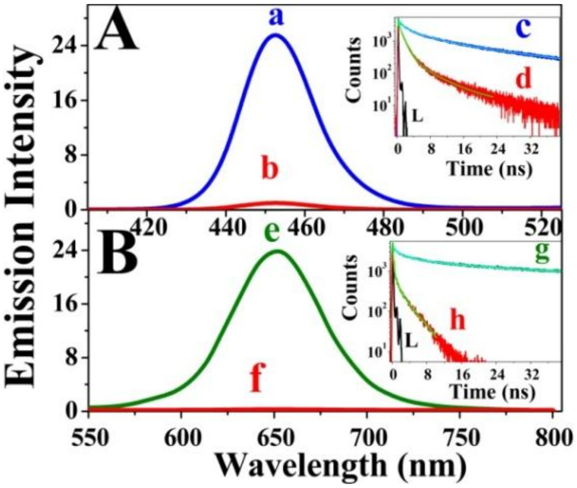

Figure 6.7: (Panel A) Photoluminescence spectra of the CdS QD in absence (a) and in presence of Br-PGR (b) after exciting at 380 nm. **Inset**: Emission decay traces of the CdS QD (c) and CdS/Br-PGR (d) composite after exciting at 374 nm and monitoring at 452 nm. (**Panel B)** Photoluminescence spectra of the CdS/CdTe QD in absence (e) and in presence of Br-PGR (f) after exciting at 500 nm. **(Inset)** Emission decay traces of the CdS/CdTe (g) and CdS/CdTe with Br-PGR (h) composite after exciting at 406 nm and monitoring at 650 nm. **L** is the excitation profile.

However no luminescence was observed from Br-PGR after exciting CdS in the CdS/Br-PGR composite system. Still we cannot rule out energy transfer process between CdS QD and Br-PGR. However, it is clearly seen from Scheme 6.1 that the VB (1.35 V versus NHE) of CdS lies below the HOMO (0. 458 V vs NHE) of Br-PGR, so the photo-excited hole in the valence band of CdS can be captured by Br-PGR, which is thermodynamically viable process. So the emission quenching can be attributed to hole transfer from photo-excited CdS to Br-PGR molecule. The hole-transfer reaction can be expressed by the equations below:

$$\mathbf{CdS + h\nu \rightarrow CdS\ (e^- + h^+)} \qquad \mathbf{(6.1)}$$

$$\mathbf{CdS\ (e^- + h^+) + Br\text{-}PGR \rightarrow CdS\ (e^-) + Br\text{-}PGR\ (h^+)} \qquad \mathbf{(6.2)}$$

To reconfirm the hole transfer process and to monitor hole transfer dynamics we have carried out time-resolved emission studies of pure CdS QD and also Br-PGR sensitized CdS QD and shown in Figure 6.7 inset. The emission decay traces of the CdS QD and CdS/Br-PGR composite have been monitored at 452 nm after exciting the samples at 374 nm laser excitation source.

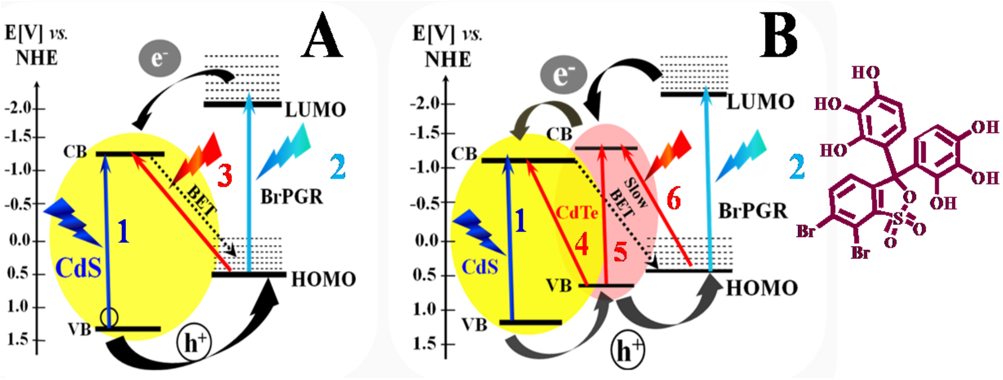

Scheme 6.1: Schematic diagram illustrating electron and hole transfer process in CdS QD (section A) and CdS/CdTe-Type-II core/shell QD (section B) sensitized by Br-PGR. **Process 1** shows excitation of CdS QD and whereas **Process 2** shows photo-excitation of Br-PGR. **Process 3** indicates direct transfer of electron from HOMO of Br-PGR to conduction band of CdS. **Process 4** shows indirect photo-excitation electron from valence band CdTe shell QD to conduction band of core CdS QD. **Process 5** shows photo-excitation of CdTe shell QD. **Process 6** indicates direct transfer of electron from HOMO of Br-PGR to conduction band of CdTe shell. Electron injection and hole transfer reaction in both composite materials are shown. Dotted line in both the scheme indicates charge recombination reaction between electron in CdS QD and Br-PGR cation radical. **BET** process is slower in case of CdS/CdTe-BrPGR composite system. Molecular structure of the Br-PGR are shown in scheme (right side).

The emission decay traces for the CdS QD can be fitted multi-exponentially with time constants τ_1 = 0.951 ns (24.2%), τ_2 = 5.59 ns (29%), τ_3 = 23.11 ns (46.8%), with τ_{avg} =12.7 ns (Trace c Figure 6.7 A). Here the short decay component (~0.951 ns) can assigned to the optically active $1S_e-1S_{3/2}$ exciton state. However the longer components, (~5.59) and (~23.11 ns) can be assigned to surface-trapped charge carriers and the dark exciton state in CdS QD.[77, 313] Interestingly the emission decay traces for CdS/Br-PGR can be fitted multi-exponentially with time constants of τ_1 = 0.16 ns (43.4%), τ_2 = 1.2 ns (51.1%), τ_3 = 5.78 ns (5.5%), with τ_{avg} =1 ns respectively (Trace trace d Figure 6.7 A). It is interesting to see that the average lifetime of the CdS/Br-PGR system is more than 12 fold shorter as compared to that of CdS QD, which confirms a hole-transfer process in the composite materials, as suggested in equation 6.2. Presumably, the observed decrease in lifetime arises due to HT from the CdS QD to Br-PGR molecule, and then, the hole-transfer rate constant can be determined through the following expression

$$\mathbf{k_{HT} = (1/\tau_{CdS/Br\text{-}PGR}) - (1/\ \tau_{CdS})} \qquad \mathbf{(6.3)}$$

Using the average lifetime values of 12.7 ns (CdS) and 1 ns (CdS/Br-PGR), the hole-transfer rate constant can be determined to be $9.2 \times 10^8\ s^{-1}$.

It has been observed that Br-PGR form strong CT complex with CdS/CdTe which indicates that charge transfer takes place in the ground state itself. To corroborate charge transfer process in the excited state we have also carried out both steady state and time resolved emission studies type II (CdS/CdTe) core-shell in presence and absence of Br-PGR adsorbate molecule to monitor charge transfer process. Figure 6.7B depicts the photoluminescence spectra of CdS/CdTe type II core/shell in absence (trace e) and in presence (trace f) of Br-PGR molecule after exciting at 530 nm. No emission was observed for pure Br-PGR after exciting at 530 nm.

Exciting CdS/CdTe type II core/shell at 530 nm, luminescence was observed in 580 – 720 nm region with emission peak at 652 nm (with quantum yield $\phi_{CdS/CdTe}$ = 2.9%). This can be attributed to indirect band gap emission. Now in presence Br-PGR the indirect photoluminescence of the core/shell completely quenches. Energy transfer between photo-excited CdS/CdTe core-shell and Br-PGR can be rule out as there is no overlap between core-shell luminescence and Br-PGR absorbance. So the emission quenching can be attributed purely due to hole transfer from CdTe to Br-PGR. The hole-transfer reaction can be expressed by the equations below:

$$\mathbf{CdS/CdTe + h\nu \rightarrow CdS\ (e^{-}) + CdTe\ (h^{+})} \qquad \mathbf{(6.4)}$$

$$\mathbf{CdTe\ (\ h^{+}) + Br\text{-}PGR \rightarrow CdTe + Br\text{-}PGR\ (h^{+})} \qquad \mathbf{(6.5)}$$

On photoexcitation of CdS/CdTe type II core shell, the photo-excited electron will be localized in conduction band of CdS core while hole will be localized in the valence band of CdTe shell (Scheme 6.1B). In presence of Br-PGR adsorbate photo-excited hole will be transferred to Br-PGR as the valence band of CdTe lies below the HOMO of Br-PGR (Scheme 6.1B). Now to verify the cascading charge transfer dynamics we have carried out time-resolved emission studies. Figure 6.7B inset shows the emission decay trace of CdS/CdTe core/shell in absence and in presence at 652 nm after exciting the samples at 406 nm laser excitation source. The emission decay trace for CdS/CdTe core/shell (Figure 6.7g) and CdS/CdTe core/shell with Br-PGR (Figure 6.7 h) can be fitted multiexponentially with time constants τ_1 = 0.17 ns (58%), τ_2 = 2.2 ns (21%), τ_3 = 19.8 ns (21%), with τ_{avg} =15 ns and τ_1 = 0.2 ns (89%), τ_2 = 1 ns (7%), τ_3 = 4.2 ns (4%), with τ_{avg} =0.42 ns. It is clearly seen that in presence of Br-PGR emission intensity drastically reduced which can be attributed due to hole transfer from photo-excited hole from type II core shell to Br-

PGR where the hole transfer rate can be monitored by using the equation below and the hole transfer rate is measured to be 2.2 X 10^9 sec^{-1}.

$$\mathbf{k_{HT} = (1/\tau_{CdS/CdTe\text{-}BrPGR}) - (1/\tau_{CdS/CdTe})} \qquad \mathbf{(6.6)}$$

From the Scheme 6.1, it is clear that a photoexcited Br-PGR molecule can inject an electron into the CB of CdS QD and in the CB of CdTe in CdS/CdTe type II core-shell.

ii. CdS, CdS/CdSe and CdS/CdTe with Re(I)-bipyridyl complex.

Similarly to examine the feasibility of both the electron and hole transfer processes in CdS/Re composite system we have depicted the CB and VB of CdS QD and the redox energy levels Re -1,2 complex in Scheme 6.2. The energy level diagram of the composite system suggests that both the CB and VB of CdS QD lie below the LUMO and HOMO levels of the Re-1,2 complex respectively. Thus the photo-excited hole in CdS can easily be captured by the Re-1,2 complex. Again the photo-excited Re molecule can inject electron to the CB of the CdS QD. To confirm hole transfer process we have carried out steady state PL measurement after exciting at 420 nm and are plotted in Figure 6.8. The steady state PL spectrum of the CdS QD (Figure 6.8a) shows emission maxima at 476 nm. Interestingly, the emission intensity of the CdS QD is completely diminished in the CdS/Re composite system (Figure 6.8b). This observation can be assigned as hole transfer from photo-excited CdS to the Re complex which is thermodynamically favourable (Scheme 6.2). At this point we would like to mention that on photo-excitation of Re-complex no emission was observed as shown in Figure 6.8c. Now the hole transfer process of the composite system can be expressed by the following equations

$$\mathbf{CdS + h\nu \rightarrow CdS\ (e^- + h^+)} \qquad \mathbf{(6.7)}$$

$$\mathbf{CdS\ (e^- + h^+) + Re\text{-}complex \rightarrow CdS\ (e^-) + Re\text{-}\ complex^+} \qquad \mathbf{(6.8)}$$

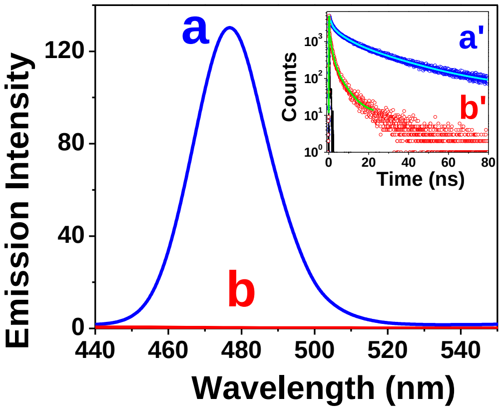

Figure 6.8: Steady state PL spectra of the CdS QD (a) in absence and (b) in presence of Re-1,2 after exciting at 420 nm. **Inset**: Emission decay traces of (a') CdS QD and (b') CdS/ Re-1,2 composite in chloroform. (λ_{ex}=445 nm λ_{em}=476 nm).

In addition to thermodynamically favourable hole transfer process, energy transfer process from photo-excited CdS QD to Re-1,2 cannot be completely ignored as there is overlap between optical absorption spectra of Re-1,2 and luminescence spectra of CdS QD. In addition to the steady state PL measurement we have also carried out time resolved PL experiment to reconfirm the emission quenching of the CdS QD in presence of the Re-1,2. Figure 6.8 inset shows the PL decay traces of CdS QD in absence and in presence of Re-1,2 at 476 nm after exciting at 445 nm laser radiation. The luminescence decay trace of CdS QD at 476 nm can be fitted using exponential parameter with the time constants τ_1 = 1 ns (24.2%), τ_2 = 5.59 ns (29%) and τ_3 = 22.11 ns (46.8%) with average lifetime (τ_{avg}) = 12.1 ns. Interestingly the emission trace of the CdS-Re-1,2 shows faster decay and the decay trace can also be fitted exponentially with decay time constants τ_1 = 0.036 ns (41.7%), τ_2 = 1.14 ns (30.11%) and τ_3 = 4.56 ns (28.11%) with average lifetime (τ_{avg}) =1.6 ns. This results clearly show the evidence of hole transfer from photo-excited CdS QD to Re-1,2 dye (Scheme 6.2) which is energetically viable process. So considering the decrease in PL life time of the CdS QD in presence of Re-complex as hole transfer we can easily calculate the hole transfer rate by using the following expression and the measured hole transfer rate is found to be 5.46x10^8 sec^{-1}.

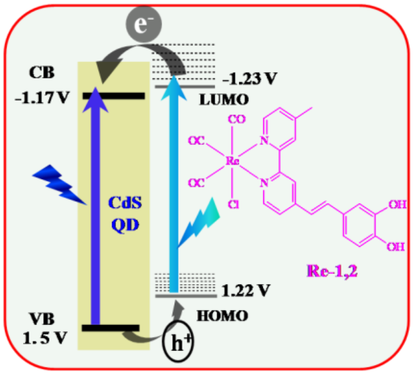

Scheme 6.2: Schematic presentation of charge transfer interaction in CdS-Re-1,2 composite system after photo-excitation. Energy levels are mentioned with respect to NHE. Molecular structure of Re-complex are shown in the scheme.

$$\mathbf{k_{HT} = (1/\tau_{CdS/Re\text{-}complex}) - (1/\ \tau_{CdS})} \qquad \mathbf{(6.9)}$$

The band alignment of both CdS/CdSe type I and CdS/CdTe type II core-shell and the redox energy levels Re -1,2 complex is shown Scheme 6.3. Figure 6.9A depicts the steady state PL spectra of CdS/CdSe core-shell in absence and in presence of Re-1,2 dye in chloroform after 550 nm excitation. The CdS/CdSe core-shell shows red shifted luminescence band with maximum intensity at ~602 nm. Interestingly the emission intensity of the CdS/CdSe core-shell is completely diminished in presence of the Re-complex (Figure 6.9b). The quenching of CdS/CdSe luminescence in presence of Re-1,2 clearly suggest the hole transfer from CdS core to Re-complex cascading via CdSe shell where all the processes are energetically feasible (Scheme 6.3 A). Again, time resolved PL experiments have been carried out to reconfirm the quenching of the CdS/CdSe luminescence in presence of Re-complex and plotted in Figure 6.9A inset. Time resolved PL decay traces of CdS/CdSe (Figure 6.9a') and CdS/CdSe with Re-complex (Figure 6.9b') at 602 nm have been carried out after exciting at 445 nm laser radiation. The faster decay trace of the CdS/CdSe-Re-1,2 composite mixture at 602 nm implies the hole transfer from core

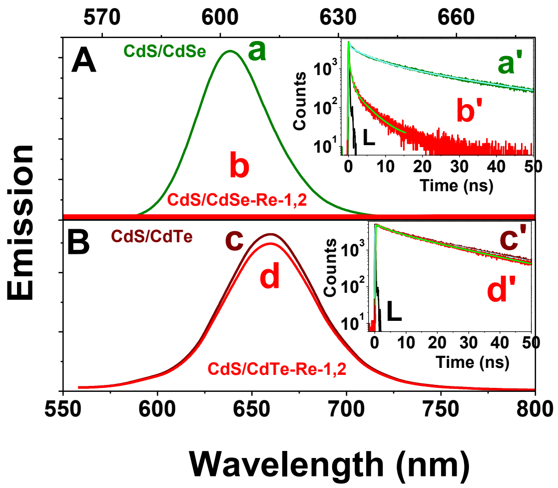

Figure 6.9: (A) PL spectra of CdS/CdSe (a) in absence and (b) in presence of Re-1,2 after exciting at 520 nm. **Inset**: Emission decay traces of (a') CdS/CdSe and (b') CdS/CdSe Re-1,2 composite (λ_{ex}=445 nm λ_{em}=602 nm). **(B)** PL spectra of CdS/CdTe (c) in absence and (d) in presence of Re-1,2 after exciting at 520 nm. **Inset**: Emission decay traces of (c') CdS QD and (d') CdS/Re-1,2 composite (λ_{ex}=445 nm λ_{em}=662 nm).

CdS/CdSe core-shell to Re-1,2 complex. The luminescence decay trace of CdS/CdSe QD at 602 nm can be fitted multi-exponentially with time constants τ_1 = 1.15 ns (25%), τ_2 = 5.12 ns (23%) and τ_3 = 22.3 ns (52%) with average lifetime (τ_{avg}) =13 ns. However, the PL decay trace of CdS/CdSe core-shell at 602 nm in presence of Re-1,2 can be fitted multi-exponentially with time constants τ_1 = 0.036 ns (90%), τ_2= 0.65 ns (6%) and τ_3 = 4 ns (4%) with average lifetime

(τ_{avg}) =0.23 ns. It is interesting to see that the emission decay rate of CdS/CdSe in presence of Re-complex is more faster as compare to CdS-Re-complex mixture . This charge transfer interaction can be expressed in terms of following equation

$$\mathbf{CdS/CdSe + h\nu \rightarrow CdS(e^{-} + h^{+})/CdSe(e^{-} + h^{+})} \qquad (6.10)$$

$$\mathbf{CdS(e^{-} + h^{+})/CdSe(e^{-} + h^{+}) \rightarrow CdS/CdSe(e^{-} + h^{+})} \qquad (6.11)$$

$$\mathbf{CdS/CdSe(e^{-} + h^{+}) \quad + \; Re\text{-}complex \rightarrow CdS/CdSe(e^{-}) + Re\text{-}complex^{+}} \qquad (6.12)$$

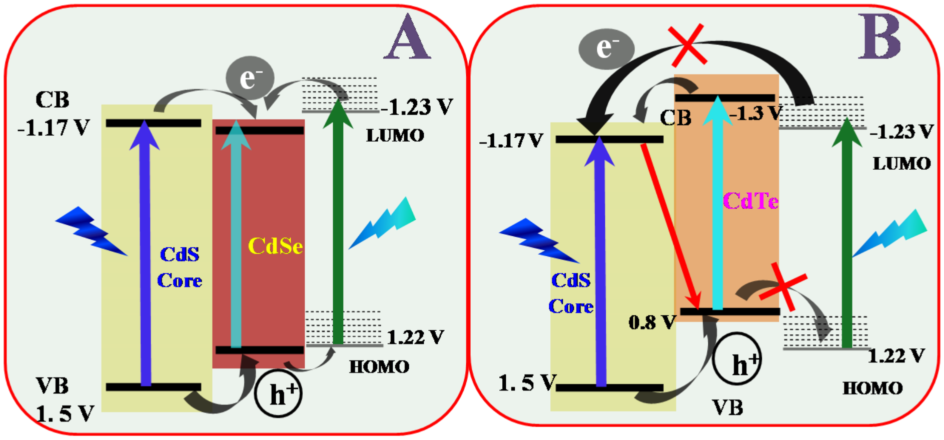

Scheme 6.3: Schematic illustration of charge delocalization and charge transfer processes in (A) CdS/CdSe type-I and (B) CdS/CdTe type-II core-shell in presence of Re-1,2 complex respectively. Energy levels are mentioned with respect to NHE.

Moreover, we have also synthesized CdS/CdTe type II core-shell and carried out PL measurements on sensitization with Re-1,2-complex after selective photo-excitation. In contrast to CdS/CdSe type I core-shell CdS/CdTe form type II core-shell structure where on photo-excitation the core-shell charge localization take place differently. The CdS/CdTe core-shell shows red shifted indirect luminescence with maximum intensity at ~660 nm (Figure 6.9c). Here we would like to mention on photo-excitation of the CdS/CdTe core-shell at 400 nm we observe only one luminescence peak at 660 nm. This clearly suggest the separation of charge carrier take place in type-II regime, where all hole are localized in the VB of CdTe shell and all electron are localized in CB of the CdS core (Scheme 6.3B). Figure 6.9B depicts PL spectra of CdS/CdTe sensitized with Re-1,2. The emission intensity of CdS/CdTe is not reduced significantly in presence of Re-1,2 after 550 nm excitation (Figure 6.9d). As the energy levels of CdS/CdTe-Re-1,2 suggest upon photo-excitation the photo-excited hole can't be captured by the Re-1,2 complex because the hole transfer process from CdTe shell to Re-complex is thermodynamically unfavourable. Slight emission quenching might be due inefficient hole leaking through CdTe shell. Similarly to reconfirm this restriction of charge delocalization we have also carried out time resolved PL measurements of pure CdS/CdTe and CdS/CdTe -Re composite mixture after exciting at 445 nm laser radiations. Interestingly the decay kinetics of CdS/CdTe-Re1,2 at 660 nm shows (Figure 6.9B inset) similar decay pattern as that of CdS/CdTe core-shell. So this observation clearly suggest that photo-excited hole transfer does not take place from CdS/CdTe core-shell to Re-1,2 complex.

6.2.4. Electron Injection Reaction:

Although the energy levels of the CdS, CdS/CdTe sensitized by Br-PGR and suggest that upon photoexcitation Br-PGR can inject electron to the CB of the corresponding NCs. But due to absence of any PL we could not able to monitor the electron injection process in this system through steady state and time resolved PL study. However, due to presence of PL of the Re-complex we could able to identify the electron injection process following selective excitation. Figure 6.10 A illustrates the emission spectra of Re-complex in absence and in presence of CdS QD after 290 nm excitation. It has been observed from Figure 6.10a that Re1,2 shows emission peak at 346 nm with low emission quantum yield (~0.1-0.2%).[341] However, emission intensity of Re-1,2 reduces in presence of CdS QD (Figure 6.10b). It is worth mention that on photo-excitation of Re-1,2 at 400 nm no emission was observed from the sensitizer molecule. This observation clearly suggest that emission of Re-1,2 molecule appears only from upper excited states. We have also excited pure CdS QD at 290 nm, however no emission was recorded in 320 – 440 nm regions. Thus the emission quenching can be assigned as electron injection from photo-excited Re-complex to CB of CdS QD and the process can be expressed according to the following equations:

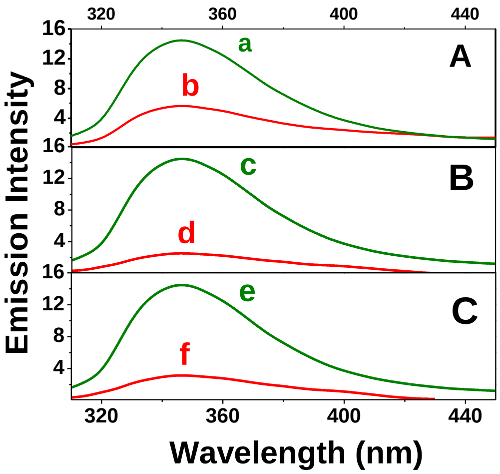

Figure 6.10: Emission spectra of the Re-1,2 **(A)** (a) in absence and (b) in presence of CdS QD, **(B)** (c) in absence and (b) in presence of CdS/CdSe type I and **(C)** (e) in absence and (f) in presence of CdS/CdTe type II after 290 nm excitation.

$$\textbf{Re-complex} + h\nu \rightarrow \textbf{Re-complex}^* \qquad (6.13)$$

$$\textbf{Re-complex}^* + \textbf{CdS} \rightarrow \textbf{CdS}(e^-) + \textbf{Re-complex}^+ \qquad (6.14)$$

Again we have also carrier out the electron injection feasibility reaction from photo-excited Re-complex to CdS/CdSe type-I and CdS/CdTe type-II core-shell system. The emission intensity of Re-complex drastically reduces in presence of both CdS/CdSe and CdS/CdTe core-shell and is shown in Figure 6.10B and Figure 6.10C respectively. In our earlier work [341] we have reported observed that photo-excited Re-1,2 dye can inject electron to the CB of the CdSe QD. Scheme 6.3 suggests that LUMO of Re-1,2 dye lies above the conduction band of CdTe QD. So electron injection from photo-excited Re-1,2 dye to both the core-shell is thermodynamically possible. So the electron injection to the CdS/CdSe and CdS/CdTe core-shell can also be expressed by following equations:

$$\textbf{Re-dye+ h}\nu \rightarrow \textbf{Re-dye *} \qquad \textbf{(6.15)}$$

$$\textbf{Re-dye * + [CdS/CdSe or CdS/CdTe]} \rightarrow \textbf{[CdS/CdSe (e}^{-}\textbf{) or CdS/CdTe (e}^{-}\textbf{)] + Re-dye}^{+} \qquad \textbf{(6.16)}$$

It is interesting to observe that hole transfer from CdS and CdS/CdSe to Re-1,2 takes place while in CdS/CdTe it is not efficient. However the electron injection is observed from photo-excited Re-complex to all the three QD systems. Now to monitor charge transfer dynamics in the above mentioned systems in early time scale we have carried out ultrafast TA spectroscopic measurements in all the above mentioned QD-composite systems and are described below.

6.2.5. Femtosecond TA Study:

i. CdS, CdS/CdTe with Br-PGR.

To corroborate charge transfer dynamics in early time scale with more accuracy in the above composite systems we have carried out femtosecond transient absorption spectroscopic measurements by exciting CdS/Br-PGR and CdS/CdTe/Br-PGR composite systems at 400 nm laser light. Figure 6.11A shows the TA spectra of photo-excited CdS/Br-PGR composite materials in different time delay, which includes bleach below 650 nm with a maximum signal at 550 nm and a broad absorption band at above 700 nm to 800 nm region. The negative absorption below 650 nm appears due to bleach signal of ground state absorption of the CdS/Br-PGR complex and it matches with steady state absorption (Figure 6.4c). The broad spectral absorption in the 700-900 nm regions can be attributed to both Br-PGR cation radical and the electrons in the conduction band in CdS QD.[298] Assignment of Br-PGR cation radical has been made on the basis of the results obtained in separate pulse radiolysis experiments,[226] where Br-PGR$^{\bullet+}$ was generated selectively by the reaction of a $N_3^{\bullet}$ radical with Br-PGR molecule in N_2O^- saturated aqueous solution. Br-PGR cation radical band is not clear in the transient spectra due to huge overlap of ground state absorption bleach in the same spectral region. Now to understand the charge transfer dynamics in ultrafast time scale in CdS/CdTe core/shell sensitized with Br-PGR system femtosecond transient measurements have been carried out after exciting the composite material at 400 nm and monitoring the transients in the

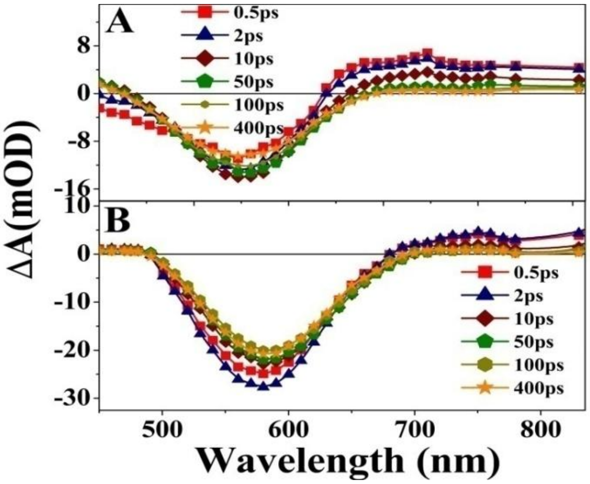

Figure 6.11: Transient absorption spectra of (A) CdS/Br-PGR and (B) CdS/CdTe-Br-PGR composite materials in chloroform at different time delay after excitation at 400 nm laser light.

visible region and shown in Figure 6.11B. The transient spectra consist of bleach below 700 nm with a maximum signal at 570 nm and a broad absorption band at above 700 nm to 900 nm region. In earlier section we have already mentioned that the positive absorption band is attributed to cation radical of Br-PGR and the CB electron of the quantum dot. The negative absorption below 700 nm can be attributed to bleach due to ground absorption of the CdS/CdTe_Br-PGR complex. Now it will be interesting to compare the spectral properties in both the above systems sensitized with Br-PGR. To compare transient spectral properties we would like to mention that we kept the same optical absorption (same O.D.) at 400 nm of the two composite mixtures. The negative absorption below 700 nm can be attributed to bleach due to ground absorption of the CdS/CdTe_Br-PGR complex. Now it will be interesting to compare the spectral properties in both the above systems sensitized with Br-PGR. The negative absorption below 700 nm can be attributed to bleach due to ground absorption of the CdS/CdTe_Br-PGR complex.

ii. CdS, CdS/CdSe and CdS/CdTe with Re(I)-bipyridyl complex.

Figure 6.12 represents TA spectrum of CdS QD and CdS-Re-1,2 composite system at different time delay after 400 nm laser excitation. The TA spectrum of CdS (Figure 6.12A) shows bleach below 480 nm with maximum intensity at 452 nm is due to 1S electronic transition. TA spectrum of CdS-Re-complex composite material is completely different from either of the pure materials and it is shown in the Figure 6.12B. The TA spectrum of the CdS-Re-composite system shows two different spectral signatures, one is bleach below 480 nm and another is positive absorption band 480 - 750 nm region with maximum intensity at 590 nm and a broad transient signal beyond 750 nm. The bleach signal can be attributed to 1S excitonic transition and the PA signal can be attributed to combination of the excited state absorption of the Re-1,2 cation radical and the CB electron of the CdS QD [298] respectively. It is interesting to see that the PA signal in 550-650 nm region of the CdS-Re composite exactly matches with the cation radical of Re-1,2 dye.[341, 343, 344] Scheme 6.2 and Figure 6.5 suggest that photo-excitation of CdS-Re-1,2 composite materials by 400 nm both hole transfer from photo-excited CdS QD to Re-1,2 and electron injection from photo-excited Re-1,2 to CB of CdS QD is thermodynamically viable

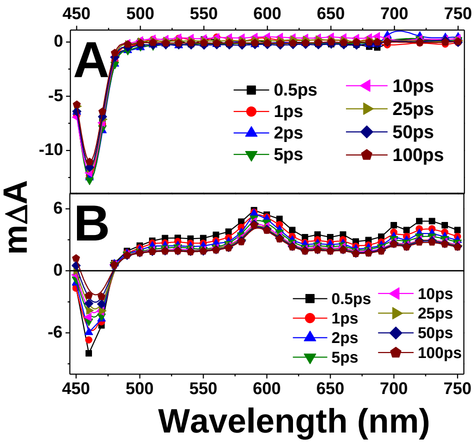

Figure 6.12: Transient absorption spectra of **(A)** CdS QD and **(B)** CdS-Re-1,2 composite system in chloroform solution at different time delay following 400 nm laser excitation. Both the cases concentration of CdS QD was kept ~1 μM.

process. So in CdS-Re-1,2 composite system charge separation takes place by both hole transfer and electron injection. Concomitantly, Figure 6.13 illustrates TA spectrum of CdS/CdSe type-I core/shell and the core-shell sensitized with Re-dye at different time delay. TA spectrum of the CdS/CdSe core-shell (Figure 6.13A) shows two negative absorption bands peaking at 454 nm and 575 nm respectively. Interestingly ground state bleach spectra of CdS/CdSe core-shell exactly match with the steady state optical spectrum as shown in Figure 6.6a. These negative absorption bands at 454 and 575 nm can be attributed to 1S excitonic bleach due to CdS core and CdSe shell respectively.[345]

Interestingly TA spectrum of the CdS/CdSe sensitized with Re- complex is completely different from that of TA spectrum of the pure CdS/CdSe core-shell. TA spectrum of CdS/CdSe-Re-1,2 composite system (Figure 6.13B) shows two negative absorption band like CdS/CdSe core-shell at 454 nm and 575 nm respectively. In addition to that a broad positive absorption band from 590 nm to 750 nm with peak at 600 nm has been observed which can be attributed to combination of cation radical of Re-1,2 dye and electron in the core-shell QD. Similarly we have also measured the TA analysis of CdS/CdTe after sensitizing with Re-complex. Figure 6.14 depicts the TA spectrum of the CdS/CdTe type-II core-shell at different time delay after 400 nm laser excitation in chloroform solution. The spectra show a narrow bleach band at 460-490 nm (peaking at 480 nm) and another broad bleach band at 550-660 nm region (peaking at 620 nm)

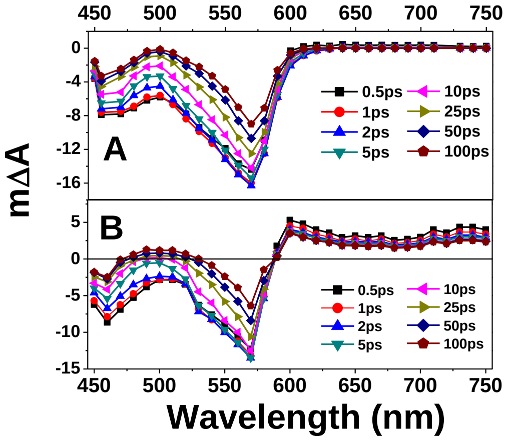

Figure 6.13: Transient absorption spectra of **(A)** CdS/CdSe QD and **(B)** CdS/CdSe-Re-1,2 composite system in chloroform solution at different time delay following 400 nm laser excitation.

which can be attributed to excitonic bleach due to 1S excitonic bleach due to CdS core QD and CdTe shell QD respectively. Apart from the excitonic bleaches, a little positive absorption band has been observed beyond 660 nm which can be attributed to the absorption due to the trapped electron in the core-shell structure arises due to lattice mismatch between CdS core and CdTe shell. However, the spectrum of the composite system (CdS/CdTe_Re) and the pure CdS/CdTe show similar signature. This observation clearly suggest that at 400 nm excitation no charge transfers interaction take place in the CdS/CdTe core-shell /Re (1, 2) composite system as observed and shown in Scheme 6.3B. In the earlier section we have observed electron injection from photo-excited Re-1,2 molecule to CdS/CdTe core-shell after exciting the sample at 290 nm

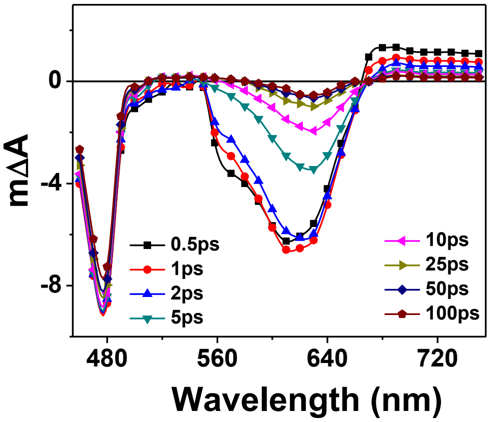

Figure 6.14: Transient absorption spectra of CdS/CdTe type-II core-shell at different time delay after 400 nm laser excitation.

through emission studies. However in the transient studies while exciting the samples at 400 nm (3.1 eV) no charge transfer interaction was observed as the excitation energy (3.1 eV) is not enough to inject electron from higher excited state of the Re-complex to CdS/CdTe core shell

(Scheme 6.3B). It is worth mention that at 400 nm excitation Re-1,2 molecule does not show any emission band correspond to the absorption band maxima at 406 nm.

6.2.6. Charge Transfer Interaction:

i. CdS, CdS/CdTe with Br-PGR.

It is clearly seen that in Figure 6.11 that the intensity of the transient bleach is almost two times higher in CdS/CdTe core-shell as compared to that of CdS QD after sensitizing with Br-PGR. Higher bleach intensity at the bleach wavelength for similar optical density at the exciting wavelength suggest better charge separation in CdS/CdTe/Br-PGR composite as compared to that in CdS/Br-PGR. Higher charge separation in core-shell might be due to result of cascading of electron and hole transfer after photo-excitation of the composite materials. To understand the charge transfer behaviour in these two systems the bleach kinetics are compared at 560 nm and 650 nm for CdS QD and CdS/CdTe core-shell sensitized with Br-PGR respectively and shown in Figure 6.15. The bleach kinetics for CdS/Br-PGR at 560 nm can be fitted with bi-exponential growth τ_1 = 100fs (84%) and τ_2 = 4.5 ps (16 %) and multi-exponential decay with time constants of τ_1 = 56 ps (24%), τ_2 = 300 ps (28.5 %), and τ_3 > 1 ns (47.5%) (Table 6.1). However the bleach kinetics at 650 nm for CdS/CdTe/Br-PGR system can be fitted with single exponential growth of 150 fs and multi-exponential decay time constants of τ_1= 4 ps (16%), τ_2 = 200 ps (7 %), and τ_3 > 1 ns (77%) (Table 6.1). The charge separation in both the above systems found to take place in three different path ways: through hole transfer from photo-excited QDs to Br-PGR, electron injection from photo-excited Br-PGR to CB of the QDs, and direct electron transfer from HOMO of Br-PGR to the CB of the QDs. Due to overlap of transient absorption of cation radical of Br-PGR, electron in the conduction of QD materials at the bleach wavelengths (560 nm and 650 nm) for both the above systems, it is very difficult to comments on different physical processes from the bleach recovery kinetics. Still we have tried to understand charge transfer dynamics from bleach kinetics in both the systems. It has been observed that growth kinetics at 560 nm can be fitted bi- exponentially.

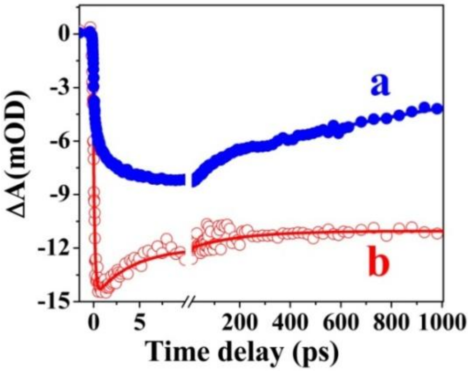

Figure 6.15: Normalized bleach recovery kinetic traces of (a) CdS QD sensitized Br-PGR at 560nm and (b) CdS/CdTe core/shell sensitized Br-PGR at 650nm in chloroform after exciting the samples at 400 nm laser light.

The faster growth component (100 fs) is attributed to electron injection from photo-excited Br-PGR to CdS QD and slower bleach growth (4 ps) can be attributed to hole transfer process from CdS QD to Br-PGR. In addition to the above two processes hole transfer from CdS/CdTe core-shell to Br-PGR also take place with ~4 ps, as determined from first bleach recovery time constant (Table 6.1).

Table 6.1: Multiexponential fitting parameter of CdS, CdS/CdTe sensitized with Br-PGR at different wavelength (λ).

System/λ(nm)	τ_{g1}	τ_{g2}	τ_1	τ_2	τ_3
CdS-BrPGR(560)	100 fs (84%)	4.5 ps (16%)	56 ps (-24%)	300 ps (-28.5%)	>1ns (-47.5%)
CdS/CdTe-BrPGR (650)	100fs (100%)		4 ps (-16%)	200 ps (-7%)	>1ns (-77%)

The multi-exponential bleach recovery kinetics which can be attributed to recombination dynamics between Br-PGR cation radical and electron in CdS QD or CdS/CdTe core-shell of different trap depth or different distance (spatial distance) from cation radical. The overall slow charge recombination is observed in the type-II regime.

ii. CdS, CdS/CdSe with Re(I)-bipyridyl complex.

Figure 6.16 shows the kinetic decay traces of CdS and CdS-Re-1,2 at different wavelengths after 400 nm laser excitation. The 1S bleach dynamics of CdS (Figure 6.16a) at 452 nm which has pulse width limited (<100 fs) growth and it recovers multi-exponentially with time constants

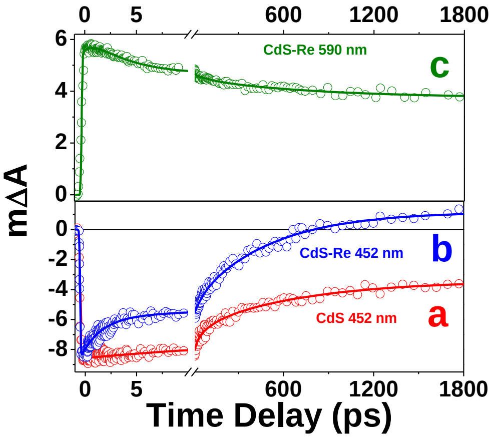

Figure 6.16: Kinetic decay traces of CdS QD (a), CdS-Re-1, 2 (b) at 452 nm and (c) CdS-Re-1,2 at 590 nm in chloroform after 400 nm laser excitation.

τ_1=20 ps (24%), τ_2 =100ps (19%), τ_3 =600ps (16%) and τ_4=>1.8 ns (41%) (Table 6.2). However, the bleach dynamic of CdS-Re-1,2 at 452 nm (Figure 6.16b) recovers faster with time constants τ_1=2 ps (41%), τ_2 =60 ps (36%) ,τ_3=500 ps (12%), and τ_4=>1.8 ns (11%) (Table 6.2). The faster bleach recovery kinetics at 1S excitonic bleach of CdS QD in presence of Re-1,2 molecule can be attributed hole transfer and/or non-radiative energy transfer to the dye molecule. However the overlap between emission spectra of CdS and optical absorption of Re-1,2 dye molecule is very poor due low absorption cross-section of Re-1,2, so hole transfer is the major process. Here the 2 ps component in the 1S bleach recovery kinetics of CdS-Re-1,2 system can be attributed to hole transfer time from CdS QD to Re-1,2. The transient kinetics at 590 nm for CdS-Re-1,2 system which has been attributed to combination of cation radical of Re-1,2 and electron in CdS QD can be fitted with bi-exponential growth with time constants of $\tau_1^g = < 100$ fs (85%) and $\tau_2^g = 900$ fs (15 %) and multi-exponential decay with time constants τ_1=4 ps (20%), τ_2 = 80ps (7%), τ_3 =400ps (7%) and τ_4=>1.8 ns (67%). This multi-exponential decay constants can be attributed to the charge recombination dynamics between electron in CdS QD and Re-1,2 cation radical. As we have already noticed the better charge separation observed in CdS/CdSe core-shell due to favourable energy level of the CdSe shell on CdS core. The charge carrier dynamics of the CdS/CdSe sensitized with Re-1,2 is plotted in the Figure 6.17.

Table 6.2: Multiexponential fitting parameter of CdS, CdS/CdSe and CdS/CdTe sensitized with Re-complex at different wavelength (λ).

Sample	λ(nm)	τ_{g1}	τ_{g2}	τ_1	τ_2	τ_3	τ_4
CdS	452	<100 fs (100%)		20 ps (24%)	100 ps (19%)	600 ps (16%)	>1.8 ns (41%)
CdS-Re-1,2	452	<100 fs (100%)		2 ps (41%)	60ps (36%)	500ps (12%)	>1.8 ns (11%)
	590	<100 fs (85%)	900fs (15%)	4 ps (20%)	80 ps (7%)	400ps (7%)	>1.8 ns (67%)
CdS/CdSe	570	<100 fs (75%)	2 ps (15%)	12 ps (35%)	100 ps (30%)	500 ps (8%)	>1.8 ns (27%)
CdS/CdSe -Re-1,2	570	<100 fs (75%)	2.5 ps (15%)	15 ps (37%)	80 ps (25%)	400 ps (24%)	>1.8 ns (14%)
	600	<100 fs (100%)		1 ps (19%)	10 ps (6%)	100 ps (7%)	>1.8 ns (68%)

From the TA spectrum of CdS/CdSe (Figure 6.12 A) we have seen that the spectrum contain two distinct bleach peaks at 452 and 570 nm. As CdS/CdSe form inverted type-I core-shell structure and all charge carrier are localized on CdSe shell upon photo-excitation. So to demonstrate charge separation and recombination dynamics we have carried the kinetic measurements at 570 nm. The bleach recovery dynamics of CdS/CdSe at 570 nm (Figure 6.17a) has bi-exponential bleach growth and the multi-exponential recovery (Table 6.2). Bi- exponential growth can be assigned as cooling of electron from upper excitonic state to the 1S state.[82] Interestingly, the bleach recovery dynamics of CdS/CdSe-Re-composite show different pattern compare to pure CdS/CdSe. The bleach dynamic at 570 nm of the composite (Figure 6.17b) has slower bleach growth and the bleach recovery is also slow down up to 100 ps. This slow bleach growth can be attributed as electron-hole decoupling due to hole transfer from CdSe shell to Re-molecule (Scheme 6.3A).

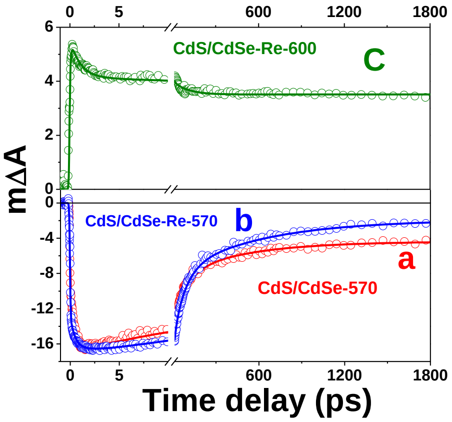

Figure 6.17: Kinetic decay traces of CdS/CdSe QD (a), CdS/CdSe-Re-1, 2 (b) at 570 nm and (c) CdS/CdSe-Re-1,2 at 600 nm in chloroform after 400 nm laser excitation.

However, the due to strong chatecholate binding of the Re^+ molecule the CR dynamics is faster as compare to CdS/CdSe core-shell. Here we would like to mention that the BET process and bleach of CdS/CdSe are overlapped due to their comparable energy levels. Similar to CdS-Re-composite mixture, the CdS/CdSe-Re-dye composite shows PA due to formation of Re-dye cation radical and the excited state dynamic is plotted in the Figure 6.17c. The kinetics of the Re-cation radical at 600 nm shows a fast decay and after that it becomes flat (fitting parameters are in the Table 6.2). The faster decay component can be attributed as electron trapping in the core and shell interface. The slower recombination of the charge carrier dynamics compare to CdS can be due to better charge separation through CdSe shell to Re-molecule. In addition to, we have also carried out the kinetics of the CdS/CdTe-Re-composite at different wavelength and we have not observed any noticeable change in the charge carrier dynamics with free CdS/CdTe core shell. This clearly tells that the charge carriers are not tunnelling through the energetically restricted CdTe shell barrier.

6.3. Conclusion:

In conclusion, ultrafast hole- and electron-transfer dynamics in different core/shell NCs sensitized by the molecular adsorbate have been demonstrated using time-resolved emission and ultrafast transient absorption techniques. We have been observed Br-PGR from strong CT complex with CdS and CdS/CdTe. Due to cascading nature of the energy levels, the better charge separation through different pathways is observed in CdS/CdTe_Br-PGR system as compared to CdS_Br-PGR. More charge separation and lesser charge recombination is observed in the type-II regime. Similarly, electron and hole transfer is also facilitated in CdS/CdSe_Re complex composite system due to inverted type I band structure of the CdS/CdSe NCs. However, the restriction of charge delocalization is noticed in CdS/CdTe_Re composite system because of higher energy CdTe shell barrier. We have also measured the hole and electron transfer time by comparing the kinetic traces. In all the cases the electron transfer is measured <100 fs while the hole transfer is varied from 900 fs to 4.5 ps. Assistance of charge separation through delocalization of charge carrier in CdS, CdS/CdTe and CdS/CdSe sensitized by molecular adsorbate can be used as better photo anode in QDSC. Restriction of charge carrier delocalization in CdS/CdTe-Re-complex can't be used in QDSC due to less charge separation.

CHAPTER-7

Carrier Cooling Dynamics in Alloy QDs

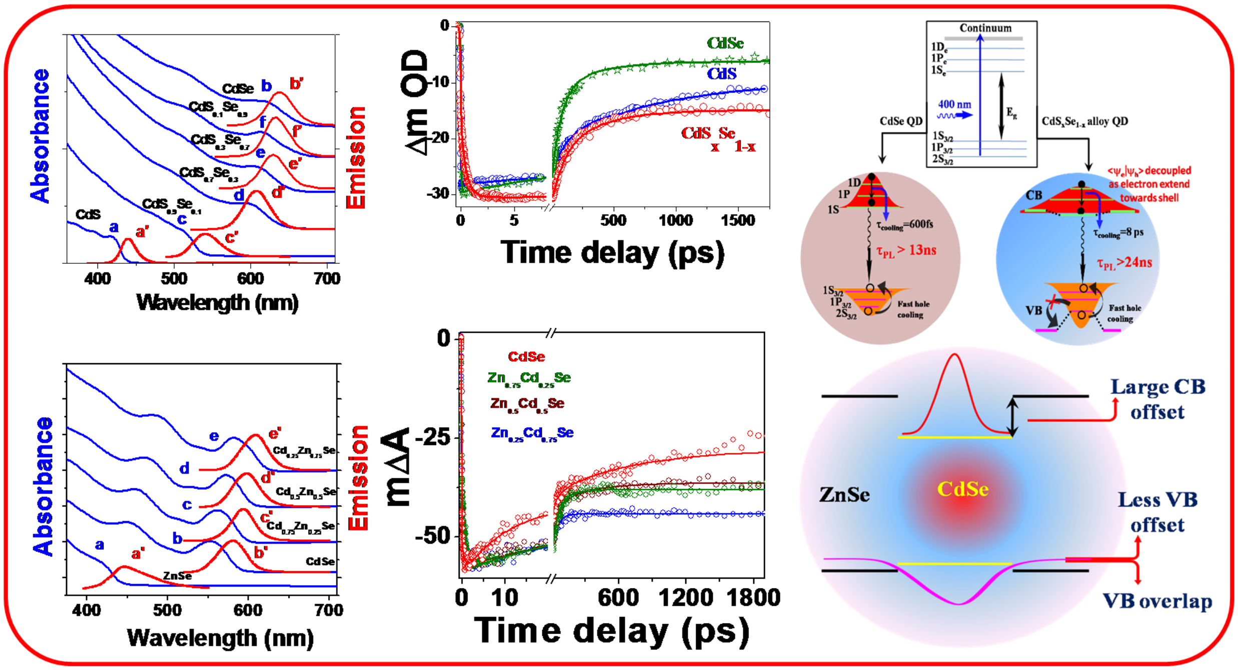

- *J. Phys. Chem. C*, **2015**,*119, 10785–10792.*
- *J. Phys. Chem. C*, **2016 Submitted.**

7.1. Introduction:

Recent developments in the field of synthesis for colloidal alloyed nanocrystals are rapidly growing attention due to their superb optical properties, tunable size and wide range of applications in several realms such as optoelectronics, light emitting diode, biomedical imaging, photo-catalysis and photovoltaic.[125, 126, 346, 347] It is more challenging for II-VI semiconductor quantum dot to manipulate the band gap without changing the size of the nanocrystals that can be easily achieved by alloying. The photo physical and optoelectronic properties of alloy QDs not only arise due to charge carrier confinement in the size quantized state but it also depends on the composition of the constituents. Thus, composition of alloy nanocrystals plays an extra degree of freedom towards selecting desirable properties which can help to design better nanostructure for novel purpose. Due to high surface to volume ratio the smaller NCs accumulate lots of surface defect states where charge carriers are trapped as a result radiative recombination processes are diminished.[93, 94] Many authors already have demonstrated high photoluminescence quantum yield in modified QDs, which are achieved either by making core/shell or by forming different kind of alloys (homogeneous, graded etc.).[116, 128, 130, 131, 319, 348]

It has been realized that alloy QDs can be used as a suitable panchromatic sensitizer to increase QDSC efficiency as compared to the pure NCs. Over the past two decades, it has been observed in various reports, that by adjusting the size of QDs it is possible to tune the band gap energy to extend their absorption range.[158, 349] It is reported in literature that PbS_xSe_{1-x} alloy QDs give better short-circuit photocurrent density (J_{SC}) as well as open circuit voltage (V_{OC}), while pure PbS show better open-circuit voltages (V_{OC}) and pure PbSe QDs give large short-circuit photocurrent densities (J_{SC}).[39] In addition to PbS_xSe_{1-x} [36, 39, 350] alloy QD, several other alloy QDs like $CdSe_{1-x}Te_x$,[351] $CdSe/Cd_xZn_{1-x}S$,[352] $Cd_xZn_{1-x}S$[353] have shown better optical and photovoltaic properties as compared to the corresponding binary QD materials. Earlier Hossain *et al*.[354] have reported that due to smaller crystal mismatch between CdS and CdSe QDs (<3.5%), CdS_xSe_{1-x} alloy QDs ($0 \leq x \leq 1$) can be synthesized in almost all possible compositions. Due to its widely modulated bandgap, CdS_xSe_{1-x} alloy QDs can be used as efficient sensitizer for QDSC.

The band structure of the ternary alloy QDs depend on constituent semiconductor. Depending on the band energy level alignment the heterostructure NCs are classified in type I and type II. Apart from the type I & II NCs, the intermediate case where the band alignment of the semiconductors are like type I structure but due to very smaller energy difference between the band structure either of the charge carrier is delocalized throughout the heterostructure. These types of NCs are known as quasi type II or type $I^{1/2}$. High stability with less surface defect states and more charge separation is required for high performance QDSC. Knowing the band energy levels of the constituent semiconductor we have chosen two different alloy CdS_xSe_{1-x} and $Cd_xZn_{1-x}Se$ where band energy of the constituent NCs suggest type I structure but due to low band offset of the corresponding semiconductor they form quasi type II structure. Most of the work on CdS_xSe_{1-x} and $Cd_xZn_{1-x}Se$ has been carried out are on synthesis, optical, electrical, photovoltaic and several other properties.[355-361] Kim *et al.* [362] and Knoll *et al*.[363] have been shown how composition helps to control the band gap and excited state dynamics of CdSeS nanowire and ZnCdSe alloy quantum dots respectively. But the charge carrier dynamics which are very important to know the reason for better optical properties like higher luminescence quantum yield and emission lifetime. Recently, Rosenthal *et al*.[348] have shown that hole trapping process can be completely eliminated in graded CdS_xSe_{1-x} alloy nanocrystals resulting very high PL quantum yield. However, the carrier cooling dynamics of these two important quasi type II NCs have not been discussed in the literature so far.

In the present chapter we have demonstrated high temperature synthesis of CdS_xSe_{1-x} and $Cd_xZn_{1-x}Se$ alloy QDs ($0 \leq x \leq 1$) with different composition in non-aqueous solvent. The morphology of the synthesized alloy QDs (mainly CdS_xSe_{1-x}) have been analyzed by XRD and HRTEM image. Femtosecond TA measurement has been carried out to comprehend the charge carrier dynamics like carrier relaxation and charge carrier recombination in ultrafast time scale for alloy QDs with different compositions and compared with constituent QDs. Electron cooling dynamics of the alloy QDs are found to be much slower in contrast to pure QDs. Among these alloy QDs the slowest electron cooling time was observed in case of $CdS_{0.7}Se_{0.3}$ alloy QD ($\tau_{CdS0.7Se0.3}$=8 ps). However, in case of $Cd_xZn_{1-x}Se$ the electron cooling time was found 5 ps in all composition and slowest charge recombination noticed in $Zn_{0.25}Cd_{0.75}Se$ alloy. Since slow electron cooling time was observed in the $CdS_{0.7}Se_{0.3}$ composition, thus in this chapter we have demonstrated the TA study of that composition in details. Along with the spectroscopic analysis of three different compositions of $Cd_xZn_{1-x}Se$ alloy QDs has also been included in this chapter.

7.2. Results and Discussion:

7.2.1. Structural Analysis.

XRD analysis, HRTEM measurements and energy dispersive X-ray (EDX) spectroscopic measurements have been carried out to determine chemical composition and morphological analysis of the synthesized alloy QDs. Figure 7.1 (left panel) shows the normalized powder XRD pattern of CdS (trace a), CdSe (trace e) and three different CdSSe alloy QDs (trace b to d). The XRD pattern of the CdS and CdSe matches with bulk zinc-blend lattice structure.[128, 324] The XRD peaks pattern of the alloy QDs appear in between CdS and CdSe QDs and it gradually shifted towards lower diffractive angle with increasing Se concentration. This observation clearly suggests that with increasing Se concentration in CdS_xSe_{1-x} alloy the crystal lattice parameter increases according to Vegard's law. Figure 7.1 (right panel) shows HRTEM image of $CdS_{0.7}Se_{0.3}$ alloy QD and the measured size was ~5nm± 0.15 nm. Figure 7.1 inset shows SAED (selective area electron diffraction pattern)

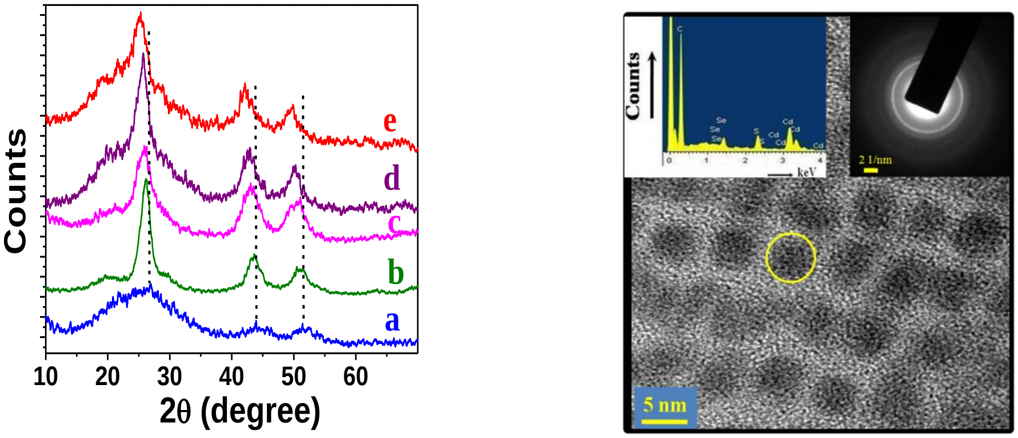

Figure 7.1: Left Panel: Powder X-ray diffraction pattern of (a) CdS, (b) $CdS_{0.7}Se_{0.3}$, (c) $CdS_{0.3}Se_{0.7}$, (d) $CdS_{0.1}Se_{0.9}$ and (e) CdSe QDs. **Right Panel:** TEM images of $CdS_{0.7}Se_{0.3}$ alloy QD, **right inset:** SAED pattern; **Left inset:** EDXA spectrum of $CdS_{0.7}Se_{0.3}$ alloy QD.

and EDXA (energy dispersive x-ray analysis) pattern of $CdS_{0.7}Se_{0.3}$ alloy QD. The EDXA spectrum of $CdS_{0.7}Se_{0.3}$ shows the peaks appear due to K and L shell electrons of Cd, S and Se which are knocked out by the high energy x-ray radiation. From these peak intensity the ratio of S and Se has been determined and it was found to be S:Se = 72:28 which closely matches with our previously calculated S and Se (S:Se=70:30) compositions.

7.2.2. Non-linear Optical Properties of Alloy QDs: Steady state UV-Vis and Photoluminescence Study:

After characterizing the QDs steady state optical absorption and emission studies have been carried out and shown in Figure 7.2A. Figure 7.2A shows the optical absorption and emission spectra of CdS_xSe_{1-x} alloy with different composition varying x = 1 to x = 0. Figure 7.2 A a,a' and 7.2 b,b' show the optical absorption spectra of CdS QD and CdSe QD which show excitonic absorption at 420 nm and 621 nm respectively. Now it is interesting to see that after incorporating Se in CdS QD optical absorption spectra can be moved to the red region of the optical spectra. As a result by changing the composition of S and Se one can easily cover the wide range optical properties.[356, 364]In the present investigation nonlinear behaviour in optical absorption has been observed in CdS_xSe_{1-x} alloy QD materials. It is interesting to see that

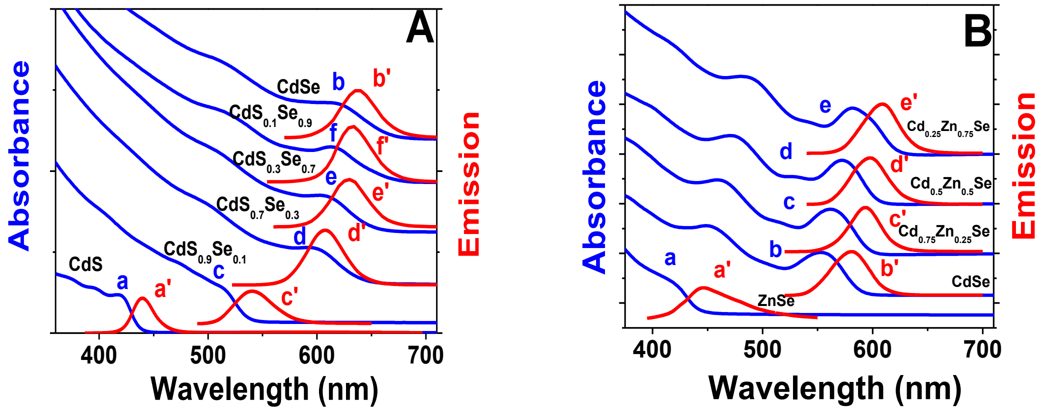

Figure 7.2: Normalized UV-Vis and PL of **(A)** (a, a’) CdS QD, (b, b’) CdSe QD, (c, c’) $CdS_{0.9}Se_{0.1}$, (d, d’) $CdS_{0.7}Se_{0.3}$, (e, e’) $CdS_{0.3}Se_{0.7}$ and (f, f’) $CdS_{0.1}Se_{0.9}$ and **(B)** (a, a’) ZnSe QD, (b, b’) CdSe QD, (c, c’) $Cd_{0.75}Zn_{0.25}Se$, (d, d’) $Cd_{0.5}Zn_{0.5}Se$, and (e, e’) $Cd_{0.25}Zn_{0.75}Se$ alloy QDs in degassed chloroform.

excitonic absorption of $CdS_{0.9}Se_{0.1}$ and $CdS_{0.7}Se_{0.3}$ alloy QDs appear at 515 nm and 595 nm respectively, which indicate presence of Se in alloy dominates the optical properties in the alloy QDs. In addition to the steady state optical absorption measurements we have also carried out steady state PL measurements for the pure and alloy QDs and shown in Figure 7.2A. Luminescence of the pure and alloy QDs were recorded after selective band edge excitation of the QD materials. CdS and CdSe QDs show band edge luminescence at 440 nm (Figure 7.2A a') and 638 nm (Figure 7.2A b') respectively. The band edge luminescence peak for the alloy QDs appear in between 440-638 nm depending on the constituent composition. The emission peak positions and band-width of the alloy QDs clearly suggest that the emissions are indeed purely due to band edge charge recombination not due to trap state emission. Non-linear behaviour on optical studies was also observed in the alloy QDs with changing composition. [129, 353, 365] Concomitantly, the normalized optical absorption and PL of spectra of the $Cd_xZn_{1-x}Se$ with respect to their constituent have been plotted in the Figure 7.2B. In contrast to the CdS_xSe_{1-x} alloy, the optical spectra (both optical absorption and PL spectra) of the all composition of the $Cd_xZn_{1-x}Se$ alloy are red shifted as compared to the pure QDs (ZnSe and CdSe). Earlier Nie *et. al.*[129] demonstrated the nonlinear behaviour in PL properties for the CdSeTe alloy QD materials, where they have observed red shifted photo luminescence for the alloy QD as compare to pure CdSe as well as CdTe quantum dots. In the present study emission peaks for the CdS_xSe_{1-x} alloy QDs appear in between CdS and CdSe QDs while the PL peaks of the $Cd_xZn_{1-x}Se$ alloy is red shifted with respect to CdSe and ZnSe. It is interesting to see that band width of the alloy QDs are broader as compared to the pure QDs. This observation suggests that the excitons in the alloy QDs might be loosely bound or decoupled as compared to that in pure QDs. However, the most interesting observation is that the emission quantum yields for the CdS_xSe_{1-x} alloy QDs are much higher as compared to that of pure QDs. For example the emission quantum yield of $CdS_{0.7}Se_{0.3}$ alloy QD (ϕ_{CdSSe}= 70%) is much higher as compared to pure CdS QD (ϕ_{CdS}= 26%) and CdSe QD (ϕ_{CdSe}= 34%). Very high emission quantum yields in the alloy QDs suggest the removal of both internal and external defect states due to alloying process.[128, 130, 348] On the other hand the emission quantum yield of the $Cd_xZn_{1-x}Se$ (ϕ_{CdZnSe}= 44%) is also increased as compare to the pure CdSe QD (ϕ_{CdSe}= 34%) and ZnSe QD (ϕ_{ZnSe}= 14%). However, the increment of emission quantum yield of the $Cd_xZn_{1-x}Se$ alloys is not as high as CdS_xSe_{1-x} alloy. As we know that the reactivity of the Se powder towards Cd ion is much higher as compared to S-powder, on the other hand the Zn-ion is less reactive with Se than Cd ion.[368] Again it has been observed from steady state optical study that the position of excitonic absorption and luminescence of alloy QDs dominated by CdSe concentration. So it can be assumed that in CdS_xSe_{1-x} and $Cd_xZn_{1-x}Se$ alloyed structure during alloying process a quasi type II core-shell type structure is formed where core is CdSe rich and shells are CdS and ZnSe rich respectively. Here the surface of the core is surrounded by another wider band gap semiconductor material (CdS and ZnSe) which helps to passivate the surface states. As a result the emission quantum yields of the alloy QDs increase enormously due to drastic reduction of non-radiative processes.

7.2.3. Excited state Radiative Life Time: TCSPC Study:

As it has been observed that the emission quantum yields for the alloy QDs are drastically increased so it's very important monitor the photoluminescence lifetimes of the alloy materials. Figure 7.3 shows the time resolved photo luminescence decay traces of pure QDs and the alloy QDs. Emission decay trace at 439 nm (Trace a Figure 7.3) for the CdS QD can be fitted multi-exponentially with time constants of τ_1 = 0.15 ns (44.2%), τ_2 = 2.4 ns (29%), τ_3 = 32.8 ns (26.8%), with τ_{avg} =9.5 ns. While the emission decay trace for CdSe at 637 nm (Trace b Figure 3) also can be fitted multi- exponentially with time constants τ_1 = 0.32 ns (35%), τ_2 = 6.1 ns (21%), τ_3 = 32.8 ns (44%), with τ_{avg} =13.3 ns. On the other hand emission decay trace of $CdS_{0.7}Se_{0.3}$ alloy at 605 nm (Trace d Figure 3) can be fitted multi exponentially with decay time constants of τ_1 = 1.3 ns (14%), τ_2= 15.2 ns (35%), τ_3 = 36.2 ns (51%), with τ_{avg} =24 ns.

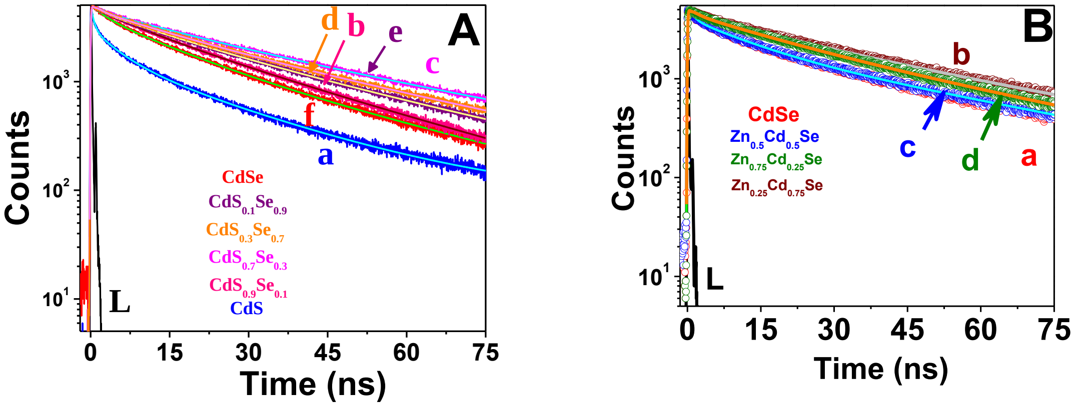

Figure 7.3: Time resolved PL decay traces of (A) (a) CdS QD (λ_{em}=439 nm) (b) $CdS_{0.9}Se_{0.1}$ (λ_{em}=540 nm) (c) $CdS_{0.7}Se_{0.3}$ (λ_{em}=605 nm) (d) $CdS_{0.3}Se_{0.7}$ (λ_{em}=630 nm) (e) $CdS_{0.1}Se_{0.9}$ (λ_{em}=633 nm) (f) CdSe (λ_{em}=637 nm) and (B) (a) CdSe QD (λ_{em}=581 nm) (b) $Zn_{0.25}Cd_{0.75}Se$ (λ_{em}=594 nm) (c) $Zn_{0.5}Cd_{0.5}Se$ (λ_{em}=598 nm) (d) $Zn_{0.75}Cd_{0.25}Se$ (λ_{em}=610 nm) in chloroform solution after exciting at 445 nm laser source.

It is interesting to see that life time of the faster component of alloy $CdS_{0.7}Se_{0.3}$ alloy QD is much longer with low contribution (1.3 ns, 14%) as compared to both CdS QD (0.15 ns, 44.2%) and CdSe QD (0.32 ns, 35%) and on the contrary the longer component of the emission decay trace increases drastically with higher contribution in case of alloy QD as compared to individual QDs. This observation clearly suggests that in alloy QDs defect states in the QD materials decreases drastically as a result we can observed both increment of average emission lifetime and also emission quantum yield in alloy QD materials. However, as the charge carrier relaxation dynamics of the CdX (X=S, Se) QD take place in sub ps time scale,[87, 89, 93, 94, 218] so the nanosecond time resolution is not enough to determine the excite state dynamics of the charge carriers. Again to understand the reason for higher luminescence quantum yield and radiative lifetime for the alloy QDs it's very important to monitor the dynamics in early time scale. Next section we have discussed ultrafast carrier relaxation dynamics of pure as well as alloy quantum dots with the help of femtosecond transient absorption spectrometer.

7.2.4. Femtosecond Transient Absorption Measurements:

i. For CdS_xSe_{1-x} *alloy*

Ultrafast femtosecond TA spectroscopy is one of the potential techniques for probing the carrier relaxation dynamics of the CdX (S, Se, and Te) semiconductor QDs.[87, 89, 93, 94, 298, 310, 325]

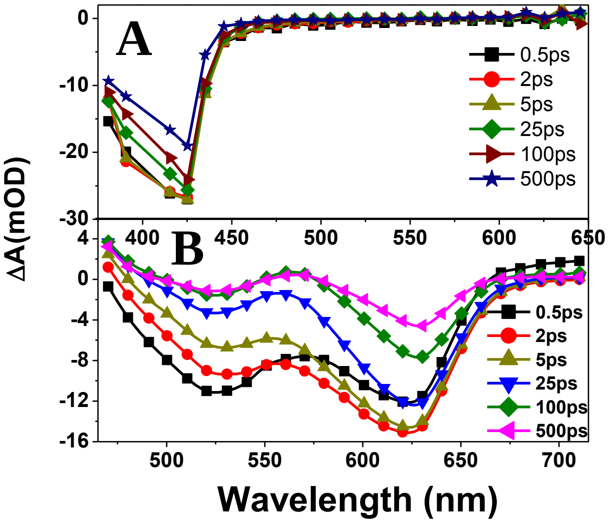

Figure 7.4: Transient absorption spectra of CdS QD (A) and CdSe QD (B) at different time delay after exciting at 400 nm laser light.

We have already noticed from earlier discussions that the optical properties of CdS_xSe_{1-x} alloy QDs are totally different as compared to pure CdS and CdSe QDs. Time resolved PL life time measurements suggest that alloy QDs have long excited state life time as compared to their parent QD materials. So it is quite obvious that excited state properties of these alloy QDs will give more information towards composition tuning optoelectronic properties. Now to understand the carrier dynamics of these alloy QDs ultrafast transient absorption spectroscopic measurements have been carried out after exciting the samples at 400 nm lasers light and probing the transient in visible region. However, before going to the details of ultrafast carrier dynamics of the CdS_xSe_{1-x} alloy QDs it is very important to monitor the carrier dynamics of the pure QD materials. Figure 7.4 illustrates femtosecond TA spectra of pure CdS (A) and CdSe (B) QDs at different time delay after exciting at 400 nm laser light in chloroform solution. We have already discussed the TA spectrum of the CdS and CdSe QDs in earlier chapter. However, for the comparison with alloy spectra we have plotted the spectrum of the constituent again in this section. The TA spectra of CdS QD shows a bleach band below 440 nm with peak maximum at 420 nm (Figure 7.4A) which can be attributed as the excitonic bleach due to 1S electronic transition. On the other hand, TA spectra of pure CdSe QD (Figure 7.4B) shows two distinct bleach bands with maximum intensity at 520 nm and at 622 nm, which can be attributed to excitonic bleaches due to 1P and 1S transitions respectively. Figure 7.5 depicts the transient absorption spectra of $CdS_{0.7}Se_{0.3}$ alloy QD which also shows two negative absorption bands with bleach maxima at 600 nm and 500 nm which can be attributed as first (1S) and third (1P) excitonic bleach respectively. It is interesting to see unlike pure CdSe and CdS QDs the appearance and disappearance time for excitonic bleach signals are quite different. Now to understand the carrier dynamics (both cooling and charge recombination), it is very important to

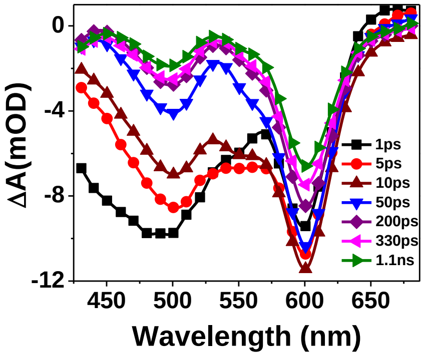

Figure 7.5: Transient absorption spectra of $CdS_{0.7}Se_{0.3}$ alloy QD at different time delay after exciting at 400 nm laser light in degassed chloroform solution.

compare the bleach recovery kinetics of the alloy QD at both the excitonic positions and also compare with the pure CdS and CdSe QDs. Here we would like to mention that we have compared the 1S bleach recovery dynamics of the alloy QDs for both pure CdSe QD and CdS QD and is shown in Figure 7.6A. Figure 7.6a shows the first excitonic bleach kinetics of CdS QD at 418 nm, which can be fitted with pulse width limited growth and multiexponential

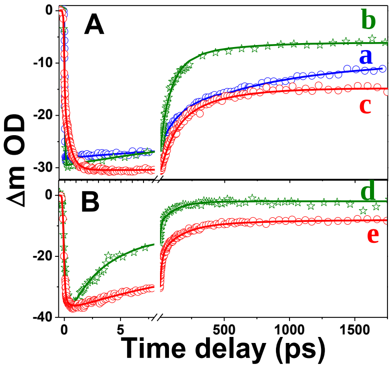

Figure 7.6: Panel A: First excitonic ($1S_e$-$1S_{3/2}$) bleach recovery decay kinetics of (a) CdS QD (418 nm), (b) CdSe QD (622nm) and (C) $CdS_{0.7}Se_{0.3}$ alloy QD (597 nm) after exciting at 400 nm laser light in chloroform solution. **Panel B:** 1P bleach recovery dynamics of (d) CdSe QD (524 nm) and (e) $CdS_{0.7}Se_{0.3}$ (500 nm) alloy QD.

recovery with time constants τ_1=25 ps (-26%), τ_2 =130ps (-38%) and τ_3=>1.8 ns (-36%) (Table 7.1). However, 1S excitonic bleach at 622 nm for CdSe QD (Figure 7.6 trace b) can be fitted with biexponential growth components with time constants of 100 fs (94%) and 600 fs (6%). Recovery kinetics of 1S bleach for CdSe QD can fitted with multi-exponential time constants of τ_1= 5 ps (-26%), τ_2=50 ps (-40%), τ_3=250 ps (-15%) and τ_4=>1.8 ns (-19%). On the other hand the first excitonic (1S) bleach $CdS_{0.7}Se_{0.3}$ alloy QD at 600 nm (figure 7.6 trace c) can also be fitted with bi-exponential growth with time constants τ_1= 150 fs (80%), τ_2= 8ps (20%). However bleach recovery can be fitted multi-exponentially with time constants of τ_1=50 ps (-35%), τ_2=300 ps (-17%) and τ_3=>1.8 ns (-48%). The reasons of slow electron cooling and detail analysis of transient data are discussed in the next section. In addition to monitoring the bleach kinetics at 1S excitonic position, bleach dynamics have also been followed at 1P excitonic position for both

Table 7.1: Emission quantum yield (ϕ), radiative life time (τ) and ultrafast charge relaxation components (τ_i) of pure CdS, CdSe and CdS_xSe_{1-x} alloy quantum dots at different wavelength (λ).

System	ϕ (%)	τ(ns)	λ(nm)	τ_{1g}	τ_{2g}	τ_1	τ_2	τ_3
CdS	24	9.5	418	<100 fs	–	25ps (-26%)	130ps (-38%)	>1.8 ns (-36%)
$CdS_{0.9}Se_{0.1}$	65	23	515	150fs (92%)	1.8 ps (8%)	5ps (-12%)	40ps(-19%), 250 ps(-21%)	>1.8 ns (-48%)
$CdS_{0.7}Se_{0.3}$	70	24	597	150fs (80%)	8ps (20%)	50ps (-35%)	300ps (-17%)	>1.8 ns (-48%)
$CdS_{0.3}Se_{0.7}$	69.5	23.5	605	150fs (75%)	5ps (25%)	50 ps (-38%)	250ps (-14%)	>1.8ns (-47%)
$CdS_{0.1}Se_{0.9}$	69.0	23.3	613	150 fs (87.5%)	4 ps (12.5%)	20 ps (-30%)	150 ps (-30%)	>1.8 ns (-40%)
CdSe	34	13.3	622	100 fs (94%)	600 fs (6%)	5 ps (-26%)	50ps (-40%) , 250 ps(-15%)	>1.8ns (-19%)

CdSe QD and $CdS_{0.7}Se_{0.3}$ alloy QD at 524 nm and 500 nm respectively and are shown in Figure 7.6B. 1P bleach recovery kinetics of CdSe at 524 nm (Figure 7.6d) can be fitted with pulse width limited (<100 fs) growth and multi-exponential recovery with the time constants τ_1=4 ps (-68%), τ_2=25 ps (-20%), τ_3=180 ps (-5%) and τ_4>1.8 ns (-7%). On the other

hand the upper excitonic bleach (1P) kinetics for the $CdS_{0.7}Se_{0.3}$ alloy QD at 500 nm (Figure 7.6e) can be fitted with biexponential growth (150 fs and 500 fs) and multi-exponential recovery with time constants τ_1=15 ps (-55%),τ_2 =100ps (-23%) and τ_3=1.8 ns (-22%).

ii. For Cd_xZn_{1-x} Se alloy

To know the carrier cooling and charge separation dynamics of the $Cd_xZn_{1-x}Se$ alloy NCs it is very important to carry out the excited state dynamics of the constituent NCs. As the

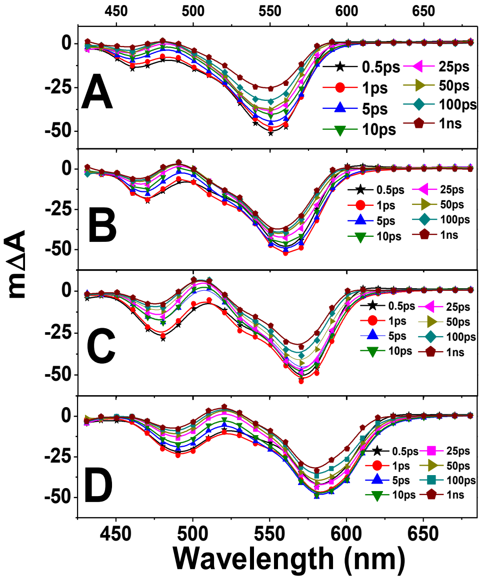

Figure7.7: TA spectra of (A) CdSe (B) $Cd_{0.75}Zn_{0.25}Se$ (C) $Cd_{0.5}Zn_{0.5}Se$ and (D) $Cd_{0.25}Zn_{0.75}Se$ in chloroform after exciting at 400 nm laser excitation.

photophysical properties of the CdZnSe is CdSe dominated so we compare the TA spectrum of the alloy QDs with CdSe QD not with ZnSe. The TA spectrum of the different composition of the $Cd_xZn_{1-x}Se$ alloy with CdSe QD is plotted in the Figure 7.7. As we have already discussed the bleach bands (551 and 462 nm) of CdSe are due to 1S and 1P electronic transition. Interestingly, the 1S and 1P bleach band of the CdZnSe alloyed structure appear at red shifted as compared to CdSe which is suggested the optical absorption spectra of the different composition of the alloy. In addition to the 1S and 1P bleach band, the 2S band is clearly coming in between the 1S and 1P bands in the all composition of the CdZnSe alloy which is absent in CdSe QDs. The 2S electronic signal is very weak in CdSe QDs which predominantly coming in the alloy structure. Hole delocalization due to the low VB off set in the graded structure which increase the transition probability of the 2S electronic state. The appearance of the 2S electronic transition is one of the evidences for the graded likes structure. As we have already mentioned in the earlier section that at 400 nm excitation higher excited state population of the CdS is not possible

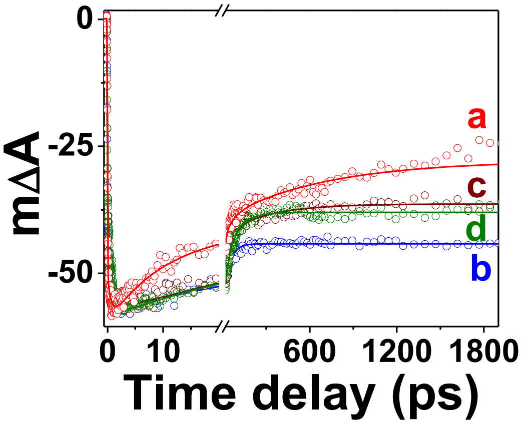

Figure7.8: First excitonic (1S) bleach recovery dynamics of (a) CdSe (b) $Zn_{0.25}Cd_{0.75}Se$ (c) $Zn_{0.5}Cd_{0.5}Se$ and (d) $Cd_{0.25}Zn_{0.75}Se$ in chloroform after exciting at 400 nm laser excitation.

because the 1S exciton appear at 420 nm. In case of ZnSe higher excited state population can't be done by 400 nm laser excitation. Thus the intra band carrier cooling dynamics of the alloy has been determined from the comparison of the 1S bleach dynamics with CdSe QDs. Figure 7.8 shows the 1S bleach recovery dynamics of the CdZnSe alloy with CdSe. The bleach dynamics are fitted biexponential growth and multiexponential recovery. All fitted parameters are summarized in the Table 7.2. The slow growth component (~5 ps) in all composition of the CdZnSe alloy is due to decoupling of electron from hole.

Table 7.2: Ultrafast 1S Excitonic Bleach Recovery Components of Pure CdSe and $Cd_xZn_{1-x}Se$ Alloy NC at Metal to Chalcogen Ratio (2:1).

Systems	λ(nm)	τ_{g1}	τ_{g2}	τ_1	τ_2	τ_3	τ_4
CdSe	553	<100fs (84%)	0.6ps (16%)	10ps (-30%)	60ps (-8%)	500ps (-13%)	>2ns (-49%)
$Zn_{0.25}Cd_{0.75}Se$	562	<100fs (65%)	5ps (35%)	40ps (-22%)	>2ns (-78%)		
$Zn_{0.5}Cd_{0.5}Se$	572	<100fs (64%)	5ps (36%)	40ps (-29%)	300ps (-6%)	>2ns (-65%)	
$Zn_{0.75}Cd_{0.25}Se$	587	<100fs (60%)	5ps (40%)	40ps (-31%)	200ps (-2%)	>2ns (-67%)	

However, the charge recombination is different in all the alloy composition. Less charge recombination is observed with $Cd_{0.75}Zn_{0.25}Se$ alloy. Although the graded like structure remove the inherent surface defect states, however, due to lattice mismatch (~6.5%) the charge carrier are trapped into the interfacial trap states. Thus with increasing zinc concentration in the alloy structure the charge recombination increases. Details carrier mechanism of these CdZnSe structure has been demonstrated in the next section.

7.2.5. Carrier Cooling Mechanism:

Main endeavour of the present chapter is to understand the charge carrier dynamics of alloy QDs, which can help to improve the optoelectronic properties, photocatalysis and photovoltaic performance of the materials. Recently Rosenthal and co-workers[17] have reported quasi-type-II band alignment in graded alloy CdS_xSe_{1-x} nanocrystals through femtosecond fluorescence upconversion spectroscopic studies. They have suggested decoupling of electron and hole in the QD materials take place due to alloying process. They have discussed the effect of alloying in carrier trapping dynamics in different composition of alloy QDs. However, effect of alloying on carrier cooling dynamics was never discussed in literature. To know the carrier dynamics, both growth and recovery kinetics has been monitored at 1S excitonic bleach wavelengths for both pure QDs and alloy QDs and are shown in Figure 7.6 and Figure 7.8,. It is very interesting to see that growth time in 1S excitonic dynamics of alloy CdS_xSe_{1-x} QDs both contribution and growth time of the second component changes bleach is single exponential pulse width limited (<100 fs) for pure CdS QD (~420 nm), however it is bi-exponential with 100 fs (94%) and 600 fs (6%) components for pure CdSe QD (~622nm). In case of CdS QD as the excitonic band appears at 420 nm, so for 400 nm excitation lower excitonic states ($1S_e$) will be populated as a result pulse-

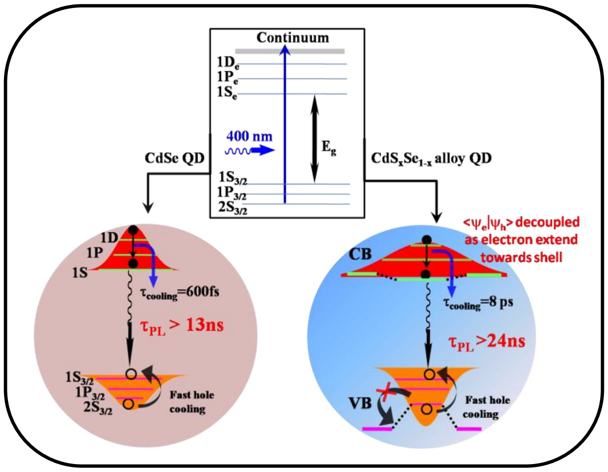

Scheme 7.1: Comparison hot carrier relaxation processes in CdSe QD and CdS_xSe_{1-x} alloy QD after exciting at 400 nm laser light in chloroform solution.

width limited growth has been observed. However, on 400 nm excitation of CdSe QD, electrons in the VB will be excited to upper excitonic states of CB (Scheme 7.1) as a result cooling of hot electrons from upper excitonic state to lower excitonic state of CB take place. So, the 600 fs time constant can be attributed to Auger assisted electron cooling process in CdSe QD. Most interestingly in case of $CdS_{0.7}Se_{0.3}$ alloy QD second growth component was observed to be 8 ps with contribution of 20% (Table 7.1). This is a significant observation for the cooling time of photo-excited charge carriers in any QD materials. The above experimental observation can be summarized in Scheme 7.1. In case of photo-excited CdSe QD, both electron and hole are localized in the excited quantum confined states of conduction and valence band respectively. The photo-excited hole influences electron thermalization which is known as Auger assisted electron cooling.[366, 367] The 600 fs component can be attributed to electron cooling time from upper excitonic states to $1S_e$ state of the conduction band (scheme 7.1).[87, 89, 93, 94, 218] However, in case of CdS_xSe_{1-x} alloy QD as we have suggested that alloy QD forms quasi type II core-shell structure where the alloy QD core will be CdSe rich due to higher reactivity between cadmium and selenium as compared to cadmium and sulphur.[368] So naturally the shell will be CdS rich. As core/shell CdSe/CdS nanocrystals have a quasi type-II band alignment we can presume that CdS_xSe_{1-x} alloy QD also form a quasi type II alignment.[319] Due to larger VB offset between the CdSe-rich core and CdS-rich shell the excited holes are confined in the core of the NC. On the other hand due to smaller CB offset between CdSe and CdS the electrons will be delocalizing through the entire NC. As a result electron and hole decouples quite efficiently in CdS_xSe_{1-x} alloy QD and maximum decoupling was found in $CdS_{0.7}Se_{0.3}$ alloy. Due to this decoupling the integral value of electron-hole wavefunction $<\psi^{CB}{}_{e}|\psi^{VB}{}_{h}>$ decreases and the Auger assisted electron cooling time in alloy QD drastically increases.[82, 94] It has clearly been observed that band gap of CdS_xSe_{1-x} alloy QD does not increase much till x =0.7, then drastically increases towards CdS. However maximum electron cooling time for the alloy QD is maximum at x = 0.7. From this observation we can conclude that with increasing "x" (where "x" is the fraction of sulphur composition in the alloy) more and more CdS shell forms around CdSe rich core which decouples the electron from the hole, as a result slower electron cooling was observed. In addition to that, the charge recombination dynamics was also determined after monitoring the bleach recovery kinetics of different QDs and alloy QDs of different compositions (Table 7.1 and Table 7.2). It is clearly seen that CR dynamics is the slowest in case of $CdS_{0.7}Se_{0.3}$ alloy QD which follows the trend of luminescence quantum yield and life time data. Our experimental results clearly demonstrate the relationship between internal structure and the chemical composition of the alloy QDs which eventually determines the fate of the exciton in quantum confined nanostructures. From steady state optical absorption and PL measurement it is very clear that the $Cd_xZn_{1-x}Se$ form graded like core shell structure. Due to higher reactivity of

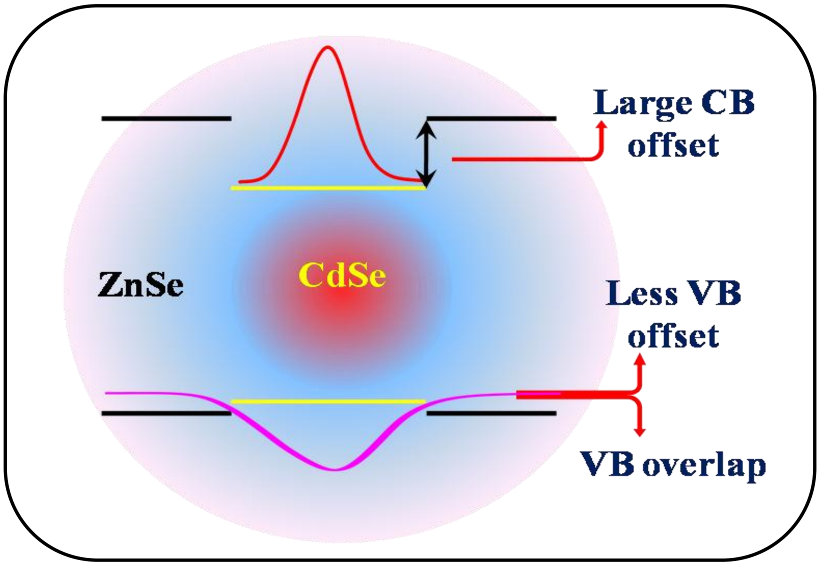

Scheme 7.2: Comparison hot carrier relaxation processes in CdSe QD and CdS_xSe_{1-x} alloy QD after exciting at 400 nm laser light in chloroform solution.

the Se towards Cd ion as compared to the Zn ion it is assumed to be in the graded like structure where the core of the NC is CdSe rich while shell is ZnSe rich. The band energy levels of the constituent in the $Cd_xZn_{1-x}Se$ alloyed structure is formed where the core is CdSe and shell is ZnSe is drawn in Scheme 7.2. Our experiment suggest that the intra band electron cooling time for all $Cd_xZn_{1-x}Se$ alloy is increases from the cooling time of the CdSe QDs. Due to larger CB off set between CdSe and ZnSe the electron in the alloyed structure is localized in CdSe rich core where the hole is delocalized through the entire NC due to very low VB off set (Scheme 7.2). Thus the delocalized hole due to low VB offset energy is decoupled from the CB electron which increases the intra band electron cooling time in the $Cd_xZn_{1-x}Se$ alloy structure.

7.3. Conclusion:

In this chapter we have demonstrated the carrier mechanism of two alloy QDs, CdS_xSe_{1-x} and $Cd_xZn_{1-x}Se$. Depending on the reactivity of the constituent the alloys formed graded like structure where both the cases core is CdSe rich as the reactivity of the Se is much higher with Cd ion. The optical absorption and PL of the different composition of CdSSe alloy has been observed non-linear behaviour in between the CdS and CdSe QDs. However, both optical absorption and PL of the CdZnSe is red shifted as compared to the pure ZnSe and CdSe. The non linear optical properties and the red shifted absorption and emission band of the CdSSe and CdZnSe respectively suggest the core-shell like structure where in both the cases core is CdSe rich. The band energy levels of these two structure suggest quasi type II aligment where electron and hole are delocalized in the CB and VB of the CdSSe and CdZnSe alloy respectively. Due to quasi type-II alignment electron is decoupled from the hole, as a result we have observed slow intra band electron cooling in both cases. The charge charge recombination is also found to be slow in all composition of these two alloy. Higher luminescence quantum yield, longer luminescence life time and slower electron cooling dynamics for alloy QDs confirm the reality of design and development of higher efficient QD solar cell.

CHAPTER-8

Improving Solar Cell Efficiency Utilizing Alloy QDs

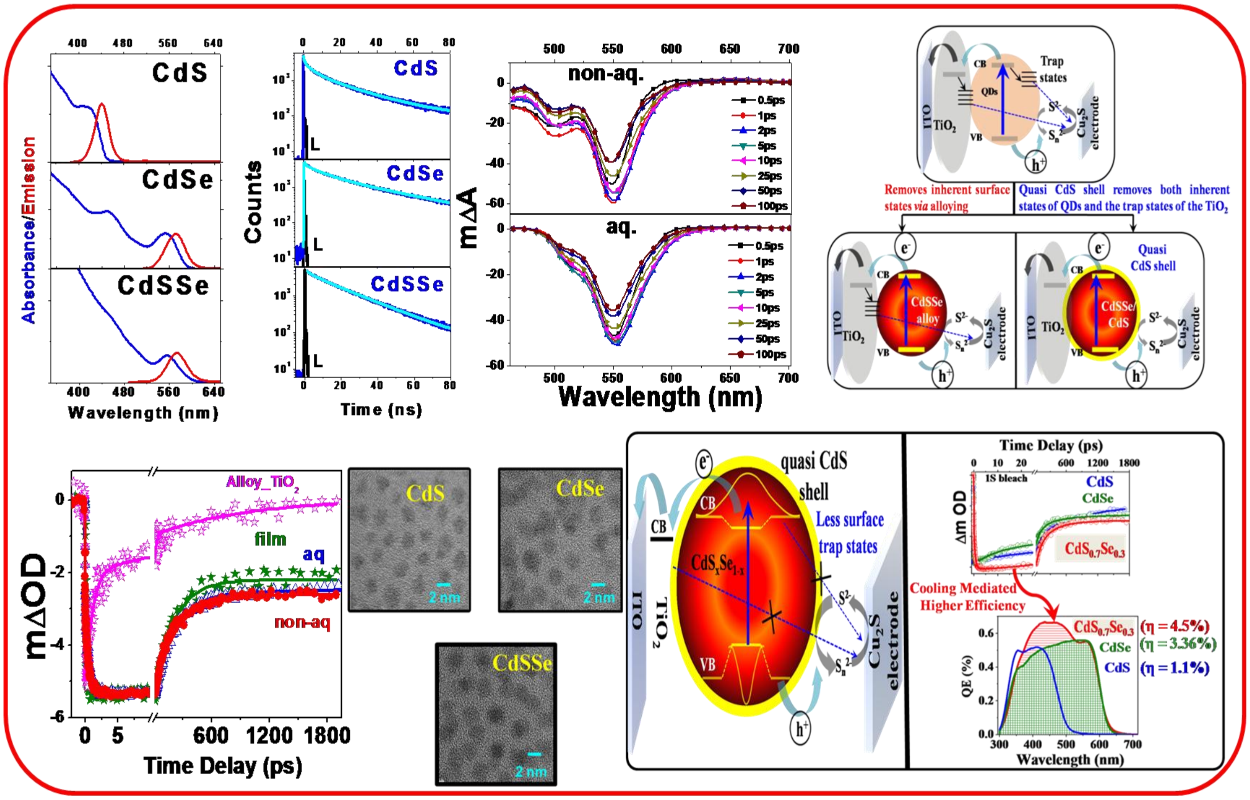

- *J. Phys. Chem. C*, **2016 Submitted.**

8.1. Introduction:

Last few years research on QDSC has been increased tremendously because of their exciting opto-electronic property such as higher extinction coefficient, optical tunability, slow carrier relaxation process, large excited state charge carrier life time, formation of multiple exciton generation, extraction of hot electrons which can break the Shockley−Queisser limit (32%), easy to characterize and of course low production cost [98, 99, 147, 148, 330, 369-371]. Especially, lower band gap II-VI [158, 372-374] and IV-VI [223, 375-378] semiconductor materials which absorb light in the visible and near infrared regions are widely used as a light harvesters in QDSC. Apart from this, some narrower semiconductor materials like $CuInS_2$ [159, 379-381], $CuInSe_2$ [39, 382], $CuInGaSe_2$ [383] and of course including organic inorganic perovskite[266, 384] have been extensively used a sensitizer in the low-cost third generation solar cell. Moreover, the excited state charge carrier life time of the QDs can also be increased through doping (usually Mn^{2+}) which boost the efficiency of the QDSC [214, 385]. Besides, utilizing the band gap engineering concept and depending on light absorbing ability often heterostructure core/shell nanocrystals, such as ZnTe/CdSe[386], CdS/CdSe, [115, 308, 387, 388] CdTe/CdS,[155] CdSeTe/CdS [389], PbS/CdS/ZnS[390], $CuInS_2$/CdS[379] core/shell/quasi shell [391] and ternary alloy QDs like, $CdSe_xTe_{1-x}$,[126] PbS_xSe_{1-x}, [39] CdSe/CdS_xSe_{1-x}/CdS [359] are used as a photo anode to generate the photo current. In this ternary alloy QDs, the size quantization and the optical tunability not only depend on the size of the QD but it also depends on the composition of the constituents. Thus composition plays an extra degree of freedom towards the optical and photo physical properties of the QDs. However, to optimize photocurrent efficiency it is necessary to optimize all the processes after characterized and measure the photovoltaic performance of a working solar cell.

Even though the QD materials have all the exciting properties, the efficiency of the QDSC has not reached at double numerical figures; whereas DSSC has crossed 13% PCE using a porphyrin based sensitizer molecule and Co (II/III) redox shuttle electrolyte [45]. The poor performance of the QDSC is due to lesser charge separation, in most of the QDSC the photogenerated electron is trapped into the internal defect states and/or recombines with electrolyte QD interface [369, 381, 392, 393]. To generate the photo-current the lower band gap sensitizer QDs are deposited on the wide band gap semiconductor such as TiO_2, ZnO etc. To deposit these sensitizer QD, two major processes are well known; direct growth technique which includes chemical bath deposition (CBD) [147, 154-156], successive ion layer absorption and reaction (SILAR) [157, 158], another process is post synthesis deposition technique which includes direct deposition like, electrophoretic technique [159] or by ligand assisted assembly [160] . Though the direct growth technique is beneficial for high coverage, growth and nucleation on the TiO_2 mesoporus surface, but, through these CBD and SILAR techniques the size and the size quantized quantum confinement of the QD can't be controlled. As a result, lot of surface defect states will generate which annihilates the charge carrier through non radiative trapping process [38, 160]. In the post synthesis deposition process; the size, size quantized states, high crystallinity, optical properties, band gap tenability and surface passivation of the sensitizer QD can easily be controlled. The direct deposition and electrophoretic techniques is not used so far due long chain ligand which prevent the loading of the QD on the TiO_2 surface. In the ligand assist deposition processes both high quality and very good deposition is maintained. Utilizing these post synthesis ligand assisted technique Zhong et al. tremendously ameliorate the photocurrent efficiency in QDSC beyond 9% using CdSeTe/CdS alloy QDs [389]. Earlier Ma et al. showed both higher short circuit current (J_{SC}) and open circuit voltage (V_{OC}) for

PbS_xSe_{1-x} alloy QD while PbSe and PbS showed only higher J_{SC} and V_{OC} respectively [39]. In alloy QD both band gap tunability and charge carrier cooling dynamics can be monitored through changing the composition. Another important type of II-VI ternary alloy QD is CdS_xSe_{1-x} which forms all possible composition because of less than 3.5% crystal mismatched in the crystals structure of CdS and CdSe [354]. The CdS_xSe_{1-x} alloy QDs show wider absorption signature [356, 361, 394], high emission quantum yield,[127] long excited state life,[127] higher photostability[357] as compare to their corresponding constituent. Thus CdS_xSe_{1-x} alloy can be directly used as sensitizer in the QDSC[355].

Herein, we have demonstrated the photophysical properties of the CdS_xSe_{1-x} alloy QDs after ligand exchanged with MPA (from non aqueous to aqueous solvent) and finally perform solar cell experiments in terms of IPCE and IV measurements. The water soluble CdS_xSe_{1-x} alloy QDs were deposited on the sintered TiO_2 film which act as photo anode in the QDSC. Four monolayer ZnS shell was coated on CdS_xSe_{1-x} through SILAR technique to passivate the alloy QDs. Using polysulfide electrolyte and Cu_2S deposited FTO glass plates as photocathode the efficiency of the QD solar cell was measured to be 3.36 (±0.1)% for CdSe and 3.75 (±0.12)% for CdS_xSe_{1-x} QDs under 1 sun illumination. However, a non-epitaxial CdS quasi shell was coated to passivate the TiO_2 surface states and followed by passivate through ZnS layer that increased PCE to 4.5 (±0.18) % which is the highest reported value for CdS_xSe_{1-x} alloy QDs.

8.2. Results and Discussion:

8.2.1. Optical properties: UV-Vis and PL study:

The morphological analysis of the CdS_xSe_{1-x} alloy QDs has been demonstrated in our earlier publication.[127] The monodispersed high luminescence CdS_xSe_{1-x} alloy QDs form zinc blend crystals structure. The main aim of the present study is to measure the photocurrent conversion efficiency of the as synthesized CdS_xSe_{1-x} alloy QDs and compare with CdS and CdSe QDs. For this purpose we have synthesized similar size non-aqueous CdS, CdSe, and CdS_xSe_{1-x} alloy QDs and finally transfer to the aqueous solution through ligand exchanged with MPA. The steady state optical absorption spectra of the CdS_xSe_{1-x} alloy QDs before and after ligand exchanged is plotted in the Figure 8.1A trace a and trace b respectively. The 1S ($1S_{3/2}$-$1S_e$) excitonic peak of the alloy QDs shifted to 6 nm blue region after ligand exchange which is due small MPA capping ligand. Moreover, the emission quantum yield of the alloy QDs is tremendously

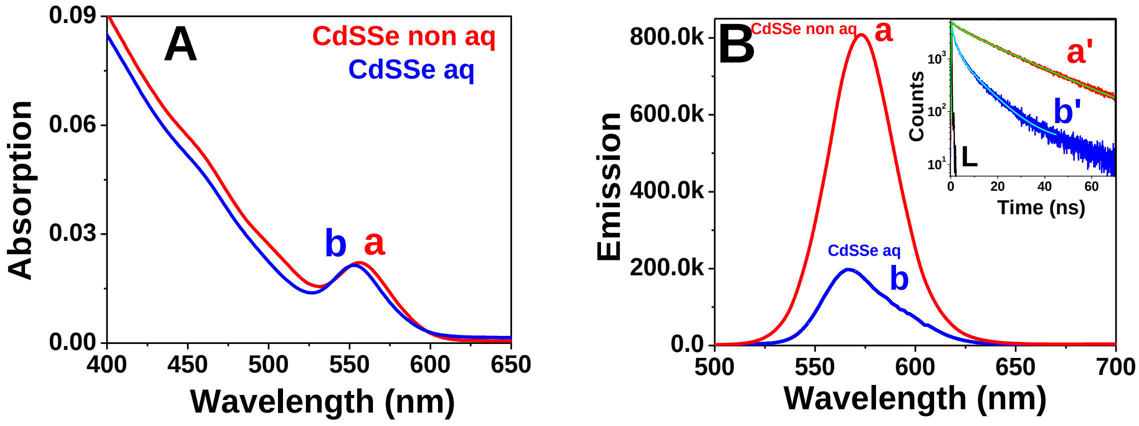

Figure 8.1: (A) UV-Visible absorption **(B)** Photoluminescence spectra of CdS_xSe_{1-x} alloy QDs (a) before and (b) after ligand exchange with MPA. **Inset:** Time resolved PL decay traces of CdSSe alloy QDs (a') before and (b') after ligand exchanged with MPA at 563 nm after exciting at 445 nm laser. "L" stands for excitation laser profile.

decreased after ligand exchanged. The PL spectra of the alloy in non-aqueous and aqueous medium are plotted in the Figure 8.1B trace a and trace b respectively after 480 nm excitation. To reconfirm the decrease of radiative recombination we have measured the time resolved PL decay trace and shown in Figure 8.1B inset. The time resolved PL decay trace at 570 nm in chloroform (trace a') shows long excited state life time which can be fitted bi-exponentially with the time constants τ_1 = 2.26 ns (27%), τ_2 = 10.8 ns (51%), and τ_3 = 37 ns (22%) with τ_{avg} = 14.2 ns. However, the PL decay trace of the MPA capped CdS_xSe_{1-x} alloy QDs at 567 nm (trace b') shows faster decay which can be fitted with the time constants τ_1 = 2.26 ns (27%), τ_2 = 10.8 ns (51%), and τ_3 = 37 ns (22%) with τ_{avg} = 14.2 ns. The faster PL decay of the MPA capped CdS_xSe_{1-x} alloy QDs which is due to the removal of holes from valence band of photoexcited alloy QDs as MPA is the hole quencher. Similar to the alloy QDs the optical properties (steady sate optical and PL studies) of the pure CdS and CdSe are also carried out and described in the earlier chapter.

8.2.2. Femtosecond Transient Absorption Measurements:

Transient absorption is one of the sophisticated techniques to investigate the excited state charge carrier relaxation dynamics at ultrafast time scale. As the photoexcited charge carrier is responsible for the photocurrent in solar cell so it is very important to know their relaxation and recombination dynamics. To optimize the solar cell performance one of the crucial and important strategy is to identify the mechanistic pathways. In our earlier report we have demonstrated longer excited state life time and slow electron cooling time for the CdS_xSe_{1-x} alloy QD as compared to both CdS as well as CdSe. In the present investigation we have compared the photovoltaic performance of CdS_xSe_{1-x} by making similar size CdSe and CdS QDs. However, before going to detail in photovoltaic performance it is very important to identify all the mechanistic processes. To recognize the carrier cooling and relaxation dynamics we have carried femtosecond transient absorption (TA) measurements after exciting the samples at 400 nm laser light and probing at UV-vis regions. Figure 8.2 illustrates the TA spectrum of the CdS_xSe_{1-x} alloy QDs at different time delay before (A) and after (B) ligand exchange with MPA in chloroform and water respectively. The TA spectrum of the CdS_xSe_{1-x} alloy QDs shows two separate bleach signal at 550 nm and

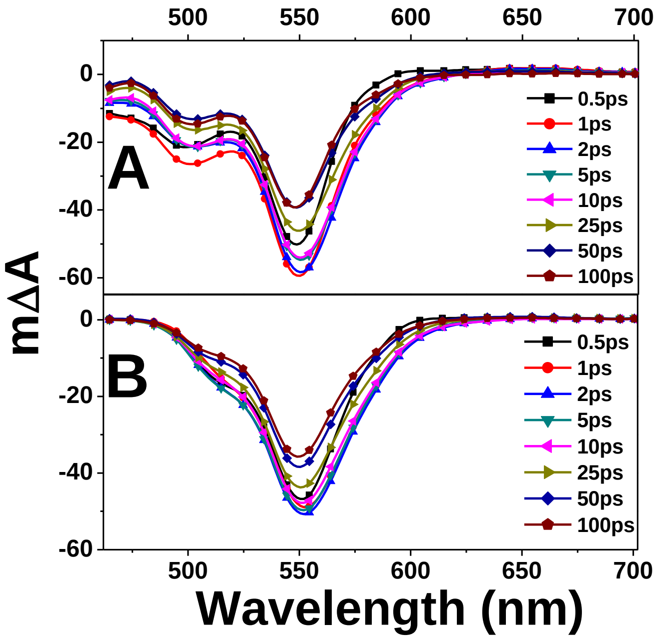

Figure 8.2: Transient absorption spectrum of CdSSe alloy QD (A) in chloroform and (B) in water after ligand exchanged with MPA at different time delay after 400 nm laser excitation.

499 nm which can be attributed to $1S_e$−$1S_{3/2}$ (1S) and 1Se−$2S_{3/2}$ (2S) optical transition respectively. Interestingly the distinct bleach due to 2S transition is not clear in case of both CdSe and CdS. In case of CdSSe alloy QD due to smaller CB band offset in CdS and CdSe, the CB of the alloy QDs will have a mixing character. As a result, due to orbital mixing of these two constituent QDs the optically weak transition (2S) becomes prominent in the alloy structure which is absent in both the pure QDs structure. The excited electron delocalization helps to increase the excited state life time of the alloy QDs. To fabricate the solar cell one of the very important processes is the properly loading of the QDs on the wider band gap semiconductor (such as TiO_2). So, it is very important to transfer the synthesized QDs in water phase using

some appropriate ligand (like MPA). The TA spectrum of the phase transferred CdS_xSe_{1-x} alloy QD is plotted in the Figure 2B. The TA spectrum of the water soluble alloy shows a broad at 550 nm bleach with a hump at 512 nm. The TA bleach signal at 550 nm is due to the 1S electronic transition. As MPA is the hole quencher so after photoexcitation the photoexcited hole will be captured by the MPA. Thus population of the 2S electronic state has been decreased in presence of the MPA. The excited state dynamics of the alloy QDs has been described in the next section.

8.2.3. Carrier Cooling and Charge Transfer Interaction:

To monitor the carrier relaxation and charge transfer dynamics, we compare transient kinetic traces at the key wavelength in ultrafast time scale. Figure 8.3 illustrates the normalized transient bleach recovery kinetics of the CdSSe alloy QDs in chloroform (trace a), in water (trace b), on film (trace c) and on TiO_2 film (trace d). In our earlier report [127] we demonstrated the slow intraband electron relaxation in CdSSe alloy QD as compare to both the constituents CdS and CdSe. The slow electron cooling of the alloy QD is observed due to delocalization of electron in the CB of the graded alloy structure which decoupled the electron hole overlap. As a result, extend of electron-hole recombination through Auger process is decreased which assist to separate the excited electron to the CB of the alloy QDs to the CB of the TiO_2. In this chapter we focused on the photovoltaic performance of the CdS_xSe_{1-x} alloy QDs and the photophysical and the interfacial electron transfer has also been discussed. The 1S bleach recovery dynamics of the CdS_xSe_{1-x} alloy QDs in chloroform and water which can be fitted bi-exponential growth with time constant τ_{1g} = 150 fs (56%), τ_{2g} = 4 ps (44%), and τ_{1g} = 150 fs (56%), τ_{2g} = 4 ps (44%) and it recovers multi-exponentially τ_1 = 20 ps (-32%), τ_2 = 100 ps (-4%), and τ_3 >1 ns (-64%) (Table 8.1) and τ_1 = 20 ps (-29%), τ_2 = 200 ps (-19%), and τ_3 >1 ns (-52%) (Table 8.1) respectively. The bleach recovery kinetics of the CdSSe alloy in these solvent is not vary significantly. However, fast charge recombination in MPA capped CdSSe alloy is due to

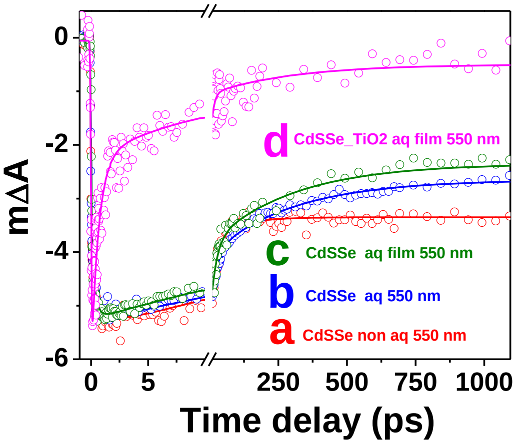

Figure 8.3: Normalized bleach recovery kinetics of CdSSe alloy QD at 550 nm in chloroform (a), in water after ligand exchanged with MPA (b), on film (c), and with TiO_2 on film (d) after 400 nm laser excitation.

very fast shuttling the hole by the ligand and after receiving the hole MPA facilitates charge recombination [325, 345, 395]. The bleach recovery of the CdSSe alloy QD on film which can also has bi-exponential growth τ_{1g} = 150 fs (56%), τ_{2g} = 4 ps (44%), and recovers multi-exponentially with time constant τ_1 = 20 ps (-34%), τ_2 = 300 ps (-20%), and τ_3 >1 ns (-46%) (Table 8.1). The faster bleach recovery as compare to solution phase which is due to the non radiative energy transfer from smaller size to the bigger size particle [396]. In film the interaction between the particles is more due to higher concentration as compare to the solution phase. Intriguingly, the bleach dynamics of CdS_xSe_{1-x} alloy on TiO_2 film has pulse width limited (<100 fs) growth and recovers very fast which can be fitted similarly with time constant τ_1 = 0.65 ps (-64%), τ_2 = 10 ps (-18%), τ_3 = 300 ps (-8%) and τ_4 >1 ns (-10%) (Table 8.1). The faster bleach recovery of the alloy on TiO_2 film which can be attributed due to interfacial electron transfer from the CB of the CdS_xSe_{1-x} to the CB of the TiO_2. The overall charge carrier processes of the alloy sensitized solar cell are summarized in the scheme 8.1. In absence of the TiO_2 the excited state charges carriers relaxed via Auger process. However, on the TiO_2 film the excited charge carrier are injected to the CB of TiO_2 before it's relax through Auger process. To ameliorate the photovoltaic performance a quasi CdS shell followed by a layer of ZnS was deposited on the CdSSe alloy film via SILAR technique. The wider band CdS not only passivates the core alloy QD but it also helps to remove the surface defect states of the TiO_2 film. Earlier Bhattacharyya et al.[391] reported the 6.41 % PCE utilizing CdTe/CdS/CdS core/shell/quasi shell structure.

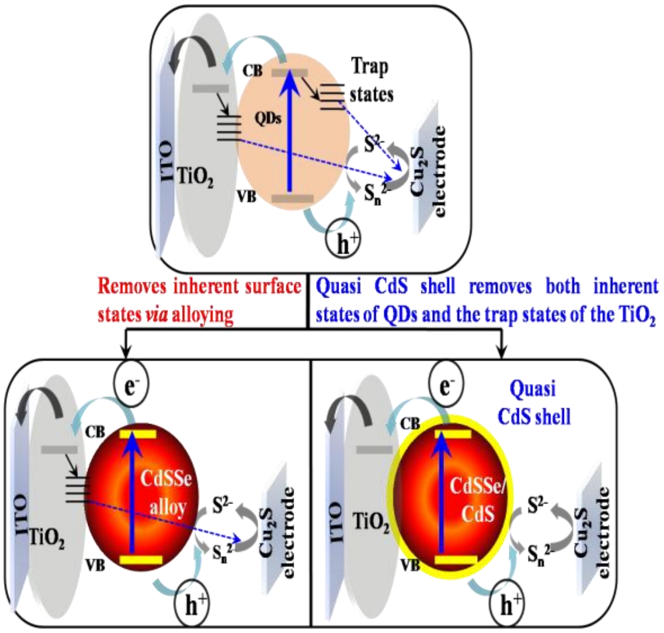

Scheme 8.1: Schematic illustration of step wise improving the PCE in QDSC; starting from CdS and CdSe QDs to CdS_xSe_{1-x} alloy and finally CdS_xSe_{1-x} alloy/quasi CdS shell has been used as sensitizer.

Table 8.1: Multi-exponential fitting parameters of CdSSe alloy QD in different environment at 550 nm. The percentages at the parenthesis represent amplitude of the corresponding exponential functions.

System	τ_{1g}	τ_{2g}	τ_1	τ_2	τ_3	τ_4
CdSSe non-aq.	150 fs (56%)	4ps (44%)	20ps (-32%)	100ps (-4%)	>1 ns (-64%)	
CdSSe aq.	150 fs (56%)	4ps (44%)	20ps (-29%)	200ps (-19%)	>1 ns (-52%)	
CdSSe_film	150 fs (56%)	4ps (44%)	20ps (-34%)	300ps (-20%)	>1 ns (-46%)	
CdSSe_TiO_2 film	<100 fs		0.65ps (-64%)	10ps (-18%)	300ps (-8%)	>1 ns (-10%)

By forming CdS shell on CdTe core the inherent surface states of the QDs could be managed. On additional CdS quasi shell which passivate the surfaces states of the mesoporus TiO_2. In the present study the inherent suface states of the sensitizer QDs has been controlled through alloying process. As the reactivity of the selenium is more as compare to sulfur with the cadmium oleate, thus the structure of the alloy will be graded like where the core is CdSe rich and the surface will be decorated by wider band gap CdSSe graded shell. As a result the inherent surfaces states of the QDs can be optimized. Futhermore, a quasi CdSe shell which improve the charge separation through removing the surface defect states of the TiO_2. The overall impovement of the PCE has been schematically illustrated in the Scheme 8.1.

8.2.4. Solar Cells Performance:

The photovoltaic performance in terms of Incident Photocurrent Conversion Efficiency (IPCE) and Current density (J_{SC}) versus voltage (V) of the mesoscopic TiO_2 films loaded with CdS, CdSe $CdS_xSe_{1-x}$and CdS_xSe_{1-x}/CdS nanocrystals were measured with 1 sun illumination generated from PEC-L01, Peccell solar simulator. Utilizing polysulfide electrolyte and Cu_2S

deposited ITO glass plates as photocathode (Scheme8.1) the solar cell performance has been measured. Figure 4A shows the I-V characteristics in the form of current density of CdS (trace a), CdSe (trace b), CdS_xSe_{1-x} (trace c) and CdS_xSe_{1-x} /CdS (trace d). The short circuit current density (J_{SC}, mA), open circuit voltage (V_{OC}, V), fill-factor (FF, %) and the photo current conversion efficiency (η, %) of the above mentioned systems are summarized in the Table 8.2. The overall efficiency of the CdS_xSe_{1-x} alloy QDs (3.75%) is found to be higher as compare to both CdS and CdSe. However, upon addition of a CdS quasi layer on the CdS_xSe_{1-x} film the efficiency increased from 3.75 % to 4.4 %. The CdS quasi layer helps to passivate the surface defect states of the TiO_2 mesoscopic film [391]. Thus electron density in the electrical circuit is increased significantly which help to build up more photo current. Figure 4B depicts the IPCE of CdS (trace a), CdSe (trace b), CdS_xSe_{1-x} (trace c) and CdS_xSe_{1-x} /CdS (trace d). In case of CdS absorption of the photoanode is restricted up to 550 nm while in case of CdSe and CdS_xSe_{1-x} it

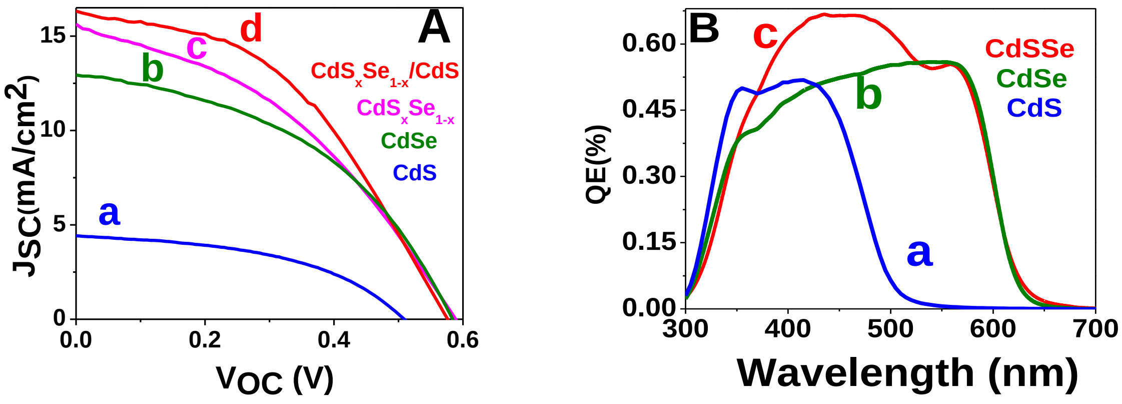

Figure 8.4: Photovoltaic performance in terms of (A) Current density (J_{SC}; mA/cm^2) *vs.* Voltage (V_{OC}; Volt) and (B) percentage of Incident Photon-to current Conversion Efficiencies (IPCE) *vs.* wavelength for (a) CdS QD, (b) CdSe, and (c) CdS_xSe_{1-x}.

extends up to 700 nm. But the value of the IPCE for CdS_xSe_{1-x} is 66% while for CdS and CdSe is 53% and 34% respectively at 463 nm. The enhancement of the IPCE for the CdSSe alloy is due to slow electron cooling and the higher extinction coefficient. It is interesting to see that in case of CdS_xSe_{1-x}/CdS system the value of IPCE is not varied significantly though it showed higher efficiency. During the QDSC performance the following reactions are take place in the overall cell:

$$\text{QDs/Alloy} + h\nu \longrightarrow \text{QDs/Alloy}\,(e^- + h^+)$$

$$TiO_2 + \text{QDs/Alloy}\,(e^- + h^+) \longrightarrow TiO_2\,(e^-) + \text{QDs/Alloy}\,(h^+)$$

$$\text{QDs/Alloy}\,(h^+) + (1/2)\,S^{2-} \longrightarrow \text{QDs/Alloy} + (1/2)\,S$$

$$(1/2)\,S + (1/2)\,S_{n-1}^{2-} \longrightarrow (1/2)\,S_n^{2-}$$

$$(1/2)\,S_n^{2-} + e^- \longrightarrow (1/2)\,S_{n-1}^{2-} + (1/2)\,S^{2-}$$

Table 8.2: QDSC performance in terms of IPCE and IV.

QD System	J_{sc} (mA/cm^2)	V_{oc} (Volt)	FF (%)	PCE (%)
CdS	3.82	0.55	51	1.06
CdSe	12.94	0.58	45	3.36
CdS_xSe_{1-x}	14.67	0.59	47	3.75
CdS_xSe_{1-x} /CdS	15.49	0.59	48	4.40

8.3. Conclusion:

Composition controlled size quantization is one of the striking property for developing the third generation QD solar cell. Varying the composition of the constituent, we observe

CdS_xSe_{1-x} alloy QDs is the superior sensitizer as compare to both CdS as well as CdSe. The slow electron cooling of CdS_xSe_{1-x} alloy QDs which is helpful for extraction of charge carrier from the sensitizer to the CB of the TiO_2. Using polysulfide electrolyte and Cu_2S deposited ITO glass plates as photocathode the efficiency of the QD solar cell was measured to be 1.1(±0.1)% for CdS, 3.36 (±0.1)% for CdSe and 3.75 (±0.12)% for CdS_xSe_{1-x} QDs under 1 Sun Illumination. When an additional non-epitaxial CdS quasi-shell was deposited on top of CdS_xSe_{1-x} film quasi-shell to passivate the TiO_2 surface states followed by ZnS passivation (TiO_2/ CdS_xSe_{1-x} /quasi-CdS/ZnS) QD solar cell the PCE increased to 4.5 (±0.18)% which is the highest reported value for CdSSe alloy QDs. The overall 20% increase of PCE is due to the quasi CdS shell which helps to separate more electrons through passivate the surface states of TiO_2.

CHAPTER-9

Summary and Outlook

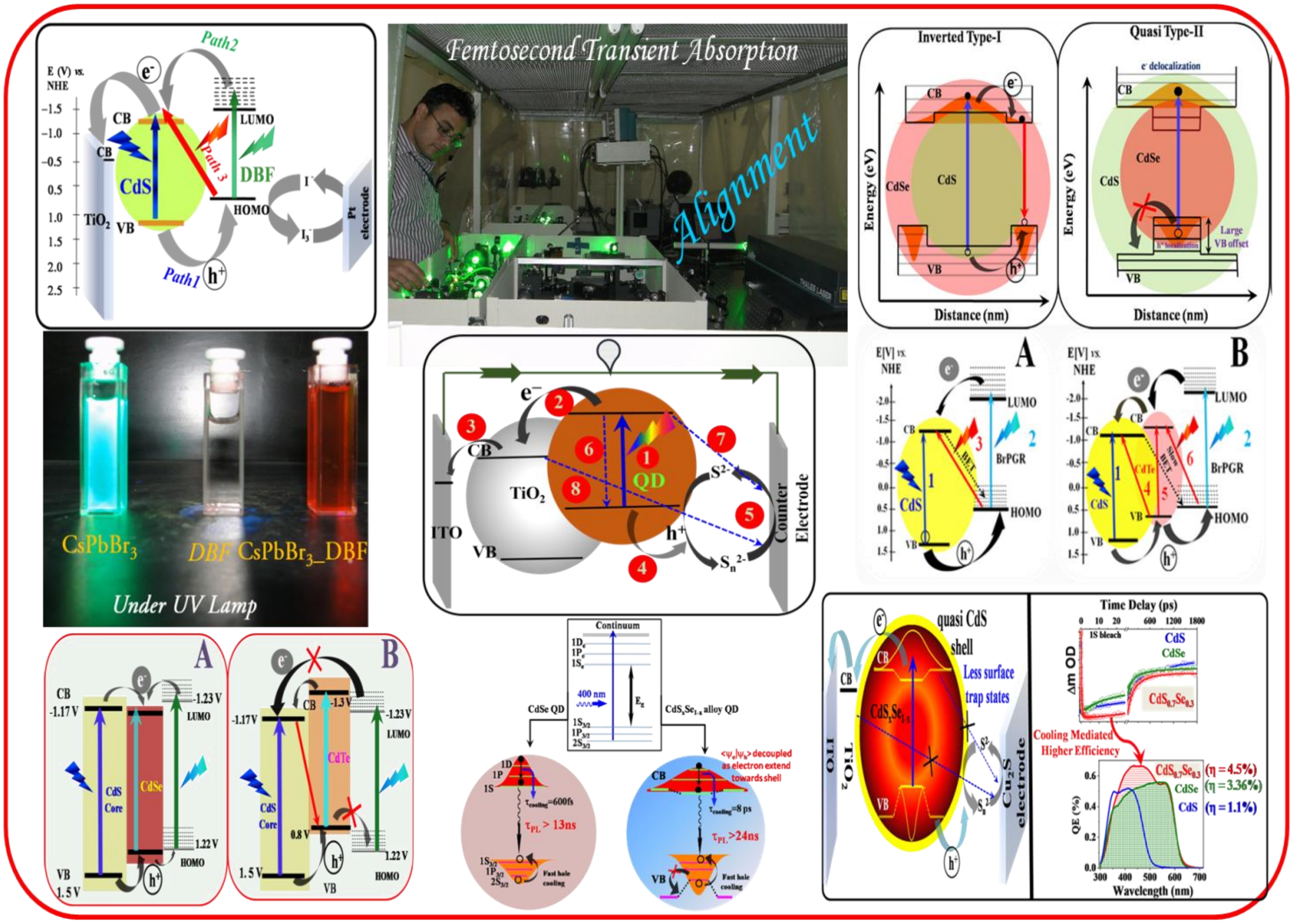

9.1. Summary

The main emphasis of this thesis is ultrafast charge transfer dynamics of the nanocrystals quantum dots in absence and in presence of molecular adsorbate. The charge transfer dynamics have been investigated utilizing different NCs in terms of colloidal quantum dots, core/shell, alloys and the various organic and inorganic molecules. The NCs have been synthesized by us; however, the dye molecules are either purchased or synthesized through collaboration. After synthesizing the NC quantum dots the morphology has been analyzed by XRD, HRTEM, EDX, and optical techniques. The charge carrier dynamics of the composite system have been carried out using time resolved PL and femtosecond transient absorption study. The NCs in different form are employed gradually depending on their application in QDSC. To alleviate PCE in QDSC, the molecular adsorbates have been introduced with the NCs which ameliorate charge separation and preclude the exciton annihilation. The experimental conclusions are relevant towards QDSC and with these ideas we could able to make working QD sensitized solar cell. The chronological results of the chapters 3 to 8 are summarized below.

The charge transfer interaction of CdS QD in presence of 4′,5′-dibromo fluorescence and two BODIPY dyes are explained in chapter 3. Limited absorption cross-section and strong exciton annihilation of the CdS QDs have been optimized by introducing DBF and the BODIPY molecules respectively. Steady state and time resolved optical absorption and PL studies indicate that charge separation in the CdS−DBF composite takes place *via* three different pathways, through hole transfer from the photoexcited CdS QD to DBF (path 1), electron injection from photoexcited DBF to the CdS QD (path 2), and finally, direct electron transfer from the ground-state (HOMO) of DBF to the CB of the QD (path 3) (photoexcitation of the CT complex). The electron and hole transfer time of this composite system has been measured to be <100 fs and

800 fs respectively. Utilizing more light absorption and better charge separation by the composite system we could able to show better PCE (1.1%) as compared to pure CdS (0.43%) and DBF (0.23%). In presence of BODIPY molecule we have been observed exciton quenching of the CdS QDs through non radiative energy transfer process. The FRET time of the composite is calculated to be 450 fs.

Multiple charge transfer processes in colloidal $CsPbBr_3$ QDs in presence of DBF molecule are described in chapter 4. Steady state optical absorption measurement suggests that DBF form strong CT complex with the CPB QDs which absorbs more and broad light in the solar spectrum. The energy levels of the CPB and DBF are determined on the basic of cyclic Voltammetric study which suggest that both CB and VB of the CPB QD lies energetically below the HOMO and LUMO of the DBF molecule respectively. The charge carrier transfer dynamics have been confirmed from steady state and time resolved PL analysis. The PL quenching of the CPB QDs reveals photo-excited hole transfer from CPB QD to DBF molecule which is thermodynamically viable. Additionally, a red shifted CT luminescence of the CPB-DBF complex has been noticed which increases with CPB concentration. The hole transfer time from photo-excited CPB QD to DBF molecule are determined to be 250 fs, where as direct electron transfer from HOMO of DBF to the CB of CPB found to be pulse-width limited (< 100 fs).

Work presented in chapter 5 is the band gap engineering and charge carrier delocalization in two different core/shell NCs, CdS/CdSe inverted type I and CdSe/CdS quasi type II, utilizing femtosecond transient absorption spectroscopy in absence and presence of different quencher molecule. Morphology of these two NCs core/shell has been analyzed from XRD and HRTEM studies. The location of charge carriers in the heterostructures has been demonstrated with the help of quenching studies with BQ (electron quencher) and Py (hole quencher) using steady-state and time-resolved PL and absorption spectroscopic techniques. The PL studies reveal quenching of both electron and hole in CdS/CdSe inverted type I core–shell in presence of both BQ and Py, respectively; however, only electron-quenching is observed in CdSe/CdS quasi-type II core–shell in the presence of BQ. Experimental observation suggests that in CdS/CdSe inverted type I core– shell both electrons and holes are localized in CdSe shell QDs; however, in CdSe/CdS quasi-type II, holes are localized in CdSe core QDs and electrons are delocalized in the CB of both CdSe core and CdS shell QDs due to the low CB offset. Electron transfer times from the core QDs to the BQ quencher through shell QDs in both the above systems are found to be pulse-width-limited (<100 fs); however, the hole transfer time from CdS core QDs to Py molecule through CdSe shell was found to be ~200 fs. Prior to charge separation in core–shell/ quencher composite systems, fast charge recombination occurs between either electron or hole in core–shell and Py^+ or BQ^-, respectively. This observation clearly suggests that quencher molecules initially captured either electron or hole, depending upon thermodynamic feasibility, and later on facilitate fast charge recombination. From our studies we can suggest that it is possible to design and synthesize core–shell heterostructures through band gap engineering where one can selectively localize electron or hole, depending upon application.

Ultrafast hole- and electron-transfer dynamics in different core/shell NCs sensitized by different molecular adsorbates are explained in chapter 6. The synthesized CdS QDs, CdS/CdSe and CdS/CdTe core/shell NCs form cubic zinc blende structure with monodispersed size distribution. The charge transfer dynamics have been carried out using an organic (Br-PGR) and an inorganic (Re (I) complex) dye molecules by time-resolved emission and ultrafast transient absorption techniques which suggest that charge separation in both composite materials takes place in multiple pathways. Steady state optical absorption studies suggest that Br-PGR forms strong CT complexes with both the CdS QD and CdS/CdTe core–shell which facilitates a higher charge separation in the excited state. Upon photo-excitation of the CdS/Br-PGR composite, charge separation takes place in different pathways like photo-excited hole transfer from the CdS QD to Br-PGR, photo-excited electron injection from Br-PGR to the CB of the CdS QD and direct electron transfer from the HOMO level of Br-PGR to the CB of the CdS QD. However, on the photoexcitation of the CdS/CdTe/Br-PGR composite material, photo-excited hole from the CdS core QD transfers to Br-PGR through the valence band of the CdTe shell and the photoexcited Br-PGR injects an electron into the CB of the CdTe shell QD which finally transfers to the CB of the CdS core QD. In addition to that, direct electron transfer from the HOMO of Br-PGR to the CB of the CdTe shell QD takes place. Due to cascading nature of the energy levels, the better charge separation through different pathways is observed in CdS/CdTe_Br-PGR system as compared to CdS_Br-PGR. More charge separation and lesser charge recombination is observed in the type-II regime. Similarly, electron and hole transfer is also facilitated in CdS/CdSe_Re complex composite system due to inverted type I band structure of the CdS/CdSe NCs. However, the restriction of charge delocalization is noticed in CdS/CdTe_Re composite system because of higher energy CdTe shell barrier. We have also measured the hole and electron transfer time by comparing the kinetic traces. In all the cases the electron transfer is measured <100 fs while the hole transfer is varied from 900 fs to 4.5 ps. Assistance of charge separation through delocalization of charge carrier in CdS, CdS/CdTe and CdS/CdSe sensitized by molecular adsorbate can be used as better photo anode in QDSC. Restriction of charge carrier delocalization in CdS/CdTe-Re-complex can't be used in QDSC due to less charge separation.

Work described in chapter 7 is on the carrier cooling dynamics of CdS_xSe_{1-x} and $Cd_xZn_{1-x}Se$ alloy QD. Both the alloy are synthesized in a single pot process in a non coordinating solvent (ODE) at ~300° C and are characterized using XRD, EDX, and HRTEM techniques. Steady state optical absorption and PL measurements of the CdS_xSe_{1-x} alloy show the nonlinear behaviour with changing chalcogenied composition. In case of $Cd_xZn_{1-x}Se$ both optical and PL spectra are red shifted with respect to the both CdSe and ZnSe. This clearly suggests that both the alloy form graded like structure where the core of the alloy is CdSe rich. The reactivity of the selenium towards cadmium oleate is more as compare to sulphur, thus the core of the CdS_xSe_{1-x} alloy structure will have CdSe rich and the graded shell are CdS rich. Similarly, the reactivity of Se is more with Cd ion than Zn ion, so like CdS_xSe_{1-x} alloy, the $Cd_xZn_{1-x}Se$ will also have CdSe core rich and ZnSe shell rich. Thus, for CdS_xSe_{1-x}, $Cd_xZn_{1-x}Se$ in both cases core is CdSe rich and shells are CdS and ZnSe rich respectively. The band alignment of these two systems suggests the quasi type-II structure. Due to smaller CB offset of the CdSe and CdS electron will be delocalized in the CdS_xSe_{1-x} graded like alloy structure. On the other hand due to smaller VB offset of the CdSe and ZnSe hole will be delocalized $Cd_xZn_{1-x}Se$ structure. Because of the delocalization of the either electron or hole in the CdS_xSe_{1-x} and $Cd_xZn_{1-x}Se$ alloy structure respectively, the intraband electron cooling time and charge separation are increased due to decoupling of the e-h in these quasi type-II structures.

Improving solar cell efficiency utilizing CdS_xSe_{1-x} alloy QD is demonstrated in chapter 8. Varying the composition of the constituent, we could able to see CdS_xSe_{1-x} alloy QDs is the superior sensitizer as compare to both CdS as well as CdSe QDs. The slow electron cooling of CdS_xSe_{1-x} alloy QDs which is helpful for extraction of charge carrier from the sensitizer to the CB of the TiO_2. The post synthesis deposition technique help to increase the particle quality by reducing the inherent surface defect states. Using polysulfide electrolyte and Cu_2S deposited ITO glass plates as photocathode the efficiency of the QD solar cell is measured to be 1.1(±0.1)% for CdS, 3.36 (±0.1)% for CdSe and 3.75 (±0.12)% for CdS_xSe_{1-x} QDs under 1 Sun Illumination. Reducing the inherent surface defect states via alloying which ameliorate the separation of charge carrier. When an additional non-epitaxial CdS quasi-shell is deposited on top of the CdS_xSe_{1-x} film the PCE increased to 4.5 (±0.18)% which is the highest reported value for CdS_xSe_{1-x} alloy QDs. The overall 20% increase of PCE is due to the quasi CdS shell which helps to separate more electrons through passivation the surface states of TiO_2.

9.2. Outlook

The investigation of the present thesis work mainly involve on the ultrafast charge transfer dynamics of colloidal NC quantum dots in absence and in presence of different organic or inorganic or quencher molecules. Changing the nature of the NCs from QDs to different heterostructure (like core/shell, alloy) we could successfully able to tune the optical properties in the entire visible region. The key conclusion of the present thesis is on improving the mechanistic pathways of the QDSC through monitoring charge carrier dynamics. Finally with this knowledge of charge carrier dynamics we have developed alloy QDSC with unprecedented ~4.5 % PCE.

Ultrafast charge transfer dynamics of CdS QDs with DBF and BODIPY have been shown better charge separation in the composite system. There are still scopes to further improve better charge separation in the composite systems. Qualitatively measure of electron and hole transfer time in the QDs/molecular system is challenging task that need to be explored. There is possibility to do systematic photo physical studies of QDs/molecular species for doing further research in this field.

Multiple charge transfer processes in $CsPbBr_3$ sensitized with DBF successfully demonstrate in the chapter 4. The main aim of this study is to improving the charge separation of CPB QDs through DBF molecule. Due to higher photo stability of the CPB QDs, it has been used successfully in the photovoltaic. However, the maximum PCE of the CPB sensitized QDs solar cell has been reported ~6.6%. Less solar light absorption by the CPB QDs is the main reason for this low efficiency which can be increase by introducing a suitable sensitizer molecule. Future work in this direction can give good results in the third generation solar cell. Apart from this, this CPB QDs can be used in different application like bio-imaging, photocatalysis, reducing blinking etc. There are multidirectional scopes of research interest on this field. In addition to the charge carrier dynamics, the carrier cooling dynamics, charge relaxation of different derivatives of these totally inorganic perovskite QDs is not well established. More work can be done on these perovskite in this direction.

The charge carrier delocalization in heterostructure core/shell NCs has been explained in this chapter. Study on core-shell NCs exploiting additional degrees of freedom such as core diameter, shell thickness and ultimately composition profile of NCs have evolved a novel field in the realm of nanosciences coined as wave function engineering. Lots of fundamental work in this direction can be looked at in future which will helps to design these materials in proper application.

Charge separation dynamics in different core/shell using organic and inorganic molecule has been demonstrated in the chapter 6. These studies show multidirectional charge separation and charge recombination dynamics of the composite systems. Charge separation is favourable in cascading nature of band alignment of the core/shell NCs and slow charge recombination is found in type-II regime. Finding a suitable molecular adsorbate which as a sensitizer as well as hole acceptor can be done in future. Further studies to explore charge separation in a superior sensitizer molecule and core/shell composite are necessary.

Our study on carrier cooling dynamics of two graded alloy QDs (CdS_xSe_{1-x} and $Cd_xZn_{1-x}Se$) has illustrated slow intraband electron cooling mediated by electron hole decoupling. The experimental results show both the alloy from graded like structure where core is CdSe rich. The quasi type-II band alignment help to passivate the surface of the NC, slowing down the intraband electron cooling time and increase the charge separation. Carrier cooling dynamics of the NC QDs is the fundamental property and endless research can be done using exciting semiconductor NC QDs.

The slow electron cooling and less surface defect states of the CdS_xSe_{1-x} alloy are beneficial for higher efficient solar cell. Here we demonstrate the photovoltaic performance of the CdS_xSe_{1-x} alloy which directly correlates with the slow electron cooling time and removal of surface detects. Research on photovoltaic performance can be explored utilizing low band gap materials with slow electron cooling time and less surface trapped states. To improve solar cell performance further studies to explore role of the mechanistic processes involved in the QDSC is required.

In future, the charge transfer dynamics of the narrow band NC QD with suitable molecular species which have been used as sensitizer as well as hole capture will be carried out using pump-probe techniques. The synthesis of different alloy QDs by changing the composition of the constituents will be addressed in future. The size quantization effect of the charge carriers will be investigated in terms of cooling dynamics, charge relaxation etc. The carrier dynamics of the different exciting materials (like inorganic/organic perovskite) which is necessary to design a suitable photovoltaic solar cell will be addressed in future.

References:

[1] Efros, A. L. *Soviet Physics Semiconductors-Ussr* **1982**, *16*, 772.

[2] Brus, L. E. *J. Chem. Phys.* **1983**, *79*, 5566.

[3] Ekimov, A. I.; Efros, A. L.; Onushchenko, A. A. *Solid State Commun.* **1985**, *56*, 921.

[4] Brus, L. E. *J. Chem. Phys.* **1984**, *80*, 4403.

[5] Kudera, S.; Zanella, M.; Giannini, C.; Rizzo, A.; Li, Y.; Gigli, G.; Cingolani, R.; Ciccarella, G.; Spahl, W.; Parak, W. J., et al. *Adv. Mater.* **2007**, *19*, 548.

[6] Widmann, F.; Simon, J.; Daudin, B.; Feuillet, G.; Rouvière, J. L.; Pelekanos, N. T.; Fishman, G. *Phys. Rev. B* **1998**, *58,* R15989.

[7] Alivisatos, A. P.; Harris, A. L.; Levinos, N. J.; Steigerwald, M. L.; Brus, L. E. *J. Chem. Phys.* **1988**, *89*, 4001.

[8] Jaeckel, G. *Z. Tech. Phys* **1926**, *6*, 301.

[9] Berry, C. R. *Physical Review* **1967**, *153*, 989.

[10] Meehan, E. J.; Miller, J. K. *J. Phys. Chem.* **1968**, *72*, 1523.

[11] Arthur, J. R. *J. Appl. Phys.* **1968**, *39*, 4032.

[12] Cho, A. Y. *J. Vac. Sci. & Tech.* **1971**, *8*, S31.

[13] Dingle, R.; Wiegmann, W.; Henry, C. H. *Phys. Rev. Lett.* **1974**, *33*, 827.

[14] Reed, M. A.; Randall, J. N.; Aggarwal, R. J.; Matyi, R. J.; Moore, T. M.; Wetsel, A. E. *Phys. Rev. Lett.* **1988**, *60*, 535.

[15] Murray, C. B.; Norris, D. J.; Bawendi, M. G. *J. Am. Chem. Soc.* **1993**, *115*, 8706.

[16] Alivisatos, A. P. *Science* **1996**, *271*, 933.

[17] Norris, D. J., in *Nanocrystal Quantum Dots, Vol. 2nd* (Ed.: V. I. Klimov), CRC Press, Boca Raton,FL, **2010**.

[18] Xia, J.-B. *Phys. Rev. B* **1989**, *40*, 8500.

[19] Murray, C. B.; Kagan, C. R.; Bawendi, M. G. *Annu. Rev. Mater. Sci.* **2000**, *30*, 545.

[20] Banin, U.; Lee, C. J.; Guzelian, A. A.; Kadavanich, A. V.; Alivisatos, A. P.; Jaskolski, W.; Bryant, G. W.; Efros, A. L.; Rosen, M. *J. Chem. Phys.* **1998**, *109*, 2306.

[21] Bratschitsch, R.; Leitenstorfer, A. *Nat Mater* **2006**, *5*, 855.

[22] Ashoori, R. C. *Nature* **1996**, *379*, 413.

[23] Coe, S.; Woo, W.-K.; Bawendi, M.; Bulovic, V. *Nature* **2002**, *420*, 800.

[24] Vdovin, E. E.; Levin, A.; Patanè, A.; Eaves, L.; Main, P. C.; Khanin, Y. N.; Dubrovskii, Y. V.; Henini, M.; Hill, G. *Science* **2000**, *290*, 122.

[25] Gong, K.; Zeng, Y.; Kelley, D. F. *J. Phys. Chem. C* **2013**, *117*, 20268.

[26] Shim, M.; Guyot-Sionnest, P. *J. Chem. Phys.* **1999**, *111*, 6955.

[27] Warburton, R. J.; Schulhauser, C.; Haft, D.; Schäflein, C.; Karrai, K.; Garcia, J. M.; Schoenfeld, W.; Petroff, P. M. *Phys. Rev. B* **2002**, *65*, 113303.

[28] Leatherdale, C. A.; Woo, W. K.; Mikulec, F. V.; Bawendi, M. G. *J. Phys. Chem. B* **2002**, *106*, 7619.

[29] Stobbe, S.; Schlereth, T. W.; Höfling, S.; Forchel, A.; Hvam, J. M.; Lodahl, P. *Phys. Rev. B* **2010**, *82*, 233302.

[30] Anikeeva, P. O.; Halpert, J. E.; Bawendi, M. G.; Bulović, V. *Nano Lett.* **2009**, *9*, 2532.

[31] Bruchez, M.; Moronne, M.; Gin, P.; Weiss, S.; Alivisatos, A. P. *Science* **1998**, *281*, 2013.

[32] Kamat, P. V. *J. Phys. Chem. C* **2007**, *111*, 2834.

[33] Zhuang, T.-T.; Liu, Y.; Sun, M.; Jiang, S.-L.; Zhang, M.-W.; Wang, X.-C.; Zhang, Q.; Jiang, J.; Yu, S.-H. *Angew. Chem. Int. Ed.* **2015**, *54*, 11495.

[34] Nozik, A. J. *Physica E: Low-dimensional Systems and Nanostructures* **2002**, *14*, 115.

[35] Green, M. A. *Third Generation Photovoltaics: Advanced Solar Energy Conversion*, **2006**.

[36] Luther, J. M.; Law, M.; Beard, M. C.; Song, Q.; Reese, M. O.; Ellingson, R. J.; Nozik, A. J. *Nano Lett.* **2008**, *8*, 3488.

[37] Kamat, P. V. *J. Phys. Chem. C* **2008**, *112*, 18737.

[38] Kamat, P. V.; Tvrdy, K.; Baker, D. R.; Radich, J. G. *Chem. Rev.* **2010**, *110*, 6664.

[39] Ma, W.; Luther, J. M.; Zheng, H.; Wu, Y.; Alivisatos, A. P. *Nano Lett.* **2009**, *9*, 1699.

[40] Barkhouse, D. A. R.; Pattantyus-Abraham, A. G.; Levina, L.; Sargent, E. H. *ACS Nano* **2008**, *2*, 2356.

[41] Tian, J.; Cao, G. *J. Phys. Chem. Lett.* **2015**, *6*, 1859.

[42] Dresselhaus, M. S.; Thomas, I. L. *Nature* **2001**, *414*, 332.

[43] Lewis, N. S. *Science* **2007**, *315*, 798.

[44] Du, J.; Du, Z.; Hu, J.-S.; Pan, Z.; Shen, Q.; Sun, J.; Long, D.; Dong, H.; Sun, L.; Zhong, X., et al. *J. Am. Chem. Soc.* **2016**, *138*, 4201.

[45] Mathew, S.; Yella, A.; Gao, P.; Humphry-Baker, R.; CurchodBasile, F. E.; Ashari-Astani, N.; Tavernelli, I.; Rothlisberger, U.; NazeeruddinMd, K.; Grätzel, M. *Nat Chem* **2014**, *6*, 242.

[46] Shockley, W.; Queisser, H. J. *J. Appl. Phys.* **1961**, *32*, 510.

[47] Kamat, P. V.; Christians, J. A.; Radich, J. G. *Langmuir* **2014**, *30*, 5716.

[48] Klimov, V. I. *Annu. Rev. Phys. Chem.* **2007**, *58*, 635.

[49] Norris, D. J. *Measurement and Assignment of the Size-Dependent Optical Spectrum in Cadmium Selenide (CdSe) Quantum Dots*, Ph.D. Thesis, **1995**.

[50] Ashcroft, N. W.; Mermin, N. D. *Solid State Physics*, Saunders, W.B., Orlando, FL, **1976**.

[51] Guzelian, A. A.; Banin, U.; Kadavanich, A. V.; Peng, X.; Alivisatos, A. P. *Appl. Phys. Lett.* **1996**, *69*, 1432.

[52] Efros, A. L. *Sov. Phys. Semicond.-USSR* **1982**, *16*, 772.

[53] Flügge, S. *Practical Quantum Mechanics, Vol. 1*, Springer, Berlin, **1971**.

[54] Efros, A. L.; Rosen, M.; Kuno, M.; Nirmal, M.; Norris, D. J.; Bawendi, M. *Phys. Rev. B* **1996**, *54*, 4843.

[55] Efros, A. L. *Phys. Rev. B* **1992**, *46*, 7448.

[56] Pankove, J. I. *Optical Processes in Semiconductors*, Dover, New York, **1971**.

[57] Altarelli, M. *in Semiconductor Superlattices and Interfaces*, A. Stella (Ed.), North Holland, Amsterdam, **1993**.

[58] Bastard, G. *Wave Mechanics Applied to Semiconductor Heterostructures*, Wiley, New York, **1988**.

[59] Ekimov, A. I.; Kudryavtsev, I. A.; Efros, A. L.; Yazeva, T. V.; Hache, F.; Schanne-Klein, M. C.; Rodina, A. V.; Ricard, D.; Flytzanis, C. *J. Opt. Soc. Am. B* **1993**, *10*, 100.

[60] Hellwege, K. H. *in Landolt-Bornstein Numerical Data and Functional Relationships in Science and Technology, New Series, Vol. 17b, Group III*, Springer-Verlag, Berlin, **1982**.

[61] Gfroerer, T. H.; Sturge, M. D.; Kash, K.; Yater, J. A.; Plaut, A. S.; Lin, P. S. D.; Florez, L. T.; Harbison, J. P.; Das, S. R.; Lebrun, L. *Phys. Rev. B* **1996**, *53*, 16474.

[62] Kittel, C. *Quantum Theory of Solids*, Wiley, New York, **1987**.

[63] Bir, G. L.; Pikus, G. E. *Symmetry and Strain-Induced Effects in Semiconductors*, Wiley, New York, **1974**.

[64] Luttinger, J. M. *Phys. Rev.* **1956**, *102*, 1030.

[65] Luttinger, J. M.; Kohn, W. *Phy. Rev.* **1955**, *97*, 869.

[66] Kane, E. O. *in Narrow Band Semiconductors. Physics and Applications, Lecture Notes in Physics, Vol. 133*, **1980**.

[67] Pidgeon, C. R.; N.Brown, R. *Phys. Rev.* **1966**, *146*, 575.

[68] Kane, E. O. *J. Phys. Chem. Solids* **1957**, *1*, 249.

[69] Norris, D. J.; Bawendi, M. G. *Phys. Rev. B* **1996**, *53*, 16338.

[70] Vahala, K. J.; Sercel, P. C. *Phys. Rev. Lett.* **1990**, *65*, 239.

[71] Sercel, P. C.; Vahala, K. J. *Phys. Rev. B* **1990**, *42*, 3690.

[72] Koch, S. W.; Hu, Y. Z.; Fluegel, B.; Peyghambarian, N. *J. Cryst. Growth* **1992**, *117*, 592.

[73] Efros, A. L.; Rodina, A. V. *Phys. Rev. B* **1993**, *47*, 10005.

[74] Nomura, S.; Segawa, Y.; Kobayashi, T. *Phys. Rev. B* **1994**, *49*, 13571.

[75] Takagahara, T. *Phys. Rev. B* **1993**, *47*, 4569.

[76] Calcott, P. D. J.; Nash, K. J.; Canham, L. T.; Kane, M. J.; Brumhead, D. *J. Lumin.* **1993**, *57*, 257.

[77] Nirmal, M.; Norris, D. J.; Kuno, M.; Bawendi, M. G.; Efros, A. L.; Rosen, M. *Phys. Rev. Lett.* **1995**, *75*, 3728.

[78] Henry, C. H.; Nassau, K. *Phys. Rev. B* **1970**, *1*, 1628.

[79] Brennan, F. K. *The Physics of Semiconductors*, Cambridge University Press, New York, NY, **1997**.

[80] Peterson, M. D.; Cass, L. C.; Harris, R. D.; Edme, K.; Sung, K.; Weiss, E. A. *Annu. Rev. Phys. Chem.* **2014**, *65*, 317.

[81] Bockelmann, U.; Bastard, G. *Phys. Rev. B* **1990**, *42*, 8947.

[82] Pandey, A.; Guyot-Sionnest, P. *Science* **2008**, *322*, 929.

[83] Lowisch, M.; Rabe, M.; Kreller, F.; Henneberger, F. *Appl. Phys. Lett.* **1999**, *74*, 2489.

[84] Benisty, H.; Sotomayor-Torrès, C. M.; Weisbuch, C. *Phys. Rev. B* **1991**, *44*, 10945.

[85] Sagar, D. M.; Cooney, R. R.; Sewall, S. L.; Dias, E. A.; Barsan, M. M.; Butler, I. S.; Kambhampati, P. *Phys. Rev. B* **2008**, *77*, 235321.

[86] Urayama, J.; Norris, T. B.; Singh, J.; Bhattacharya, P. *Phys. Rev. Lett.* **2001**, *86*, 4930.

[87] Klimov, V. I.; McBranch, D. W. *Phys. Rev. Lett.* **1998**, *80*, 4028.

[88] Kang, K. I.; Kepner, A. D.; Gaponenko, S. V.; Koch, S. W.; Hu, Y. Z.; Peyghambarian, N. *Phys. Rev. B* **1993**, *48*, 15449.

[89] Guyot-Sionnest, P.; Shim, M.; Matranga, C.; Hines, M. *Phys. Rev. B* **1999**, *60*, R2181.

[90] Klimov, V.; Mikhailovsky, A.; McBranch, D.; Leatherdale, C.; Bawendi, M. *Phys. Rev. B* **2000**, *61*, R13349.

[91] An, J. M.; Califano, M.; Franceschetti, A.; Zunger, A. *J. Chem. Phys.* **2008**, *128*, 164720.

[92] Narvaez, G. A.; Bester, G.; Zunger, A. *Phys. Rev. B* **2006**, *74*, 075403.

[93] Kambhampati, P. *Acc. Chem. Res.* **2011**, *44*, 1.

[94] Kambhampati, P. *J. Phys. Chem. C* **2011**, *115*, 22089.

[95] Ellingson, R. J.; Beard, M. C.; Johnson, J. C.; Yu, P.; Micic, O. I.; Nozik, A. J.; Shabaev, A.; Efros, A. L. *Nano Lett.* **2005**, *5*, 865.

[96] Klimov, V. I. *J. Phys. Chem. B* **2006**, *110*, 16827.

[97] Beard, M. C.; Luther, J. M.; Semonin, O. E.; Nozik, A. J. *Acc. Chem. Res.* **2013**, *46*, 1252.

[98] Semonin, O. E.; Luther, J. M.; Choi, S.; Chen, H.-Y.; Gao, J.; Nozik, A. J.; Beard, M. C. *Science* **2011**, *334*, 1530.

[99] Nozik, A. J.; Beard, M. C.; Luther, J. M.; Law, M.; Ellingson, R. J.; Johnson, J. C. *Chem. Rev.* **2010**, *110*, 6873.

[100] Luther, J. M.; Beard, M. C.; Song, Q.; Law, M.; Ellingson, R. J.; Nozik, A. J. *Nano Lett.* **2007**, *7*, 1779.

[101] Guyot-Sionnest, P.; Wehrenberg, B.; Yu, D. *J. Chem. Phys.* **2005**, *123*, 074709.

[102] Cooney, R. R.; Sewall, S. L.; Dias, E. A.; Sagar, D. M.; Anderson, K. E. H.; Kambhampati, P. *Phys. Rev. B* **2007**, *75*, 245311.

[103] Cooney, R. R.; Sewall, S. L.; Anderson, K. E. H.; Dias, E. A.; Kambhampati, P. *Phys. Rev. Lett.* **2007**, *98*, 177403.

[104] Robel, I.; Bunker, B. A.; Kamat, P. V.; Kuno, M. *Nano Lett.* **2006**, *6*, 1344.

[105] Saari, J. I.; Dias, E. A.; Reifsnyder, D.; Krause, M. M.; Walsh, B. R.; Murray, C. B.; Kambhampati, P. *J. Phys. Chem. B* **2013**, *117*, 4412.

[106] Mooney, J.; Krause, M. M.; Saari, J. I.; Kambhampati, P. *Phys. Rev. B* **2013**, *87*, 081201.

[107] Garrett, M. D.; Bowers, M. J.; McBride, J. R.; Orndorff, R. L.; Pennycook, S. J.; Rosenthal, S. J. *J. Phys. Chem. C* **2008**, *112*, 436.

[108] Underwood, D. F.; Kippeny, T.; Rosenthal, S. J. *J. Phys. Chem. B* **2001**, *105*, 436.

[109] Talapin, D. V.; Rogach, A. L.; Kornowski, A.; Haase, M.; Weller, H. *Nano Lett.* **2001**, *1*, 207.

[110] Manna, L.; Scher, E. C.; Li, L.-S.; Alivisatos, A. P. *J. Am. Chem. Soc.* **2002**, *124*, 7136.

[111] Talapin, D. V.; Mekis, I.; Götzinger, S.; Kornowski, A.; Benson, O.; Weller, H. *J. Phys. Chem. B* **2004**, *108*, 18826.

[112] Brovelli, S.; Schaller, R. D.; Crooker, S. A.; García-Santamaría, F.; Chen, Y.; Viswanatha, R.; Hollingsworth, J. A.; Htoon, H.; Klimov, V. I. *Nat Commun* **2011**, *2*, 280.

[113] Talapin, D. V.; Nelson, J. H.; Shevchenko, E. V.; Aloni, S.; Sadtler, B.; Alivisatos, A. P. *Nano Lett.* **2007**, *7*, 2951.

[114] Balet, L. P.; Ivanov, S. A.; Piryatinski, A.; Achermann, M.; Klimov, V. I. *Nano Lett.* **2004**, *4*, 1485.

[115] Pan, Z.; Zhang, H.; Cheng, K.; Hou, Y.; Hua, J.; Zhong, X. *ACS Nano* **2012**, *6*, 3982.

[116] Kim, S.; Fisher, B.; Eisler, H.-J.; Bawendi, M. *J. Am. Chem. Soc.* **2003**, *125*, 11466.

[117] Lo, S. S.; Mirkovic, T.; Chuang, C.-H.; Burda, C.; Scholes, G. D. *Adv. Mater.* **2011**, *23*, 180.

[118] Hewa-Kasakarage, N. N.; El-Khoury, P. Z.; Tarnovsky, A. N.; Kirsanova, M.; Nemitz, I.; Nemchinov, A.; Zamkov, M. *ACS Nano* **2010**, *4*, 1837.

[119] Wu, K.; Hill, L. J.; Chen, J.; McBride, J. R.; Pavlopolous, N. G.; Richey, N. E.; Pyun, J.; Lian, T. *ACS Nano* **2015**, *9*, 4591.

[120] Chuang, C.-H.; Lo, S. S.; Scholes, G. D.; Burda, C. *J. Phys. Chem. Lett.* **2010**, *1*, 2530.

[121] Allione, M.; Ballester, A.; Li, H.; Comin, A.; Movilla, J. L.; Climente, J. I.; Manna, L.; Moreels, I. *ACS Nano* **2013**, *7*, 2443.

[122] Kobayashi, Y.; Chuang, C.-H.; Burda, C.; Scholes, G. D. *J. Phys. Chem. C* **2014**, *118*, 16255.

[123] Korgel, B. A.; Monbouquette, H. G. *Langmuir* **2000**, *16*, 3588.

[124] Rogach, A. L.; Harrison, M. T.; Kershaw, S. V.; Kornowski, A.; Burt, M. G.; Eychmüller, A.; Weller, H. *physica status solidi (b)* **2001**, *224*, 153.

[125] Li, L.; Lu, H.; Yang, Z.; Tong, L.; Bando, Y.; Golberg, D. *Adv. Mater.* **2013**, *25*, 1109.

[126] Pan, Z.; Zhao, K.; Wang, J.; Zhang, H.; Feng, Y.; Zhong, X. *ACS Nano* **2013**, *7*, 5215.

[127] Maity, P.; Debnath, T.; Ghosh, H. N. *J. Phys. Chem. C* **2015**, *119*, 10785.

[128] Swafford, L. A.; Weigand, L. A.; Bowers, M. J.; McBride, J. R.; Rapaport, J. L.; Watt, T. L.; Dixit, S. K.; Feldman, L. C.; Rosenthal, S. J. *J. Am. Chem. Soc.* **2006**, *128*, 12299.

[129] Bailey, R. E.; Nie, S. *J. Am. Chem. Soc.* **2003**, *125*, 7100.

[130] Sarma, D. D.; Nag, A.; Santra, P. K.; Kumar, A.; Sapra, S.; Mahadevan, P. *J. Phys. Chem. Lett.* **2010**, *1*, 2149.

[131] Kaniyankandy, S.; Rawalekar, S.; Ghosh, H. N. *J. Mater. Chem. C* **2013**, *1*, 2755.

[132] Ancona, M. G.; Kooi, S. E.; Kruppa, W.; Snow, A. W.; Foos, E. E.; Whitman, L. J.; Park, D.; Shirey, L. *Nano Lett.* **2003**, *3*, 135.

[133] Lam, C.; Zhang, Y. F.; Tang, Y. H.; Lee, C. S.; Bello, I.; Lee, S. T. *J. Cryst. Growth* **2000**, *220*, 466.

[134] Burda, C.; Chen, X.; Narayanan, R.; El-Sayed, M. A. *Chem. Rev.* **2005**, *105*, 1025.

[135] Thessing, J.; Qian, J.; Chen, H.; Pradhan, N.; Peng, X. *J. Am. Chem. Soc.* **2007**, *129*, 2736.

[136] LaMer, V. K.; Dinegar, R. H. *J. Am. Chem. Soc.* **1950**, *72*, 4847.

[137] Murray, C. B.; Sun, S.; Gaschler, W.; Doyle, H.; Betley, T. A.; Kagan, C. R. *IBM J. Res. Dev.* **2001**, *45*, 47.

[138] Liu, H.; Owen, J. S.; Alivisatos, A. P. *J. Am. Chem. Soc.* **2007**, *129*, 305.

[139] Steckel, J. S.; Yen, B. K. H.; Oertel, D. C.; Bawendi, M. G. *J. Am. Chem. Soc.* **2006**, *128*, 13032.

[140] Marcus, R. A. *J. Chem. Phys.* **1956**, *24*, 966.

[141] Marcus, R. A. *Annu. Rev. Phys. Chem.* **1964**, *15*, 155.

[142] Marcus, R. A.; Sutin, N. *Biochimica et Biophysica Acta (BBA) - Reviews on Bioenergetics* **1985**, *811*, 265.

[143] Yan, S. G.; Prieskorn, J. S.; Kim, Y.; Hupp, J. T. *J. Phys. Chem. B* **2000**, *104*, 10871.

[144] Dang, X.; Hupp, J. T. *J. Am. Chem. Soc.* **2002**, *122*, 10956.

[145] *Electron Transfer in Chemistry*, V. Balzani, Wiley-VCH, Weinheim, **2001**.

[146] Watson, D. F.; Meyer, G. J. *Annu. Rev. Phys. Chem.* **2005**, *56*, 119.

[147] Kamat, P. V. *J. Phys. Chem. Lett.* **2013**, *4*, 908.

[148] Barea, E. M.; Shalom, M.; Giménez, S.; Hod, I.; Mora-Seró, I.; Zaban, A.; Bisquert, J. *J. Am. Chem. Soc.* **2010**, *132*, 6834.

[149] Sargent, E. H. *Nat Photon* **2012**, *6*, 133.

[150] Hetsch, F.; Xu, X.; Wang, H.; Kershaw, S. V.; Rogach, A. L. *J. Phys. Chem. Lett.* **2011**, *2*, 1879.

[151] Maldonado, S.; Fitchi, A. G.; Lewis, N. S.; Archer, M. A.; Nozik, A. J. *Semiconductor/Liquid Junction Photoelectrochemical Solar Cells*, **2010**.

[152] Bard, A. J.; Stratmann, M.; Licht, S. **2007**.

[153] Bisquert, J.; Cahen, D.; Hodes, G.; Rühle, S.; Zaban, A. *J. Phys. Chem. B* **2004**, *108*, 8106.

[154] Tian, J.; Gao, R.; Zhang, Q.; Zhang, S.; Li, Y.; Lan, J.; Qu, X.; Cao, G. *J. Phys. Chem. C* **2012**, *116*, 18655.

[155] Yu, X.-Y.; Lei, B.-X.; Kuang, D.-B.; Su, C.-Y. *Chemical Science* **2011**, *2*, 1396.

[156] Lee, Y.-L.; Lo, Y.-S. *Adv. Funct. Mater.* **2009**, *19*, 604.

[157] Becker, M. A.; Radich, J. G.; Bunker, B. A.; Kamat, P. V. *J. Phys. Chem. Lett.* **2014**, *5*, 1575.

[158] Lee, H.; Wang, M.; Chen, P.; Gamelin, D. R.; Zakeeruddin, S. M.; Grätzel, M.; Nazeeruddin, M. K. *Nano Lett.* **2009**, *9*, 4221.

[159] Santra, P. K.; Nair, P. V.; George Thomas, K.; Kamat, P. V. *J. Phys. Chem. Lett.* **2013**, *4*, 722.

[160] Li, W.; Zhong, X. *J. Phys. Chem. Lett.* **2015**, *6*, 796.

[161] Warren, B. E. *X-Ray Diffraction*, Dover Publications, **1990**.

[162] Authier, A. *Dynamical Theory of X-Ray Diffraction*, IUCr & Oxford Science Publication., **2001**.

[163] Joint Committee on Powder Diffraction Standards (JCPDS), International Centre for Diffraction Data (ICDD), Swarthmore, PA. .

[164] Cowley, J. M.; Smith, D. J. *Acta Crystallographica Section A* **1987**, *43*, 737.

[165] Williams, D. B.; Carter, C. B. *Transmission Electron Microscopy: A Textbook for Materials Science, Vol. 2nd ed*, **2009**.

[166] Howie, A.; Whelan, M. J. *Proceedings of the Royal Society of London A: Mathematical, Physical and Engineering Sciences* **1961**, *263*, 217.

[167] Reimer, L. *Transmission Electron Microscopy: Physics of Image Formation and Microanalysis*, Springer, **1997**.

[168] Otten, M. T.; Coene, W. M. J. *Ultramicroscopy, Vol. 48*, **1993**.

[169] Erni, R. *Aberration-Corrected Imaging in Transmission Electron Microscopy: An Introduction*, Imperial College Press, London, **2010**.

[170] Reimer, L.; Kohl, H. *Transmission Electron Microscopy: Physics of Image Formation, Vol. 4th Edition*, Springer Science + Business Media, **2008**.

[171] Hollas, J. M. *Modern Spectroscopy*, 3rd Ed., John Wiley and Sons, **1996**.

[172] Bernath, P. F. *Spectra of Atoms and Molecules*, Oxford University Press, **1995**.

[173] Smith, B. C. *Quantitative Spectroscopy: Theory and Practice*, Academic Press, **2002**.

[174] Lakowicz, J. R. *Principles of Fluorescence Spectroscopy*, 3rd ed., Springer, New York, **2006**.

[175] Albani, J. R. *Principles and applications of Fluorescence Spectroscopy*, Blackwell Publishing, **2007**.

[176] Crosby, G. A.; Demas, J. N. *J. Phys. Chem.* **1971**, *75*, 991.

[177] O'Connor, D. V.; Phillips, D. *Time-Correlated Single-Photon Counting*, Academic Press: London, **1984**.

[178] Becker, W. *Advanced Time-Correlated Single Photon Counting Techniques*, Springer, **2005**.

[179] Kahlow, M. A.; Jarzęba, W. o.; DuBruil, T. P.; Barbara, P. F. *Rev. Sci. Instrum.* **1988**, *59*, 1098.

[180] Shah, J. *IEEE Journal of Quantum Electronics* **1988**, *24*, 276.

[181] Shah, J. *Ultrafast Spectroscopy of Semiconductors and Semiconductor Nanostructures*, 2nd Ed., Springer, **1999**.

[182] Foggi, P.; Bussotti, L.; Neuwahl, F. V. R. *International Journal of Photoenergy* **2001**, *3*, 103.

[183] Moulton, P. F. *J. Opt. Soc. Am. B* **1986**, *3*, 125.

[184] Harrison, J.; Finch, A.; Rines, D. M.; Rines, G. A.; Moulton, P. F. *Opt. Lett.* **1991**, *16*, 581.

[185] Demtröder, W. *Laser Spectroscopy: Basic Concept and Instrumentation*, 3rd edition, Springer (India) Private Limited, **2004**.

[186] Sanchez, A.; Fahey, R. E.; Strauss, A. J.; Aggarwal, R. L. *Opt. Lett.* **1986**, *11*, 363.

[187] Abramczyk, H. *Introduction to Laser Spectroscopy*, Elsevier, **2005**.

[188] Steinmeyer, G.; Sutter, D. H.; Gallmann, L.; Matuschek, N.; Keller, U. *Science* **1999**, *286*, 1507.

[189] Brabec, T.; Spielmann, C.; Curley, P. F.; Krausz, F. *Opt. Lett.* **1992**, *17*, 1292.

[190] Asaki, M. T.; Huang, C.-P.; Garvey, D.; Zhou, J.; Kapteyn, H. C.; Murnane, M. M. *Opt. Lett.* **1993**, *18*, 977.

[191] Sarukura, N.; Ishida, Y.; Nakano, H. *Opt. Lett.* **1991**, *16*, 153.

[192] Zhu, X.; Piché, M.; Goodnob, G. D.; Miller, R. J. D. *Opt. Comm.* **1998**, *145*, 123.

[193] Martin, M. M.; Hynes, J. T. *Femtochemistry and Femtobiology: Ultrafast Events in Molecular Science*, Elsevier, 1st edition, **2004**.

[194] Strickland, D.; Mourou, G. *Opt. Comm.* **1985**, *56*, 219.

[195] Rullière, C. *Femtosecond Laser Pulses: Principles and Experiments*, Springer Science + Business Media, **2005**.

[196] Georges, P.; Estable, F.; Salin, F.; Poizat, J. P.; Grangier, P.; Brun, A. *Opt. Lett.* **1991**, *16*, 144.

[197] Treacy, E. *IEEE Journal of Quantum Electronics* **1969**, *5*, 454.

[198] Diels, J.-C.; Rudolph, W. *Ultrashort Laser Pulse Phenomena: Fundamentals, Techniques, and Applications on a Femtosecond Time Scale*, 2nd edition, Academic Press, Elsevier, **2006**.

[199] Fielden, E. M. *in The Study of Fast Processes and Transient Species by Electron Pulse Radiolysis Edited: J. H. Baxendale, F. Busi, Vol. 59*, Springer, **1982**.

[200] Benasson, R. V.; E, J. L.; Trusscott, T. G. *Flash Photolysis and Pulse Radiolysis*, Pergamon, Oxford University Press, Oxford, **1983**.

[201] Yu, W. W.; Peng, X. *Angew. Chem. Int. Ed.* **2002**, *41*, 2368.

[202] Yu, W. W.; Qu, L.; Guo, W.; Peng, X. *Chem. Mater.* **2003**, *15*, 2854.

[203] Protesescu, L.; Yakunin, S.; Bodnarchuk, M. I.; Krieg, F.; Caputo, R.; Hendon, C. H.; Yang, R. X.; Walsh, A.; Kovalenko, M. V. *Nano Lett.* **2015**, *15*, 3692.

[204] Nan, W.; Niu, Y.; Qin, H.; Cui, F.; Yang, Y.; Lai, R.; Lin, W.; Peng, X. *J. Am. Chem. Soc.* **2012**, *134*, 19685.

[205] Peng, X.; Schlamp, M. C.; Kadavanich, A. V.; Alivisatos, A. P. *J. Am. Chem. Soc.* **1997**, *119*, 7019.

[206] Guin, S. K.; Pillai, J. S.; Ambolikar, A. S.; Saha, A.; Aggarwal, S. K. *RSC Advances* **2013**, *3*, 17977.

[207] Carey, G. H.; Abdelhady, A. L.; Ning, Z.; Thon, S. M.; Bakr, O. M.; Sargent, E. H. *Chem. Rev.* **2015**, *115*, 12732.

[208] Snaith, H. J. *J. Phys. Chem. Lett.* **2013**, *4*, 3623.

[209] Burda, C.; Chen, X.; Narayanan, R.; El-Sayed, M. A. *Chem. Rev.* **2005**, *105*, 1025.

[210] Stewart, J. T.; Padilha, L. A.; Bae, W. K.; Koh, W.-K.; Pietryga, J. M.; Klimov, V. I. *J. Phys. Chem. Lett.* **2013**, *4*, 2061.

[211] Choi, S.; Jin, H.; Bang, J.; Kim, S. *J. Phys. Chem. Lett.* **2012**, *3*, 3442.

[212] Mora-Seró, I.; Bisquert, J. *J. Phys. Chem. Lett.* **2010**, *1*, 3046.

[213] Hod, I.; Zaban, A. *Langmuir* **2014**, *30*, 7264.

[214] Wang, J.; Li, Y.; Shen, Q.; Izuishi, T.; Pan, Z.; Zhao, K.; Zhong, X. *J. Mater. Chem. A* **2016**, *4*, 877.

[215] Robel, I.; Subramanian, V.; Kuno, M.; Kamat, P. V. *J. Am. Chem. Soc.* **2006**, *128*, 2385.

[216] Huang, J.; Huang, Z.; Yang, Y.; Zhu, H.; Lian, T. *J. Am. Chem. Soc.* **2010**, *132*, 4858.

[217] Song, N.; Zhu, H.; Jin, S.; Lian, T. *ACS Nano* **2011**, *5*, 8750.

[218] Nozik, A. J. *Annu. Rev. Phys. Chem.* **2001**, *52*, 193.

[219] Tisdale, W. A.; Williams, K. J.; Timp, B. A.; Norris, D. J.; Aydil, E. S.; Zhu, X.-Y. *Science* **2010**, *328*, 1543.

[220] Yang, Y.; Rodríguez-Córdoba, W.; Xiang, X.; Lian, T. *Nano Lett.* **2012**, *12*, 303.

[221] Robel, I.; Kuno, M.; Kamat, P. V. *J. Am. Chem. Soc.* **2007**, *129*, 4136.

[222] Morris-Cohen, A. J.; Frederick, M. T.; Cass, L. C.; Weiss, E. A. *J. Am. Chem. Soc.* **2011**, *133*, 10146.

[223] Lee, H.; Leventis, H. C.; Moon, S.-J.; Chen, P.; Ito, S.; Haque, S. A.; Torres, T.; Nüesch, F.; Geiger, T.; Zakeeruddin, S. M., et al. *Adv. Funct. Mater.* **2009**, *19*, 2735.

[224] Choi, H.; Nicolaescu, R.; Paek, S.; Ko, J.; Kamat, P. V. *ACS Nano* **2011**, *5*, 9238.

[225] Wang, Y.; Hang, K.; Anderson, N. A.; Lian, T. *J. Phys. Chem. B* **2003**, *107*, 9434.

[226] Ramakrishna, G.; Ghosh, H. N.; Singh, A. K.; Palit, D. K.; Mittal, J. P. *J. Phys. Chem. B* **2001**, *105*, 12786.

[227] Förster, T. *Ann. Phys.* **1948**, *437*, 55.

[228] Scholes, G. D. *Annu. Rev. Phys. Chem.* **2003**, *54*, 57.

[229] Mor, G. K.; Basham, J.; Paulose, M.; Kim, S.; Varghese, O. K.; Vaish, A.; Yoriya, S.; Grimes, C. A. *Nano Lett.* **2010**, *10*, 2387.

[230] Hardin, B. E.; Hoke, E. T.; Armstrong, P. B.; Yum, J.; Comte, P.; Mcgehee, M. D.; Nazeeruddin, K.; Gra, M.; Fre, J. M. J. *Nat. Photonics* **2009**, *3*, 406.

[231] Hadar, I.; Halivni, S.; Even-Dar, N. a.; Faust, A.; Banin, U. *J. Phys. Chem. C* **2015**, *119*, 3849.

[232] Sen, T.; Patra, A. *J. Phys. Chem. C* **2012**, *116*, 17307.

[233] Dana, J.; Debnath, T.; Maity, P.; Ghosh, H. N. *J. Phys. Chem. C* **2015**, *119*, 2046.

[234] Quach, A. D.; Crivat, G.; Tarr, M. A.; Rosenzweig, Z. *J. Am. Chem. Soc.* **2011**, *133*, 2028.

[235] Clapp, A. R.; Medintz, I. L.; Mauro, J. M.; Fisher, B. R.; Bawendi, M. G.; Mattoussi, H. *J. Am. Chem. Soc.* **2004**, *126*, 301.

[236] Snee, P. T.; Tyrakowski, C. M.; Page, L. E.; Isovic, A.; Jawaid, A. M. *J. Phys. Chem. C* **2011**, *115*, 19578.

[237] Dworak, L.; Matylitsky, V. V.; Ren, T.; Basché, T.; Wachtveitl, J. *J. Phys. Chem. C* **2014**, *118*, 4396.

[238] Crooker, S. A.; Hollingsworth, J. A.; Tretiak, S.; Klimov, V. I. *Phys. Rev. Lett.* **2002**, *89*, 186802.

[239] Scholes, G. D.; Andrews, D. L. *Phys. Rev. B* **2005**, *72*, 125331.

[240] Curutchet, C.; Franceschetti, A.; Zunger, A.; Scholes, G. D. *J. Phys. Chem. C* **2008**, *112*, 13336.

[241] Rogach, A. L.; Klar, T. A.; Lupton, J. M.; Meijerink, A.; Feldmann, J. *J. Mater. Chem.* **2009**, *19*, 1208.

[242] Shankar, K.; Feng, X.; Grimes, C. A. *ACS Nano* **2009**, *3*, 788.

[243] Sadhu, S.; Haldar, K. K.; Patra, A. *J. Phys. Chem. C* **2010**, *114*, 3891.

[244] Choi, H.; Santra, P. K.; Kamat, P. V. *ACS Nano* **2012**, *6*, 5718.

[245] Buhbut, S.; Itzhakov, S.; Tauber, E.; Shalom, M.; Hod, I.; Geiger, T.; Garini, Y.; Oron, D.; Zaban, A. *ACS Nano* **2010**, *4*, 1293.

[246] Walker, B. J.; Bulović, V.; Bawendi, M. G. *Nano Lett.* **2010**, *10*, 3995.

[247] Zheng, K.; Žídek, K.; Abdellah, M.; Zhu, N.; Chábera, P.; Lenngren, N.; Chi, Q.; Pullerits, T. *J. Am. Chem. Soc.* **2014**, *136*, 6259.

[248] Hoffman, J. B.; Choi, H.; Kamat, P. V. *J. Phys. Chem. C* **2014**, *118*, 18453.

[249] Rajh, T.; Chen, L. X.; Lukas, K.; Liu, T.; Thurnauer, M. C.; Tiede, D. M. *J. Phys. Chem. B* **2002**, *106*, 10543.

[250] Maity, P.; Debnath, T.; Akbar, A.; Verma, S.; Ghosh, H. N. *J. Phys. Chem. C* **2013**, *117*, 17531.

[251] Singh-Rachford, T.; Haefele, A.; d Ziessel, R.; Castellano, F. N. *J. Am. Chem. Soc.* **2008**, *130*, 16164.

[252] Rettig, W. *Angew. Chem.* **1986**, *25*, 971.

[253] Hu, R.; Lager, E.; Aguilar-Aguilar, A.; Liu, J.; Lam, J. W. Y.; Sung, H. H. Y.; Williams, I. D.; Zhong, Y.; Wong, K. S.; Pen˜a-Cabrera, E., et al. *J. Phys. Chem. C* **2009**, *113*, 15845.

[254] Zhang, C.; Zhao, J. W., S.; Wang, Z.; Wu, W.; Ma, J.; Guo, S.; Huang, L. *J. Am. Chem. Soc.* **2013**, *135*, 10566.

[255] Konstantatos, G.; Sargent, E. H. *Nat Nano* **2010**, *5*, 391.

[256] Kamat, P. V. *Acc. Chem. Res.* **2012**, *45*, 1906.

[257] Talapin, D. V.; Lee, J.-S.; Kovalenko, M. V.; Shevchenko, E. V. *Chem. Rev.* **2010**, *110*, 389.

[258] Lee, M. M.; Teuscher, J.; Miyasaka, T.; Murakami, T. N.; Snaith, H. J. *Science* **2012**, *338*, 643.

[259] Ahn, N.; Son, D.-Y.; Jang, I.-H.; Kang, S. M.; Choi, M.; Park, N.-G. *J. Am. Chem. Soc.* **2015**, *137*, 8696.

[260] Park, N.-G. *J. Phys. Chem. Lett.* **2013**, *4*, 2423.

[261] Chen, W.; Wu, Y.; Yue, Y.; Liu, J.; Zhang, W.; Yang, X.; Chen, H.; Bi, E.; Ashraful, I.; Grätzel, M., et al. *Science* **2015**, *350*, 944.

[262] Kulbak, M.; Gupta, S.; Kedem, N.; Levine, I.; Bendikov, T.; Hodes, G.; Cahen, D. *J. Phys. Chem. Lett.* **2016**, *7*, 167.

[263] Swarnkar, A.; Chulliyil, R.; Ravi, V. K.; Irfanullah, M.; Chowdhury, A.; Nag, A. *Angew. Chem. Int. Ed.* **2015**, *54*, 15424.

[264] Nedelcu, G.; Protesescu, L.; Yakunin, S.; Bodnarchuk, M. I.; Grotevent, M. J.; Kovalenko, M. V. *Nano Lett.* **2015**, *15*, 5635.

[265] Wu, K.; Liang, G.; Shang, Q.; Ren, Y.; Kong, D.; Lian, T. *J. Am. Chem. Soc.* **2015**, *137*, 12792.

[266] Akkerman, Q. A.; D'Innocenzo, V.; Accornero, S.; Scarpellini, A.; Petrozza, A.; Prato, M.; Manna, L. *J. Am. Chem. Soc.* **2015**, *137*, 10276.

[267] Kim, Y.; Yassitepe, E.; Voznyy, O.; Comin, R.; Walters, G.; Gong, X.; Kanjanaboos, P.; Nogueira, A. F.; Sargent, E. H. *ACS Appl. Mater. Interfaces* **2015**, *7*, 25007.

[268] Yakunin, S.; Protesescu, L.; Krieg, F.; Bodnarchuk, M. I.; Nedelcu, G.; Humer, M.; De Luca, G.; Fiebig, M.; Heiss, W.; Kovalenko, M. V. *Nat Commun* **2015**, *6*, **DOI:10.1038/ncomms9515**.

[269] Walters, G.; Sutherland, B. R.; Hoogland, S.; Shi, D.; Comin, R.; Sellan, D. P.; Bakr, O. M.; Sargent, E. H. *ACS Nano* **2015**, *9*, 9340.

[270] Kulbak, M.; Cahen, D.; Hodes, G. *J. Phys. Chem. Lett.* **2015**, *6*, 2452.

[271] Pan, J.; Sarmah, S. P.; Murali, B.; Dursun, I.; Peng, W.; Parida, M. R.; Liu, J.; Sinatra, L.; Alyami, N.; Zhao, C., et al. *J. Phys. Chem. Lett.* **2015**, *6*, 5027.

[272] Bekenstein, Y.; Koscher, B. A.; Eaton, S. W.; Yang, P.; Alivisatos, A. P. *J. Am. Chem. Soc.* **2015**, *137*, 16008.

[273] Zhang, X.; Lin, H.; Huang, H.; Reckmeier, C.; Zhang, Y.; Choy, W. C. H.; Rogach, A. L. *Nano Lett.* **2016**, *16*, 1415.

[274] Christians, J. A.; Miranda Herrera, P. A.; Kamat, P. V. *J. Am. Chem. Soc.* **2015**, *137*, 1530.

[275] Jeon, N. J.; Noh, J. H.; Yang, W. S.; Kim, Y. C.; Ryu, S.; Seo, J.; Seok, S. I. *Nature* **2015**, *517*, 476.

[276] Zhang, D.; Eaton, S. W.; Yu, Y.; Dou, L.; Yang, P. *J. Am. Chem. Soc.* **2015**, *137*, 9230.

[277] Zhang, F.; Zhong, H.; Chen, C.; Wu, X.-g.; Hu, X.; Huang, H.; Han, J.; Zou, B.; Dong, Y. *ACS Nano* **2015**, *9*, 4533.

[278] Tyagi, P.; Arveson, S. M.; Tisdale, W. A. *J. Phys. Chem. Lett.* **2015**, *6*, 1911.

[279] Hoke, E. T.; Slotcavage, D. J.; Dohner, E. R.; Bowring, A. R.; Karunadasa, H. I.; McGehee, M. D. *Chemical Science* **2015**, *6*, 613.

[280] Hassan, Y.; Song, Y.; Pensack, R. D.; Abdelrahman, A. I.; Kobayashi, Y.; Winnik, M. A.; Scholes, G. D. *Adv. Mater*. **2016**, *28*, 566.

[281] Abdelhady, A. L.; Saidaminov, M. I.; Murali, B.; Adinolfi, V.; Voznyy, O.; Katsiev, K.; Alarousu, E.; Comin, R.; Dursun, I.; Sinatra, L., et al. *J. Phys. Chem. Lett.* **2016**, *7*, 295.

[282] Zhang, W.; Saliba, M.; Moore, D. T.; Pathak, S. K.; Hörantner, M. T.; Stergiopoulos, T.; Stranks, S. D.; Eperon, G. E.; Alexander-Webber, J. A.; Abate, A., et al. *Nat Commun* **2015**, *6*, **DOI:10.1038/ncomms7142**.

[283] Manser, J. S.; Reid, B.; Kamat, P. V. *J. Phys. Chem. C* **2015**, *119*, 17065.

[284] Maculan, G.; Sheikh, A. D.; Abdelhady, A. L.; Saidaminov, M. I.; Haque, M. A.; Murali, B.; Alarousu, E.; Mohammed, O. F.; Wu, T.; Bakr, O. M. *J. Phys. Chem. Lett.* **2015**, *6*, 3781.

[285] Park, Y.-S.; Guo, S.; Makarov, N. S.; Klimov, V. I. *ACS Nano* **2015**, *9*, 10386.

[286] Cai, B.; Xing, Y.; Yang, Z.; Zhang, W.-H.; Qiu, J. *Energy & Environmental Science* **2013**, *6*, 1480.

[287] Luo, J.; Im, J.-H.; Mayer, M. T.; Schreier, M.; Nazeeruddin, M. K.; Park, N.-G.; Tilley, S. D.; Fan, H. J.; Grätzel, M. *Science* **2014**, *345*, 1593.

[288] Sutherland, B. R.; Hoogland, S.; Adachi, M. M.; Wong, C. T. O.; Sargent, E. H. *ACS Nano* **2014**, *8*, 10947.

[289] Noh, J. H.; Im, S. H.; Heo, J. H.; Mandal, T. N.; Seok, S. I. *Nano Lett.* **2013**, *13*, 1764.

[290] Zhao, Y.; Nardes, A. M.; Zhu, K. *J. Phys. Chem. Lett.* **2014**, *5*, 490.

[291] Guo, Z.; Manser, J. S.; Wan, Y.; Kamat, P. V.; Huang, L. *Nat Commun* **2015**, *6*, **doi:10.1038/ncomms8471**.

[292] Stranks, S. D.; Eperon, G. E.; Grancini, G.; Menelaou, C.; Alcocer, M. J. P.; Leijtens, T.; Herz, L. M.; Petrozza, A.; Snaith, H. J. *Science* **2013**, *342*, 341.

[293] Shi, D.; Adinolfi, V.; Comin, R.; Yuan, M.; Alarousu, E.; Buin, A.; Chen, Y.; Hoogland, S.; Rothenberger, A.; Katsiev, K., et al. *Science* **2015**, *347*, 519.

[294] Burschka, J.; Pellet, N.; Moon, S.-J.; Humphry-Baker, R.; Gao, P.; Nazeeruddin, M. K.; Gratzel, M. *Nature* **2013**, *499*, 316.

[295] Jeon, N. J.; Lee, J.; Noh, J. H.; Nazeeruddin, M. K.; Grätzel, M.; Seok, S. I. *J. Am. Chem. Soc.* **2013**, *135*, 19087.

[296] Christians, J. A.; Fung, R. C. M.; Kamat, P. V. *J. Am. Chem. Soc.* **2014**, *136*, 758.

[297] Pattanasattayavong, P.; Yaacobi-Gross, N.; Zhao, K.; Ndjawa, G. O. N.; Li, J.; Yan, F.; O'Regan, B. C.; Amassian, A.; Anthopoulos, T. D. *Adv.Mater.* **2013**, *25*, 1504.

[298] Maity, P.; Debnath, T.; Ghosh, H. N. *J. Phys. Chem. Lett.* **2013**, *4*, 4020.

[299] Maity, P.; Debnath, T.; Chopra, U.; Ghosh, H. N. *Nanoscale* **2015**, *7*, 2698.

[300] El-Sayed, M. A. *Acc. Chem. Res.* **2004**, *37*, 326.

[301] Currie, M. J.; Mapel, J. K.; Heidel, T. D.; Goffri, S.; Baldo, M. A. *Science* **2008**, *321*, 226.

[302] García-Santamaría, F.; Chen, Y.; Vela, J.; Schaller, R. D.; Hollingsworth, J. A.; Klimov, V. I. *Nano Lett.* **2009**, *9*, 3482.

[303] Talapin, D. V.; Gaponik, N.; Borchert, H.; Rogach, A. L.; Haase, M.; Weller, H. *J Phys Chem B* **2002**, *106*.

[304] Müller, J.; Lupton, J. M.; Lagoudakis, P. G.; Schindler, F.; Koeppe, R.; Rogach, A. L.; Feldmann, J.; Talapin, D. V.; Weller, H. *Nano Lett.* **2005**, *5*, 2044.

[305] Lupo, M. G.; Della Sala, F.; Carbone, L.; Zavelani-Rossi, M.; Fiore, A.; Lüer, L.; Polli, D.; Cingolani, R.; Manna, L.; Lanzani, G. *Nano Lett.* **2008**, *8*, 4582.

[306] Khon, E.; Lambright, K.; Khnayzer, R. S.; Moroz, P.; Perera, D.; Butaeva, E.; Lambright, S.; Castellano, F. N.; Zamkov, M. *Nano Lett.* **2013**, *13*, 2016.

[307] Rainò, G.; Stöferle, T.; Moreels, I.; Gomes, R.; Hens, Z.; Mahrt, R. F. *ACS Nano* **2012**, *6*, 1979.

[308] Yang, Z.; Chen, C.-Y.; Liu, C.-W.; Chang, H.-T. *Chem. Commun.* **2010**, *46*, 5485.

[309] Zhang, Q.; Guo, X.; Huang, X.; Huang, S.; Li, D.; Luo, Y.; Shen, Q.; Toyoda, T.; Meng, Q. *Phys. Chem. Chem. Phys.* **2011**, *13*, 4659.

[310] Debnath, T.; Maity, P.; Ghosh, H. N. *Chemistry – A European Journal* **2014**, *20*, 13305.

[311] Ma, X.; Mews, A.; Kipp, T. *J. Phys. Chem. C* **2013**, *117*, 16698.

[312] Boldt, K.; Ramanan, C.; Chanaewa, A.; Werheid, M.; Eychmüller, A. *J. Phys. Chem. Lett.* **2015**, *6*, 2590.

[313] Verma, S.; Kaniyankandy, S.; Ghosh, H. N. *J. Phys. Chem. C* **2013**, *117*, 10901.

[314] Greytak, A. B.; Allen, P. M.; Liu, W.; Zhao, J.; Young, E. R.; Popovic, Z.; Walker, B. J.; Nocera, D. G.; Bawendi, M. G. *Chemical Science* **2012**, *3*, 2028.

[315] Borys, N. J.; Walter, M. J.; Huang, J.; Talapin, D. V.; Lupton, J. M. *Science* **2010**, *330*, 1371.

[316] Talapin, D. V.; Koeppe, R.; Götzinger, S.; Kornowski, A.; Lupton, J. M.; Rogach, A. L.; Benson, O.; Feldmann, J.; Weller, H. *Nano Lett.* **2003**, *3*, 1677.

[317] Chen, O.; Zhao, J.; Chauhan, V. P.; Cui, J.; Wong, C.; Harris, D. K.; Wei, H.; Han, H.-S.; Fukumura, D.; Jain, R. K., et al. *Nat Mater* **2013**, *12*, 445.

[318] Saba, M.; Minniberger, S.; Quochi, F.; Roither, J.; Marceddu, M.; Gocalinska, A.; Kovalenko, M. V.; Talapin, D. V.; Heiss, W.; Mura, A., et al. *Adv. Mater.* **2009**, *21*, 4942.

[319] Bae, W. K.; Padilha, L. A.; Park, Y.-S.; McDaniel, H.; Robel, I.; Pietryga, J. M.; Klimov, V. I. *ACS Nano* **2013**, *7*, 3411.

[320] Zhu, G.; Pan, L.; Xu, T.; Sun, Z. *ACS Appl. Mater. Interfaces* **2011**, *3*, 1472.

[321] Klimov, V. I. *J. Phys. Chem. B* **2000**, *104*, 6112.

[322] Boldt, K.; Schwarz, K. N.; Kirkwood, N.; Smith, T. A.; Mulvaney, P. *J. Phys. Chem. C* **2014**, *118*, 13276.

[323] Rawalekar, S.; Kaniyankandy, S.; Verma, S.; Ghosh, H. N. *J. Phys. Chem. C* **2010**, *114*, 1460.

[324] Mohamed, M. B.; Tonti, D.; Al-Salman, A.; Chemseddine, A.; Chergui, M. *J. Phys. Chem. B* **2005**, *109*, 10533.

[325] Kaniyankandy, S.; Rawalekar, S.; Verma, S.; Palit, D. K.; Ghosh, H. N. *Phys. Chem. Chem. Phys.* **2010**, *12*, 4210.

[326] Knowles, K. E.; Malicki, M.; Weiss, E. A. *J. Am. Chem. Soc.* **2012**, *134*, 12470.

[327] Malicki, M.; Knowles, K. E.; Weiss, E. A. *Chem. Commun.* **2013**, *49*, 4400.

[328] Aruda, K. O.; Bohlmann Kunz, M.; Tagliazucchi, M.; Weiss, E. A. *J. Phys. Chem. Lett.* **2015**, *6*, 2841.

[329] Talapin, D. V.; Lee, J.-S.; Kovalenko, M. V.; Shevchenko, E. V. *Chem. Rev.* **2009**, *110*, 389.

[330] Kramer, I. J.; Sargent, E. H. *ACS Nano* **2011**, *5*, 8506.

[331] Kovalenko, M. V.; Manna, L.; Cabot, A.; Hens, Z.; Talapin, D. V.; Kagan, C. R.; Klimov, V. I.; Rogach, A. L.; Reiss, P.; Milliron, D. J., et al. *ACS Nano* **2015**, *9*, 1012.

[332] McGuire, J. A.; Joo, J.; Pietryga, J. M.; Schaller, R. D.; Klimov, V. I. *Acc. Chem. Res.* **2008**, *41*, 1810.

[333] Klimov, V. I.; Mikhailovsky, A. A.; McBranch, D. W.; Leatherdale, C. A.; Bawendi, M. G. *Phys. Rev. B* **2000**, *61*, R13349.

[334] Zhu, H.; Song, N.; Lian, T. *J. Am. Chem. Soc.* **2011**, *133*, 8762.

[335] Zhu, H.; Song, N.; Lian, T. *J. Am. Chem. Soc.* **2010**, *132*, 15038.

[336] Shalom, M.; Albero, J.; Tachan, Z.; Martínez-Ferrero, E.; Zaban, A.; Palomares, E. *J. Phys. Chem. Lett.* **2010**, *1*, 1134.

[337] Wang, Y.-F.; Wang, H.-Y.; Li, Z.-S.; Zhao, J.; Wang, L.; Chen, Q.-D.; Wang, W.-Q.; Sun, H.-B. *J. Phys. Chem. C* **2014**, *118*, 17240.

[338] Sykora, M.; Petruska, M. A.; Alstrum-Acevedo, J.; Bezel, I.; Meyer, T. J.; Klimov, V. I. *J. Am. Chem. Soc.* **2006**, *128*, 9984.

[339] Koposov, A. Y.; Szymanski, P.; Cardolaccia, T.; Meyer, T. J.; Klimov, V. I.; Sykora, M. *Adv. Funct. Mater.* **2011**, *21*, 3159.

[340] Huang, J.; Stockwell, D.; Huang, Z.; Mohler, D. L.; Lian, T. *J. Am. Chem. Soc.* **2008**, *130*, 5632.

[341] Debnath, T.; Maity, P.; Banerjee, T.; Das, A.; Ghosh, H. N. *J. Phys. Chem. C* **2015**, *119*, 3522.

[342] Choi, H.; Kamat, P. V. *J. Phys. Chem. Lett.* **2013**, *4*, 3983.

[343] Banerjee, T.; Kaniyankandy, S.; Das, A.; Ghosh, H. N. *J. Phys. Chem. C* **2013**, *117*, 3084.

[344] Kar, P.; Banerjee, T.; Verma, S.; Sen, A.; Das, A.; Ganguly, B.; Ghosh, H. N. *Phys. Chem. Chem. Phys.* **2012**, *14*, 8192.

[345] Maity, P.; Debnath, T.; Ghosh, H. N. *J. Phys. Chem. C* **2015**, *119*, 26202.

[346] Pan, A.; Zhou, W.; Leong, E. S. P.; Liu, R.; Chin, A. H.; Zou, B.; Ning, C. Z. *Nano Lett.* **2009**, *9*, 784.

[347] Lu, J.; Lim, X.; Zheng, M.; Mhaisalkar, S. G.; Sow, C.-H. *ACS Nano* **2012**, *6*, 8298.

[348] Keene, J. D.; McBride, J. R.; Orfield, N. J.; Rosenthal, S. J. *ACS Nano* **2014**, *8*, 10665.

[349] Santra, P. K.; Kamat, P. V. *J. Am. Chem. Soc.* **2013**, *135*, 877.

[350] Smith, D. K.; Luther, J. M.; Semonin, O. E.; Nozik, A. J.; Beard, M. C. *ACS Nano* **2011**, *5*, 183.

[351] Hou, B.; Parker, D.; Kissling, G. P.; Jones, J. A.; Cherns, D.; Fermín, D. J. *J. Phys. Chem. C* **2013**, *117*, 6814.

[352] Boldt, K.; Kirkwood, N.; Beane, G. A.; Mulvaney, P. *Chem. Mater*. **2013**, *25*, 4731.

[353] Wu, J.-C.; Zheng, J.; Zacherl, C. L.; Wu, P.; Liu, Z.-K.; Xu, R. *J. Phys. Chem. C* **2011**, *115*, 19741.

[354] Hossain, M. A.; Jennings, J. R.; Mathews, N.; Wang, Q. *Phys. Chem. Chem. Phys.* **2012**, *14*, 7154.

[355] Song, X.; Wang, M.; Deng, J.; Yang, Z.; Ran, C.; Zhang, X.; Yao, X. *ACS Appl. Mater. Interfaces* **2013**, *5*, 5139.

[356] Aubert, T.; Cirillo, M.; Flamee, S.; Van Deun, R.; Lange, H.; Thomsen, C.; Hens, Z. *Chem. Mater.* **2013**, *25*, 2388.

[357] Chen, Z.; Peng, W.; Zhang, K.; Zhang, J.; Yanagida, M.; Han, L. *Nanoscale* **2012**, *4*, 7690.

[358] Junpeng, L.; Cheng, S.; Minrui, Z.; Mathews, N.; Hongwei, L.; Gin Seng, C.; Xinhai, Z.; Mhaisalkar, S. G.; Chorng Haur, S. *J. Phys. Chem. C* **2011**, *115*, 19538.

[359] Silva, A. C. A.; da Silva, S. W.; Morais, P. C.; Dantas, N. O. *ACS Nano* **2014**, *8*, 1913.

[360] Li, G.; Jiang, Y.; Wang, Y.; Wang, C.; Sheng, Y.; Jie, J.; Zapien, J. A.; Zhang, W.; Lee, S.-T. *J. Phys. Chem. C* **2009**, *113*, 17183.

[361] Garrett, M. D.; Dukes Iii, A. D.; McBride, J. R.; Smith, N. J.; Pennycook, S. J.; Rosenthal, S. J. *J. Phys. Chem. C* **2008**, *112*, 12736.

[362] Kim, J.-P.; Christians, J. A.; Choi, H.; Krishnamurthy, S.; Kamat, P. V. *J. Phys. Chem. Lett.* **2014**, *5*, 1103.

[363] Zhong, X.; Han, M.; Dong, Z.; White, T. J.; Knoll, W. *J. Am. Chem. Soc.* **2003**, *125*, 8589.

[364] Pan, A.; Yang, H.; Liu, R.; Yu, R.; Zou, B.; Wang, Z. *J. Am. Chem. Soc.* **2005**, *127*, 15692.

[365] Ingole, P. P.; Markad, G. B.; Saraf, D.; Tatikondewar, L.; Nene, O.; Kshirsagar, A.; Haram, S. K. *J. Phys. Chem. C* **2013**, *117*, 7376.

[366] Efros, A. L.; Kharchenko, V. A.; Rosen, M. *Solid State Commun.* **1995**, *93*, 281.

[367] Cragg, G. E.; Efros, A. L. *Nano Lett.* **2010**, *10*, 313.

[368] Bae, W. K.; Char, K.; Hur, H.; Lee, S. *Chem. Mater*. **2008**, *20*, 531.

[369] Zhao, K.; Pan, Z.; Mora-Seró, I.; Cánovas, E.; Wang, H.; Song, Y.; Gong, X.; Wang, J.; Bonn, M.; Bisquert, J., et al. *J. Am. Chem. Soc.* **2015**, *137*, 5602.

[370] Zhao, K.; Pan, Z.; Zhong, X. *J. Phys. Chem. Lett.* **2016**, 406.

[371] Radich, J. G.; Dwyer, R.; Kamat, P. V. *J. Phys. Chem. Lett.* **2011**, *2*, 2453.

[372] Sun, W.-T.; Yu, Y.; Pan, H.-Y.; Gao, X.-F.; Chen, Q.; Peng, L.-M. *J. Am. Chem. Soc.* **2008**, *130*, 1124.

[373] Baker, D. R.; Kamat, P. V. *Adv. Funct. Mater*. **2009**, *19*, 805.

[374] Kongkanand, A.; Tvrdy, K.; Takechi, K.; Kuno, M.; Kamat, P. V. *J. Am. Chem. Soc.* **2008**, *130*, 4007.

[375] Leventis, H. C.; O'Mahony, F.; Akhtar, J.; Afzaal, M.; O'Brien, P.; Haque, S. A. *J. Am. Chem. Soc*. **2010**, *132*, 2743.

[376] Tachan, Z.; Shalom, M.; Hod, I.; Rühle, S.; Tirosh, S.; Zaban, A. *J. Phys. Chem. C* **2011**, *115*, 6162.

[377] Kim, S.; Marshall, A. R.; Kroupa, D. M.; Miller, E. M.; Luther, J. M.; Jeong, S.; Beard, M. C. *ACS Nano* **2015**, *9*, 8157.

[378] Schaller, R. D.; Klimov, V. I. *Phys. Rev. Lett.* **2004**, *92*, 186601.

[379] Li, T.-L.; Lee, Y.-L.; Teng, H. *Energy & Environmental Science* **2012**, *5*, 5315.

[380] Luo, J.; Wei, H.; Huang, Q.; Hu, X.; Zhao, H.; Yu, R.; Li, D.; Luo, Y.; Meng, Q. *Chem. Commun.* **2013**, *49*, 3881.

[381] Pan, Z.; Mora-Seró, I.; Shen, Q.; Zhang, H.; Li, Y.; Zhao, K.; Wang, J.; Zhong, X.; Bisquert, J. *J. Am. Chem. Soc.* **2014**, *136*, 9203.

[382] Li, W.; Pan, Z.; Zhong, X. *J. Mater. Chem. A* **2015**, *3*, 1649.

[383] Nelson, J. *The Physics of Solar Cells*, **2003**.

[384] Grancini, G.; Marras, S.; Prato, M.; Giannini, C.; Quarti, C.; De Angelis, F.; De Bastiani, M.; Eperon, G. E.; Snaith, H. J.; Manna, L., et al. *J. Phys. Chem. Lett.* **2014**, *5*, 3836.

[385] Santra, P. K.; Kamat, P. V. *J. Am. Chem. Soc.* **2012**, *134*, 2508.

[386] Jiao, S.; Shen, Q.; Mora-Seró, I.; Wang, J.; Pan, Z.; Zhao, K.; Kuga, Y.; Zhong, X.; Bisquert, J. *ACS Nano* **2015**, *9*, 908.

[387] Yu, X.-Y.; Liao, J.-Y.; Qiu, K.-Q.; Kuang, D.-B.; Su, C.-Y. *ACS Nano* **2011**, *5*, 9494.

[388] Hossain, M. A.; Jennings, J. R.; Koh, Z. Y.; Wang, Q. *ACS Nano* **2011**, *5*, 3172.

[389] Yang, J.; Wang, J.; Zhao, K.; Izuishi, T.; Li, Y.; Shen, Q.; Zhong, X. *J. Phys. Chem. C* **2015**, *119*, 28800.

[390] de la Fuente, M. S.; Sánchez, R. S.; González-Pedro, V.; Boix, P. P.; Mhaisalkar, S. G.; Rincón, M. E.; Bisquert, J.; Mora-Seró, I. *J. Phys. Chem. Lett.* **2013**, *4*, 1519.

[391] Sahasrabudhe, A.; Bhattacharyya, S. *Chem. Mater.* **2015**, *27*, 4848.

[392] Mora-Seró, I.; Giménez, S.; Fabregat-Santiago, F.; Gómez, R.; Shen, Q.; Toyoda, T.; Bisquert, J. *Acc. Chem. Res.* **2009**, *42*, 1848.

[393] Hodes, G. *J. Phys. Chem. C* **2008**, *112*, 17778.

[394] Allen, P. M.; Bawendi, M. G. *J. Am. Chem. Soc.* **2008**, *130*, 9240.

[395] Rawalekar, S.; Kaniyankandy, S.; Verma, S.; Ghosh, H. N. *J. Phys. Chem. C* **2009**, *114*, 1460.

[396] Kagan, C. R.; Murray, C. B.; Nirmal, M.; Bawendi, M. G. *Phys. Rev. Lett.* **1996**, *76*, 1517.